Super-resolution Fluorescence Microscopy

by

Shaoheng Li

(Under the Direction of Peter Kner)

Abstract

In biological research and biomedical imaging, visualizing cellular structures in detail is essential for advancing scientific understanding. Traditional fluorescence microscopy is limited by diffraction, making it insufficient for observing complex cellular processes such as mitochondrial dynamics and protein synthesis. This limitation has driven the development of super-resolution microscopy, which allows imaging beyond the diffraction limit. This dissertation presents two advanced super-resolution methods: Self-Interference Digital Holography-based 3D Single Molecule Localization Microscopy (SIDH-based 3D-SMLM) and 2D Non-linear Pattern Depletion Structured Illumination Microscopy (2D PD-NSIM).

SIDH-based 3D-SMLM combines digital holography with single molecule localization to achieve nanometer-scale resolution across a large axial range without mechanical refocusing, addressing the axial range limitations of traditional 3D-SMLM with Point Spread Function (PSF) engineering. A computational aberration correction approach further improves SIDH's performance. Numerical simulations show that optimized SIDH achieves lateral localization precision between 5 and 58 nm and axial precision between 13 and 80 nm at low signal-to-noise ratios (SNR). Experimental results show successful reconstruction of a 100 nm microsphere with low photon budgets ($\sim 4,200$ photons) over a 10 μm axial range. The guide-star-free adaptive optics method improves the Strehl ratio to as high as 0.98, restoring localization precision close to the ideal case even under strong aberrations.

The second method, 2D PD-NSIM, uses structured illumination and reversible fluorescent proteins to capture higher frequency information from the sample. This approach introduces non-linear effects, surpassing the conventional 2-fold resolution improvement of linear SIM, achieving sub-80 nm resolution, particularly suited for real-time super-resolution live-cell imaging. The dissertation details the principles, implementation, and results of 2D PD-NSIM.

This work offers significant advancements in super-resolution microscopy. Chapter 1 covers the basics of fluorescence microscopy and super-resolution techniques, while Chapters 2 and 3 detail the SIDH and PD-NSIM methods. Chapters 4 and 5 focus on optimizing SIDH, and Chapter 6 presents the experimental results for 2D PD-NSIM using rsEGFP2. Chapter 7 explores further polarization optimization to enhance PD-NSIM performance, concluding with a summary of findings in Chapter 8.

Index words: [Super-resolution microscopy, Fluorescence microscopy, Single Molecule Localization Microscopy, Self-Interference Digital Holography, Non-linear Structured Illumination Microscopy, live-cell imaging, Digital holography.]

Super-resolution Fluorescence Microscopy

by

Shaoheng Li

B.S., Henan University, China, 2018
M.S., University of Georgia, 2020

A Dissertation Submitted to the Graduate Faculty of the
University of Georgia in Partial Fulfillment of the Requirements for the Degree.

Doctor of Philosophy

Athens, Georgia

2024

Super-resolution Fluorescence Microscopy

by

Shaoheng Li

Major Professor: Peter Kner

Committee: Xianqiao Wang
Daiyichi Kamiyama
Mable Fok

Electronic Version Approved:

Ron Walcott
Dean of the Graduate School
The University of Georgia
December 2024

Acknowledgments

Firstly, I would like to express my deepest gratitude to my advisor, Dr. Peter Kner, for his guidance, support, and encouragement throughout my PhD journey. His professionalism, expertise, and patience have been invaluable in helping me shape this dissertation. His work ethic will continue to influence the way I conduct research.

I would also like to extend my sincere thanks to my committee members, Dr. Daichi Kamiyama, Dr. Xianqiao Wang, and Dr. Mable Fok. Thank you to Dr. Daichi Kamiyama for providing professional support during our collaboration. I am especially grateful to to Dr. Xianqiao Wang for being my Master's mentor and for his continuous support. I am also thankful to Dr. Mable Fok for her insightful suggestions and comments throughout my PhD journey.

I am also grateful to my colleagues and friends for their collaboration and assistance. Special thanks to my dear friend, Dr. Ning Liu, and my colleague, Dr. Ruizhe Lin, for their technical support and constructive discussions.

Thank you to my favorite person, Dr. Omar El Hajj, for his support, his bad and good jokes, and for always being himself.

Special thanks to Meadow, Pi, and Fungal.

Lastly, thanks to my mom, Ms. Yi Li, for her unconditional love and belief in me. Mom, a thousand times, thank you.

Contents

List of Figures

Chapter 1

Introduction

In the field of biological research and biomedical imaging, seeing intricate details within samples is crucial for major discoveries. Over time, many microscopy techniques have emerged, each using distinct principles to reveal what's invisible to the naked eye. Among these, the introduction of fluorescence microscopy was a significant discovery, revolutionizing the way we identify specific cellular structures and events. Fluorescence microscopy was first introduced by Heimstadt in 1911 [1], it uses fluorophores as markers to highlight specific parts of cells. By applying techniques such as Immunocytochemistry, transfection, and direct binding, these markers attach to distinct cellular components. When excited by light, these fluorophores emit light, allowing biologist to study many fine structures in cells, or other biological molecules. Moreover, the non-toxic nature of fluorescence microscopy offers a unique advantage for studying events inside living organism, tissues, and animals.

In the late 19 th century, Ernst Abbe identified that the resolution of fluorescence microscopy depends on the wavelength of light emitted by the sample (λ) and the numerical aperture of the objective (NA) [2], known as the 'diffraction limit.' The lateral and axial Abbe limits are defined as,

$$R_{xy} = \frac{\lambda}{2NA}, R_z \approx \frac{2\lambda}{NA^2} \tag{1.1}$$

For high numerical apertures, the diffraction limit of fluorescence microscopy is about 250 nm. However, there are many structures and events in cells that require observation at even higher resolution. For example, mitochondrial dynamics [3] involves intricate processes such as fusion, fission, and movement, which can provide insight into cellular health and energy production. Similarly, understanding the nuances of ribosomes and protein synthesis [4] is critical, as even slight variations or errors in these processes can result in malfunctioning proteins or diseases. Being able to observe these events with greater detail can offer deeper insights into cellular functions and mechanisms. Scientists in recent decades have worked to push the resolution beyond the diffraction limit, leading to the advent of super-resolution microscopy. Eric Betzig, Stefan Hell, and William Moerner received the Nobel Prize in Chemistry 2014 for their significant contributions to the development of super-resolution microscopy.

I start this chapter by introducing the principles of fluorescence microscopy and the optical imaging system. This segues into a basic discussion of the point spread function (PSF), which provides a

foundational understanding of the diffraction limit. Subsequently, I present an overview of existing super-resolution imaging methods. A more detailed discussion of the super-resolution methods relevant to this dissertation is covered in Chapters 2 and 3. Finally, I wrap up this chapter by outlining the scope of this dissertation.

1.1 Principle of fluorescence microscopy.

1.1.1 Jablonski diagram.

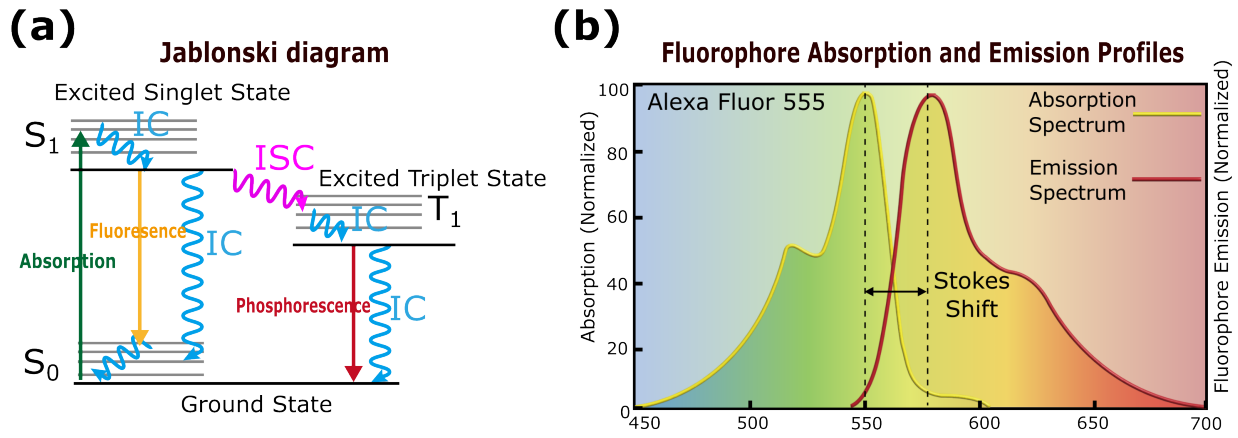

Figure 1.1: (a) Jablonski diagram showing the energy transitions in fluorescence. (b)Excitation and emission spectra of Alexa Flour 555.

Fluorescence Microscopy fundamentally relies on the interactions between light and matter, explained by the Jablonski diagram [5], as illustrated in Figure 1.1 (a). The interactions begin with a molecule in its ground electronic state, S_0 , absorbing radiation. This absorption process, represented as $S_0 \rightarrow S_1$ in the Jablonski diagram, is determined as much by the energy difference between the S_0 and S_1 states. A key observation to make here is that while we primarily assume molecules have singlet ground states, electronic absorption can involve transitions between vibrational energy levels as well. The energy differences between these vibrational levels correspond to the infrared region of the electromagnetic spectrum, which is the basis for infrared and Raman spectroscopy. However, in fluorescence microscopy, the focus is on electronic transitions, where the energy differences are in the ultraviolet or visible range, leading to the emission of fluorescence. Therefore, while vibrational energy levels are relevant in the context of infrared spectroscopy, fluorescence microscopy primarily involves electronic transitions.[6].

Following absorption, most molecules experience relaxation, mainly involving vibrational relaxation within the electronic state of S1 and subsequent fluorescence back to the ground state. However, other

non-radiative processes, such as internal conversion (IC) and intersystem crossing (ISC), may also occur. The latter, ISC, results in the molecule transitioning to a long-lived spin triplet T1 state, causing the molecule to be "dark" during this state, essentially pausing the absorption-fluorescence cycle. This stage can sometimes lead to photobleaching due to interactions with oxygen. If, however, the molecule returns to the electronic ground state from T1, it emits what we term phosphorescence instead of fluorescence.

Relaxation between vibrational levels in the electronic state S_1 before fluorescence emission can cause a redshift in the emitted light compared to the absorbed light, termed 'The Stokes shift'. For example, Alexa Fluor 555, as shown in Figure 1.1(b), gets excited at its absorption peak, which is typically around 555 nm, then it emits fluorescence at a longer wavelength, with an emission peak close to 565 nm. This 10 nm difference between absorption and emission wavelengths ensures that there is clear separation between the excitation and emission spectra, allowing for efficient fluorescence detection without interference from the excitation light. Consequently, a dichroic mirror can be used to separate the excitation from the emission, as shown in Figure 1.2(a). Moreover, the rates of these various processes—such as absorption, vibrational relaxation, internal conversion, intersystem crossing, and fluorescence emission—determine the overall outcomes in terms of fluorescence intensity, the likelihood of phosphorescence, and the extent of photobleaching. For instance, a higher rate of intersystem crossing to the triplet state can increase the probability of phosphorescence or photobleaching, while efficient vibrational relaxation and internal conversion lead to non-radiative energy loss, reducing fluorescence intensity. Therefore, understanding and controlling these rate processes is crucial for optimizing fluorescence signals and minimizing photobleaching in microscopy.

1.1.2 Basic Fluorescence microscopy.

The basic schematic of a fluorescence microscope is discussed in this section. More details about the specific methods used in this dissertation will be provided later in Chapter 2 and 3. As we mentioned in Section 1.1.1, fluorescence microscopy takes advantage of the Stokes shift between the absorption and emission spectra of the fluorescent molecules. As shown in Figure 1.2(a), the illumination light is first transmitted through an excitation filter, which selectively passes only the portion of the light spectrum that's suitable for exciting the fluorophore being studied. The emitted light from the sample then reflects off the dichroic mirror and is transmitted through the emission filter. As a result, only the light emitted from a specific fluorophore is detected by the detector, while the rest of the spectrum is effectively blocked. Therefore, all fluorescence microscopes contain three principal components: an illumination path, emission path, and a detector, as shown in Figure 1.2(a).

Illumination Path: All fluorescence microscopes require an illumination source to excite the fluorophores. Ideal sources exhibit a narrow spectral bandwidth, such as LEDs or lasers. The importance of the narrowed bandwidth of the light source lies in their ability to provide streamlined illumination, simplifying the filtering of undesired light. The strategies employed for illumination can vary significantly, determined predominantly by the geometry. A comprehensive examination of these methods is provided in ref [7, 8]. While various illumination strategies exist, the work presented in this dissertation is based on wide-field fluorescence microscopy and light-sheet illumination microscopy.

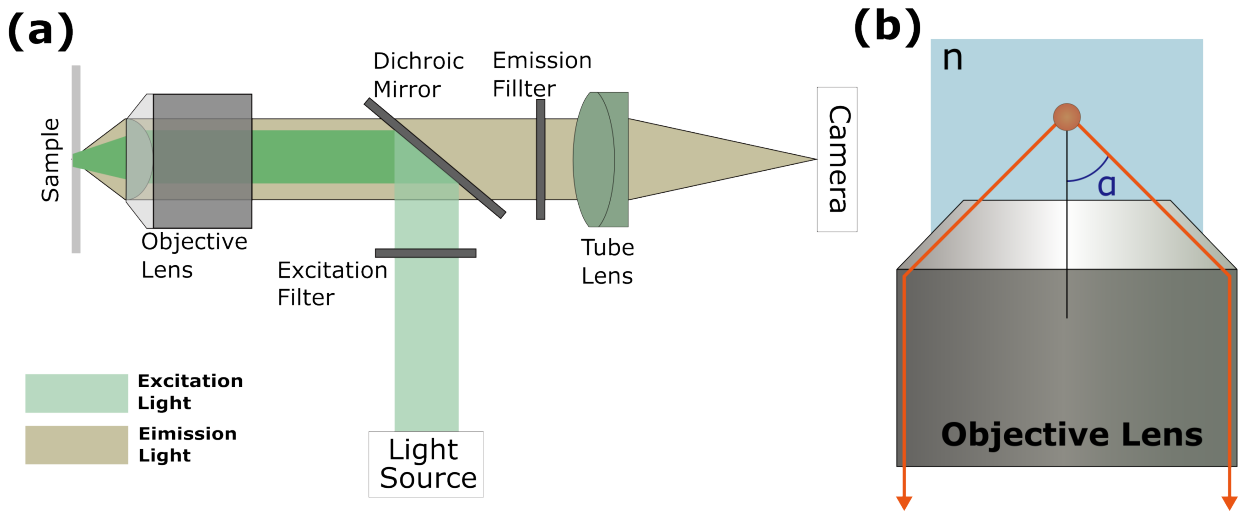

Figure 1.2: (a) Basic fluorescence microscope schematic. (b) Numerical aperture (NA). The objective collects light rays in a cone up to a limiting (half-) angle α with respect to the optical axis (black line). The objective immersion medium has refractive index n. The NA is given by Equation 1.2

Wide-field fluorescence microscopy involves simultaneous illumination over a large area within the biological sample, with fluorescence detection executed via a camera. Notably, the two most common techniques under wide-field fluorescence microscopy are total internal reflection fluorescence (TIRF) and epi-illumination. The work in this dissertation employed TIRF with non-linear structure illumination microscopy, details of TIRF will be discussed in Chapter 3.

Rather than illuminating the entire volume of the sample, as with epi illumination, light sheet illumination concentrates on illuminating a thin section of the sample, as shown in Figure 1.3. It offers two critical benefits when imaging biological samples. First, it enhances the signal-to-background ratio, allowing for clearer, more detailed images. Second, it prolongs the usable imaging time by reducing photobleaching of fluorescent probes that are not within the focused illumination volume. The simplest light sheet is formed by a cylindrical lens, which focuses the light in only one dimension. The illumination objective then focuses the light sheet, which is directed into the sample and excites only the plane of interest. In this dissertation, we proposed to combine a novel tilted light sheet illumination technique with our optical setup to perform single-molecule super-resolution 3D imaging.

Emission Path: After the fluorescence from the sample is emitted, the emission light needs to be collected effectively. The efficient collection is facilitated through the deployment of meticulously designed optical systems. While several components contribute to the overall performance of a fluorescence microscope, the objective lens and tube lens play essential roles in the capture and relay of emitted light to the detector. At the heart of the microscope's optical system is the objective lens, a complex assembly

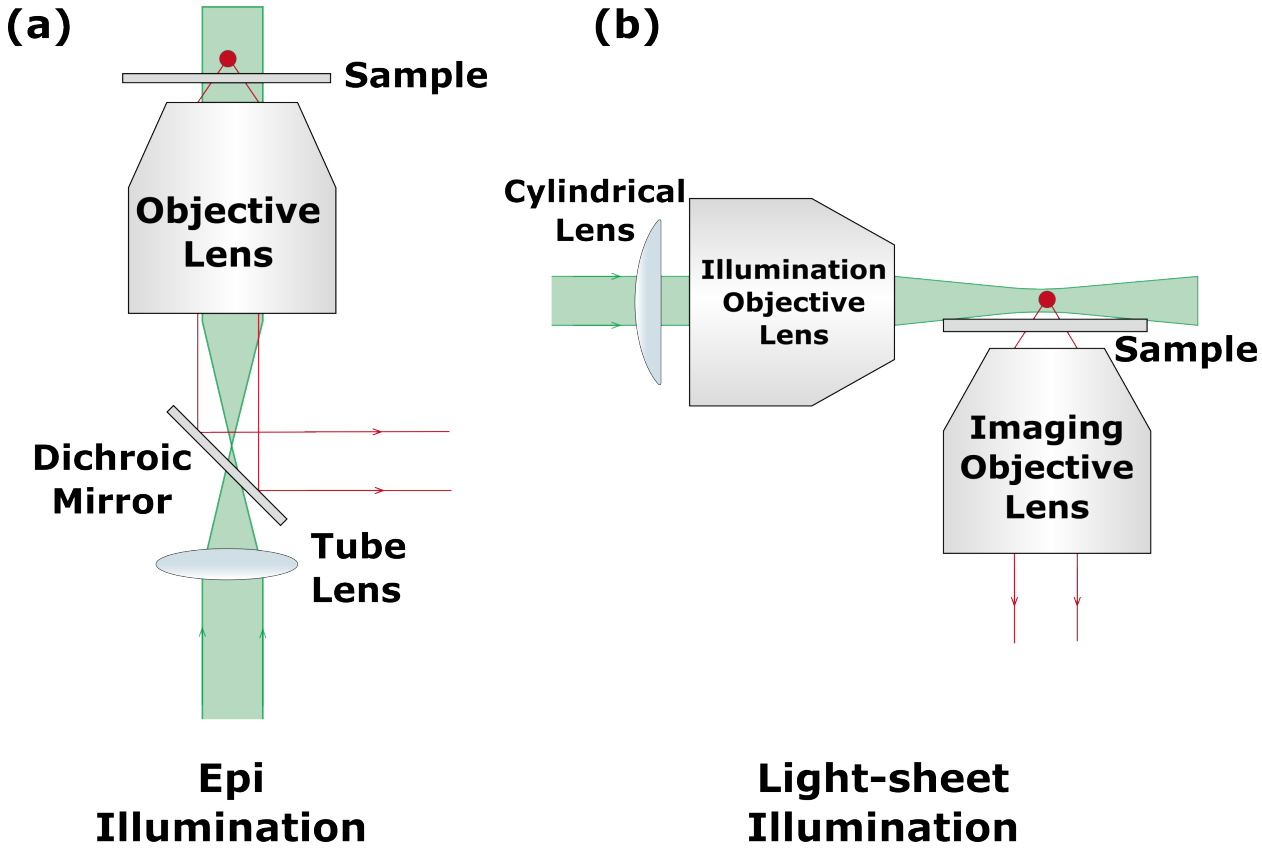

Figure 1.3: (a) Epi illumination. (b) Light-sheet illumination.

of multiple elements and interfaces [9]. It's essential to understand that while an objective lens appears as a single unit, it houses a series of optical components engineered to minimize aberrations, deliver a broad flat field, and ensure optimal collection efficiency. Specifically, there are three critical parameters that define an objective lens: immersion medium, magnification and numerical aperture (NA).

The most common immersion mediums include air, water, standard immersion oil, or silicone oil. Each medium has a distinct refractive index, which influences the, resolution, quality, and depth of imaging. It's essential to choose the appropriate objective and pair it with the appropriate immersion medium that matches the refractive index of the biological sample. In the context of this dissertation, inverted microscopes utilizing oil immersion were the preferred choice.

Magnification is a determinant of the level of detail observable. In a compound microscope, magnification (M) is determined by the ratio of the focal lengths of the tube lens to the objective lens $M = f_{TL}/f_{obj}$ [5, 8]. However, given the fixed nature of modern commercial microscope tube lenses and the interchangeability of objective lenses, M is predominantly governed by the focal length of the objective lens. For

single-molecule fluorescence imaging, which requires sub-diffraction pixel sizes, high magnifications are crucial.

NA is a defining characteristic of the objective lens that determines the collection efficiency and resolution. Defined by the equation,

$$NA = n \cdot \sin\alpha \tag{1.2}$$

where n represents the refractive index of the immersion medium and α denotes the half-angle of the light cone the objective lens can gather, as shown in Figure 1.2(b). A higher NA indicates a greater ability to resolve finer details and gather more light, thereby producing brighter and sharper images. As we mentioned in Equation 1.2, mathematically, resolution (R) is inversely proportional to NA. While air immersion objectives operate with an NA less than 1, single-molecule detection demands higher NA (~ 1.4) to collect as much of the signal as possible. TIRF also requires a high-NA objective to allow the incident light to reach the supercritical angle [10]. However, while higher NA provides excellent resolving power, higher NA objectives are limited by a shallow depth-of-field and potential aberrations due to manufacturing challenges.

After the objective lens collimates the emission, the tube lens focuses the light to create the image. Notably, different manufacturers have proprietary focal lengths for their tube lenses, meaning that cross-brand compatibility might not yield the expected magnification. Eventually, when an isolated fluorescence point source is positioned in the focal plane of the objective lens and aligns with the optical axis, the tube lens creates an image affected by diffraction within the optical system. The details of this diffraction-induced blurring, vital for understanding image quality, are explored later in Section 1.2.

Detection: It's important to point out that for microscopy applications, particularly single-molecule imaging, accurate and precise spatial sampling is very important. The ideal sampling rate ensures that the camera captures all the details provided by the microscope. According to the Nyquist theorem, to accurately reconstruct a signal without aliasing, it must be sampled at least twice as frequently as its highest frequency component. In the context of microscopy, this implies that the pixel size of the detector should be smaller than half the size of the system's resolution. For a conventional fluorescence Wide Field Microscope, the Nyquist critical sampling distance is given by:

$$\Delta_x = \frac{\lambda_{\text{em}}}{4n\sin(\alpha)}$$

$$\Delta_z = \frac{\lambda_{\text{em}}}{2n\left(1-\cos(\alpha)\right)}$$

where n is the Lens Refractive Index (usually 1.515 for immersion oil), α is the half-aperture angle of the objective, λ_{em} is the Emission Wavelength, and Δ_x, Δ_z are the Sampling Distances in the lateral and axial direction respectively. This is about one half of the microscope resolution.

In traditional microscope setups, the camera is placed directly after the tube lens, capturing the image as projected. However, in some optical systems aiming for higher magnification or resolution beyond what's provided by the objective and tube lens alone, additional magnifying optics can be inserted before

the camera. This ensures that the camera's sensor effectively utilizes the full resolution capacity of the optical system. For the detection schemes, generally, there are two categories: raster-scanning methods and widefield microscopy methods. A distinguishing characteristic of raster-scanning techniques, like confocal microscopy, is the implementation of a pinhole positioned preceding the detector. This configuration serves to filter off-axis and out-of-focus fluorescence, thereby enhancing contrast in the resultant images. On the other hand, widefield microscopes demand an continuous array of pixels to generate a full image. Silicon charge-coupled devices (CCD) or complementary metal-oxide-semiconductor (CMOS) cameras dominate the field. In the field of single-molecule fluorescence imaging, the inherently weak signals mandate the use of even more sensitive detectors. Hence, electron-multiplying CCD (EMCCD) and scientific CMOS (sCMOS) cameras become the preferred choices, both of which are used in this dissertation for different super-resolution imaging applications.

EMCCDs, much like their traditional CCD counterparts, measure excited photoelectrons. These excited electrons collect at each pixel and are read out sequentially row-by-row from the sensor. A crucial distinguishing step in EMCCDs is the electron multiplication process. The EMCCD amplifies the signal even before read-out, which is especially beneficial in low-light conditions. Photons incident on an EMCCD generate photoelectrons that, rather than being read out immediately, first traverse on-chip gain stages. Here, through impact ionization propelled by a voltage bias, each primary photoelectron can generate multiple secondary photoelectrons. This on-chip multiplication significantly enhances the signal, effectively reducing the read noise to sub-electron levels after amplification. For instance, Andor's iXon Ultra 897 EMCCD camera achieves a read noise of less than 1 electron root mean square (rms) with Electron Multiplying (EM) gain enabled [11]. Similarly, Teledyne's EMCCD sensors are engineered to elevate electron signals above the read noise floor, maximizing sensitivity for low-light imaging [12]. However, it's worth noting that the multiplication mechanism is inherently stochastic, leading to some excess noise and an effective reduction in photon counts. Despite this limitation, the sensitivity, high quantum efficiency, particularly in the red spectrum, and signal amplification features make EMCCD detectors exceptionally adept for single-molecule imaging, spinning disk confocal, quantum imaging, single photon counting, etc[13–16]. However, the limited frame rate of the EMCCD camera ($\sim 100 fps$) does not allow high speed imaging.

On the other hand, sCMOS cameras have come to the forefront as viable alternatives to EMCCDs. Each pixel in an sCMOS is read out in grouped formations like rows. While sCMOS cameras typically exhibit slightly higher readout noise and reduced quantum efficiency compared to EMCCDs, they deliver higher frame rates (up to several 100 fps) and support larger pixel arrays, making them well-suited for fast imaging applications(ex. wide-field microscopy, line scanning confocal, etc.) [13, 17].

In conclusion, EMCCDs outperform sCMOS cameras in ultra-low-light regimes, where their high sensitivity compensates for excess noise. In contrast, sCMOS cameras excel in higher photon-count conditions, where their superior speed and resolution outweigh the impact of their higher read noise. This makes sCMOS cameras particularly advantageous for high-throughput imaging and dynamic studies, while EMCCDs remain the preferred choice for detecting weak fluorescence signals [15, 18].

1.1.3 Fluorescent probes.

Fluorescence microscopy fundamentally relies on effective fluorescent labeling to achieve specificity in imaging biological samples. While natural autofluorescence can be detected, it often provides a weak signal, reducing image contrast and clarity [19]. To overcome this limitation, fluorescent probes are used to specifically target and visualize particular molecules or structures within complex biological samples. Fluorescent probes for microscopy can be broadly divided into three general groups: organic dyes, biological fluorescent proteins, and quantum dots.

Organic dyes are small synthetic molecules known for their high quantum yields and versatility in bioconjugation. They can be chemically modified and cross-linked to macromolecules, such as antibodies, biotin, or avidin, without significantly altering their biological function. However, antibodies typically do not penetrate intact cellular or subcellular membranes in living cells due to their large size, necessitating fixation of antigenic material to maintain its natural localization within the cell. Consequently, the use of organic dyes in immunofluorescence is generally limited to fixed (i.e., dead) cells. Advancements, such as genetically encoded tags like SNAP and Halo, have enabled the labeling of specific proteins of interest with modified organic dyes in live-cell imaging [20–24]. However, as organic dyes are non-genetically encoded probes, introducing them into live cells remains more challenging compared to using biological fluorescent proteins.

Fluorescent proteins are genetically encoded markers that enable the expression of chromophores within living cells, facilitating the direct observation of protein dynamics in real-time. A pivotal advancement in this field was Osamu Shimomura's 1962 discovery of green fluorescent protein (GFP) from the jellyfish Aequorea victoria, which revolutionized cell biology by allowing researchers to tag and visualize proteins in live cells [25]. Since then, a diverse array of fluorescent proteins has been developed, including derivatives of the original GFP and other proteins such as phycobiliproteins (e.g., allophycocyanin, phycocyanin, phycoerythrin, and phycoerythrocyanin). The benefit of these types of fluorophores is that expression plasmids can be introduced into either bacteria, cells, organs or whole organisms, to drive expression of that fluorophore either alone or fused to a protein of interest in the context of the biological processes studied [26–28].

Quantum dots are nanocrystals with unique chemical properties. Their emission wavelength is inversely related to their size: smaller QDs emit higher-energy (bluer) light, while larger QDs emit lower-energy (redder) light. This size-dependent emission allows for precise tuning of their optical properties, enabling multiplexed imaging where multiple targets are labeled and distinguished simultaneously. Additionally, QDs exhibit exceptional photostability, resisting photobleaching and maintaining fluorescence over extended periods, which is advantageous for long-term imaging studies. However, their relatively larger size (2-50nm) and potential toxicity (due to the presence of heavy metals), can be limitations in certain biological applications such as live cell imaging [29, 30].

1.1.4 Fluorescent probes for super-resolution imaging.

The use of fluorescent probes in super-resolution imaging in this dissertation is also categorized into into photoactivatable fluorescent proteins (PA-FPs) and non-genetically encoded probes (organic dyes and quantum dots [29, 30]), each with its own pros and cons depending on the imaging application [26–28].

PA-FPs have emerged as revolutionary tools in the domain of super-resolution microscopy due to their unique ability to switch between dark and emitting states upon exposure to specific light wavelengths. Originally derived from naturally occurring fluorescent proteins, these engineered molecules have been tailored to possess distinct photoactivation properties, allowing for precise temporal and spatial control over their fluorescence. In general, PA-FPs can be classified as photoconvertible (irreversible photoactivation) and photoswitchable (reversible photoactivation) FPs. Photoconvertible FPs undergo an irreversible conversion, either from a non-fluorescent to a fluorescent state or from one emission wavelength to another. Examples include PA-GFP [31] and PA-mCherry [32], which convert emission state from dark to bright, as well as EosFP [33] and Kaede [34], both of which convert their emission color from green to red under certain light condition. On the other hand, photoswitchable FPs (such as rsEGFP [35]) can reversibly toggle between fluorescent and non-fluorescent states under specific light conditions [36]. Details of photoswitchable FPs are discussed in Chapter 3. The primary advantage of using FPs, as we mentioned earlier, is the ease with which they can be fused with target proteins, making live cell imaging more feasible. However, a challenge remains in their relatively low photon budget [36]. The photon budget, which denotes the number of photons an individual fluorescent molecule can emit before photobleaching, is a key factor in determining the resolution in super-resolution techniques, particularly in localization microscopy.

In contrast, if achieving the highest possible resolution is the priority, particularly in static or fixed samples, often necessitates the use of organic dyes. Organic dyes, owing to their superior photophysical properties, can emit a significantly larger number of photons before undergoing photobleaching, resulting in enhanced resolution, especially in single molecule localization microscopy. Notable examples include Alexa Fluor 488 [37], Cy3B [38], and Alexa Fluor 647 [39]. The performance of these dyes can be further optimized with chemical additives, such as thiols and oxygen scavengers in the imaging buffer, which improve their photostability, fine-tune their on-off duty cycles, and enhance their sensitivity to light activation [24, 40, 41]. However, as mentioned earlier, while organic dyes outperform FPs in terms of brightness, they present challenges for live-cell imaging. These challenges include the need for more complex labeling strategies, which can be invasive and may disrupt the natural cellular environment.

1.2 Optical imaging system.

1.2.1 *4-f* Imaging System

To better understand the optical imaging systems that are involved in this dissertation, I will first introduce a 4-f optical imaging system. In general, A 4-f imaging system contains two optical lenses with respective focal lengths of f_1 and f_2 set a distance of $f_1 + f_2$ from one another, as shown in Figure 1.4. The object is placed in the front focal plane of the first lens and the image is created in the back focal plane of the second

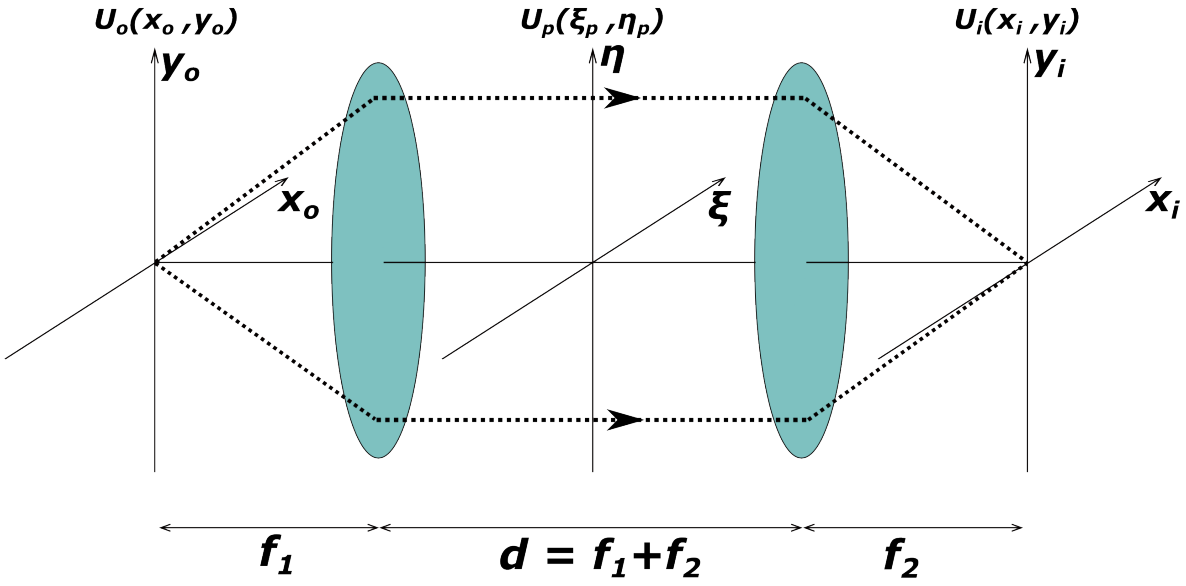

Figure 1.4: Schematic of 4-f optical system.

lens. This configuration means that the complete system spans a total of four focal lengths, calculated as $2f_1 + 2f_2$.

In a 4f optical imaging system, the spatial arrangement of the lenses and the inclusion of a pupil function, $U_p(\xi_p, \eta_p)$, are crucial for understanding the optical processing of the system. When an object is placed at the front focal plane of the first lens, it ensures that the light emanating from it undergoes a Fourier transform by the time it reaches the back focal plane of the first lens [42].Therefore, for the imaging system shown in Figure 1.4, the optical field at the pupil plane is:

$$U_p(\xi_p, \eta_p) = P(\xi_p, \eta_p)\frac{1}{i\lambda f_1}\iint U_o(x_o, y_o)\exp\left[-i\frac{2\pi}{\lambda f_1}(\xi x_o + \eta y_o)\right]dx_o dy_o \tag{1.3}$$

where λ is the emission wavelength, and $P(\xi_p, \eta_p)$ is the pupil function. For a microscopy system with a circular pupil:

$$P(\xi_p, \eta_p) = \begin{cases} 1, & \text{for } \sqrt{\xi_p^2 + \eta_p^2} \leq R \\ 0, & \text{for } \sqrt{\xi_p^2 + \eta_p^2} > R \end{cases} \tag{1.4}$$

where R is the pupil radius. In the case of the 4-f system in Figure1.4, R equals to the lens radius. For a optical system using an objective, R equals to the pupil radius of the objective lens, $NA \cdot f_o$, where f_o is the objective focal length. The pupil function represents the relative amplitude and phase of the field on the surface of a so-called reference sphere that intersects the optics axis in the plane of the system's

exit pupil. The pupil, acting as an aperture, can selectively transmit or block certain spatial frequency components of the light. By adjusting the pupil function, it offers the capability to manipulate the image in the spatial frequency domain directly, providing a powerful tool for tasks like image enhancement, filtering, or other frequency-based modifications. For instance, if the pupil function were to block higher spatial frequencies, it would act as a low-pass filter, blurring the resultant image.

Then, the second lens essentially inverts the process, taking the Fourier-transformed of the pupil-modulated field and performing a second Fourier transform on it to form the final image. By another Fresnel diffraction integral on the field from the pupil, the field at the image plane can be obtained:

$$\begin{aligned} U_i(x_i, y_i) &= \frac{1}{i\lambda f_2} \iint U_p(\xi, \eta) \exp\left[-i\frac{2\pi}{\lambda f_2}(\xi x_i + \eta y_i)\right] d\xi d\eta \\ &= -\frac{1}{i\lambda^2 f_1 f_2} \iint \left\{ \iint P(\xi, \eta) \exp\Big[-i\frac{2\pi}{\lambda}\{(x_i - Mx_o)\xi \right. \\ &\quad \left. + (y_i - My_o)\eta\}\Big] d\xi_p d\eta_p \right\} U_o(x_o, y_o) dx_o dy_o \end{aligned} \tag{1.5}$$

where $M = -\frac{f_2}{f_1}$, the minus sign includes the image inversion. From the equation above we can see that the 4-f system is a linear system with the impulse response (or in optics, the coherent amplitude spread function) $h(x, y)$,

$$h(x_i, y_i) = -\frac{1}{\lambda^2 f_1 f_2} \iint P(\xi_p, \eta_p) \exp\left[-i\frac{2\pi}{\lambda f_2}(\xi_p x_i + \eta_p y_i)\right] d\xi_p d\eta_p \tag{1.6}$$

After scaling the object coordinates with the system magnification to create object coordinates in the image plane at the right magnification as $x'_o = Mx_o$, $y'_o = My_o$. Then the object-image relationship becomes,

$$U_i(x_i, y_i) = \iint U_o\left(x'_o, y'_o\right) h(x_i - y'_o, y_i - y'_o) dx'_o dy'_o \tag{1.7}$$

In order to determine the irradiance $I_i(x_i, y_i)$ recorded by a photo-detector placed in the image plane, the square of the image amplitude is time-averaged. Then the expression of the image intensity of the coherent system can thus defined as the square of the convolution product of the object signal and the amplitude spread function:

$$I_i(x_i, y_i) =< \left| h(x_i, y_i) \otimes U_o\left(x'_o, y'_o\right) \right|^2 > \tag{1.8}$$

1.2.2 Point Spread Function.

Fluorescent molecules act as independent light sources that are incoherent, meaning that the photons released by different molecules don't maintain a consistent phase connection. Therefore, fluorescence microscope is an incoherent imaging system [42]. The foundation for understanding this system is the incoherent point spread function (PSF), which is the modulus squared of the coherent amplitude spread

function from Equation 1.6:

$$PSF(x,y) = H(x,y) = |h(x,y)|^2 \tag{1.9}$$

For a set of fluorescent molecules arranged in the focal plane $O(x,y)$ (referred to as the object), the image $I(x,y)$ detected by the camera is determined by the convolution with the microscope's PSF, which is:

$$I(x,y) = |h(x,y)|^2 \otimes |O(x,y)|^2 \tag{1.10}$$

The size of the PSF is a critical parameter in evaluating the resolution of an optical imaging system. The PSF indicates the extent to which a point is blurred in an acquired image. Specifically, when $O(x,y)$ equals to the Dirac delta function,$\delta(x,y)$, such that the object is a point source, then the captured image is the PSF. In a fluorescence microscope, the theoretical representation of the PSF for a point source is determined by the pupil function of the system. For an idealized case that the aperture is a uniformly illuminated circular aperture or if a uniform flattop beam is used, the PSF forms an Airy diffraction pattern in the far-field due to Fraunhofer diffraction, as shown in Figure 1.5(a). The central bright area of this pattern is referred to as the Airy disk. This Airy pattern represents the ideal PSF for such a system. However, deviations from a uniformly illuminated aperture or the presence of aberrations can alter the PSF and, consequently, affect resolution and contrast. The intensity distribution of the Airy pattern at the camera plane is:

$$I_{\text{Airy}}(x,y,z) = \frac{z^2 I_0^2 \text{NA}^2}{x^2+y^2} \left| J\left(k\text{NA}\sqrt{x^2+y^2}\right)\right|^2 \tag{1.11}$$

where $J(\cdot)$ denotes a Bessel function of the first kind, and the isotropic point source,$\delta(x,y)$, is placed at a distance z away from the lens. I_0 is the amplitude and k is the wavenumber. Then the width of the Airy disk/PSF, defined by the first zero of its radial profile, is given by,

$$w \approx \frac{1.22\lambda}{\text{NA}} \tag{1.12}$$

Clearly, reducing the wavelength or increasing the NA can narrow the width. However, considering the typical wavelengths (over 400nm) and NAs (below 1.5) used in fluorescence microscopy, the smallest PSF size in two-dimensions is approximately 250nm. In another word, the Airy disk describes the best focused spot of light that a perfect circular lens can provide. The Rayleigh resolution criterion provides an estimate for the smallest distance, as shown in Figure 1.5(b), at which two Airy patterns can be clearly differentiated from each other, given by,

$$d_{\text{Rayleigh}} \approx \frac{2}{w} = \frac{0.61\lambda}{\text{NA}} \tag{1.13}$$

Moreover, in real experiments, the size of the experimental PSF can be determined by the full width at half maximum (FWHM) of the distribution of the PSF, which corresponds to the smallest displacement

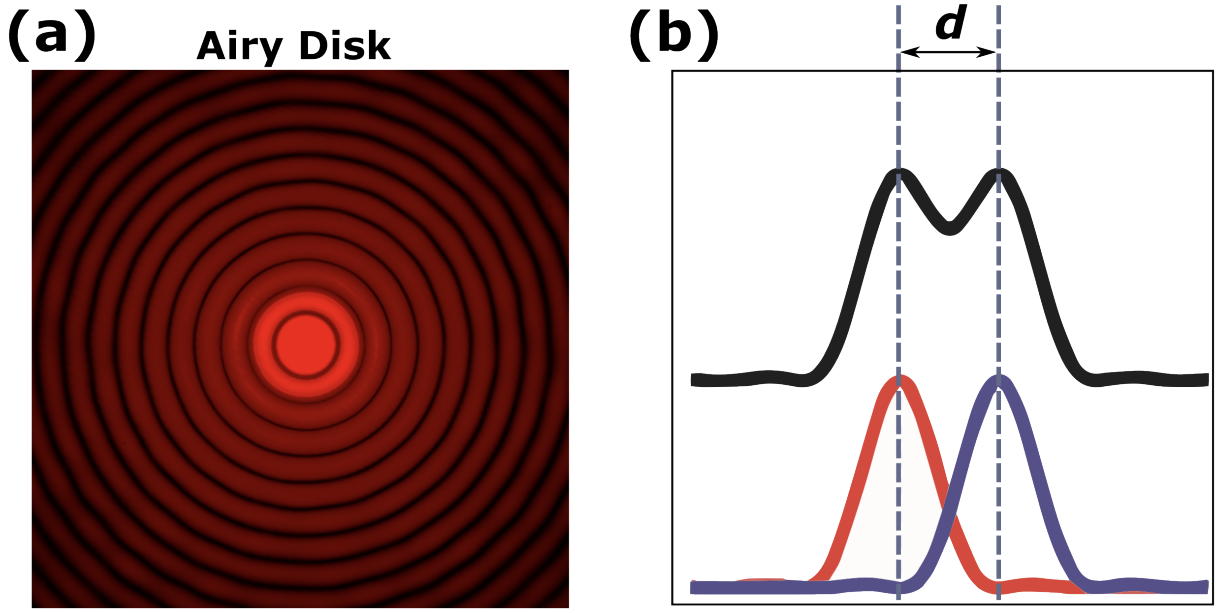

Figure 1.5: (a) Intensity profile of "Airy Disk". (b) Overlap of Airy functions defines the resolution.

between two fluorophores that can be resolved. For the Gaussian distribution, a common approximation of the PSF shape,

$$FWHM = 2\sqrt{2\ln 2}\,\sigma \approx 2.355\,\sigma \tag{1.14}$$

Furthermore, a 3D PSF can be generated by including the defocus in the calculation of the PSF, so the response becomes a function of both lateral position and axial defocus.

1.2.3 Optical transfer function.

The Optical Transfer Function (OTF) is defined as the Fourier Transform of the PSF:

$$OTF(k_x, k_y) = \mathcal{F}\{PSF(x, y)\} = \mathcal{F}\{|h(x, y)|^2\} \tag{1.15}$$

Essentially, the OTF is a measure of the imaging system's capability to reproduce or transfer different spatial frequencies, and thereby is the frequency response of the system. Moreover, the incoherent OTF is given by the autocorrelation of the coherent OTF [42]. Figure 1.6 shows the frequency transmission for both the incoherent and coherent 2D OTF when operating with a circular aperture. A significant observation here is the attenuation of high-frequency information as it approaches the resolution limit

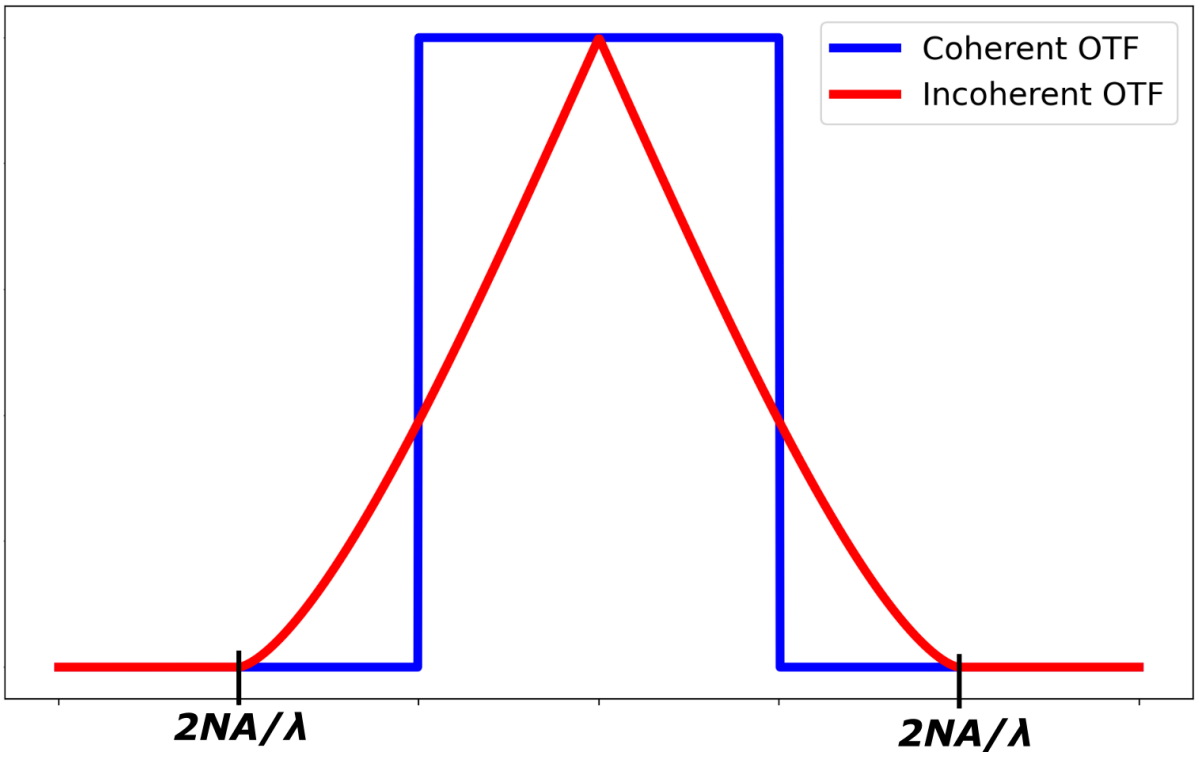

Figure 1.6: Normalized frequency support across the 2D OTF under coherent and incoherent illumination.

in the incoherent case. The region of support under coherent illumination is limited to NA/λ and the steep drop off results in ringing artifacts that degrade image quality.

In conclusion, the PSF represents the distribution of light intensity in the image plane produced by a point source. The shape and characteristics of the PSF are directly influenced by aberrations in the optical system, which can cause the image of a point source to deviate from an ideal point-like image. The PSF provides insight into the spatial characteristics and potential imperfections of an optical system. And the OTF is the Fourier transform of the PSF and describes the frequency response of the optical system, indicating how effectively system transfers information across different spatial frequencies.

As we mentioned, the diffraction limit plays a pivotal role in optical microscopy, impacting the OTF by determining its region-of-support. Any details or frequencies that lie outside this region-of-support are omitted from the final image, thereby constraining the resolution of the system. As shown in Figure 1.6, for a standard fluorescence microscope, the two-dimensional region-of-support, determined by the diffraction limit, is given by:

$$k_{x,y} \leq \frac{2\mathrm{NA}}{\lambda} \tag{1.16}$$

1.3 Introduction of super-resolution methods.

Over the last twenty years, a variety of methods, collectively referred to as super-resolution fluorescence microscopy, have been pioneered to surpass the diffraction limit. These super resolution methods can be placed in two main categories: deterministic methods which might use patterned excitation light to achieve super-resolution, and stochastic methods which take advantage of the random reduction of the number of simultaneously fluorescing fluorophores.

Deterministic method includes techniques such as Stimulated Emission Depletion Microscopy (STED), which achieves resolutions in the range of 60 to 70 nm, and Structured Illumination Microscopy (SIM) [8, 43], which can discern structures as small as approximately 100 nm.

Stochastic methods, mainly fall under the category of Single Molecule Localization microscopy (SMLM), include techniques such as Stochastic Optical Reconstruction Microscopy (STORM) [44] and Photo-activated Localization Microscopy (PALM) [44]. STORM achieves remarkable resolutions between 10-20 nm, while PALM offers a range between 10-50 nm. Other significant stochastic techniques include direct STORM (dSTORM), ground-state depletion microscopy (GSDIM) [45], points accumulation for imaging in nanoscale topography (PAINT) [46, 47], each presenting their own unique advantages and limitations.

Deterministic methods necessitate the use of fluorophores that maintain their stability during the imaging phase. Stochastic methods rely on the detection of emission signal from single fluorophores, often achieved through techniques like reversible photoswitching of these synthetic molecules [48]. Stochastic super-resolution imaging, due to its remarkable sensitivity at the single-molecule level, delivers enhanced details on the molecular scale, such as precise coordinates of individual molecules, aiding in more detailed cluster analyses. Nevertheless, every method showcases the capability to image beyond the traditional diffraction limit, and there are comprehensive reviews available that discuss the pros and cons of each approach [43, 44, 49]. The methods presented in this dissertation are based on SMLM and SIM. Therefore, I will shortly introduce the background of these two methods respectively here.

1.3.1 Single Molecule Localization microscopy (SMLM).

Principle of 2D SMLM.

In 1989, W.E. Moerner pioneered a method to detect individual molecules, primarily by measuring fluorescent absorption rather than emission [51]. This technique laid the groundwork for later developments in single-molecule detection. In 1995, Betzig introduced the idea of using single-molecule localization microscopy (SMLM) in biological imaging, it wasn't until 2006 that the approach was demonstrated with densely labeled biological samples [52]. SMLM offers a unique approach to microscopy by focusing on pinpointing the position of individual fluorophores, thereby isolating them from their larger group. Unlike other microscopy techniques, SMLM doesn't rely on intricate beam shaping for enhanced resolution.

With fluorescent microscopes functioning as incoherent imaging systems, each fluorescent probe within the sample is imaged independently, ensuring their concurrent emissions do not coherently in-

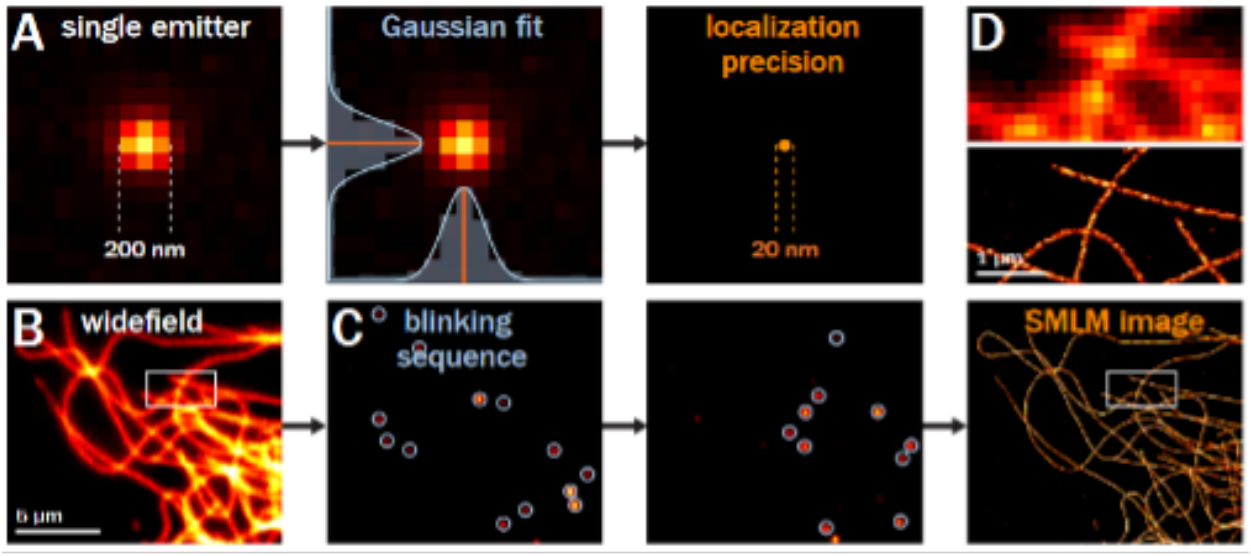

Figure 1.7: Principle of SMLM. (a) Epifluorescence image of a single emitter, showing the 200 nm width of the PSF (left) that is fitted using Gaussian curves (center) to determine its position with a 20 nm precision (right). (b). Epi-fluorescence image of microtubules in a COS cell (top) and corresponding cartoon (bottom). (c). During SMLM acquisition, a blinking mode of fluorescence emission is induced, and thousands of frames are recorded, containing individual blinking events that can be fitted to localize each emitter. (d). After processing, all localizations are plotted to generate the SMLM images (bottom). Top panel is a zoom corresponding to the box highlighted in the full image and shows the gain in resolution with much thinner microtubules (top).[50]

terfere. Consequently, the end image is essentially the sum of the PSFs of the individual probes in the sample. The principle behind SMLM, as shown in Figure 1.7, is straightforward: if a single molecule emits photons generating a PSF on the camera, the center can be localized. To facilitate this, only a small subset of the fluorophores is photoactivated to the on state, while the majority stay in the dark state. By repeating this localization process until every fluorophore is identified and located, resolution beyond the diffraction limit can then be achieved. In real experiments, individual molecules often emit weak signals that require careful filtering and efficient detection. A small number of photons are captured, making the signal inherently noisy due to the Poisson statistics of photon emission.

Therefore, in localization microscopy, resolution isn't restricted by diffraction but by the localization precision of the single emitter, which, in real experiments, is influenced by various factors such as standard deviation of PSF, the number of collected photons, effective pixel size of the image, and number of background photons. While the centroid, or the average photon position, is the most basic position estimator, there are more advanced estimators that are often favored due to the centroid's tendency to be skewed towards the region of interest's (ROI) center when background is present. Some of the demonstrated

non-fitting estimators include the virtual window center-of-mass, radial symmetry [53], and Fourier domain algorithms [54]. These techniques are computationally efficient and eliminate the need for PSF or noise modeling. On the other hand, basic 2D functions, like a Gaussian or Airy function, can be utilized to represent the PSF, paired with fitting criteria like least squares or maximum likelihood estimation [55, 56]. Thompson et al. [57], provide an approximation for the variance of the localization uncertainty:

$$(\Delta x)^2 = \frac{s^2}{N} + \frac{a^2}{12N} + \frac{8\pi s^4 b^2}{a^2 N^2} \tag{1.17}$$

where s represents the standard deviation of the PSF. N denotes the number of photons detected, with more photons detected leading to better precision. a is the effective pixel size of the image, and b represents the background noise.

In ideal imaging conditions with a perfect detector, the localization uncertainty predominantly arises from the PSF width and the number of photons collected. But in real situations, the camera is divided into pixels, and such division introduces pixelation noise, which can escalate the uncertainty. Specifically, reducing the effective pixel size can reduce pixelation noise, but increase the background noise. The delicate balance point between these two effects determines the optimal pixel size for the imaging system. For achieving the best image clarity, the effective pixel size should be, in many cases, approximately equal to the standard deviation of the PSF. In practical applications like imaging, the properties of the subject being observed can also influence the optimal pixel size. For instance, fluorescent proteins emit fewer photons than fluorescent dyes. Due to this lower photon yield, PALM typically uses a pixel size ranging between 100 to 130 nm. In contrast, STORM often involves fluorescent dyes, tends to employ a slightly smaller pixel size, ranging from 70 to 100 nm [58].

Moreover, another valuable tool in evaluating the localization precision is the Cramér-Rao lower bound (CRLB) [59, 60]. Originating from estimation theory, the CRLB sets the minimum variance (or best precision) that any unbiased estimator can achieve based on a specific noise model. One estimator that approaches the CRLB, especially when dealing with the Poisson distribution of photon detections, is the maximum likelihood estimator. More details regarding CRLB can be found in references [60, 61].

Based on the fundamental principles of SMLM, various techniques, like PALM, STORM, dSTORM, and DNA-based PAINT (DNA-PAINT), have been developed. PALM [49], STORM [44], and DNA-PAINT [62] all rely on similar imaging principles, althoug the details differ. PALM involves the use of photo-activatable fluorescent proteins, which do not require buffer that is toxic to the cell. While STORM uses organic dye pairs (such as Cy3 and Cy5) as fluorescent probes for imaging. Although PALM is able to perform live imaging and has the potential of imaging any protein of interest within the cell regardless of the availability of antibodies or other affinity reagents, STORM generally has a better localization precision than PALM. dSTORM combine the commonly used organic fluorophores (such as AF 647, CF 647, AF 680, CF 680, etc.) with specialized buffers and lasers to induce photoswitching without relying on a dye pair. The labeling of DNA-PAINT is done by the affinity between distinct DNA strands, and the buffer of DNA-PAINT is mild compared to STORM buffer and does not change its chemical properties over time. However, due to the abundance of images in the solution which produce strong out-of-focus

light, DNA-PAINT has pronounced background [62]. Therefore, optical sectioning is needed for DNA-PAINT by using TIRF illumination or a Spinning Disk [62]. SMLM methods have been extended to 3D imaging.

Background of 3D SMLM.

The last section introduced the principle of SMLM in the lateral direction only. However, most real-world imaging systems operate in a three-dimensional space. It's important for biological imaging to be able to image the axial direction that spans both above and below the microscope's focal plane. Theoretically, an emitter's axial location can be determined by its PSF and then localized with a 3D PSF model. However, the shape of the standard PSF tends to change relatively slowly and blur quickly when it moves away from focus, as shown in first row of Figure 1.8. This means that the detection of the emitter's axial information requires extremely bright emitters that generates far more photons than single molecules can [63]. Moreover, in the absence of aberrations, the standard PSF is symmetric about the focal plane, leading to uncertainties in determining exact axial positioning. The axial Abbe resolution limit is also worse than the lateral Abbe resolution limit. To overcome the limitations associated with the standard PSF, various optical techniques have been introduced. A comprehensive review of these techniques can be found in ref [63].

Some involve multifocus methods that simultaneously captures several focal planes by splitting the fluorescence equally among two channels, which are defocused with respect to one another [64]. Then, by integrating the data from both channels, the axial symmetry is disrupted, resulting in improved 3D localization accuracy spanning, for biplane imaging, approximately $1.5\mu m$ [65]. Incorporating more planes allows for a broader depth of field capture, though it comes at the expense of needing more cameras or sacrificing some lateral field of view on a single camera [65–67]. However, a limitation of multifocal techniques that cover a wide axial range is the inefficient utilization of the signal, particularly at the boundaries of the focal stack. At these extremes, a significant portion of the signal gets distributed into planes that are too defocused to yield valuable data [63].

Another alternative group of methods, which are also the most popular 3D SMLM methods, is based on PSF engineering. By controlling the wavefront of the system, the axial information of the emitter can be encoded in the shape of the PSF. A number of engineered PSFs have been designed for 3D single-molecule localization. The most common one is to use a weak cylindrical lens to introduce astigmatic aberrations, as shown in the second row of Figure 1.8, into the detection path, and providing an axial resolution of $50 - 70$nm. However, the axial range is limited to 600nm. There have been other PSFs that can expand the imaging axial range. The Double-helix PSF, in the third row of Figure 1.8 provides a $2 - 3\mu m$ axial range, and the Tetrapod PSF, in the fourth row of Figure 1.8, provides an axial range up to $20\mu m$ [68]. However, increasing of PSF size also increases the possibility of the PSF overlapping, which results in poor localization performance in high-density 3D localization situations. To solve this, deep learning has been used for analyzing dense fields of overlapping emitters with engineered PSFs. Moreover, deep learning has also been used to design an optimal PSF for 3D localization of dense emitters [69], as shown in the bottom row of Figure 1.8. But the maximum depth of field so far is still limited to a few microns [68–70].

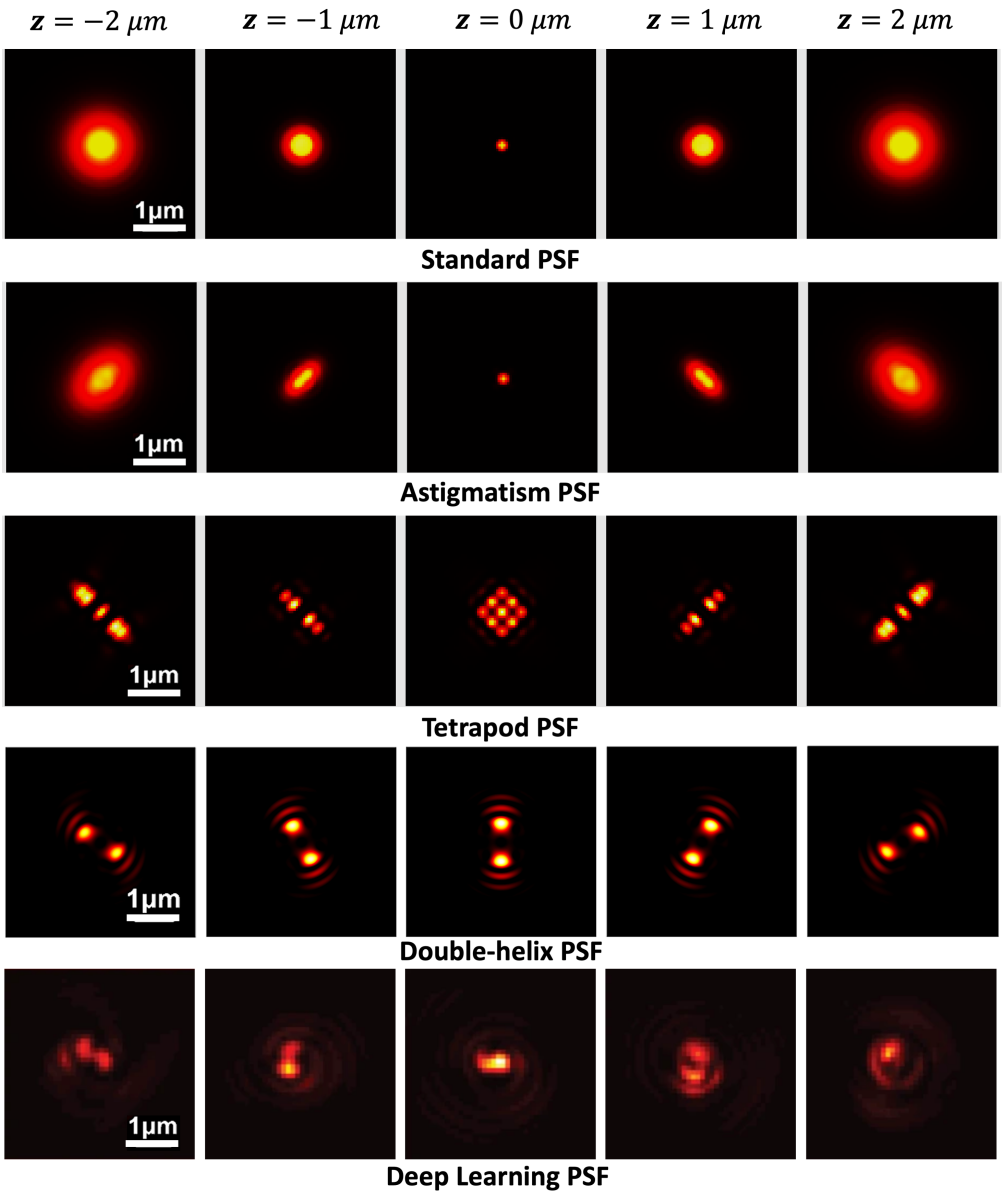

Figure 1.8: Various experimentally measured PSFs for 3D localization microscopy shown as a function of the axial position of the emitter

Even though SMLM stands out among all the super-resolution methods due to its outstanding resolution, there are still some disadvantages for SMLM. As we mentioned, SMLM relies on collecting sample information over time by capturing many images (>10,000 frames) where molecules are sparsely distributed within an individual frame, then the acquired PSFs need to be precisely fitted to determine the centroid. However, acquiring and processing raw data to get a super-resolution image can take hours.

Specifically, higher spatial resolution requires detecting more molecules to meet the Nyquist criterion, which in turn needs longer data acquiring time. By taking advantage of advanced sCMOS cameras, it can cut down data acquisition time. But this method is still restricted by the structure's dynamic process, sample labeling density, and the brightness and blinking rate of fluorescent probes. These shortcomings make real-time live imaging in SMLM particularly challenging. Achieving real-time SMLM visualization necessitates advancements in both fitting algorithms and computer hardware.

1.3.2 2D Linear Structured Illumination Microscopy.

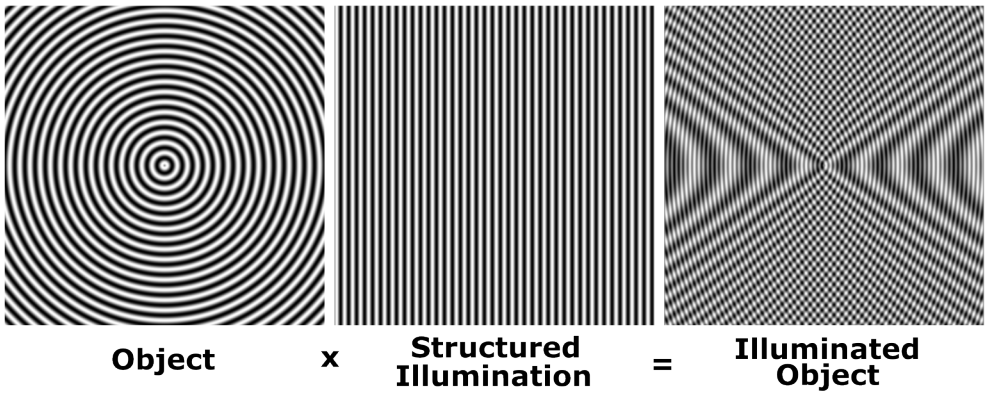

Figure 1.9: Moiré fringes

SIM, another very popular super-resolution method, offers a revolutionary approach to surpassing the diffraction limits from the perspective of the frequency domain, unlike SMLM's focus on modulation in spatial domain. The principle of this technique lies in the concept of illuminating the sample with sinusoidal patterned light modulating the emission fluorescence intensity to induce Moiré fringes with a lower spatial frequency, as shown in Figure 1.9. This can shift out-of-band frequency information into the passband of the microscope objective, enabling the reassignment of information to the correct object spectrum location, and thus achieving higher resolution images.

Historically, the exploration of SIM began in the late 1990s. Initially, the system proposed by Neil and Wilson utilized incoherent illumination and was grounded in the principle of projecting a single spatial frequency grid pattern onto the sample plane [71, 72]. This method ensured that only the in-focus plane section was modulated, giving it optical sectioning capability - a contrast to widefield fluorescence microscopy. However, the technique couldn't achieve the super-resolution, as the highest modulation frequencies had attenuated fringe contrast due to the inherently weak response in the incoherent OTF, plus the higher spatial frequencies are attenuated more than the lower frequencies. Later on, Heintzmann and Cremer in 1999 developed a second SIM approach which utilized coherent illumination [73]. Gustafsson then optimized this method, which illuminated the sample using sinusoidal patterns created by interference of two light beams emerging from a diffraction grating. This method maintained the contrast of the structured illumination pattern even at high modulation frequencies, near the cutoff frequency of the

microscope objective lens. As a result, super-resolution became achievable with coherent illumination SIM. Since then, SIM has been integrated with various imaging techniques including TIRF [74, 75], light sheet microscopy [76], highly inclined and laminated optical sheet (HiLo) [77], etc.

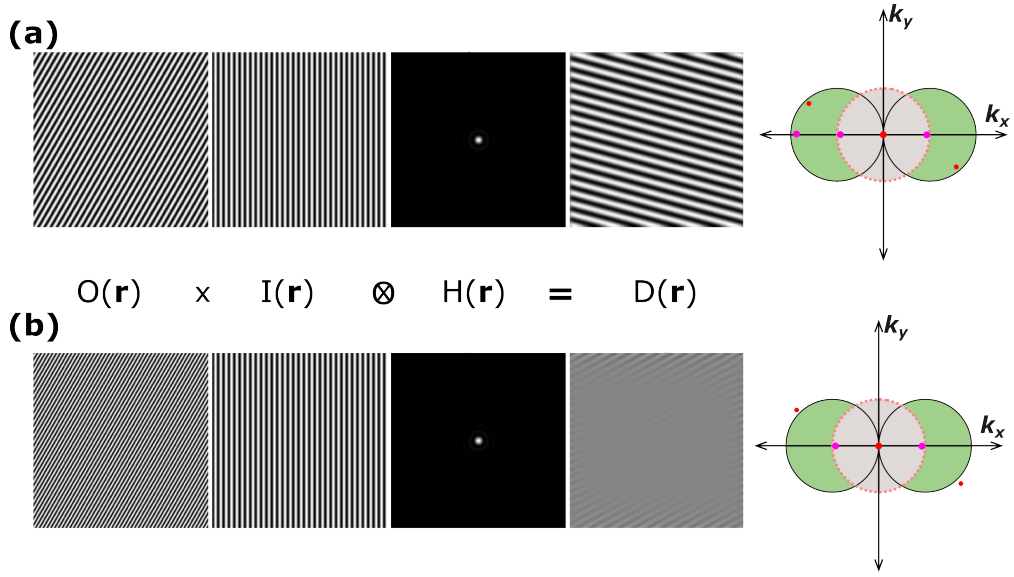

Figure 1.10: Principle of linear SIM in spatial domain and frequency domain. (a) Object with frequency smaller than 2-fold of OTF size. (b) Object with frequency bigger than 2-fold of OTF size. The red dots in the k space indicate the frequency of the object. The pink dots in the k space indicate the frequency of the illumination pattern

To mathematically understand the principle of structured illumination microscopy, the image forming processes in both the spatial and frequency domain need to be studied. As was mentioned in Section 1.2.2, the observed image $D(\mathbf{r})$ is proportional to the convolution of the emission distribution from the sample ($O(\mathbf{r})$) with the system's PSF, $H(\mathbf{r})$, as shown in Figure 1.10:

$$D(r) = O(r)I(r) \otimes H(r) \tag{1.18}$$

where $\mathbf{r} = (x, y)$ is the position vector. $I(\mathbf{r})$ represent the intensity distribution of the illumination sinusoidal pattern,

$$I(r) = 1 - \cos(2\pi \mathbf{p} \cdot \mathbf{r} + \phi) \tag{1.19}$$

where $\mathbf{p}$ is the wave vector of the sinusoidal illumination pattern and ϕ is the phase of the illumination pattern. By using the convolution theorem, the Fourier transform of observed image $D(\mathbf{r})$ is,

$$\begin{aligned} \tilde{D}(\mathbf{k}) &= \tilde{H}(\mathbf{k}) \cdot \left[\tilde{I}(\mathbf{k}) \otimes \tilde{O}(\mathbf{k})\right] \\ &= \tilde{H}(\mathbf{k}) \cdot \tilde{O}(\mathbf{k}) - \tilde{H}(\mathbf{k}) \cdot \frac{1}{2}\tilde{O}(\mathbf{k} - \mathbf{p})e^{-i\phi} - \tilde{H}(\mathbf{k}) \cdot \frac{1}{2}\tilde{O}(\mathbf{k} + \mathbf{p})e^{i\phi} \end{aligned} \tag{1.20}$$

Since $\tilde{H}(\mathbf{k})$ is is the Fourier transform of the system's PSF $H(\mathbf{r})$, $\tilde{H}(\mathbf{k})$ is the system's OTF. As one can see, $\tilde{D}(\mathbf{k})$ is a linear combination of three terms, including the original widefield image $\tilde{H}(\mathbf{k}) \cdot \tilde{O}(\mathbf{k})$ and two additional images, centered at $-\mathbf{p}$ and $+\mathbf{p}$, as shown in Figure 1.10(a). Some of the regions ($-\mathbf{p}$ and $+\mathbf{p}$) fall outside of the system's OTF support, signifying high-frequency details that usually remain unseen. But, in this context, they become visible in the form of low-frequency Moiré patterns.

It's impossible to separate the three components of Equation 1.20 from just one image. Therefore, for 2D linear SIM, three distinct SIM images of the object need to be captured, each corresponding to a different illumination phase. These phases are typically set $\varphi_1 = 0^o$, $\varphi_2 = 120^o$, and $\varphi_3 = 240^o$.

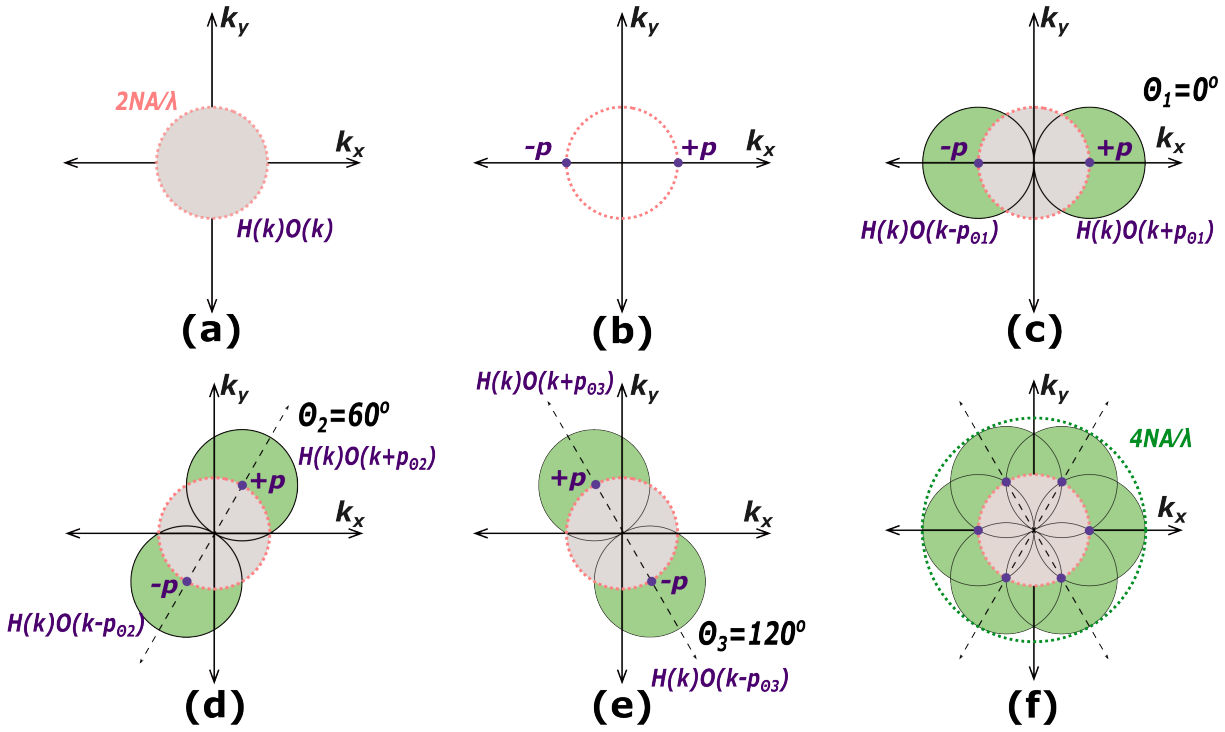

Figure 1.11: Illustrations of the image acquisition in 2D SIM. (a) Observable frequency content of object in frequency space is limited by optical systemOTF, H_k. (b) Frequency content of sinusoidal illumination pattern relative to optical system OTF. (c, d, e) Observed frequency content of structured illuminated object is a linear combination of frequency content within three OTF copies, see Equation 1.20. (f) By illuminating the object sequentially with sinusoidally varying illumination pattern at three different angular orientations (0°, 60°, and 120°), object's frequency information extends 2-fold of the system's OTF. (g) Separately obtained frequency contents are eventually merged to reconstruct a super-resolved image of the object.

Through this process, the data with high frequency information in one specific direction can be acquired, as shown in Figure 1.11(c). To cover the isotropic space, Figure 1.11(f), the process needs to be repeated for other orientations of the illumination pattern, as shown in Figure 1.11(d) and (e). For 2D

linear SIM, nine different images need to be acquired in order to reconstruct one high resolution SIM image after the numerical reconstruction process. The highest resolution improvement is determined by the diffraction limit which limits the wave vector of the illumination pattern, **p**. Thus, to maximize resolution, it's important to use an illumination pattern with the highest possible spatial frequency. Given the difference between the emission wavelength (λ_{em}) and the illumination wavelength (λ_{ex}) in a fluorescence microscope, the lateral frequency extension power of linear SIM is capped at $1 + \lambda_{em}/\lambda_{ex}$. When the NA for the illumination path matches that of emission path, the limit for the illumination pattern frequency **p** is capped at $\mathbf{p} = 2NA/\lambda_{ex}$, less than the edge of the system's OTF. This results in a new resolution limit of $4NA/\lambda_{ex}$. Therefore, employing linear structured illumination through the objective close to the fluorophore's emission wavelength permits at most a doubling of the resolution of a conventional widefield fluorescence microscope.

Compare with SMLM, SIM has its own advantages that cannot be surpassed by other super-resolution methods. First of all, SIM, especially compare with SMLM, lowers the requirements on sample preparation dramatically. Any fluorescent sample that is used in widefield fluorescence microscopy, is compatible with SIM. Another advantage of SIM is the imaging speed. For live cell imaging, temporal resolution is extremely important. However, most of the current super-resolution methods achieve remarkable spatial resolution often at the expense of diminished temporal resolution, such as STORM, PALM, and STED [78]. SIM has demonstrated its capability in live cell real-time imaging. However, the resolution enhancement offered by linear SIM is capped at a two-fold improvement. As shown in Figure 1.10(a), the objects with low spatial frequency can be resolved since the entire frequency components are contained inside the frequency domain, which is 2-fold larger than diffraction limited domain. However, as shown in Figure 1.10(b), for the objects with higher spatial frequency, the high frequency components are beyond the boundary and cannot be obtained by linear SIM. Consequently, the resolution improvement achievable with linear SIM is limited to approximately 100 nm due to the two-fold extension of the spatial frequency bandwidth. To achieve higher resolution, it is necessary to incorporate nonlinear effects into the SIM system. This approach modifies the fluorophores emission to exhibit a nonlinear response on the illumination intensity, enabling the detection of higher-order harmonics and extending the resolution beyond the linear SIM limit. The principles and implementation of nonlinear SIM will be detailed in Chapter 3.

1.4 Outline of this dissertation.

In this dissertation, two different super-resolution imaging methods are reported: Self Interference Digital Holography based Single Molecule Localization Microscopy (SIDH-SMLM), and 2D Non-linear Structure Illumination Microscopy (2D-NSLM). In Chapter 1, I have set the stage by introducing the fundamentals of fluorescence microscopy, laying out the mechanics of the optical imaging system, and presenting a comprehensive overview of super-resolution methods related to this dissertation. Venturing into the specialized field of holography, Chapter 2 introduces the principles of Self Interference Digital Holography (SIDH) in biological imaging. By combining SIDH with SMLM, this chapter proposes an

innovative 3D super resolution imaging method that can achieve nanometer precision over a wide axial range without mechanical refocusing. Chapter 3 focuses on the principle of 2D-NSIM, exploring its potential to exceed the resolution limitations of linear SIM. Chapter 4 reported the study of optimizing the SIDH setup. Chapter 5 shows the senseless adaptive optics for SIDH. Chapter 6 shows the methods and results for 2D PD-NSIM. Chapter 7 further discusses the potential optimization can be explored to improve the performance of PD-NSIM setup. The last chapter concludes the dissertation and explored future research directions.

Chapter 2

Self-interference digital holography for single-molecule localization.

As mentioned in last chapter, due to the constrained axial range in SMLM, 3D super-resolution imaging of whole cells is still a challenge. The maximum depth of field so far is still limited to a few microns [68–70]. Here, our group proposes an innovated method that combines Self-Interference Digital Holography (SIDH) with SMLM to achieve 3D super resolution imaging with a large axial range. In this chapter, I will first provide a brief introduction to the background of holography in biological imaging. Then, I will introduce the principle of SIDH and the proposed SIDH-based SMLM system. I will then address the previous studies from our group. The background of system's aberration correction of SIDH will also be reviewed. Finally, I will conclude with the proposed studies and aims regarding the SIDH-based SMLM system.

2.1 Digital Holography.

Holography, a technique of recording a scene in its entirety, was invented by Dennis Gabor in 1947, during his endeavors to enhance the resolution of electron microscopes [79, 80]. Unlike conventional imaging methods, which primarily capture intensity, holography stands out for recording both intensity and phase information of the sample. The phase information is indirectly detected by recording an interference pattern, which is referred to as the "hologram" of the object wave and the reference wave. This is achieved by recording the interference pattern formed between the light reflected from an object (object wave) and a reference light wave, resulting in a hologram [79]. This foundational principle opens doors for 3D imaging through holography.

At the early development stage of conventional optical holography, it uses photographic film as the recording medium which cannot be processed in real-time. With the rise of high-resolution CCD/CMOS devices and rapid development of computer technology, the realm of holography has transitioned into

the digital era. Starting at 1994, digital holography has emerged and become an increasingly active field in optical research. Digital holography shares its foundational principles with conventional holography and is characterized by two distinct phases: recording and reconstruction. Specifically, a digital sensor captures the interference pattern between the object and reference beams when illuminated with, mostly, coherent light. This interference pattern, the digital hologram, holds the key to the object's phase information. Through the diffraction theory, numerical methods can then decode this hologram, reproducing an 3D image of the original object. The true power of digital holography lies in its ability to access the complex optical fields, which removed the need for physical holographic plates and chemical processing, promising real-time applications. However, its dependence on coherent light waves, where the waves have a constant phase relationship, is a significant restriction for most optical imaging systems (such as telescopes and fluorescence microscopes) that mainly use incoherent or natural light. As a result, conventional applications of digital holography have been limited, given the challenges of creating holograms with incoherent light.

2.2 Self-interference Digital Holography (SIDH).

As mentioned earlier, most traditional forms of holography are obtained with coherent light sources, resulting in its limited application in incoherent optical system, such as fluorescence microscopy, in which there is no statistical correlation between the waves emitted from various points of the object. However, recent innovations have led to the creation of incoherent digital holograms, essentially allowing incoherent light, emitted from objects, to interfere with itself. As the term 'self-interference' refers to the method of forming the holograms with incoherent light, 'digital holography' refers to the reconstruction of the recorded hologram them, self-interference digital holography (SIDH) has paved the way for capturing 3D optical information more efficiently and accurately compare with conventional 3D scanning microscopy. SIDH enables the creation of an interference pattern that captures the wavefront from fluorescent signals, allowing for the reconstruction of a 3D image of the fluorescence emission over a large depth of field without mechanical refocusing [81–83].

SIDH splits the incoherent light emitted from the sample into two beams, which are individually phase-modulated before being recombined in a shared plane to generate interference fringes. The phase modulation can be a spherical phase, introduced to the beam by a curved mirror or lens. The density of the interference fringes then contains information on the object's axial position [81]. The interferometer, shown in Figure 2.1, can be either a Michelson interferometer or a spatial light modulator (SLM). In this section we will discuss the theoretical analysis for two configurations of SIDH that we used in our simulations. Configuration 1, Figure 2.1(a), uses a plane wave and a spherical wave (focal length f_d), while configuration 2, Figure 2.1(b), uses two spherical waves (focal lengths f_{d1} and f_{d2}) to form the interference pattern [81].

For the basic configuration of SIDH shown in Figure 2.1(a), a Fresnel hologram of a point object is obtained when the two interfering beams are plane and spherical waves. The definition of a Fresnel

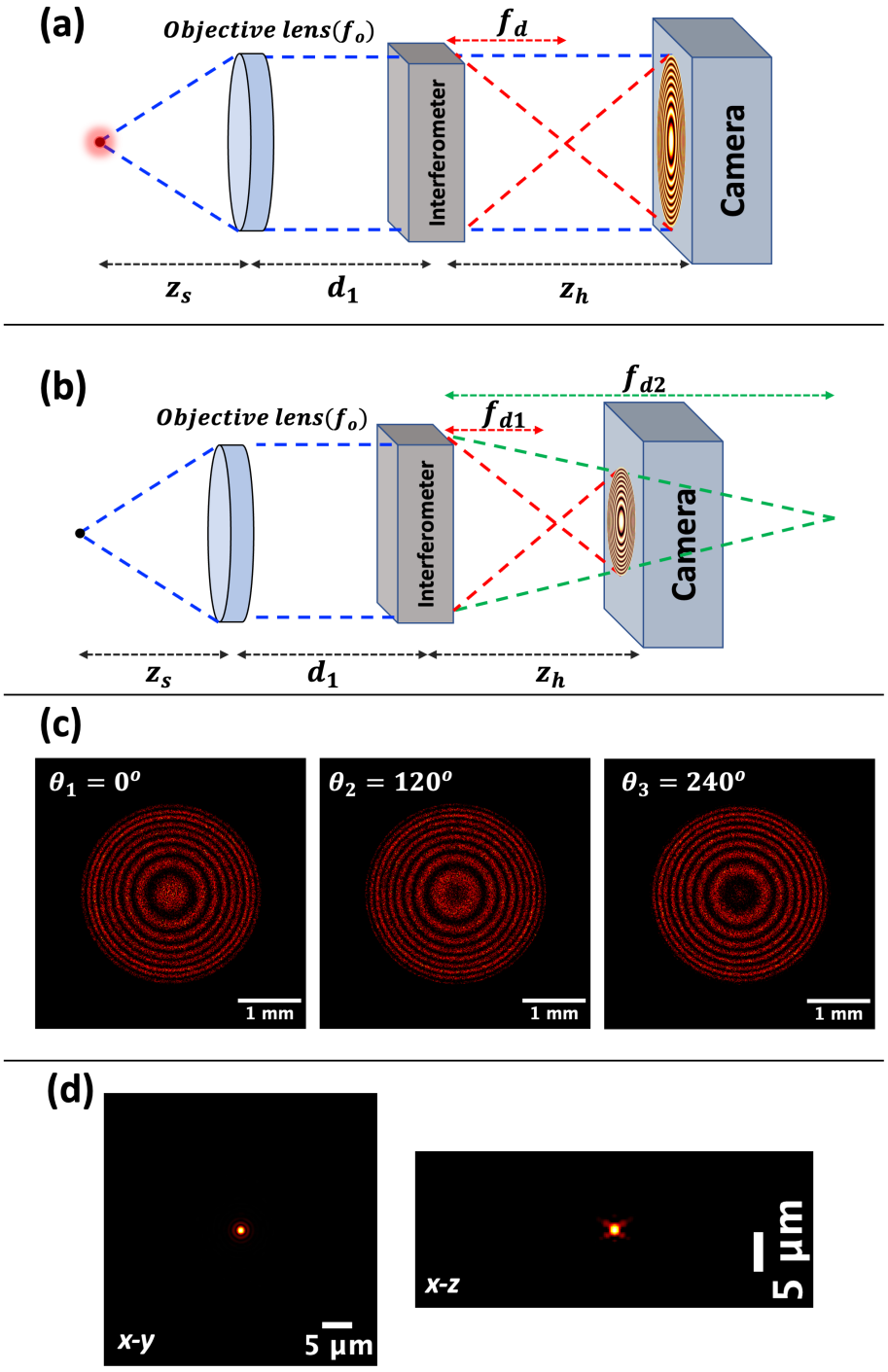

Figure 2.1: (a) Optical setup for SIDH configuration 1.: one plane wave one spherical wave configuration. (b) Optical setup for SIDH configuration 2: two spherical waves configuration. (c) The point spread holograms detected at the camera plane with different phases of $\theta_1 = 0^o$, $\theta_2 = 120^o$, and $\theta_3 = 240^o$.(d) The reconstructed PSF in lateral and axial directions.

hologram is any hologram that contains a convolution between an object function and a quadratic phase function.

For a point object located at $\mathbf{r}_s = (x_s, y_s)$, with a distance z_s from a positive lens with a focal length of f_o, produces a diverging wavefront that can be described by linear phase function $L\left(-\frac{\mathbf{r}_s}{z_s}\right)$ and quadratic phase function $Q\left(\frac{1}{z_s}\right)$ on the lens plane as $C_1(\mathbf{r}_s)L\left(-\frac{\mathbf{r}_s}{z_s}\right)Q\left(\frac{1}{z_s}\right)$, where $C_1(\mathbf{r}_s)$ is a complex constant dependent on the object's location. Right after the lens, which has a transmission function $Q\left(-\frac{1}{f_o}\right)$, the complex amplitude of the wave becomes $C_1(\mathbf{r}_s)L\left(-\frac{\mathbf{r}_s}{z_s}\right)Q\left(\frac{1}{z_s}\right)Q\left(-\frac{1}{f_o}\right)$. After further propagating an additional distance of d_1, the complex amplitude at the interferometer plane becomes $C_1(\mathbf{r}_s)L\left(-\frac{\mathbf{r}_s}{z_s}\right)Q\left(\frac{1}{z_s}\right)Q\left(-\frac{1}{f_o}\right)\otimes Q\left(-\frac{1}{d_1}\right)$. Then the interference hologram can be achieved when the interferometer reflectance function $R(x_d, y_d)$ is [81]:

$$R(x_d, y_d) = \frac{1}{2} + \frac{1}{2}\exp\left[-\frac{i\pi}{\lambda f_d}(x_d^2 + y_d^2) + i\theta\right] = \frac{1}{2} + \frac{1}{2}Q\left(-\frac{1}{f_d}\right)\exp(i\theta) \tag{2.1}$$

where f_d is the focal length of the diffractive lens that creates the spherical wave, the paraxial approximation of the spherical wave is then represented by the quadratic phase function as $Q\left(-\frac{1}{f_d}\right)$, and the first constant term $\frac{1}{2}$ represents the reflected plane wave. λ represents the central wavelength of the emitted light. The θ is the phase shift needed later to eliminate the twin image and the bias term. With the Equation 2.1, the complex amplitude right after the interferometer becomes $C_1(\mathbf{r}_s)L\left(-\frac{\mathbf{r}_s}{z_s}\right)Q\left(\frac{1}{z_s}\right)Q\left(-\frac{1}{f_o}\right)\otimes Q\left(\frac{1}{d_1}\right)\left[\frac{1}{2} + \frac{1}{2}Q\left(-\frac{1}{f_d}\right)\exp(i\theta)\right]$.

After further propagating a distance z_h, the intensity profile of the recorded hologram at the digital camera plane can be expressed as:

$$\begin{aligned} I_c(x,y) &= \left| C_1(\mathbf{r}_s)L\left(-\frac{\mathbf{r}_s}{z_s}\right)Q\left(\frac{1}{z_s}\right)Q\left(-\frac{1}{f_o}\right)\otimes \right. \\ &\qquad \left. Q\left(\frac{1}{d_1}\right)\left[\frac{1}{2} + \frac{1}{2}\exp(i\theta)Q\left(-\frac{1}{f_d}\right)\right]\otimes Q\left(\frac{1}{z_h}\right)\right|^2 \\ &= \left| C_2(\mathbf{r}_s)L\left(-\frac{\mathbf{r}_s f_e}{z_s(f_e + d_1)}\right)Q\left(\frac{1}{f_e + d_1}\right) \right. \\ &\qquad \left. \left[\frac{1}{2} + \frac{1}{2}\exp(i\theta)Q\left(-\frac{1}{f_d}\right)\right]\otimes Q\left(\frac{1}{z_h}\right)\right|^2 \end{aligned} \tag{2.2}$$

where f_e is expressed as $f_e = \frac{z_s f_o}{z_s - f_o + d_1}$. After calculating the square magnitude in Equation 2.2, the point spread hologram (PSH) for any source point located at (x_s, y_s, z_s) can be expressed as:

$$\begin{aligned} I_n(x,y) &= A_0 \left(2 + \exp\left\{\frac{i\pi}{\lambda z_r}\left[\left(x - \frac{z_h f_e x_s}{z_s(f_e+d_1)}\right)^2 + \left(y - \frac{z_h f_e y_s}{z_s(f_e+d_1)}\right)^2\right] + i\theta_n\right\}\right. \\ &\quad \left. + \exp\left\{\frac{-i\pi}{\lambda z_r}\left[\left(x - \frac{z_h f_e x_s}{z_s(f_e+d_1)}\right)^2 + \left(y - \frac{z_h f_e y_s}{z_s(f_e+d_1)}\right)^2\right] - i\theta_n\right\}\right) \\ &= A_0 \left(2 + \exp\left\{\frac{i\pi}{\lambda z_r}\left[(x - M_T x_s)^2 + (y - M_T y_s)^2\right] + i\theta_n\right\}\right. \\ &\quad \left. + \exp\left\{\frac{-i\pi}{\lambda z_r}\left[(x - M_T x_s)^2 + (y - M_T y_s)^2\right] - i\theta_n\right\}\right) \end{aligned} \tag{2.3}$$

where A_0 is a constant, θ_n is the nth phase shift applied to one of the waves by the interferometer. M_T is the transverse magnification of the system, expression of M_T is provided later. z_r is the reconstruction distance of the image of the point source, which will be different for different configurations [83]. f_e and z_r are given separately later for the two configurations shown in Figure 2.1. Details of the mathematical derivation for obtaining Equation 2.3 from Equation 2.2 can be found in Appendix 4.

Equation 2.3 contains three terms. The first term is a constant intensity bias term. The other two terms are holograms of the point source. The third term is the complex conjugate of the second and represents the twin-image of the hologram. To eliminate the twin image and bias term, three images of the same object are recorded with different phase constants of $\theta_1 = 0°$, $\theta_2 = 120°$, and $\theta_3 = 240°$, as shown in Figure 2.1(c). The final complex hologram H_F is an algebraic combination of the three images and is given by,

$$\begin{aligned} H_F(x,y) &= I_1(x,y)[\exp(\pm i\theta_3) - \exp(\pm i\theta_2)] \\ &\quad + I_2(x,y)[\exp(\pm i\theta_1) - \exp(\pm i\theta_3)] \\ &\quad + I_3(x,y)[\exp(\pm i\theta_2) - \exp(\pm i\theta_1)] \\ &= 6\sin\left(\frac{2\pi}{3}\right)\exp\left(\frac{i\pi}{\lambda z_r}[(x - M_T x_s)^2 + (y - M_T y_s)^2]\right) \end{aligned} \tag{2.4}$$

where $I_n(x,y)$ is the image corresponding to θ_n. Then, a final 3D image of the object is reconstructed from $H_F(x,y)$ by applying the Fresnel propagation formula, as shown in Figure 2.1(d), is given by:

$$g(x,y,z) = H_F(x,y) * \exp\left[\pm\frac{i\pi}{\lambda z_r}(x^2 + y^2)\right] \tag{2.5}$$

where $*$ denotes convolution and z_r is a function of the position of the object (z_s), the axial location of the reconstruction.

Configuration 1: When the object is in the focal plane, $z_s = f_o$. The reconstruction distance z_r for configuration 1 is then given by:

$$z_r = \begin{cases} \pm(z_h - f_d), & z_s = f_o \\ \pm\left(\frac{(f_1+z_h)(f_e+d_1+z_h)}{f_1-f_e-d_1}\right), & z_s \neq f_o \end{cases} \tag{2.6}$$

where

$$f_e = \frac{f_o z_s}{f_o - z_s}, \quad f_1 = \frac{f_d(f_e + d_1)}{f_d - (d_1 + f_e)}$$

.

Depending on whether the first or second exponential term from Equation 2.3 is selected, the sign "$\pm$" denotes the image reconstructed from either the virtual or real hologram image. The transverse magnification (M_T) of the system can be calculated using the imaging equation of each lens in the system and taking the product of each of the magnifications. The M_T is given by:

$$M_T = \begin{cases} \frac{z_h}{f_o}, & z_s = f_o \\ \frac{z_h f_e}{z_s(d_1+f_e)}, & z_s \neq f_o \end{cases} \tag{2.7}$$

Configuration 2: For configuration 2, the hologram is formed by the interference of two spherical waves as shown in Figure 2.1(b). f_{d1} and f_{d2} are the focal lengths of the two spherical elements in the interferometer. The transverse magnification (M_T) is the same as for configuration 1, given in Equation 2.7. The reconstruction distance (z_r) for configuration 2 is given by:

$$z_r = \begin{cases} \pm\left(\frac{(z_h-f_{d1})(z_h-f_{d2})}{f_{d1}+f_{d2}}\right), & z_s = f_o \\ \pm\left(\frac{z_{f1}z_{f2}}{z_d^2(f_{d1}-f_{d2})}\right), & z_s \neq f_o \end{cases} \tag{2.8}$$

where

$$z_{f1} = z_h z_d - f_{d1}(z_d + z_h), \quad z_{f2} = z_h z_d - f_{d2}(z_d + z_h)$$

$$z_d = \frac{z_s(f_o - d_1) + f_o d_1}{f_o - z_s}$$

2.3 SIDH based SMLM.

The method proposed by our group, combining SIDH with SMLM, has the potential to perform 3D super-resolution imaging on the nanometer precision level over a large axial range without mechanical refocusing. When imaging single molecules, the emission light from the same single molecule is split and then interfered with itself to generate a hologram of the source [84]. The previous works form our group has demonstrated localization of fluorescent microspheres using SIDH [84, 85]. Imaging fluorescent microspheres, holograms could be imaged and reconstructed from emission of as few as 13,000 photons.

We demonstrated that SIDH can achieve a localization precision of 5 nm laterally and 40 nm axially with an emitter signal level of 49,000 detected photons. However, the conventional fluorophores used in SMLM typically generate only a few hundred to a few thousand photons in the presence of background levels on the order of 10 photons per pixel. To understand the possible performance of SIDH, we investigated the theoretical limit of SIDH localization precision by computing the CRLB, which is commonly used to evaluate the performance of any specified 3D localization technique [85].

CRLB provides the theoretically best precision that can be obtained for a certain estimator. In SMLM, CRLB provides the theoretical best localization precision that can be achieved by a technique with a given number of emission photons and a given background level. By calculating the CRLB for SIDH of single emitters, our group has demonstrated that SIDH can achieve 5 nm localization precision in all three dimensions over a 20 μm axial range with high SNR. However, although the localization precision of SIDH is better than the astigmatic PSF or the Cropped Oblique Secondary Astigmatism (COSA) PSF [86] with no background noise, it declines to 125 nm for the emission of 6000 photons with background noise levels (10 photons/pixel) that are typically seen in SMLM of single cells [41, 83]. The high sensitivity to background noise in SIDH is due to the large diameter of the hologram (about 2-4 mm2 at the camera) which makes the SNR for SIDH significantly lower than the SNR for the astigmatic and the Gaussian PSFs, thereby degrading the precision of the system. Given that SMLM requires a high SNR to detect local intensity maxima for optimal localization precision, it's critical to enhance the SNR by improving the light efficiency of SIDH.

To address these issues, we propose to conduct numerical simulations to analyze and optimize the SIDH performance for better photon emission utilization and enhanced SNR across a large axial range. The related work was published in Optics Express [87].

2.4 Aberration correction for SIDH.

2.4.1 Background of optical system's aberration.

Optical systems, with their intricate design and delicate arrangement, strive to achieve the perfection of ideal systems. However, despite their precision and sophistication, real-world optical systems inevitably encounter certain limitations and deviations from their theoretical idealities. These discrepancies from the expected outcome can be attributed to what is known as optical aberrations. Optical aberrations arise from a myriad of factors, ranging from imperfections in the very design and fabrication of the optical components to their alignment within the imaging assembly. Moreover, external factors, such as the sample being imaged, can also induce aberrations. A heterogeneous biological sample might introduce fluctuations in the refractive index, or systematic effects arising from its geometry might disrupt the intended imaging outcome.

One fundamental aspect of understanding aberrations pertains to the light source used. The theoretical models often consider monochromatic light, but in real-world scenarios, especially in room-temperature fluorescence microscopy experiments, emitted light encompasses a spectrum of wavelengths.

The consequence of this spectral variety manifests as chromatic aberration. Due to the wavelength-dependent refractive indices of optical components, different wavelengths focus on diverse locations, leading to a dispersion effect and consequent blurring of the PSF.

While these aberrations pose challenges, there are potential solutions to it. Achromatic lenses, for instance, are meticulously designed to focus multiple wavelengths to a singular point, thereby reducing the effects of chromatic aberration. These lenses, given their precision, come at a high cost, which underscores the investment required to achieve near-perfect imaging. Moreover, spectral filtering strategies can also be employed to curtail the bandwidth of the final image, provided it doesn't compromise the image's intensity.

Beyond chromatic considerations, the light's amplitude and phase can also be distorted by aberrations. Uniform amplitude reduction might diminish the PSF's intensity without altering its shape, whereas non-uniform reductions reshape the PSF. Interestingly, certain systems leverage this effect. Apodization, for example, suppresses the Airy disk rings to yield a Gaussian PSF profile. Phase aberrations, on the other hand, alter the distribution of light without affecting the PSF's intensity. Given the low signal levels in SMLM, reshaping the PSF without photon loss becomes imperative.

2.4.2 Zernike Polynomials.

In an optical system, the perfect or ideal wavefront is typically represented as a planar or spherical shape. The passage of light through real optical systems often introduces deviations from this ideal shape. These deviations, commonly termed as wavefront aberrations, which can be generally modeled as the phase variation in the pupil plane of the objective lens. This means that any imaging system with optical aberrations can be characterized by introducing a phase variance term to the pupil function. If $\Psi(\xi, \eta)$ represents the aberration function in the system and $P(\xi, \eta)$ is the pupil function of the system, then the aberrated pupil $P_{ab}(\xi, \eta)$ is,

$$P_{ab}(\xi, \eta) = P(\xi, \eta) \cdot \exp[i\Psi(\xi, \eta)] \tag{2.9}$$

The aberration function $\Psi(\xi, \eta)$ can be expanded into a set of orthonormal functions, allowing the optical aberration to be described by a sequence of coefficients corresponding to a series of basic modes. As microscopy systems have circular pupils, Zernike polynomials are the most popular one that can mathematically describe the phase variance at the pupil's plane. These polynomials, defined as $Z_n^m(\rho, \phi)$ with radial coordinate, are a comprehensive and orthogonal group of eigenfunctions defined over the unit circle,

$$Z_n^m(\rho, \phi) = \begin{cases} R_n^m(\rho)\sin(m\phi), & \text{odd} \\ R_n^m(\rho)\cos(m\phi), & \text{even} \end{cases} \tag{2.10}$$

where $R_n^m(\rho)$ is the radial polynomial, n and m are integers with $n \geq m \geq 0$. And $R_n^m(\rho)$ is,

$$R_n^m(\rho) = \begin{cases} \sum_{l=0}^{\frac{n-m}{2}} \frac{(-1)^l (n-l)!}{l!\left(\frac{n+m}{2}-l\right)!\left(\frac{n-m}{2}-l\right)!} \rho^{n-2l}, & \text{for } (n-m) \text{ even} \\ 0, & \text{for } (n-m) \text{ odd} \end{cases} \tag{2.11}$$

Figure 2.2 shows the first fifteen Zernike polynomials, represented up to five orders, that can describe a wide range of aberrations commonly found in optical systems, such as astigmatism, coma or spherical aberration. Table 2.1 shows their corresponding functional forms.

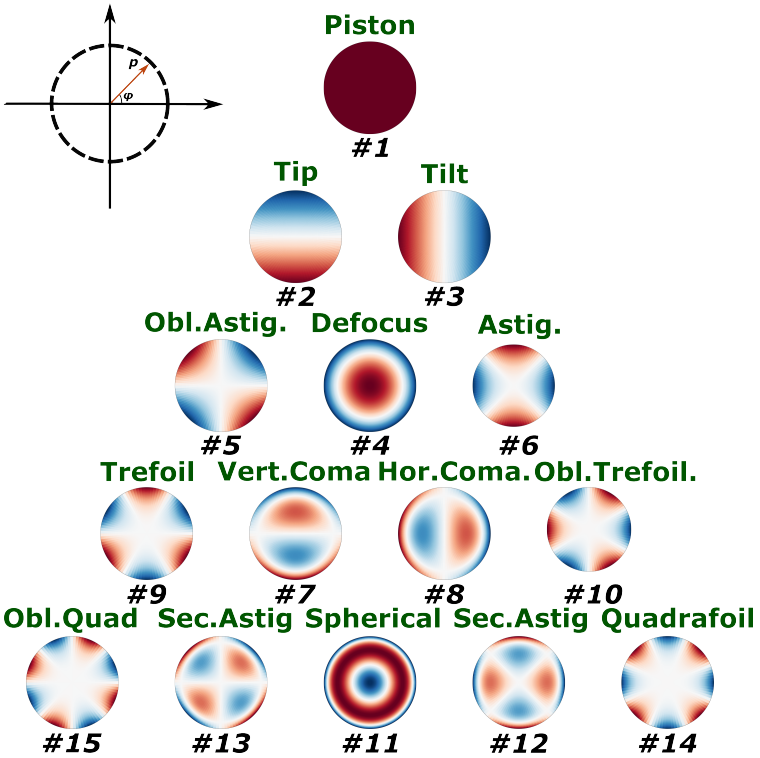

Figure 2.2: The Zernike polynomials

2.4.3 Adaptive Optics.

With utilizing the Zernike Modes, adaptive optics (AO) becomes an effective solution in either diffraction-limited or super-resolution microscopy systems. At its core, AO's task is to identify wavefront distortions, which often arise from optical aberrations, and make the necessary adjustments in real-time during the imaging process. Modern technological advancements, especially in the domain of deformable mirrors (DM) and liquid-crystal spatial light modulators (SLM), have afforded scientists the tools to precisely tweak the phase profile of light beams. With this ability in hand, the goals then shift to accurately measuring these optical aberrations. Depends on how the aberration is measured, there are mainly two group of AO in optical microscopy: direct wavefront sensing method , and indirect wavefront sensing method [88, 89].

Direct wavefront sensing method mostly needs a guide star, a wavefront sensor, a feedback loop, and a wavefront modulating component (such as DM or SLM). Depending on the microscopy technique, different mechanisms are employed to produce the guide star. The most common wavefront sensor used in AO system is the Shack-Hartmann wavefront sensor (SHWFS). It features a grid of micro-lenses. Every micro-lens reproduces a version of the source's image, but at a diminished resolution, on its focal plane. By gauging the shift of the image within each sub-aperture relative to its typical position or a set reference point, the local tilt can be determined. One of the advantages of this method is its dynamic wavefront correction capacity due to its fast response time allows the DM to be adjusted for every image frame. However, direct wavefront sensing struggles in scenarios where isolated, bright guide stars are lacking or when out-of-focus light is present, making it unsuitable for certain microscope types such as widefield microscope. The method's complexity, coupled with its inefficiency in dense or heavily scattering samples, also poses challenges.

Indirect Wavefront Sensing method, gets rid of the need for a dedicated wavefront sensor and guide star, this method uses techniques like the pupil segmentation method, works by illuminating pupil segments in sequence, capturing the consequent image shifts in the focal plane to determine the local wavefront slope [90]. Wavefront aberrations are then either algorithmically reconstructed or directly measured using interferometry. However, the need for sparse labeled objects, as each pupil segment is a measurement at a low NA, can be a limitation. An alternative approach, sensor-less AO method, corrects aberrations through iterative wavefront adjustments. It distorts the pupil profile with known aberration modes, like Zernike polynomials [91], while an image metric evaluates the aberration amplitude for each mode. The system's optimization is iterative, aiming to maximize the metric value. Compare with direct wavefront sensing method, sensor-less AO is compatible with most microscopes, resilience to scattering, and also has lower cost. However, it takes more time to acquire data.

2.4.4 Background of SIDH's aberration correction.

SIDH in this dissertation is used to extend the imaging depth of SMLM, but in cases with variable sample depths, light interference can distort aberration detection. In recent developments, there are methods that incorporated the principles of AO into the realm of incoherent digital holography for wavefront measurement and compensation [92]. One of the methods, developed by Kim, is known as Incoherent Digital Holographic Adaptive Optics (IDHAO). In this approach, a guide star hologram and quadrature phase-shifted interferograms are used to generate complex holograms. These holograms are then numerically propagated to produce aberration-corrected complex holograms. Based on the principle of IDHAO, Kim and his team later developed Fourier transform digital holographic adaptive optics imaging system (FTDHAO), which numerical propagation is avoided by obtaining the phase aberration through the inverse Fourier Transform of the guide-star hologram [93]. Compare with IDHAO, the correction of FTDHAO takes place at the eye pupil, instead of the CCD plane. However, both of the methods above need a guide star hologram. An alternative guide star free approach, proposed by Wang and his team, uses computational method to apply the aberration correction phase mask, obtained by sharpness metric function [94], on the virtual pupil plane of the reconstructed image. But the correction steps need to be

repeated for all possible reconstruction depths, which slowed down the correction speed. Considering that one super-resolution SMLM image usually consists of thousands of stacked frames collected over time [95], Man's method is not ideal for SMLM.

In this dissertation, we propose a fast, guide-star free, computational sensorless-AO method for SIDH, capable of correcting optical aberrations over a large axial range without incorporating any adaptive elements into the system. The key innovation of our method is to computationally propagate the detected complex holograms to a virtual pupil plane. By manipulating the modal aberrations in the propagation kernel, we can estimate the phase of the holograms and construct a phase correction mask at the virtual pupil plane. Our algorithm iteratively searches for the optimal correction strength of each Zernike mode, and the virtual correction phase mask is adjusted accordingly. The final aberration correction is then applied at the virtual pupil plane, and the complex holograms at the virtual pupil plane are then back-propagated to obtain the aberration-free complex holograms at the camera plane. The aberration-free complex holograms can then be reconstructed over the entire axial imaging range without repeating the correction steps. Our simulation results demonstrate that the Strehl ratio of the reconstructed image can improve from 0.71 to 0.98, and the SIDH localization precision can be restored to near the ideal case. Our experimental results further demonstrate that our method is robust for real applications. Moreover, our reconstruction process is 10 times faster than Man's [95], which makes it suitable for SMLM and single particle tracking (SPT).

2.4.5 This work.

One of the primary objectives of this dissertation is to significantly optimize the performance of SIDH. Specifically, Chapter 4 presents numerical simulations that analyze and optimize SIDH performance for better photon emission utilization and enhanced signal-to-noise ratio (SNR) across a large axial range. By integrating a tilted light-sheet (LS) illumination into the optimized SIDH system to remove background light and further reduce background noise, I experimentally demonstrated the potential of the optimized LS-SIDH setup by successfully imaging a 100 nm microsphere emitting approximately 4,200 photons over a 10 μm axial range. Chapter 5 proposes a fast, guide-star free computational aberration correction method for SIDH. The method can correct optical aberrations in low signal light conditions over the entire imaging axial range without any additional hardware. I use a sensorless-AO method in a virtual pupil plane to optimize the wavefront based on a frequency-space metric. Using this method, I demonstrate an improvement in both the Strehl ratio up to ~ 0.98 and the SIDH localization precision to near the ideal case.

Chapter 3

Principle of 2D Non-linear Structure illumination microscopy.

SMLM requires hundreds of raw images to reconstruct one super resolution image, but 2D linear SIM only requires 9 raw images, which makes SIM more suitable for live imaging [43, 74, 96]. However, as mentioned in Section 1.3.2, SIM can only improve the optical resolution by a factor of two because the strength of resolution is proportional to the spatial frequency of the structured illumination [43, 74, 97]. In this dissertation, we will explore the development of 2D Non-linear Structured Illumination Microscopy (2D-NSIM) to overcome the limitations of traditional linear SIM in enhancing optical resolution.

3.1 Principle of Non-linear Structure illumination microscopy.

3.1.1 Theoretically unlimited resolution improvement.

Understanding the principles of 2D nonlinear SIM requires examining the image formation processes in both the spatial and frequency domains. As mentioned in Section 1.3.2, a conventional, diffraction-limited imaging system can be described mathematically by multiplying the object with the illumination function and then convolving the result with the system's PSF. This convolution gives rise to the OTF in the frequency domain, which sets the diffraction limit for spatial frequencies that can be observed. In linear SIM, structured illumination is employed to break the diffraction limit. However, linear SIM's resolution enhancement remains limited to approximately two-fold because the spatial frequency of the illumination patterned cannot exceed the OTF. Therefore, when the spatial frequency of the object exceeds a domain twice the size of the diffraction limit, linear SIM fails to capture this information. This is where NSIM steps in. NSIM operates on the principle of introducing a nonlinear response of the fluorescence emission to the intensity of the excitation light, to introduce higher frequency harmonics, so that the OTF copies can be generated to contain even higher frequency information. Specifically, with

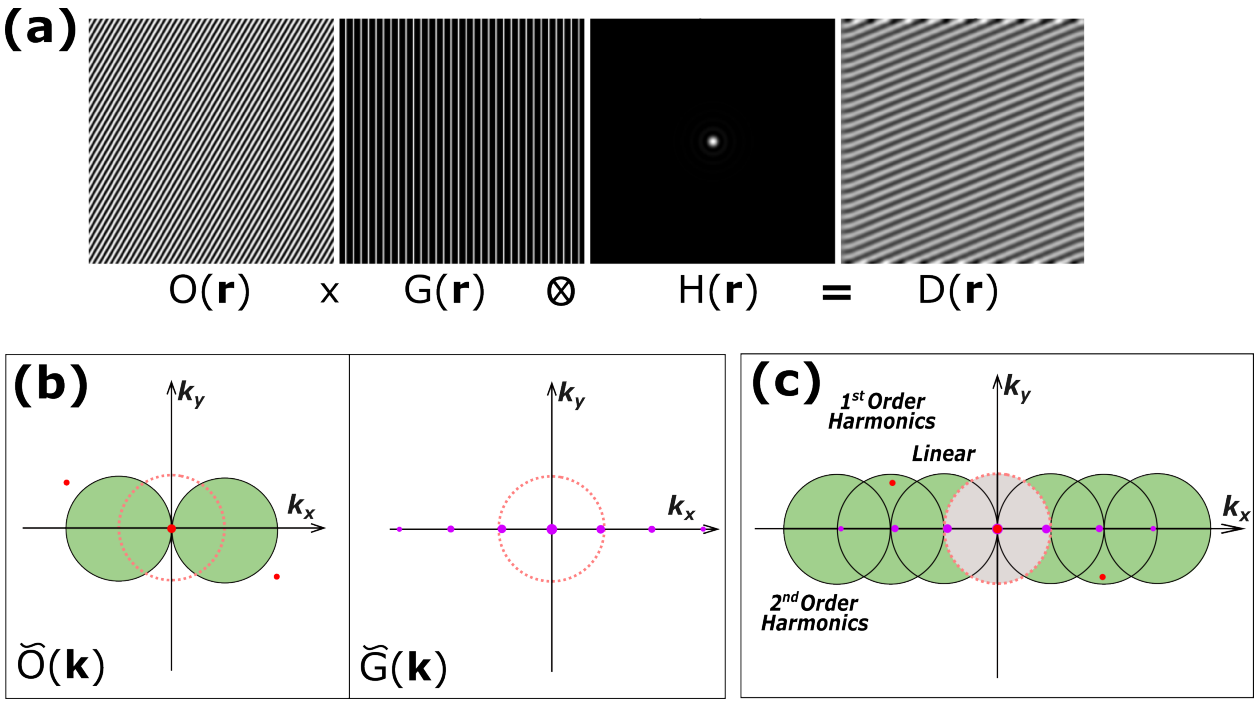

Figure 3.1: (a) Imaging formation of NSIM. (b) Frequency-space representation of object and effective illumination pattern. (c) Frequency-space representation of NSIM.

a linear sinusoidal illumination pattern $I(\mathbf{r})$, the nonlinear response of the fluorescence emission can be expressed as a power series with an infinite number of terms, which is then given by:

$$N[I(\mathbf{r})] = a_0 + a_1 I(\mathbf{r}) + a_2 I^2(\mathbf{r}) + a_3 I^3(\mathbf{r}) + \cdots + a_n I^n(\mathbf{r}) \tag{3.1}$$

$N[\cdot]$ describes the nonlinear behavior of the sample in response to the illumination light. Consider a one-dimensional sinusoidal illumination pattern:

$$I(\mathbf{r}) = 1 - \cos(2\pi \mathbf{p} \cdot \mathbf{r} + \phi) \tag{3.2}$$

where $\mathbf{r}$ is the position vector, $\mathbf{p}$ is the frequency vector of illumination light, and ϕ is the phase shift of the illumination pattern. Then the quadratic and higher powers in Equation 3.1 will lead to the effective intensity of the emission light $G(\mathbf{r})$ containing harmonics at multiples of $\mathbf{p}$:

$$\begin{aligned} G(\mathbf{r}) = N[I(\mathbf{r})] = b_0 &+ b_1 \cos(2\pi \mathbf{p} \cdot \mathbf{r} + \phi) + b_2 \cos(4\pi \mathbf{p} \cdot \mathbf{r} + 2\phi) \\ &+ b_3 \cos(6\pi \mathbf{p} \cdot \mathbf{r} + 3\phi) + \cdots + b_m \cos(2m\pi \mathbf{p} \cdot \mathbf{r} + m\phi) \end{aligned} \tag{3.3}$$

where m is the harmonic order, the coefficients b_m can be calculated from Equation 3.1 and 3.2 for any given nonlinearity $N[\cdot]$. When the phase, ϕ, of the illumination pattern is equal to zero, the b_m are equal to the coefficients of the cosine Fourier series of the function $G(\mathbf{r})$. If the nonlinearity $N[\cdot]$ is nonpolynomial, both the power series (Equation 3.1) and the Fourier series (Equation 3.3) will contain an infinite number of terms.

After transforming Equation 3.3 to the frequency domain by Fourier transform:

$$\begin{aligned}\tilde{G}(\mathbf{k}) &= b_0\delta(\mathbf{k}) + b_1\delta(\mathbf{k}+\mathbf{p})e^{i\phi} + b_1\delta(\mathbf{k}-\mathbf{p})e^{-i\phi} \\ &\quad + b_2\delta(\mathbf{k}+2\mathbf{p})e^{i2\phi} + b_2\delta(\mathbf{k}-2\mathbf{p})e^{-i2\phi} \\ &\quad + \cdots + b_m\delta(\mathbf{k}-m\mathbf{p})e^{-im\phi} \\ &= b_0\delta(\mathbf{k}) + \sum_{m=1}^{\infty} b_m\left[\delta(\mathbf{k}+m\mathbf{p})e^{im\phi} + \delta(\mathbf{k}-m\mathbf{p})e^{-im\phi}\right]\end{aligned} \tag{3.4}$$

where $\delta(\mathbf{k})$ denotes the Dirac delta function, $\mathbf{k} = (k_x, k_y)$ is the reciprocal space coordinate vector. As we can see from Equation 3.4, the resulting excitation light contains an infinite number of higher-order harmonics at integer multiples of the fundamental spatial frequency $\mathbf{p}$.

Therefore, in the spatial domain, NSIM can create a Moiré pattern even for objects that are beyond the capabilities of linear SIM, as illustrated in Figure 3.1(a). The Moiré pattern contains high spatial frequency information, which after applying a specialized reconstruction algorithm discussed in section 3.2, results in a super-resolved image. In the frequency domain, the use of a nonlinear excitation light results in a frequency shift by higher harmonic orders, enabling the capture of spatial frequency information that was previously unreachable. As shown in Figure 3.1(b), the harmonics introduced by the nonlinear pattern effectively shift high-frequency information into a domain that is inside the diffraction limit boundary. As the nonlinearity increases, more high frequency harmonic elements emerge, enabling the OTF replicas to expand and detect higher frequency information. Then, the information of the object is isolated from the higher-order harmonics and then reassembled at their correct positions in the frequency domain. In principle, the number of pattern harmonics, and thus the number of contributing information components, is infinite, as shwon in Equation 3.4 [97, 98]. In practice, however, only a finite number m of information components are strong enough to rise above the noise level.

3.1.2 NSIM Implementation Approaches

There are different approaches to using sinusoidal illumination to generate a non-sinusoidal effective excitation in NSIM.

Saturated NSIM.

The first approach is saturated NSIM [97], which utilizes the saturation of the excited state to generate the nonlinearity, as shown in Figure 3.2. In this case, the nonlinear response is realized by applying a sinusoidal illumination with very high excitation intensity.

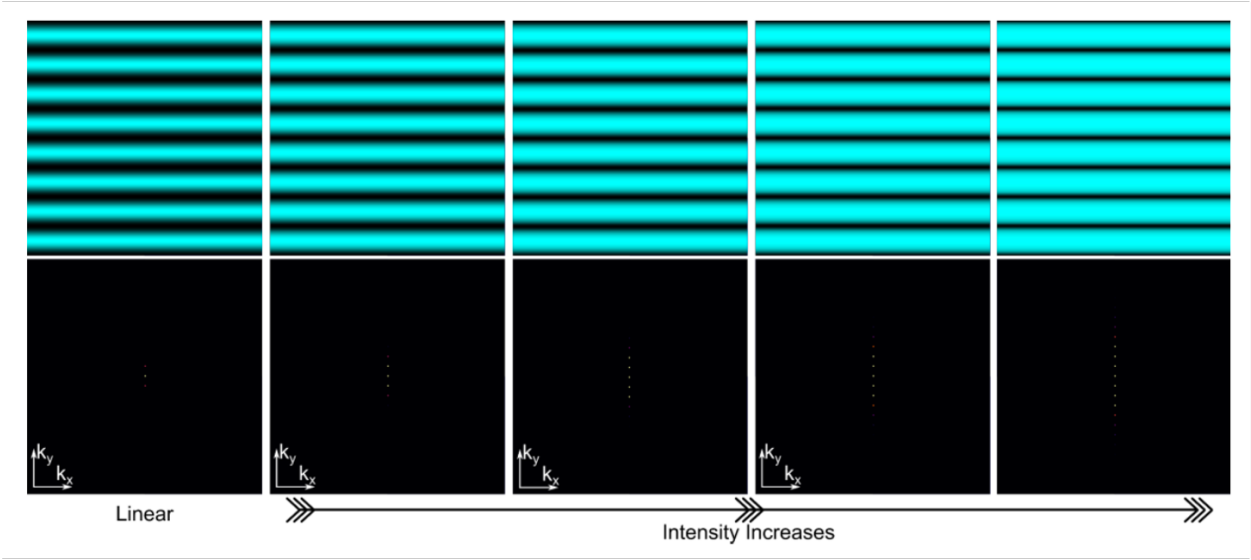

Figure 3.2: Simulation demonstration of saturated NSIM with increasing light intensities. Top row: spatial images of the saturated emission patterns. Bottom row: the Fourier transform of the corresponding pattern.

Since each molecule, on average, can emit at most one photon per lifetime, it cannot respond linearly to illumination intensities above one photon per absorption cross section per lifetime. Therefore, as the peak intensity of the illumination light rises near or above this threshold, the pattern of emission rate per fluorophore takes on a nonsinusoidal shape (the peaks of the sinusoidal wave start to flatten), which contains the desired series of harmonics with higher spatial frequency than the illumination pattern itself (Figure 3.2). However, the severe phototoxicity and photobleaching caused by the high illumination intensity can damage biological samples. Moreover, when most fluorescent molecules are emitting photons under such strong illumination light, the emission intensity becomes almost even, leaving only a few molecules in a non-emissive state. This creates an image with a poor signal-to-background ratio, making it challenging to achieve the expected resolution.

Reversibly photoswitchable fluorescent proteins based NSIM.

Alternatively, reversibly photoswitchable fluorescent proteins (rsFP) based NSIM, has been the most popular method of acquiring NSIM. As mentioned in Section 1.1.3, rsFPs can reversibly toggle between fluorescent and non-fluorescent states by the illuminating light at specific wavelengths. The switching mechanism of rsFPs is a light-induced cis-trans isomerization of the chromophore. The isomerization can lead to shifts in the chromophore's planarity, reshaping the pocket it resides in or adjusting the hydrogen-bond network surrounding it, which in turn affects its fluorescence capability. Most of rsFPs exhibit

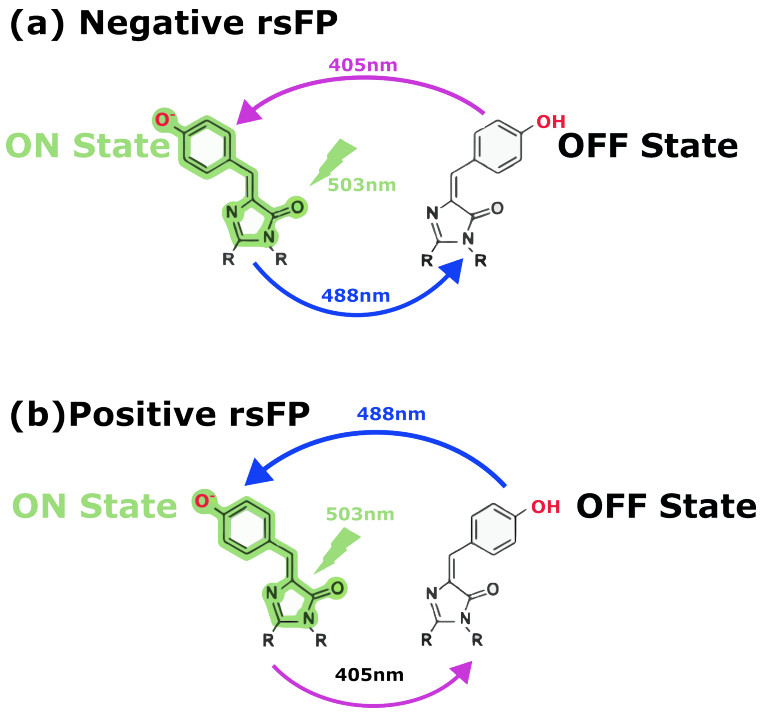

Figure 3.3: Mechanism of reversibly photoswitchable fluorescent proteins. (a) Negative rsFP, figure shows cis-trans isomerization in Dronpa as example. (b) Positive rsFP, figure shows trans-cis isomerization in Padron.[35, 99–102]

a chromophore in the off-state trans-conformation and an on-state cis-conformation. Based on their switching mode, there are mainly two categories of rsFPs, positive rsFPs (such as Padron and Kohinoor [101, 102]) and negative rsFPs (such as Dronpa [100, 101]), as shown in Figure 3.3. In the negative switching mode, rsFPs can be switched off with the wavelength that excites fluorescence, as shown in Figure 3.3(a). For positive switching rsFPs, the wavelength that excites fluorescence also switches the rsFPs from its off-state to on-state, as shown in Figure 3.3(b). Rainer Heintzmann and his team demonstrated NSIM using positive rsFP, Kohinoor [102]. However, because the light used for activation, deactivation and excitation of positive rsFPs is simultaneously present, it decreases the probability of an individual molecule to stay in the non-fluorescence state. Such a disconnect between the assumed behavior of the sample and the actual behavior of individual molecules results in only a modest improvement in NSIM resolution beyond the two-fold enhancement seen with linear SIM [102]. Therefore, most of NSIM studies use negative rsFPs to generate the desired nonlinearity.

Depending on the characteristics of different proteins, there are mainly two different acquisition methods for negative rsFPs: patterned activation approach, and patterned depletion approach.

Patterned activation approach: In the patterned activation approach, fluorophores in the sample are initially in a nonfluorescent (OFF) state, then a portion of the fluorophores are photoactivated to a

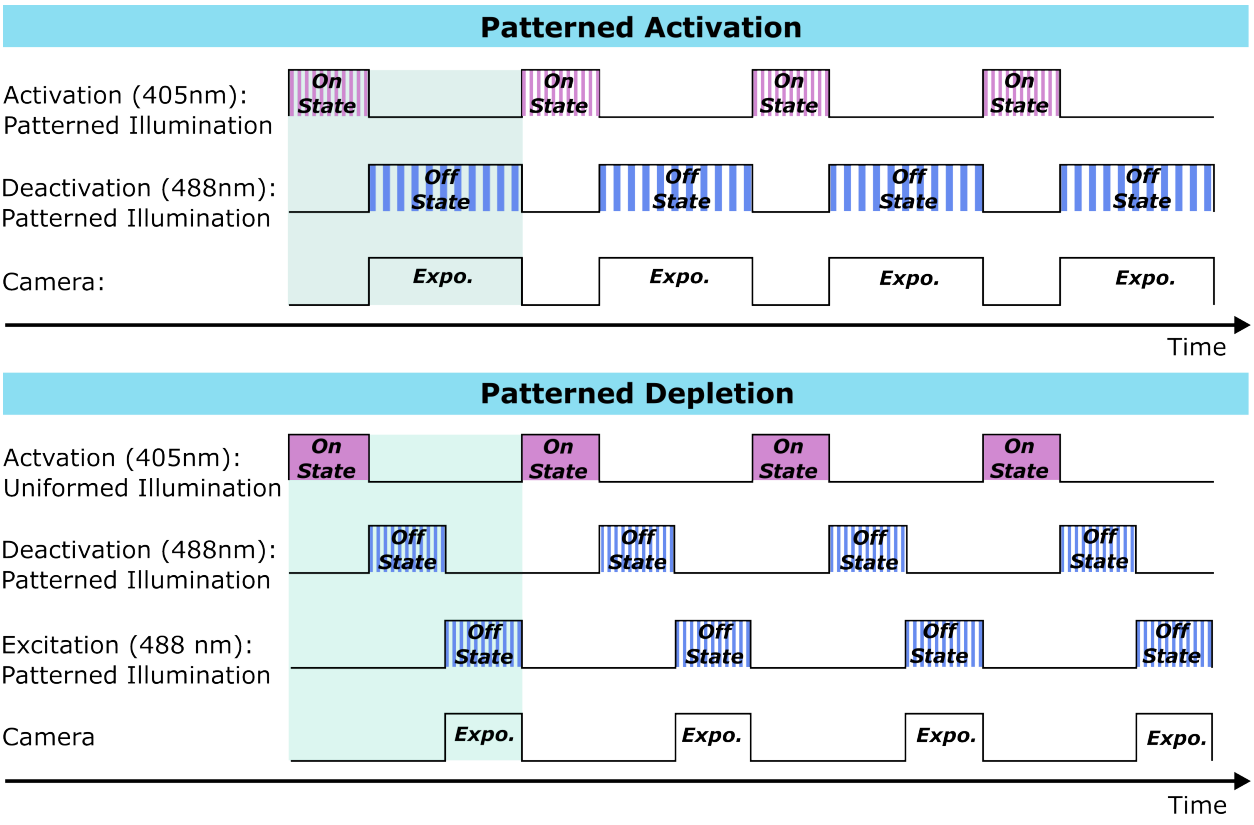

Figure 3.4: Trigger timings for different rsFP based NSIM acquization methods

fluorescent state (ON) using activation patterned illumination light (I_{act}).Then the same illumination pattern is applied to the sample again with the excitation illumination light (I_{ex}).However, due to the wavelength difference between the activation laser and excitation laser, the chromatic aberration happens even for achromatic relay lenses. Therefore, it's important to compensate for chromatic aberration and achieve identical periods at the sample plane, which the sinusoidal patterns of 405 nm activation light and 488 nm excitation and deactivation light must be aligned to precisely overlap one another. A detailed guide for compensation method can be found in ref [75]

Since the multiplication of two cosine wave with frequency $\mathbf{p}$ results in a cosine wave with doubled frequency $2\mathbf{p}$, the OTF copies now can be shifted to $6\mathrm{NA}/\lambda$ with the spatial resolution improved by a factor of three instead of two. By boosting the intensity of the activation light (I_{act}) and extending its duration (τ_{act}), fluorophores close to the activation peaks are more likely to become fully saturated in their fluorescent state. As $I_{act} \cdot \tau_{act}$ increases, the likelihood that a fluorophore remains in its initial non-fluorescent (OFF) state diminishes exponentially. However, achieving full saturation could lead to a reduction in nonlinearity. Therefore, in PA-NSIM, the goal is to carefully tune $I_{act} \cdot \tau_{act}$ to maximize

nonlinearity without fully saturating the activation peaks. With the protein's characteristic decay constant (Ω_{act}), the probability of a fluorophore being in an activated (ON) state after the activation process can be calculated as,

$$p_{\text{act}}(\mathbf{r}) = 1 - \exp\left(-\frac{I_{\text{act}} \cdot \tau_{\text{act}}}{\Omega_{\text{act}}}\right) \tag{3.5}$$

where

$$I_{\text{act}} = \frac{I_0}{2}[1 - \cos(2\pi \mathbf{p} \cdot \mathbf{r} + \phi)].$$

And during the excitation process, the excitation light used to read out the activated fluorophores can also deactivate the fluorophores with depletion decay constant Ω_{dep}. Therefore, the probability that an active fluorophore remains on after the period of t can be calculated as [103],

$$p_{\text{ex}}(\mathbf{r}, t) = \frac{1}{1 + I_{\text{ex}}(\mathbf{r}) \cdot t/\Omega_{\text{dep}}} \tag{3.6}$$

Then, the actual fluorescence emission detected by the camera,$D_{\text{img}}(\mathbf{r})$, is calculated as a temporal integral with T as the total readout exposure time:

$$D_{\text{img}}(\mathbf{r}) = O(\mathbf{r}) \int_0^T I_{\text{ex}}(\mathbf{r}) \cdot [p_{\text{act}}(\mathbf{r}) \cdot p_{\text{ex}}(\mathbf{r}, t)]\, dt \otimes H(\mathbf{r})) \tag{3.7}$$

where $O(\mathbf{r})$ stands for the object being illuminated, and $H(\mathbf{r})$ is the system's PSF.. As we see, shorter activation times result in stronger nonlinearities. The top row of Figure 3.4 shows the trigger timing for the patterned activation approach.

Patterned depletion approach: In the patterned depletion approach, all fluorophores in the sample are initially in the fluorescent (ON) state by uniform illumination, as shown in the bottom row of Figure 3.4 [98]. Then, the fluorophores are deactivated to the nonfluorescent (OFF) state by the deactivating sinusoidal illumination patterned light (I_{deact}) with an exposure time of t_{deact}. The probability that a fluorophore remains in the active state is,

$$p_{\text{deact}}(\mathbf{r}, t_{\text{deact}}) = \frac{1}{1 + I_{\text{deact}}(\mathbf{r}) t_{\text{deact}}/\Omega_{\text{dep}}} \tag{3.8}$$

Finally, the excitation sinusoidal illumination patterned light (I_{ex}), with the same period of I_{deact} but with phase shift by π, further deactivates the fluorophores to the off-state with an exposure time of t_{ex}. Then the probability that an active fluorophore remains after the excitation process is,

$$p_{\text{ex}}(\mathbf{r}, t_{\text{ex}}) = \frac{1}{1 + I_{\text{ex}}(\mathbf{r}) t_{\text{ex}}/\Omega_{\text{dep}}} \tag{3.9}$$

Therefore, with T as the total readout exposure time, the actual fluorescence emission detected on the camera is:

$$D_{\text{img}}(\mathbf{r}) = O(\mathbf{r}) \int_0^T I_{\text{ex}}(\mathbf{r}) \cdot [p_{\text{deact}}(\mathbf{r}, t_{\text{deact}}) \cdot p_{\text{ex}}(\mathbf{r}, t_{\text{ex}})]\, dt \otimes H(\mathbf{r}) \tag{3.10}$$

The nonlinearity of the final detected image $D_{\text{img}}(\mathbf{r})$ can be mathematically validated by series expansions of the fractional term and the exponential function. The fractional term can be expanded using a Taylor series, which gives:

$$\frac{1}{1+\frac{I\cdot t}{\Omega}} = 1 - \frac{I\cdot t}{\Omega} + \left(\frac{I\cdot t}{\Omega}\right)^2 - \left(\frac{I\cdot t}{\Omega}\right)^3 + \cdots \tag{3.11}$$

And for the exponential function:

$$\exp\left(-\frac{I\cdot t}{\Omega}\right) = 1 - \frac{I\cdot t}{\Omega} + \frac{\left(\frac{I\cdot t}{\Omega}\right)^2}{2!} - \frac{\left(\frac{I\cdot t}{\Omega}\right)^3}{3!} + \frac{\left(\frac{I\cdot t}{\Omega}\right)^4}{4!} \cdots \tag{3.12}$$

The high frequency terms arise from the powers of the cosine function is given by [75, 98]:

$$\cos^{2n}(2\pi\mathbf{p}\cdot\mathbf{r}+\phi) = \frac{1}{2^{2n}}\binom{2n}{n} + \frac{1}{2^{2n-1}}\sum_{p=0}^{n-1}\binom{2n}{p}\cos[2(n-p)(2\pi\mathbf{p}\cdot\mathbf{r}+\phi)] \tag{3.13}$$

$$\cos^{2n+1}(2\pi\mathbf{p}\cdot\mathbf{r}+\phi) = \frac{1}{4^{n}}\sum_{p=0}^{n}\binom{2n+1}{p}\cos[(2n+1-2p)(2\pi\mathbf{p}\cdot\mathbf{r}+\phi)] \tag{3.14}$$

Moreover, the successful implementation of NSIM is critically dependent on the photoswitching properties of the rsFP. The ideal rsFP for NSIM must meet several standards. Firstly, since the photoswitching dynamics will determine the image acquisition speed of NSIM, the fluorophore must switch rapidly between the on and off states. Second, the switching must be reversible and must survive a sufficiently large number of switching cycles. Third, in order to detect the expected nonlinear pattern, the ideal rsFPs must remain in the non-fluorescent state stably for at least hundreds of switching cycles.

Therefore, although NSIM can have theoretically unlimited resolution, in real experiments, the final resolution is affected by the strength of the nonlinear response of the emission patterns, which only the frequency orders that are strong enough to rise above the noise level are distinguishable. For different acquisition methods, rsFP based NSIM approaches require way less illumination intensity compared to saturated NSIM [97]. Moreover, rsFPs based NSIM has been experimentally demonstrated in ref [75, 98, 102, 104]. Details are discussed in Section 3.4.

3.2 Reconstruction of 2D-NSIM.

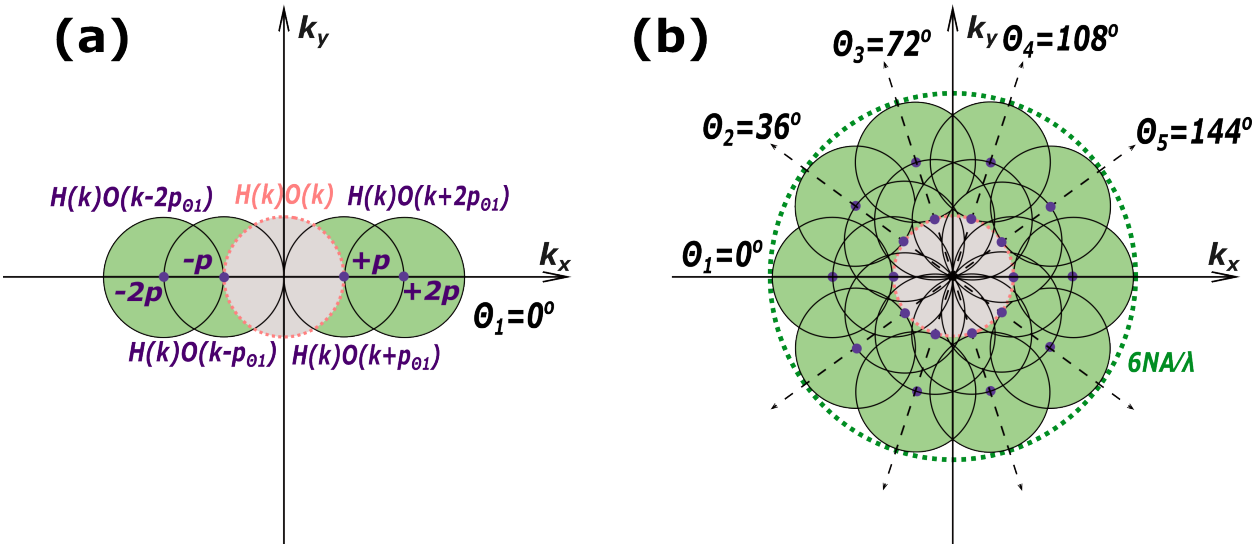

Figure 3.5: (a) Frequency content of first higher-order harmonic order NSIM within 5 circular regions. (b) Effective OTF of first higher-order harmonic order NSIM after rotating 5 angles.

Below $\mathbf{p}$ denotes the frequency of the linear pattern, φ_n denotes the nth linear phase shift, m, an integer,represents the harmonic order, and $a_{n,m}$ represents the modulation depth of specific frequency component [103]. The image that is detected by the camera is given by,

$$D_n(\mathbf{r}) = \sum_m \{O(\mathbf{r}) \cdot a_{n,m} \exp[i(2\pi m \mathbf{pr} + m\varphi_n)]\} \otimes H(\mathbf{r}) \tag{3.15}$$

where $H(\mathbf{r})$ is the system's PSF. After applying the Fourier transform to Equation 3.15, we get the expression for D in the Fourier Domain,

$$\tilde{D}_n(\mathbf{k}) = \sum_m \{\tilde{O}(\mathbf{k} - m\mathbf{p}) \cdot a_{n,m} \exp(im\varphi_n)\} \cdot \tilde{H}(\mathbf{k}) \tag{3.16}$$

Including only the first higher-order harmonic term is included ($|m| \leq 2$), as shown in Figure 3.5(a). As $\tilde{H}(\mathbf{k})$ is the system OTF, $\tilde{D}_n(\mathbf{k})$ is a linear combination of frequency content within five circular regions of the specimen: $\tilde{O}(\mathbf{k})$ centered at origin, linear order $\tilde{O}(\mathbf{k}-\mathbf{p})$ and $\tilde{O}(\mathbf{k}+\mathbf{p})$, and first harmonic order $\tilde{O}(\mathbf{k}-2\mathbf{p})$ and $\tilde{O}(\mathbf{k}+2\mathbf{p})$. Five different SIM images, $D_0(\mathbf{r})$, $D_1(\mathbf{r})$, $D_2(\mathbf{r})$, $D_3(\mathbf{r})$ and $D_4(\mathbf{r})$, of the sample are acquired corresponding to five different illumination phases. Typically, $\varphi_0 = 0$, $\varphi_1 = \frac{2\pi}{5}$, $\varphi_2 = \frac{4\pi}{5}$, $\varphi_3 = \frac{6\pi}{5}$, and $\varphi_4 = \frac{8\pi}{5}$. Therefore, the five copies of OTF can be separated through the linear

combination of the acquired images as follows:

$$\begin{bmatrix} \tilde{D}_1(\mathbf{k}) \\ \tilde{D}_2(\mathbf{k}) \\ \tilde{D}_3(\mathbf{k}) \\ \tilde{D}_4(\mathbf{k}) \\ \tilde{D}_5(\mathbf{k}) \end{bmatrix} = M \begin{bmatrix} \tilde{O}(\mathbf{k})\tilde{H}(\mathbf{k}) \\ \tilde{O}(\mathbf{k}-\mathbf{p})\tilde{H}(\mathbf{k}) \\ \tilde{O}(\mathbf{k}+\mathbf{p})\tilde{H}(\mathbf{k}) \\ \tilde{O}(\mathbf{k}-2\mathbf{p})\tilde{H}(\mathbf{k}) \\ \tilde{O}(\mathbf{k}+2\mathbf{p})\tilde{H}(\mathbf{k}) \end{bmatrix} \tag{3.17}$$

where

$$M = \begin{bmatrix} 1 & a_{0,1}\exp(i\varphi_0) & a_{0,1}\exp(-i\varphi_0) & a_{0,2}\exp(2i\varphi_0) & a_{0,2}\exp(-2i\varphi_0) \\ 1 & a_{1,1}\exp(i\varphi_1) & a_{1,1}\exp(-i\varphi_1) & a_{1,2}\exp(2i\varphi_1) & a_{1,2}\exp(-2i\varphi_1) \\ 1 & a_{2,1}\exp(i\varphi_2) & a_{2,1}\exp(-i\varphi_2) & a_{2,2}\exp(2i\varphi_2) & a_{2,2}\exp(-2i\varphi_2) \\ 1 & a_{3,1}\exp(i\varphi_3) & a_{3,1}\exp(-i\varphi_3) & a_{3,2}\exp(2i\varphi_3) & a_{3,2}\exp(-2i\varphi_3) \\ 1 & a_{4,1}\exp(i\varphi_4) & a_{4,1}\exp(-i\varphi_4) & a_{4,2}\exp(2i\varphi_4) & a_{4,2}\exp(-2i\varphi_4) \end{bmatrix}$$

The rest of the reconstruction process is similar to linear SIM. The five copies of the OTF are separated by left-multiplying the inverse matrix M^{-1} on both sides of Equation 3.17. With the information of the pattern's orientation, frequency, and relative phase, we can then accurately reassemble the OTF copies, as shown in Figure 3.5(a).

The phase, frequency, and modulation depth for shifted OTF copies are determined by comparing the overlap regions in reciprocal space between the shifted term $\tilde{O}(\mathbf{k}-\mathbf{p})\tilde{H}(\mathbf{k})$ and widefield term $\tilde{O}(\mathbf{k})\tilde{H}(\mathbf{k})$ for the linear term, and between $\tilde{O}(\mathbf{k}-2\mathbf{p})\tilde{H}(\mathbf{k})$ and linear term $\tilde{O}(\mathbf{k}-\mathbf{p})\tilde{H}(\mathbf{k})$ for the nonlinear term. If we take the linear shift term $\tilde{O}(\mathbf{k}-\mathbf{p})$ as an example, then we will have,

$$\tilde{O}(\mathbf{k}-\mathbf{p}) = \mathcal{F}\left\{\mathcal{F}^{-1}\left\{\tilde{O}(\mathbf{k})\right\} \cdot \exp\left[-i2\pi(\mathbf{pr})\right]\right\} \tag{3.18}$$

With correct $\mathbf{p}$, the overlap region of the two terms should contain the same information, except for noise and a constant factor $a_{n,1}\exp(i\varphi_n)$. The initial phase φ_n and modulation depth $a_{n,1}$ can be obtained by complex linear regression of the widefield term against the shifted term,

$$\sum M\left\{\tilde{O}(\mathbf{k})\tilde{H}(\mathbf{k})\right\} = a_{n,1}\exp(i\varphi_n)\sum M\left\{\tilde{O}(\mathbf{k}-\mathbf{p})\tilde{H}(\mathbf{k})\right\} \tag{3.19}$$

where $M\{*\}$ is the filter function used to isolate the area of overlap. And the proportionality constant is then estimated as:

$$a_{n,1}\exp(i\varphi_n) = \sum M\left\{\frac{[\tilde{O}(\mathbf{k})\tilde{H}(\mathbf{k})]^* \cdot \tilde{O}(\mathbf{k}-\mathbf{p})\tilde{H}(\mathbf{k}-\mathbf{p})}{|\tilde{O}(\mathbf{k})\tilde{H}(\mathbf{k})|^2}\right\} \tag{3.20}$$

Consequently, with the accurate value of $\mathbf{p}$, the proportionality constants in the region where the OTFs overlap exhibit phases that are nearly uniformly constant. This leads to the highest amplitude in the complex summation. A grid for parameter searching can then be established to search all the frequencies,

featuring a set of distinct spatial frequencies that vary around the approximate value of $\mathbf{p}$. The frequency that aligns with the peak value in the search grid is the accurate frequency for the corresponding order. The searching process can be performed in an iterative manner, each time using a more refined search grid that's focused on the frequency determined in the preceding broader search. If we define the concise notation for the separated information components as:

$$\tilde{R}_m(\mathbf{k} - m\mathbf{p}) = b_m \tilde{H}(\mathbf{k})\tilde{O}(\mathbf{k} + m\mathbf{p}) \tag{3.21}$$

Then the estimate $\tilde{O}_m(\mathbf{k})$ is given by:

$$\tilde{O}_m(\mathbf{k}) = \frac{\tilde{R}_m(\mathbf{k})}{b_m \tilde{H}(\mathbf{k} + m\mathbf{p})} \tag{3.22}$$

The noise variance of $\tilde{O}_m(\mathbf{k})$ is inversely proportional to $|b_m \tilde{H}(\mathbf{k} + m\mathbf{p})|^2$ (details can be found in ref [87]). After getting all the correct parameters, the different information components $\tilde{D}_n(\mathbf{k})$ are then re-assembled using a generalized Wiener filter [88] to regularized $\tilde{O}_m(\mathbf{k})$ with a Wiener parameter α^2 in the denominator. Then the regularized estimate, $\tilde{O}_r(\mathbf{k})$, of the true object $\tilde{O}(\mathbf{k})$ is given by:

$$\tilde{O}_r(\mathbf{k}) = \frac{\sum \tilde{O}_m(\mathbf{k})|b_m \tilde{H}(\mathbf{k} + m\mathbf{p})|^2}{\sum |b_m \tilde{H}(\mathbf{k} + m\mathbf{p})|^2 + \alpha^2} \tag{3.23}$$

$$\tilde{O}_r(\mathbf{k}) = \frac{\sum b_m^* \tilde{H}^*(\mathbf{k} + m\mathbf{p})\tilde{R}_m(\mathbf{k})}{\sum |b_m \tilde{H}(\mathbf{k} + m\mathbf{p})|^2 + \alpha^2} \tag{3.24}$$

As the example only includes the first higher-order harmonic term, the $\tilde{O}_r(\mathbf{k})$ is given by:

$$\begin{aligned} \tilde{O}_r(\mathbf{k}) = &\frac{b_0^* \tilde{H}^*(\mathbf{k})\tilde{R}_0(\mathbf{k}) + b_1^* \tilde{H}^*(\mathbf{k} + \mathbf{p})\tilde{R}_1(\mathbf{k}) + b_{-1}^* \tilde{H}^*(\mathbf{k} - \mathbf{p})\tilde{R}_{-1}(\mathbf{k})}{|b_0 \tilde{H}(\mathbf{k}) + b_1 \tilde{H}(\mathbf{k} + \mathbf{p}) + b_{-1} \tilde{H}(\mathbf{k} - \mathbf{p}) + b_2 \tilde{H}(\mathbf{k} + 2\mathbf{p}) + b_{-2} \tilde{H}(\mathbf{k} - 2\mathbf{p})|^2 + \alpha^2} \\ + &\frac{b_2^* \tilde{H}^*(\mathbf{k} + 2\mathbf{p})\tilde{R}_2(\mathbf{k}) + b_{-2}^* \tilde{H}^*(\mathbf{k} - 2\mathbf{p})\tilde{R}_{-2}(\mathbf{k})}{|b_0 \tilde{H}(\mathbf{k}) + b_1 \tilde{H}(\mathbf{k} + \mathbf{p}) + b_{-1} \tilde{H}(\mathbf{k} - \mathbf{p}) + b_2 \tilde{H}(\mathbf{k} + 2\mathbf{p}) + b_{-2} \tilde{H}(\mathbf{k} - 2\mathbf{p})|^2 + \alpha^2} \end{aligned} \tag{3.25}$$

To cover the whole isotropic space in the frequency domain, the process needs to be performed for at least 5 orientations with angles shown in Figure 3.5(b). Finally, an estimate of the object in spatial domain is obtained by an inverse Fourier transform of $\tilde{O}_r(\mathbf{k})$.

3.3 Principle of TIRF-SIM.

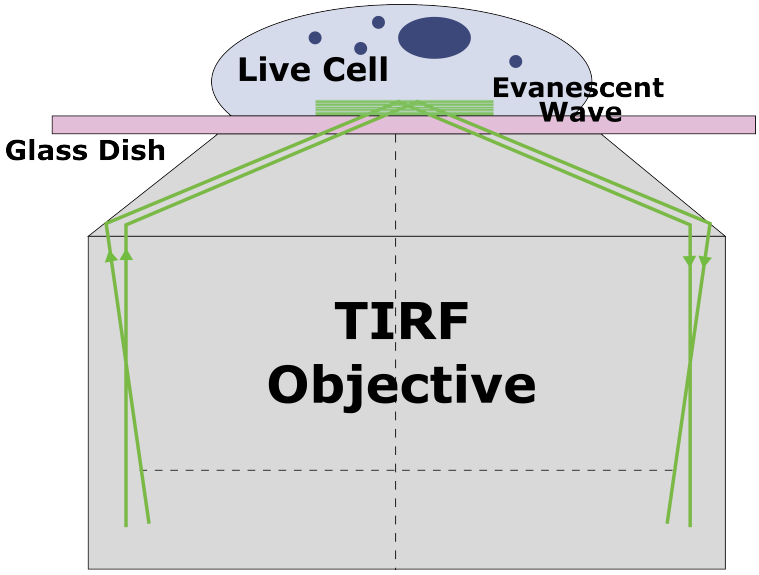

Figure 3.6: Schematic of TIRF illumination

As mentioned in Chapter 1, TIRF is a specialized widefield technique that focuses on illuminating molecules at the coverslip surface. The thickness of the sample that is illuminated is often less than 100 nanometers thick. This enables high-contrast imaging with minimal background noise, making TIRF an invaluable tool for single-molecule studies, membrane biology, and other applications requiring high SNR. As shown in Figure 3.6, The core principle of TIRF is rooted in Snell's Law of Refraction, which describes how light behaves when it travels from one medium into another with a different refractive index. When light passes from a medium with a higher refractive index (e.g., glass) to one with a lower refractive index (e.g., water or air), the light ray is refracted away from the normal line perpendicular to the interface between the two media. If the incident angle is greater than a certain critical angle, the light will no longer pass through the interface but will instead be totally internally reflected. This total internal reflection creates an "evanescent wave," an electromagnetic field that propagates along the interface. The intensity of this evanescent wave decays exponentially with distance from the interface, effectively forming a very thin illumination zone. When fluorescent molecules come into this narrowly confined field, they become excited and subsequently emit fluorescence. By focusing on such a narrow axial plane, TIRF reduces background fluorescence and increases the SNR, allowing for the observation of fine details that might otherwise be obscured. Despite these axial advantages, it's important to note that the lateral resolution of TIRF is still subject to the diffraction limit, although advances such as structured illumination can improve this aspect. TIRF has been demonstrated both with SIM [75, 105, 106] and NSIM [98].

3.4 Experimental results from other groups.

As mentioned in Section 3.1.2, rsFP based NSIM is the most popular approach to NSIM imaging, and it has been demonstrated experimentally. The rsFPs that have been used for NSIM studies so far are Dronpa [98], rsEGFP2 [75, 104], Skylan-NS [75, 104], and Kohinoor [102]. A comprehensive study of characteristic of different rsFPs can be reviewed in ref [107], [104] and [101].

Rego et al. [98] successfully demonstrated a lateral resolution of 50 nm using pattern depletion TIRF-NSIM with Dronpa to image purified microtubules in fixed CHO cells by capturing 63 (7 phases for 9 orientations) readout images. Although Dronpa has the capability to photoswitch, its switching rate is slow, requiring about 0.4 seconds of exposure to turn off with approximately 20 $W/cm^2$of 488 nm light. This limits the imaging speed of NSIM when using Dronpa. Moreover, another significant limitation with Dronpa was its inability to go beyond 15 switching cycles before substantial bleaching set in. Achieving even this limited performance necessitated the use of toxic anti-bleaching chemicals, which precludes its application in live-cell imaging.

Li and colleagues [75] utilized Skylan-NS to perform patterned activation NSIM to observe intracellular dynamics in living cells by lattice light sheet microscopy. It demonstrated a spatial resolution of approximately 60 nm and a time resolution of around 40 frames per second. However, the use of patterned activation approach requires a challenging perfect illumination alignment that the 405 nm illumination pattern needs to precisely align with the 488 nm illumination pattern at every position. Moreover, compare with other rsFPs, the contrast ratio of Skylan-NS reduces rapidly, which results in a poor nonlinearity as the number of switching cycles increase. In conclusion, rsFPs based NSIM requires the rsFPs to be highly stable and capable of enduring at least hundreds of switching cycles between their fluorescent and non-fluorescent states.

Moreover, another complexity in using rsFPs lies in the binary nature of the fluorescent molecule's state—either 'on' or 'off'. For example, the model assumes a sample at a certain position might contribute, say, 20% of its brightness during readout after being switched off with an 80% chance. In reality, an individual molecule will either be entirely "on" (100% brightness) or "off" (0% brightness). This disconnect between the assumed behavior of the sample and the actual behavior of individual molecules can be expected to contribute to the artefacts in the final reconstructed image. These deviations can be averaged out if many molecules contribute to a pixel or undergo numerous switching cycles while contributing to the results. Therefore, it's more beneficial to prioritize the protein's ability to survive more switching cycles without deteriorating, which has been a key driver for recent advancements in the development of new fluorescent proteins capable of a greater number of switching cycles. Therefore, we propose to utilize rsEGFP2 to obtain 2D pattern depletion NSIM (PD-NSIM) imaging as rsEGFP2 has long fluorescence decay and fast switching time, and pattern depletion approach has lower requirement on system alignment compare with PA-NSIM. Details of the characteristic of rsEGFP2 is introduced in Chapter 6.

3.5 This work.

As previously mentioned, live-cell imaging with PA-NSIM has been widely studied, however, Li et al.'s work provides only theoretical resolution without demonstrating real data or Fourier space information [75, 104, 108]. And PD-NSIM has not been demonstrated in live-cell imaging, nor has it been implemented using the rsEGFP2 protein. In this dissertation, I present the first demonstration of 2D pattern depletion NSIM (2D PD-NSIM) live-cell imaging using the rsEGFP2 protein. The imaging system and data acquisition process were optimized to enhance the strength of the nonlinear response. Using 2D PD-NSIM, we successfully imaged actin filaments in U2OS cells, achieving sub-80 nm resolution in live-cell imaging. The experimental design and results of 2D PD-NSIM are discussed in detail in Chapter 6. Chapter 7 explores future directions for polarization optimization in the SIM setup, which could potentially improve NSIM performance further.

Chapter 4

Optimizing self-interference digital holography for single-molecule localization

As mentioned in Chapter 2, SIDH can image incoherently emitting objects over large axial ranges from three two-dimensional images. By combining SIDH with SMLM, incoherently emitting objects can be localized with nanometer precision over a wide axial range without mechanical refocusing. Previous work from our group has demonstrated the localization of fluorescent microspheres using SIDH [84, 85]. Imaging fluorescent microspheres, holograms could be imaged and reconstructed from emission of as few as $13,000$ photons [84]. We demonstrated that SIDH can achieve a localization precision of 5nm laterally and 40 nm axially with an emitter signal level of $49,000$ detected photons. However, the conventional fluorophores used in SMLM typically generate only a few hundred to a few thousand photons in the presence of background, and the background light substantially degrades the performance of SIDH due to the relatively large size of the point spread hologram.

To understand the possible performance of SIDH, a previous study by our group investigated the theoretical limit of the precision of SIDH localization by computing the CRLB [85]. CRLB provides the theoretically best precision that can be obtained for a certain estimator.In SMLM, CRLB provides the theoretical best localization precision that can be achieved by a technique with a given number of emission photons and a given background level. By calculating the CRLB for SIDH of single emitters, our group has demonstrated that SIDH can achieve 5 nm localization precision in all three dimensions over a 20 μm axial range with high SNR. However, although the localization precision of SIDH is better than the astigmatic PSF or the Cropped Oblique Secondary Astigmatism (COSA) PSF [85] with no background noise, it declines to ~ 125 nm for the emission of 6000 photons with background noise levels of ~ 10 photons/pixel) that are typically seen in SMLM of single cells [41, 86]. The high sensitivity to background noise in SIDH is due to the large diameter of the hologram (about $2-4\text{mm}^2$ at the camera in ref [84, 85]) which makes the SNR for SIDH significantly lower than the SNR for the astigmatic and the Gaussian PSFs, thereby degrading the precision of the system. Given that SMLM requires a high SNR to detect

local intensity maxima for optimal localization precision, it's critical to enhance the SNR by improving the light efficiency of SIDH.

To address these issues, in this chapter, I conducted numerical simulations to analyze and optimize the SIDH performance for better photon emission utilization and enhanced SNR across a large axial range. Specifically, the optimal hologram radius (R_h) for different levels of background photons is studied for two different configurations as mentioned in section 2.2. The results show that by reducing the size of the hologram, SIDH based SMLM can achieve a localization precision of better than 60 nm laterally and 80 nm axially over a $10\mu m$ axial range under the conditions of low signal level (6000 photons) with 10 photons/pixel of background noise. Moreover, I then verified our simulation findings with experiments, and I incorporated light-sheet (LS) illumination into the optimized SIDH system to remove background light, further reducing the background noise [109]. The experimental results demonstrate that with the optimal optical setup, SIDH can reconstruct the point spread hologram (PSH) from as few as $\sim 2,120$ photons. Furthermore, with an emitter signal level of as few as $\sim 4,200$ photons, the PSH can be reconstructed over an axial range of 10μm.

4.1 Methods

4.1.1 Specific layout of SIDH's simulation setup

As mentioned in Chapter 2, SIDH splits the incoherent light emitted from the sample into two beams, which are individually phase-modulated before being recombined to generate interference fringes. The phase modulation can be a spherical phase, introduced to the beam by a curved mirror or lens. The density of the interference fringes then contains information on the object's axial position [82, 110]. In this section, I will discuss the specific layout of the two configurations that I used in the simulations. While the general theoretical analysis of SIDH can be found in section 2.2.

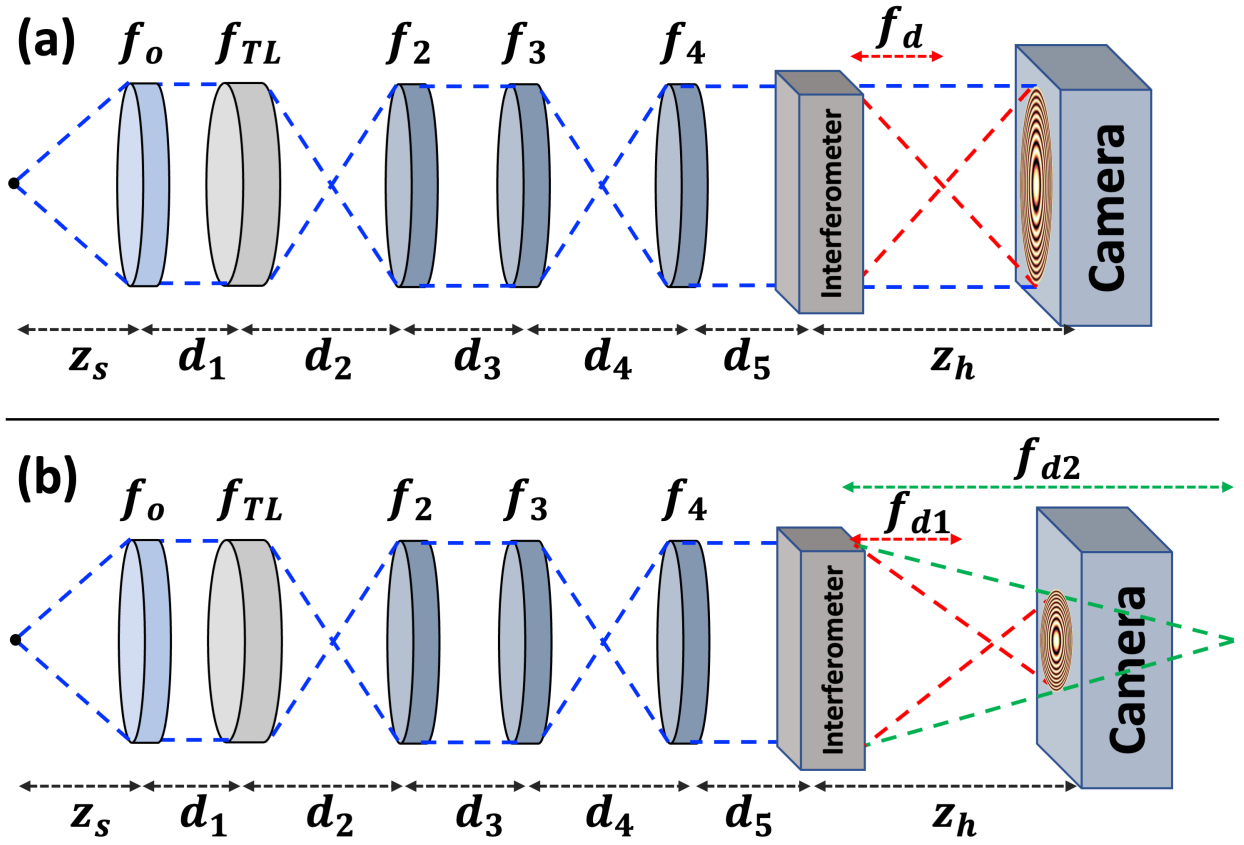

Figure 4.1: (a) Optical setup for SIDH configuration 1: one plane wave one spherical wave configuration. (b) Optical setup for SIDH configuration 2: two spherical wave configuration.

Configuration 1: one plane wave one spherical wave

In configuration 1, shown in Figure 4.1(a), the hologram is formed by the interference between one spherical wave and one plane wave. The focal length of the objective lens (f_0) is 3 mm with an NA of 1.42. The objective is followed by a tube lens ($f_{TL} = 180$mm) and an achromatic lens ($f_2 = 120$mm) which form an image of the pupil plane. The relay lenses f_3 and f_4 control the radius of the beam before it enters the interferometer R_e. In the interferometer, one half of the light is modulated by an element with focal length f_d. z_s is the position of the object and $z_s = f_0$ when the object is in the focal plane. The reconstruction distance z_r for configuration 1 is then given by:

$$z_r = \begin{cases} \pm(z_h - f_d), & z_s = f_0 \\ \pm\left(\frac{(f_6+z_h)(f_5+d_5+z_h)}{f_6-f_5-d_5}\right), & z_s \neq f_0 \end{cases} \tag{4.1}$$

where

$$f_{e1} = \frac{f_0 z_s}{f_0 - z_s}, \quad f_{e2} = \frac{f_{TL}(d_1 + f_{e1})}{f_{TL} - (d_1 + f_{e1})}, \quad f_{e3} = \frac{f_2(d_2 + f_{e2})}{f_2 - (d_2 + f_{e2})}$$
$$f_{e4} = \frac{f_3(d_3 + f_{e3})}{f_3 - (d_3 + f_{e3})}, \quad f_{e5} = \frac{f_4(d_4 + f_{e4})}{f_4 - (d_4 + f_{e4})}, \quad f_6 = \frac{f_d(d_5 + f_{e5})}{f_d - (d_5 + f_{e5})}$$

Depending on whether the first or second exponential term from Equation 2.3 is selected, the sign "$\pm$" denotes the image reconstructed from either the virtual or real hologram image. The transverse magnification (M_T) of the system can be calculated using the imaging equation of each lens in the system and taking the product of each of the magnifications. The M_T is given by:

$$M_T = \begin{cases} \frac{z_h}{f_0}, & z_s = f_0 \\ \frac{z_h f_{e1} f_{e2} f_{e3} f_{e4} f_{e5}}{z_s(d_1+f_{e1})(d_2+f_{e2})(d_3+f_{e3})(d_4+f_{e4})(d_5+f_{e5})}, & z_s \neq f_0 \end{cases} \tag{4.2}$$

Configuration 2: two spherical waves

For configuration 2, the hologram is formed by the interference of two spherical waves as shown in Figure 4.1(b). f_{d1} and f_{d2} are the focal lengths of the two spherical elements in the interferometer. The M_T of configuration 2 is the same as for configuration 1, given in Equation 4.2. The reconstruction distance for configuration 2 is given by:

$$z_r = \begin{cases} \pm \frac{(z_h - f_{d1})(z_h - f_{d2})}{(f_{d1} + f_{d2})}, & z_s = f_0 \\ \pm \left(\frac{z_{f1} z_{f2}}{z_d^2 (f_{d1} - f_{d2})} \right), & z_s \neq f_0 \end{cases} \tag{6}$$

where

$$z_{f1} = z_h z_d - f_{d1}(z_d + z_h), \quad z_{f2} = z_h z_d - f_{d2}(z_d + z_h)$$

and

$$z_d = \frac{f_4 z_{d4}}{f_4 - z_{d4}} + d_5, \quad z_{d4} = \frac{f_3 z_{d3}}{f_3 - z_{d3}} + d_4, \quad z_{d3} = \frac{f_2 z_{d2}}{f_2 - z_{d2}} + d_3,$$
$$z_{d2} = \frac{f_{TL} z_{d1}}{f_{TL} - z_{d1}} + d_2, \quad z_{d1} = f_e + d_1$$

4.1.2 Method of studying the relationship between detected hologram size and localization precision

As mentioned, our previous studies [41, 86] demonstrate that SIDH requires optimization to achieve high SNR and high localization precision in the presence of background light. To achieve this, the light efficiency of the SIDH system must be maximized and the background noise must be as low as possible. Therefore, in our numerical simulations, we examine the relationship between the detected hologram size (R_h) and the localization precision of SIDH. The radius of the hologram at the digital camera plane is calculated by using the ABCD ray transfer matrix framework as follows:

Configuration 1:

the radius of the plane wave at the digital camera plane:

$$\begin{bmatrix} r_{\text{plane}} \\ \gamma_{\text{plane}} \end{bmatrix} = \begin{bmatrix} 1 & z_h \\ 0 & 1 \end{bmatrix} \begin{bmatrix} 1 & d_5 \\ 0 & 1 \end{bmatrix} \begin{bmatrix} 1 & 0 \\ -\frac{1}{f_4} & 1 \end{bmatrix} \begin{bmatrix} 1 & d_4 \\ 0 & 1 \end{bmatrix} \begin{bmatrix} 1 & 0 \\ -\frac{1}{f_3} & 1 \end{bmatrix} \begin{bmatrix} 1 & d_3 \\ 0 & 1 \end{bmatrix} \begin{bmatrix} 1 & 0 \\ -\frac{1}{f_2} & 1 \end{bmatrix} \begin{bmatrix} 1 & d_2 \\ 0 & 1 \end{bmatrix} \begin{bmatrix} 1 & 0 \\ -\frac{1}{f_{TL}} & 1 \end{bmatrix} \begin{bmatrix} 1 & d_1 \\ 0 & 1 \end{bmatrix} \begin{bmatrix} 1 & 0 \\ -\frac{1}{f_0} & 1 \end{bmatrix} \begin{bmatrix} 1 & z_s \\ 0 & 1 \end{bmatrix} \begin{bmatrix} h_{\text{enter}} \\ \gamma_{\text{enter}} \end{bmatrix} \tag{4.3}$$

the radius of the spherical wave at the digital camera plane:

$$\begin{bmatrix} r_{f_d} \\ \gamma_{f_d} \end{bmatrix} = \begin{bmatrix} 1 & z_h \\ 0 & 1 \end{bmatrix} \begin{bmatrix} 1 & 0 \\ -\frac{1}{f_d} & 1 \end{bmatrix} \begin{bmatrix} 1 & d_5 \\ 0 & 1 \end{bmatrix} \begin{bmatrix} 1 & 0 \\ -\frac{1}{f_4} & 1 \end{bmatrix} \begin{bmatrix} 1 & d_4 \\ 0 & 1 \end{bmatrix} \begin{bmatrix} 1 & 0 \\ -\frac{1}{f_3} & 1 \end{bmatrix} \begin{bmatrix} 1 & d_3 \\ 0 & 1 \end{bmatrix} \begin{bmatrix} 1 & 0 \\ -\frac{1}{f_2} & 1 \end{bmatrix} \begin{bmatrix} 1 & d_2 \\ 0 & 1 \end{bmatrix} \begin{bmatrix} 1 & 0 \\ -\frac{1}{f_{TL}} & 1 \end{bmatrix} \begin{bmatrix} 1 & d_1 \\ 0 & 1 \end{bmatrix} \begin{bmatrix} 1 & 0 \\ -\frac{1}{f_0} & 1 \end{bmatrix} \begin{bmatrix} 1 & z_s \\ 0 & 1 \end{bmatrix} \begin{bmatrix} h_{\text{enter}} \\ \gamma_{\text{enter}} \end{bmatrix} \tag{4.4}$$

Configuration 2:

$$\begin{bmatrix} r_{f_{dn}} \\ \gamma_{f_{dn}} \end{bmatrix} = \begin{bmatrix} 1 & z_h \\ 0 & 1 \end{bmatrix} \begin{bmatrix} 1 & 0 \\ -\frac{1}{f_{dn}} & 1 \end{bmatrix} \begin{bmatrix} 1 & d_5 \\ 0 & 1 \end{bmatrix} \begin{bmatrix} 1 & 0 \\ -\frac{1}{f_4} & 1 \end{bmatrix} \begin{bmatrix} 1 & d_4 \\ 0 & 1 \end{bmatrix} \begin{bmatrix} 1 & 0 \\ -\frac{1}{f_3} & 1 \end{bmatrix} \begin{bmatrix} 1 & d_3 \\ 0 & 1 \end{bmatrix} \begin{bmatrix} 1 & 0 \\ -\frac{1}{f_2} & 1 \end{bmatrix} \begin{bmatrix} 1 & d_2 \\ 0 & 1 \end{bmatrix} \begin{bmatrix} 1 & 0 \\ -\frac{1}{f_{TL}} & 1 \end{bmatrix} \begin{bmatrix} 1 & d_1 \\ 0 & 1 \end{bmatrix} \begin{bmatrix} 1 & 0 \\ -\frac{1}{f_o} & 1 \end{bmatrix} \begin{bmatrix} 1 & z_s \\ 0 & 1 \end{bmatrix} \begin{bmatrix} h_{enter} \\ \gamma_{enter} \end{bmatrix} \tag{4.5}$$

Then the radius of the detected hologram, R_h, is the radius of the overlap area between the two waves:

$$R_h = \min(r_{\text{plane}}, r_{\text{spherical}}) \quad \text{or} \quad R_h = \min(r_{f_{d1}}, r_{f_{d2}}) \tag{4.6}$$

for configuration 1 and configuration 2, respectively. r_{plane} and $r_{\text{spherical}}$ are the radii of the two beams at the camera plane in configuration 1. $r_{f_{d1}}$ and $r_{f_{d2}}$ are the radii of the two beams in configuration 2.

We expect the localization precision in the absence of background to be best for larger R_h, but with background the SNR will be worse as the radius increases because more background photons will be

captured by the hologram. Therefore, optimizing the hologram size should allow for the best localization precision in the presence of background. Our simulations explore two methods to change R_h.

The first method is to keep the interferometer settings fixed and change the size of the detected hologram R_h by changing the distance between the interferometer and the digital camera z_h (These results are discussed in Section 4.3.1). When the relay lenses f_3 and f_4 are 120 mm and 700 mm respectively, the beam radius at the entrance to the interferometer, R_e, is 2.36 mm. The focal length of the spherical wave f_d is chosen as 300 mm. Figure 4.2(a) shows the relationship of R_h and z_h for configuration 1, and the R_h vanishes when the digital camera is placed at a distance of $z_h = 300$ mm. For configuration 2, the relay lenses f_3 and f_4 are the same as in configuration 1 with R_e of 2.36 mm. The focal lengths of the two spherical waves, f_{d1} and f_{d2} are 300 mm and 700 mm, respectively. Figure 4.2(b) shows the relationship of R_h and z_h for configuration 2. Before the two spherical waves perfectly overlap with each other, $z_h < z_p$, where z_p stands for the perfect overlap position of the two waves, R_h is determined by the spherical wave with the shorter focal length (f_{d1}). When $z_h > z_p$, R_h is determined by the spherical wave with the longer focal length (f_{d2}).

The second method of changing the hologram radius is to change the interferometer settings while the camera is fixed at $z_h = z_p$. For configuration 1, the beam radius before entering the interferometer, R_e, equals the detected hologram radius R_h when the camera is at $z_h = z_p$. Therefore, by adjusting the relay lenses f_3 and f_4 to modify R_e, R_h will be adjusted. Figure 4.2(c) shows the relationship between the relay lens magnification and R_h when the camera is placed at $z_h = z_p$. f_d is fixed at 300 mm. The camera position is fixed at $z_h = z_p = 600$ mm. For configuration 2, as previously discussed, both spherical waves contribute to determining the hologram radius. Thus, with f_{d1} fixed, the focal length of f_{d2} will be modified to change R_h. In this case, when the camera is fixed at $z_h = z_p$, R_h will change along with z_p. z_p is calculated as follows:

$$z_p = f_{d1} + \frac{f_{d1}(f_{d2} - f_{d1})}{f_{d2} + f_{d1}}, \quad f_{d1} < f_{d2} \tag{4.7}$$

Then, R_p for configuration 2, Figure 4.1(b), can be calculated by Equation 4.5 and 4.6 with $z_h = z_p$, where $R_p = r_{f_{d1}} = r_{f_{d2}}$. f_{d1} is fixed at 300 mm. f_3 and f_4 are fixed at 120 mm and 100 mm, respectively, which provides a fixed R_e of 2.84 mm. By increasing f_{d2}, R_h (where $R_h = R_p$) will asymptotically approach the R_p of configuration 1 under identical optical settings, as demonstrated in Figure 4.2(d).

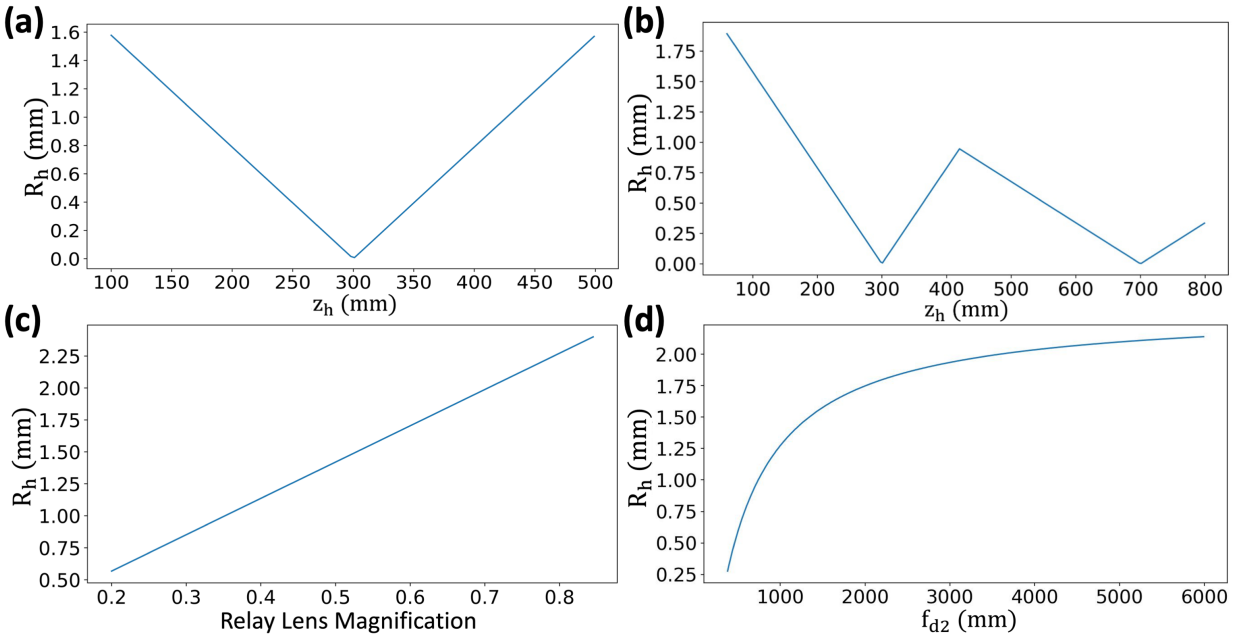

Figure 4.2: (a) Detected hologram radius (R_h) of configuration 1 when the camera is placed at different (z_h) distances away from the interferometer. (b) Detected hologram radius (R_h) of configuration 2 when the camera is placed at different (z_h) distances away from the interferometer. (c) The relationship between the interferometer settings and detected hologram radius at the perfect overlap position $(z_h = z_p = 600$ mm) for configuration 1. The pupil radius before the relay lenses is 2.84 mm. (d) The relationship between the interferometer settings and hologram radius at the perfect overlap position $(z_h = z_p)$ for configuration 2.

4.1.3 Description of the simulations

The pixel size for all the simulations in this thesis is set to 16 μm. The image size is set to 512 px $\times$ 512 px. In the simulations, each raw frame captures a hologram featuring a single fluorophore emitting with a total signal level of N = 6000 photons at the emission wavelength of 670 nm. The fluorescent molecule is simulated using a delta function and is positioned at the center of the simulated volume. Each raw data stack contains 3 raw frames of the simulated fluorophore with different phase constants of $\theta_1 = 0°$, $\theta_2 = 120°$, $\theta_3 = 240°$. Then each raw data stack will be reconstructed and analyzed to determine the locations of the single molecules. 100 raw hologram data stacks of the fluorescent molecule are generated with different background noise levels (from $\beta = 0$ photons/pixel to $\beta = 10$ photons/pixel). After adding the background noise to the hologram stack, Poisson noise is applied to the images. Then the image stack is reconstructed using Equation 2.5, and the coordinates of the molecule are calculated by localizing the center of the PSF. Specifically, the lateral reconstructed image is cropped to 32 px $\times$ 32 px (512 μm $\times$ 512 μm), and a 2D Gaussian fit is applied to the x-y plane to obtain the lateral localization

coordinates. To determine axial localization coordinates, we first reconstructed the hologram data axially with a step size of 100 nm over a 10 μm axial range. We then obtained the axial intensity plot (x-z plane) of the reconstructed data and cropped it to 32 px $\times$ 32 px (512 μm $\times$ 512 μm). A 2D Gaussian fit was then applied in the x-z plane to determine the axial localization coordinates of the molecule. To calculate the localization precision, the standard deviation (STD) of the localized coordinates are found from the 100 individual simulated data stacks. The data points for the hologram radius $R_h < 0.2$ mm are excluded because the PSH is too small to be sampled with the pixel size, resulting in the axial FWHM diverging below this radius. All the simulations were performed by custom written Python code [111].

4.1.4 Experimental setup and light-sheet optimization

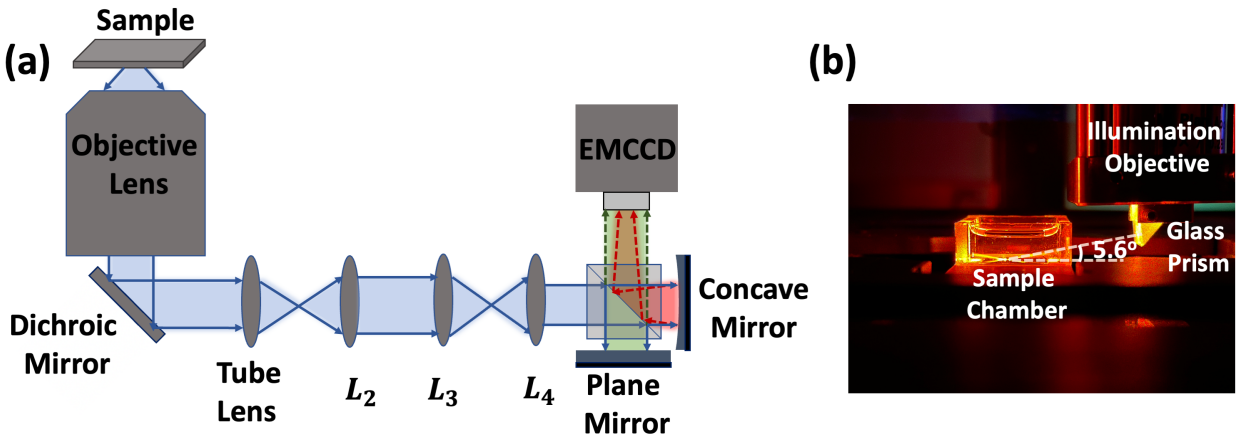

Figure 4.3: (a) Schematic of the imaging path of the SIDH setup. The blue square represents a beam splitter (BS). Interference will be observed as long as the path difference between the two arms of the interferometers is no greater than half the coherence length of the light source. The focal length of the tube lens is 180 mm. The focal length of L_2 is set to $f_2 = 120$ mm. The focal lengths of the relay lenses L_3 and L_4 are $f_3 = 200$ mm and $f_4 = 100$ mm, respectively. The focal length of the concave mirror is $f_d = 300$ mm. (b) The custom-designed sample chamber for tilted light-sheet (LS) illumination pathway. In the light-sheet setup, the excitation lasers are initially shaped using a cylindrical lens with a focal length of 200 mm (not shown). They are then introduced into the illumination objective and subsequently reflected by the glass prism. As the excitation lasers enter the imaging chamber, the incident angle of the tilted light-sheet is approximately 5.6°. The schematic of the whole imaging system can be found in Appendix 5.

Figure 4.3(a) shows a schematic of the imaging path of our SIDH system. The system is a custom-built inverted widefield microscope equipped with an oil-immersion objective (PlanApoN, 60x, 1.42 NA, Olympus, Japan) mounted on a piezoelectric objective scanner (Smaract, Germany). The back-pupil plane of

the objective was demagnified using a tube lens ($f_{TL} = 180$ mm, UTLU, Olympus, USA) and an achromatic lens L_2 ($f_2 = 120$ mm). A pair of relay lenses L_3 and L_4 in a 4f configuration were added before the interferometer to have accurate control over R_e. To generate interference, we use a Michelson interferometer instead of an SLM, shown in Figure 4.3(a). In this way, the light efficiency of the SIDH system is tremendously improved since the light loss due to the polarization sensitivity of the SLM is removed. The Michelson interferometer was placed 100 mm away from L_4 with a concave mirror ($f_d = 304.80$ mm, #32-818 $\lambda/4$ Precision Spherical Mirror, Edmund Optics, USA) on one arm and a plane mirror on the other arm. The plane mirror was mounted on a piezoelectric translational stage (NFL5DP20, Thorlabs, USA) to implement the phase-shifts required to acquire three images. The fluorescence was detected with an electron-multiplying charge-coupled (EMCCD) camera (Andor iXon-897 Life, UK) which was placed 127 mm away from the interferometer.

Furthermore, in order to remove the out-of-focus light and reduce the background encountered when imaging single emitters using SIDH, we extended our illumination setup by adding a tilted light-sheet illumination pathway to the optimized SIDH setup [109]. The light sheet is formed by a cylindrical lens with a focal length of 200 mm, which focuses the light in only one dimension onto a mirror. The mirror plane is imaged onto the back aperture of a long working distance illumination objective (378-803-3, 10x, NA 0.28, Mitutoyo, Japan) by two lenses in a 4f configuration. The illumination objective then focuses the light sheet, which is directed into the sample chamber at an angle of about 5.6° using a glass prism (PS908L-A, Thorlabs), as shown in Figure 4.3(b). The prism is held using a custom-designed prism holder which is mounted using a cage system on a three-axis translational stage (XRN25P-K2, Thorlabs, USA).

Experiments using both widefield epi-illumination and light-sheet illumination were performed to demonstrate the improved performance of light-sheet SIDH. The excitation lasers (OBIS 561 nm, 200 mW and 647 nm, 120 mW, Coherent, USA) can be either introduced into the epi-illumination path or sent to the light sheet illumination path. The path is easily switched with a flip mirror. The fluorescence emitted by the sample is separated from the laser excitation light using a dichroic mirror (XF2054,485-555-650TBDR, Omega, USA), a multi-band bandpass filter (FF01-446/523/600/677-25, Semrock, USA), and notch filters (ZET561NF notch filter and NF01-488/647 notch filter, Semrock, USA).

100 nm red fluorescent beads (FluoSpheres Carboxylate-Modified Microspheres, Excitation/Emission: 580/605 nm, Catalog number: F8801, Invitrogen, USA) and 40 nm dark red fluorescent beads (FluoSpheres Carboxylate-Modified Microspheres, Excitation/Emission: 647/680 nm, Catalog number: F8789, Invitrogen, USA) were used in our experiments. The sample chamber was manufactured by attaching a glass coverslip (Fisher Premium Cover Glass, no. 1.5, Fisher Scientific, USA) to the bottom of a commercial glass cuvette (704-000-20-10, Hellma, Germany) using nail polish. Beads were dried on the coverslip and Immersion oil (Type DF Immersion Oil, Cargille Laboratories, USA) was then added to the chamber to maintain the refractive index matching, Figure 4.3(b). After imaging, the bottom coverslip could be detached, and the chamber could be cleaned and reused.

4.2 Results

4.2.1 Effect of changing camera position

In this section, we will present the simulation results studying the relationship between the detected hologram radius (R_h) and localization precision by changing the digital camera position (z_h).

Configuration 1: one plane wave one spherical wave

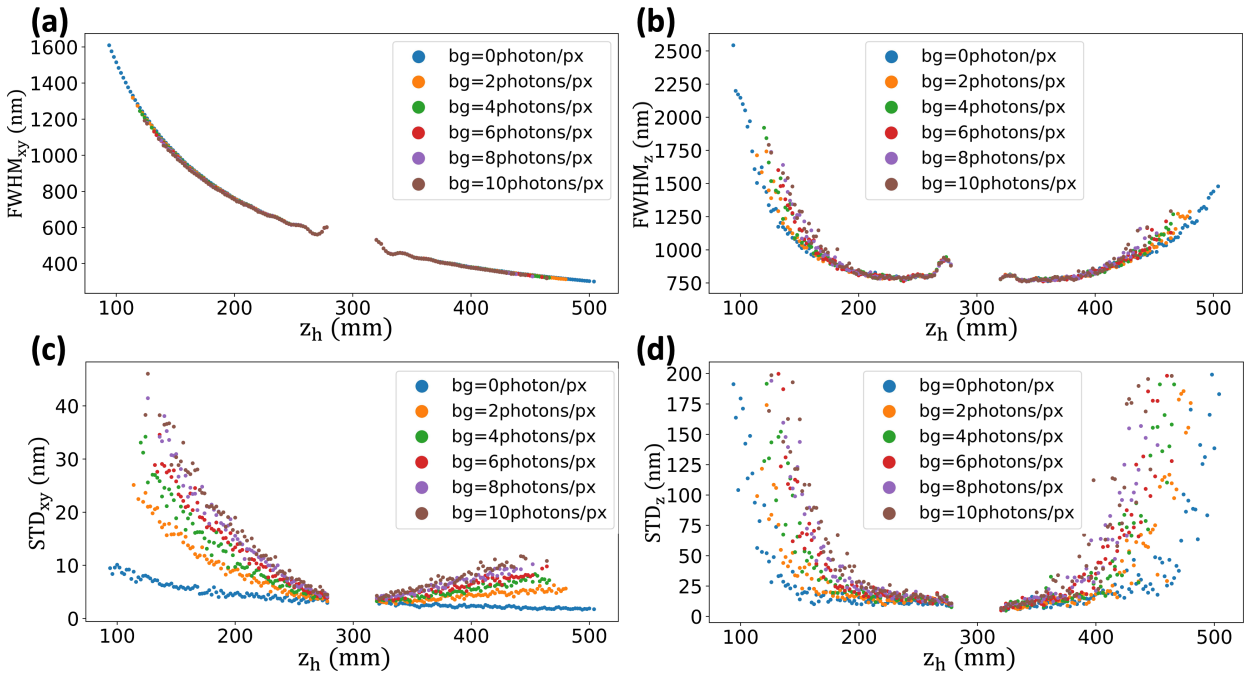

Figure 4.4: (a) The lateral PSF FWHM of SIDH configuration 1. (b) The axial PSF FWHM of SIDH configuration 1. (c) Lateral localization precision of SIDH configuration 1. (d) Axial localization precision of SIDH configuration 1. STD refers to the standard deviation of the localized coordinates. "bg" in legend refers to the background noise level (in photons/pixel). Total signal level is N = 6000 photons. The datapoints for $R_h < 0.2$mm are excluded.

Figure 4.4(a) and (b) show the lateral and axial PSF FWHM, respectively, while Figure 4.4(c) and (d) show the corresponding lateral and axial localization precision under different background noise levels.

In the absence of background noise, the localization precision of SIDH is determined by the PSF FWHM and the photon number, and the localization precision is smaller than 10 nm for all camera positions (z_h). In this case, increasing the ratio $\frac{z_h}{f_d}$ in SIDH decreases the lateral FWHM of the PSF thereby improving the lateral localization precision. The maximum resolving power is achieved for the ratio

$\frac{z_h}{f_d} = 2$ when the camera is at the position of perfect overlap between the two beams ($z_h = 600\,\text{mm}$) [81]. Likewise, the axial localization precision is dictated by both the axial PSF size and the level of background noise. However, contrary to the lateral PSF FWHM, improvement in the axial PSF FWHM is observed when z_h approaches f_d, but not so close that the PSH has no fringes encoding the axial position [112]. Moreover, the size of the PSH decreases as z_h approaches f_d, thereby increasing the SNR of the PSH. This, in turn, contributes to improved axial localization precision.

However, the presence of the background noise significantly affects the localization precision of SIDH in both the lateral and axial directions due to the large size of the PSH. It can be seen from Figure 4.4(c) and (d) that the overall localization precision gets worse when the background noise increases for all camera positions. However, the background noise has a smaller effect on localization precision when z_h is closer to f_d, where R_h is smaller, increasing the SNR. For a background noise level of $\beta = 10$ photons/pixel ($N = 6000$ photons), when $z_h = 172\,\text{mm},\ R_h = 1\,\text{mm}$ and the lateral and axial localization precision of SIDH are 24 nm and 63 nm, respectively. When $z_h = 428\,\text{mm},\ R_h = 1\,\text{mm}$ and, the lateral and axial localization precision of SIDH are 8 nm and 179 nm, respectively. When $172\,\text{mm} < z_h < 428\,\text{mm},\ R_h < 1\,\text{mm}$, the lateral localization precision of configuration 1 reaches the minimum value of 3.8nm with $R_h = 0.2\,\text{mm}$ while $z_h = 326\,\text{mm}$, and the axial localization precision achieves 10nm at the same z_h. It's clear that decreasing the size of the hologram significantly increases the number of photons per pixel, thereby making it easier to detect holograms under low SNR conditions. Furthermore, for the same value of R_h, $z_h > f_d$ has a better lateral localization precision than $z_h < f_d$, which demonstrates the effect of the lateral PSF size mentioned earlier.

Configuration 2: two spherical waves

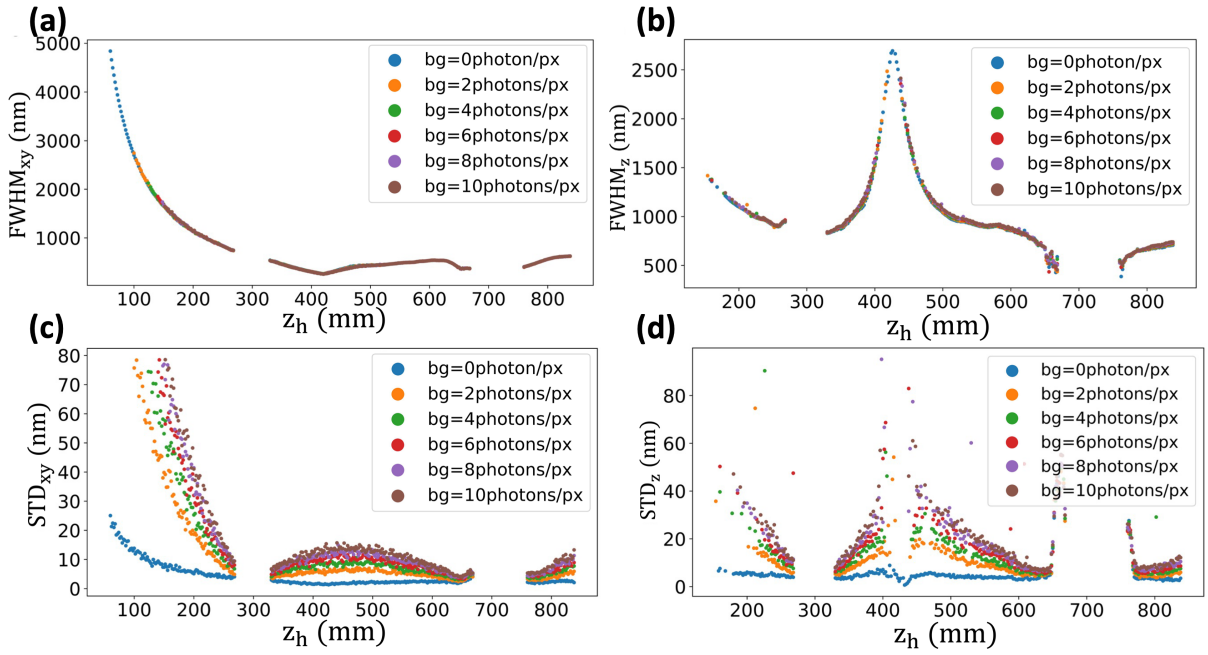

Figure 4.5: (a) The lateral PSF FWHM of SIDH configuration 2. (b) The axial PSF FWHM of SIDH configuration 2. (c) Lateral localization precision of SIDH configuration 2. (d) Axial localization precision of SIDH configuration 2. Total signal level is $N = 6000$ photons. The datapoints for $R_h < 0.2$ mm are excluded. f_{d1} (300 mm) and f_{d2} (700 mm) are the focal lengths of the two spherical elements in the interferometer.

Figure 4.5(a) and (b) show the lateral and axial PSF FWHM, respectively, while Figure 4.5(c) and (d) show the corresponding lateral and axial localization precision under different background noise levels. The results show that localization precision adheres to the same pattern observed in configuration 1, where a decrease in R_h significantly improves the localization precision, especially in high background noise scenarios. This improvement is attributed to the enhancement of signal-to-noise ratio (SNR) conditions. The axial localization precision is poor at the perfect overlap position ($z_h = z_p = 420$ mm) because the relationship between z_r and z_h has zero slope here [112, 113].

Moreover, in order to image across the entire axial range, it is necessary to not place the camera in the range of $f_{d1} < z_h < f_{d2}$ to ensure that the values of the reconstruction distance (z_r) are not symmetric across the focal plane, which makes the axial PSF too large for good localization precision. Especially at the perfect overlap position ($z_h = z_p = 420$ mm), where the lateral PSF size is minimized but the axial PSF becomes too large to be localized. For $z_h < f_{d1}$ and $z_h > f_{d2}$, compared with configuration 1, configuration 2 has worse performance for the localization precision under the same R_h conditions. For example, at a background level of 10 photons per pixel, when $R_h = 1$ mm (at $z_h = 172$ mm),

configuration 1 provides a localization precision of 22 nm (lateral) and 47 nm (axial), while configuration 2 provides a localization precision of 67 nm (lateral) and the axial PSF is too large to be localized.

4.2.2 Effect of changing the entrance beam radius with the camera fixed at the perfect overlap position (z_p)

In this section, we explore the results of simulations studying the relationship between localization precision and R_h by changing the radius of the beam entering the interferometer while maintaining the camera at the position of perfect overlap ($z_h = z_p$). Because the axial PSF size is poor at this position, we will only consider the lateral precision results in this section.

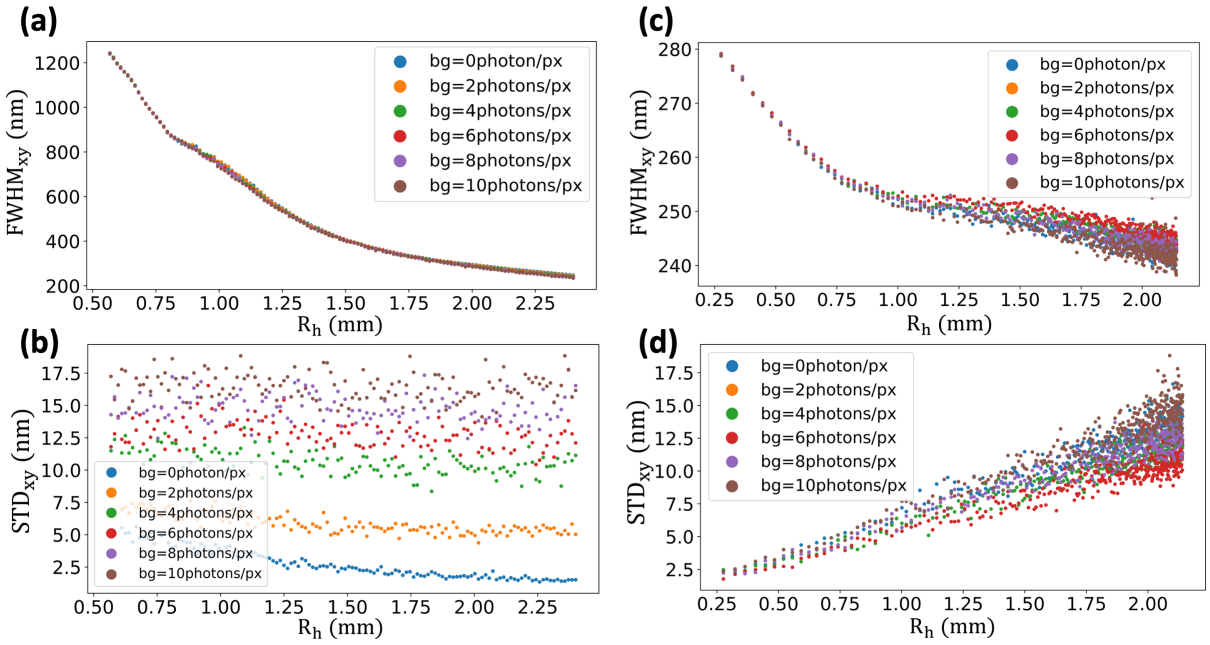

Figure 4.6: (a) The lateral PSF FWHM with different $R_h(z_h = z_p = 600\text{mm})$ under different background noise levels for configuration 1. (b) The lateral localization precision with different $R_h(z_h = z_p = 600\text{mm})$ under different background noise levels for configuration 1. (c) The lateral PSF FWHM with different $R_h(z_h = z_p)$ under different background noise levels for configuration 2. (d) The lateral localization precision with different $R_h(z_h = z_p)$ under different background noise levels for configuration 2. Total signal level is $N = 6000$ photons.

Configuration 1: one plane wave one spherical wave

Figure 4.6(a) and (b) show the effect of R_h on the PSF FWHM and lateral localization precision, respectively. It can be seen from Figure 4.2(c) that there is a linear relationship between the relay lenses magnification and R_h, and the lateral PSF FWHM of configuration 1 gets smaller when R_h gets bigger.

In the absence of background noise, the localization precision shows the same changing trend with the PSF size. However, when the background noise level increases, the localization precision is worse and remains relatively constant vs. R_h. This is because the decrease of the PSF FWHM gives a positive effect on the localization precision when R_h gets bigger, which compensates for the negative effect from the background noise.

Configuration 2: two spherical waves

Figure 4.6(c) and (d) respectively illustrate the changes in lateral PSF FWHM and localization precision under varying R_h conditions for configuration 2. The performance of localization precision, Figure 4.6(d), remains consistent under different levels of background noise because the lateral PSF size (Figure 4.6(c)) undergoes a relatively minor variation (about 40 nm), compared to configuration 1 (about 1000 nm), across the entire R_h range. Moreover, the impact of background noise on localization precision increases as R_h increases. This is due to the relationship between R_h and f_{d2}, Figure 4.2(d), which makes the negative impact of the background noise dominate the localization precision as R_h increases. The PSF FWHM of configuration 2 gets better when f_{d2} gets bigger, which indicates that the PSF FWHM of configuration 2 asymptotically approaches the PSF FWHM of configuration 1 for the same R_e.

4.2.3 Optimal settings for 3D imaging

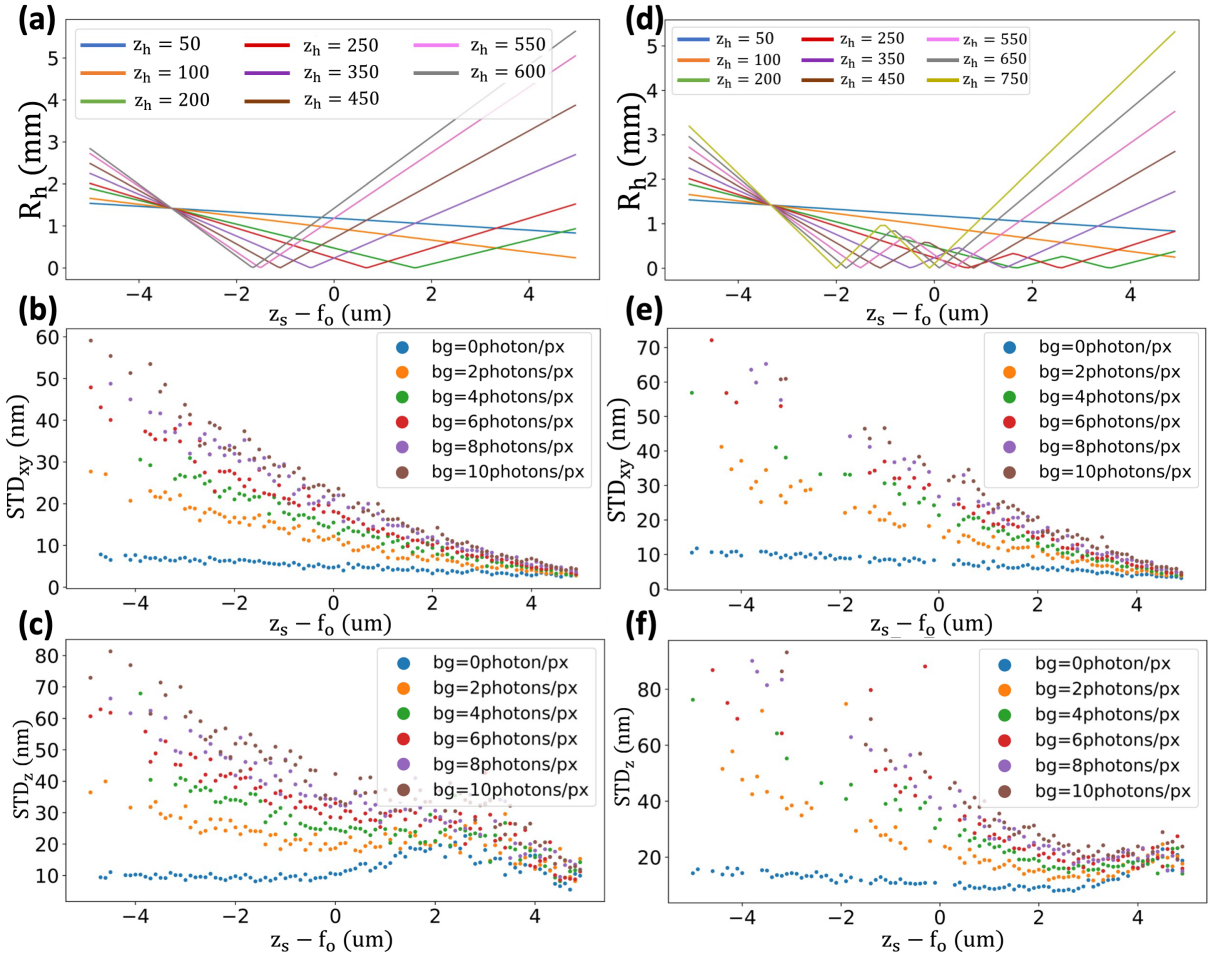

Figure 4.7: (a) Relationship of object axial position and detected hologram radius with different camera distances for configuration 1. (b) Lateral localization precision for configuration 1 with the different background noise levels when $z_h = 100$ mm. (c) Axial localization precision for configuration 1 with the different background noise levels $z_h = 100$ mm. (d) Relationship of object axial position and detected hologram radius with different camera distances for configuration 2. (e) Lateral localization precision for configuration 2 with the different background noise levels when $z_h = 100$ mm. (f) Axial localization precision for configuration 2 with the different background noise levels when $z_h = 100$ mm. Total signal level is $N = 6000$ photons.

In the previous section, we saw that, at the background level of 10 photons per pixel, R_h needs to stay in the range 1.38 mm to 0.21 mm to achieve high localization precision. However, the simulations performed in the last two sections only simulated the case of $z_s = f_o$, in which the object is in focus. In order

to do 3D SMLM imaging over a large axial range, the hologram size and the corresponding localization precision when the object is out-of-focus ($z_s \neq f_o$) also need to be considered and optimized. Figure 7(a) and (d) show the relationship between the object axial position (z_s) and hologram radius (R_h) for SIDH configuration 1 and SIDH configuration 2, respectively, for different camera positions. For configuration 1, R_e is set to 1.42 mm and $f_d = 300$ mm. For configuration 2, R_e is also set to 1.42 mm with $f_d1 = 300$ mm and $f_d2 = 700$ mm.

It can be seen from Figure 4.7(a) and (d) that the closer the camera is placed to the interferometer, the smaller the variation in R_h over the 10 μm axial range. Furthermore, when the camera is placed after 150 mm ($z_h > 150$ mm), the beam will come to a focus within the desired axial range, and the hologram cannot be reconstructed over the whole axial range. Drawing from the conclusions in Section 3.1, optimal lateral FWHM in a SIDH system demands that the camera be placed at the perfect overlap position, and optimal axial FWHM in a SIDH system demands the camera be placed close to the interferometer focal point. But it's important to keep the camera as close as possible to the interferometer to image a large axial range, which limits the optimization of R_h to changing R_e. Moreover, if the camera is placed too close to the interferometer, the FWHM, in both axial and lateral directions, becomes excessively large (Figure 4.4), thereby worsening the localization precision. Therefore, it's important to find a balanced position of the camera to obtain the desired axial imaging range and good localization precision performance. By adjusting the magnification of the relay lenses (f_3 and f_4), thereby changing R_e, it is possible to maintain the detected hologram radius R_h within a range of $1.4mm$ to $0.3mm$ across the entire $10\mu m$ axial range.

Figure 4.7(b), (c) and Figure 4.7(e), (f) show the localization precision over the 10 μm axial range under different background noise levels for configuration 1 and configuration 2, respectively. z_h is set to 100 mm for both configurations because it is difficult, experimentally, to place the camera closer to the interferometer than that. The results show that under low SNR conditions (N = 6000 photons with background noise of 10 $\frac{\text{photons}}{\text{pixel}}$), the optimized SIDH has the potential to achieve a lateral localization precision of 5 nm to 58 nm and axial localization precision of 13 nm to 80 nm over an axial range of 10 μm for configuration 1. With similar optical settings, SIDH configuration 1 has an overall better localization performance than configuration 2.

4.2.4 Experimental results

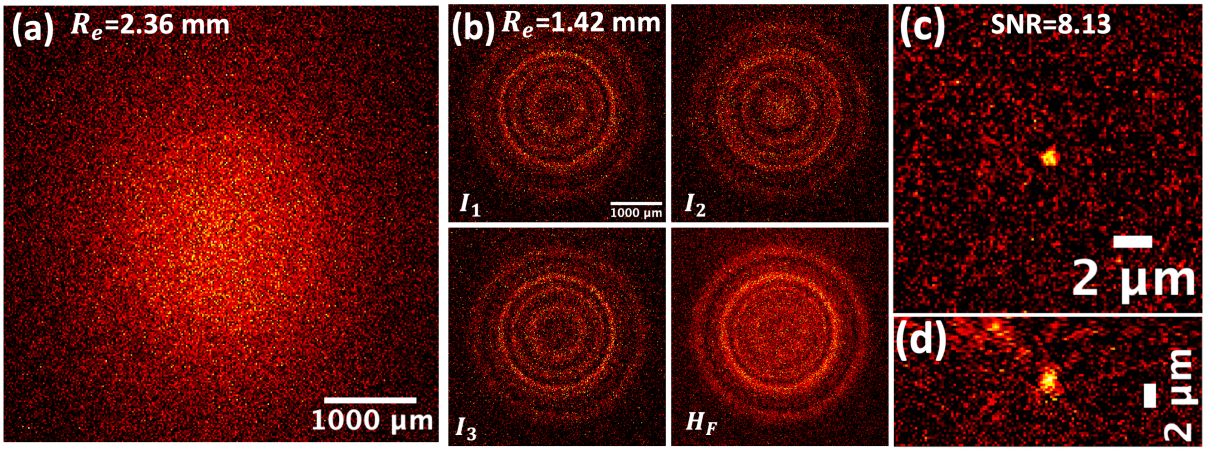

Figure 4.8: PSH of 100 *nm* (561/605) nanosphere with ∼4200 photons for SIDH setup with different R_e. (a) PSH of SIDH setup with $R_e = 2.36\ mm$. (b) PSH of SIDH setup with $R_e = 1.42\ mm$. The top left figure shows the PSH with the shift phase of 0 degree (I_1). The top right figure shows the PSH with the shift phase of 120 degree (I_2). The bottom left figure shows the PSH with the shift phase of 240 degree (I_3). The bottom right figure shows the magnitude of the final complex hologram (H_F). (c) Lateral view of the image reconstructed by back-propagating the hologram shown in (b). (d) Axial view of the image reconstructed by back-propagating the hologram shown in (b). The camera is placed 127 *mm* away from the Michelson interferometer for both experiments. The SNR was calculated as the ratio of mean signal to the mean of the standard deviation of the background (mean sig/mean std).

To demonstrate the performance of optimized SIDH, we performed experiments with different R_e values under the same imaging conditions. A bead was brought into focus and the three images were taken with the phase of one path shifted for each image. 100 nm fluorescent microspheres were imaged by epi-illumination and the results are shown in Figure 4.8. Each hologram is acquired in one 5 ms exposure and the calibrated EM gain setting was 500. 100 nm red beads were excited with a 561 nm laser with an irradiance of 0.02 kW/cm^2. An average of ∼4,200 signal photons are collected from a bead in one image. Figure 4.8(a) shows the PSH of the SIDH setup with $R_e = 2.36$ mm. Figure 4.8(b) shows the PSH of the optimized SIDH setup with $R_e = 1.42$ mm. Figure 4.8(c) shows the background subtracted reconstructed image of Figure 4.8(b) while Figure 4.8(a) could not be reconstructed due to the low SNR.

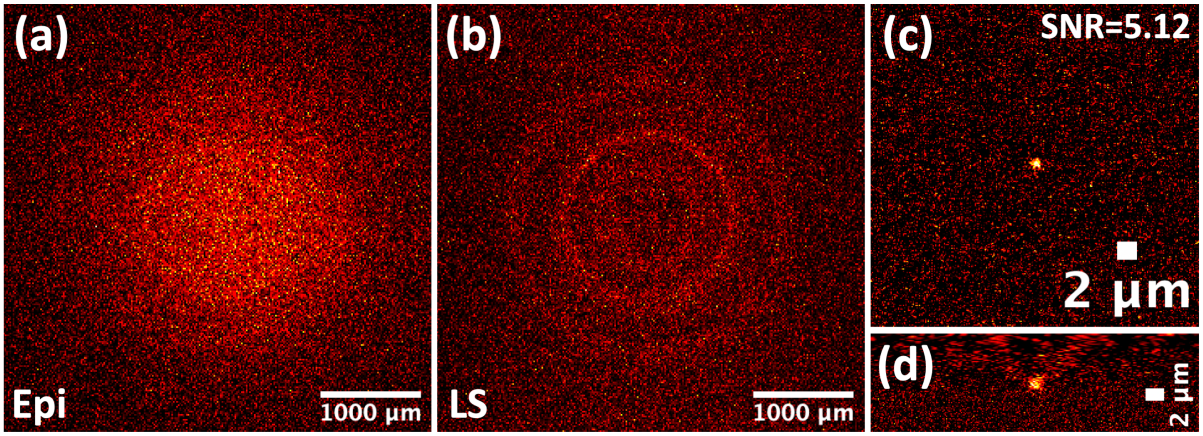

Figure 4.9: PSH of 40 nm dark red (647/680) nanosphere at ∼2120 signal photons light levels with different illumination pathways. (a) The PSH of 40 nm nanosphere with epi-illumination. (b) The PSH of 40 nm nanosphere with light-sheet illumination. (c) Lateral view of the image reconstructed by back-propagating the hologram shown in (b). (d) Axial view of the image reconstructed by back-propagating the hologram shown in (b). The SNR was calculated as the ratio of mean signal to the mean of the standard deviation of the background (mean sig/mean std).

To further demonstrate optimized SIDH at lower light levels, we imaged a 40 nm dark red fluorescent nanosphere with the light sheet excitation scheme at ∼2,120 signal photons to compare the image quality between the light sheet and epi-illumination with the optimized SIDH system. Figure 4.9(a) and (b) show the PSH of SIDH with epi-illumination and light-sheet illumination, respectively. Figure 4.9(c) shows the reconstructed image of Figure 4.9(b) while the PSH shown in Figure 4.9(a) was not able to be reconstructed.

To demonstrate 3D imaging with our SIDH system with light-sheet illumination, 100 nm beads emitting ∼4,200 photons were imaged. A bead was brought into focus, and the three holographic images were recorded. The bead was then scanned along the optical axis using the piezoelectric objective lens positioner over an axial range of 10 μm, with three images collected at every axial position. The first row of Figure 4.10 shows how the density of the hologram fringes and hologram radius change smoothly as a function of the axial position of the emitter. In order to reconstruct the hologram to form an image of a single bead, three consecutive images with different phases are acquired which are then combined and reconstructed. The second and third rows of Figure 4.10 show the results of reconstructing the images by reconstructing the hologram at the appropriate reconstruction distance. Results demonstrate that using the optimized optical setup, we can accurately image small particles (100 nm) emitting low numbers of photons (∼4,200 photons) over larger axial ranges (10 μm). The SNR for reconstructed images varies over the axial range, even when the emitter is emitting the same number of photons. The reconstruction SNR does not strictly increase as Rh decreases. This can be attributed to the fact that the density of the

interference fringes becomes too high and is under-sampled at the smallest R_h values, adding noise to the reconstruction.

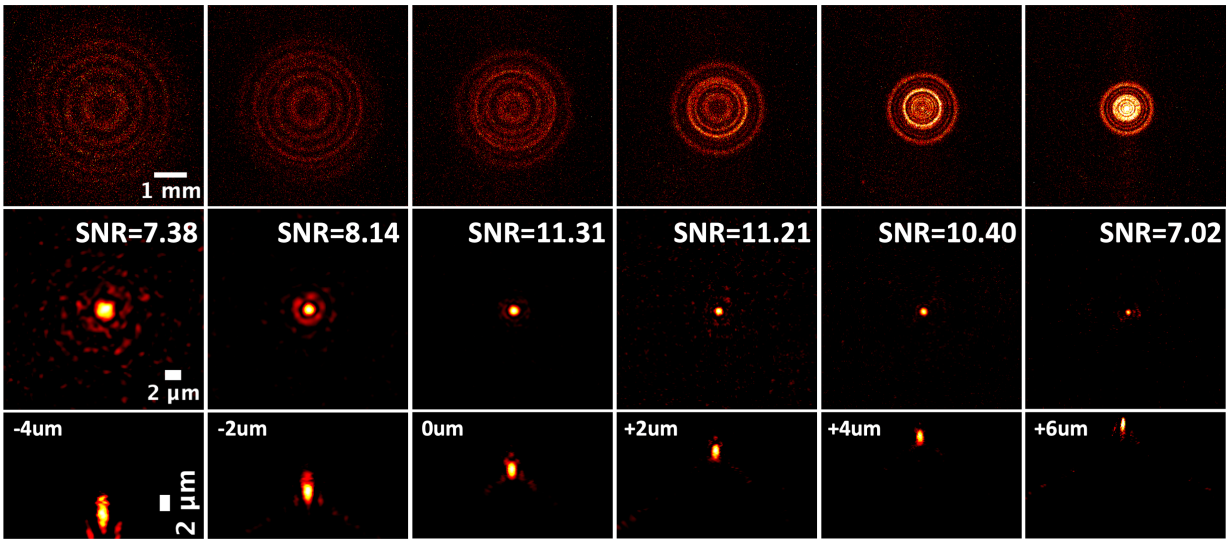

Figure 4.10: 3D imaging of a single 100 nm fluorescent bead at ∼4200 signal photons light level with light-sheet illumination SIDH. First row shows the PSH of the 100 nm fluorescent bead at different axial planes, the images were acquired in one 5 ms frame with an irradiance of 0.02 kW/cm^2. Second and third rows show the lateral and axial view of the reconstructed images, respectively. The SNR was calculated as the ratio of mean signal to the mean of the standard deviation of the background (mean sig/mean std).

We then experimentally demonstrated the proposed localization precision by imaging a 100 nm fluorescent bead with 8400 photons at the background level of 13 photons per pixel. With 50 detected datapoints, weobtain a localization precision of 30 nm laterally and 38 nm axially, as shown in Figure 4.11

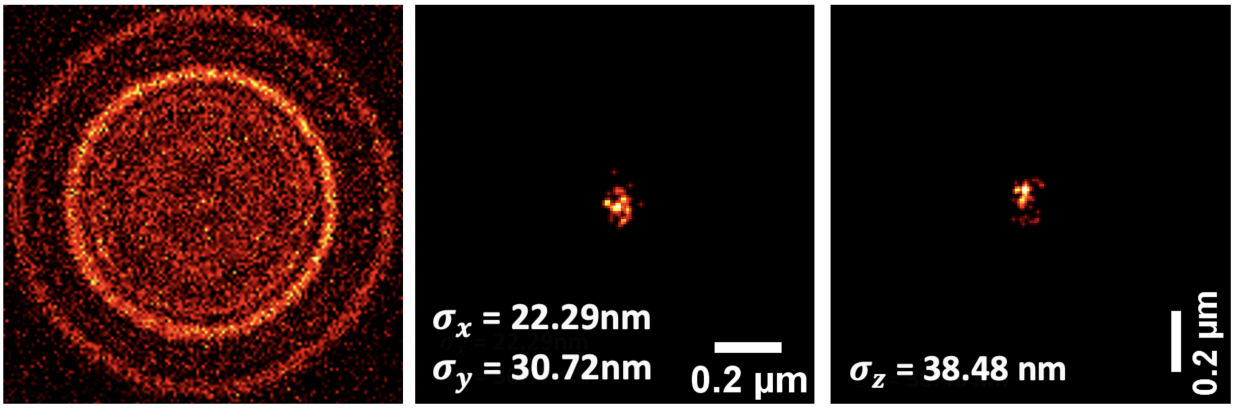

Figure 4.11: The PSH of a 100 nm nanosphere (emitting 8,400 photons) with light-sheet illumination (left). 50 PSH were collected, reconstructed and localized. The localizations are displayed in the lateral plane (center image) and in the x-z plane (right image).

4.3 Conclusion

We have performed simulations to analyze the dependence of localization precision on detected hologram size in SIDH using two different configurations, one with one spherical and one plane wave and another with two spherical waves to form the interference hologram. The results show that decreasing the size of the hologram significantly improves the SNR of holograms when background light is present, thereby improving the localization precision of SIDH. We also analyzed the relationship between the object's axial position and detected hologram radius with different camera distances using two different configurations. Based on our simulations, we have determined four guidelines that can be used to optimize our existing SIDH system to obtain a desired localization precision:

1. The detected hologram radius needs to be as small as possible to increase the SNR. But it needs to be at least $R \sim \sqrt{\lambda z_r}$ to capture the axial information in the hologram. For our system, at the light signal level of 6000 photons with 10 photons/pixel background noise, the detected hologram radius needs to be smaller than 1.38 mm in order to be well detected and reconstructed.

2. The camera needs to be as close to the interferometer as possible in order to limit the variation of the detected hologram radius. The closer the camera is to the interferometer, the greater the possible axial range of imaging.

3. Because the camera position determines the imaging axial range and is fixed, the beam size before entering the interferometer needs to be minimized (~ 1.4 mm) to ensure the detected hologram radius stays small enough to be reconstructed and provide a good localization precision for the entire axial range.

4. The SIDH configuration with one plane and one spherical wave provides better localization performance than the configuration with two spherical waves under similar optical settings.

Based on our simulation results with the optimized parameters, SIDH can achieve a lateral localization precision of 5 nm to 58 nm and axial localization precision of 13 nm to 80 nm with an axial range of 10 μm at low light signal conditions (light signal level of 6000 photons with 10 photons/pixel background noise). This indicates that SIDH could be a useful approach to 3D SMLM over large axial ranges. We have also performed experiments with the optimized SIDH system to demonstrate our simulation results. The reduction of beam size before entering the interferometer significantly improves the light efficiency of the system which makes it possible to detect as few as $\sim$4,200 photons using optimized SIDH with epi-illumination. Furthermore, light sheet illumination has been combined with our SIDH system to further reduce the background. We demonstrate that using light sheet illumination, as few as $\sim$2,120 photons can be detected in a hologram. We also demonstrate that by placing the camera close to the interferometer, we can successfully reconstruct a 100 nm microsphere with $\sim$4,200 photons over a 10 μm axial range. In our future work, we will further optimize our setup based on our simulation results. This includes positioning the camera even closer to the interferometer to achieve a larger axial range and modifying the setup to capture hologram data in a single shot. We then plan to experimentally demonstrate the localization performance of our setup using fluorophores, such as Alexa Fluor 647, under SMLM imaging conditions. Ultimately, our goal is to image biological samples with SIDH.

Chapter 5

Self-interference digital holography with computational aberration correction

As the previous section demonstrated, point-like sources emitting as few as 4,200 photons can be reconstructed over a 10 μm axial range by optimized SIDH-LS setup, and as few as $\sim 2,120$ photons can be detected in a hologram. SIDH-based SMLM has the potential to achieve a lateral localization precision of 5 nm to 58 nm and an axial localization precision of 13 nm to 80 nm over an axial range of 10 μm under low light signal conditions (light signal level of 6000 photons with up to 10 photons/pixel background noise) [84, 85]. However, real-world optical systems inevitably contain optical aberrations that affect the localization performance of SIDH and must be corrected, especially for large volume 3D imaging.

As mentioned in Section 2.4, optical aberrations arise from numerous factors, including fabrication of the optical components, misalignment within the imaging system, and sample-induced aberrations. AO is an effective solution for correcting aberrations in both diffraction-limited and super-resolution microscopy systems [89, 94, 114–119].Unlike conventional microscopy systems that require additional optical elements, such as deformable mirrors, to modulate the phase of the emission light, SIDH captures holograms that have the phase information encoded already. Therefore, the aberration correction in SIDH can be applied to the detected holograms without requiring any additional hardware.

In this chapter, I propose a fast, guide-star free, computational sensorless-AO method for SIDH, capable of correcting optical aberrations over a large axial range without incorporating any adaptive elements into the system. The key innovation of our method is to computationally propagate the detected complex holograms to a virtual pupil plane. By manipulating the modal aberrations in the propagation kernel, we can estimate the phase of the holograms and construct a phase correction mask at the virtual pupil plane. Our algorithm iteratively searches for the optimal correction strength of each Zernike mode, and the virtual correction phase mask is adjusted accordingly. The final aberration correction is then applied at the virtual pupil plane, and the complex holograms at the virtual pupil plane are then backpropagated to obtain the aberration-free complex holograms at the camera plane. The aberration-free complex holo-

grams can then be reconstructed over the entire axial imaging range without repeating the correction steps. Our simulation results demonstrate that the Strehl ratio of the reconstructed image can improve from 0.71 to 0.98, and the SIDH localization precision can be restored to near the ideal case. Our experimental results further demonstrate that our method is robust for real applications. Moreover, our reconstruction process is 10 times faster than Man's [95], which makes it suitable for SMLM and single particle tracking (SPT).

5.1 Methods

5.1.1 Principle of aberration correction algorithm for SIDH.

In traditional digital holography, interference between the object and reference beams is recorded as a hologram using coherent illumination, encoding the information of the object in the interference pattern. However, the need for coherent light restricts the versatility of conventional holography. SIDH overcomes the need for a coherent light source by splitting the emission wavefront from the sample and recombining it with different phase modifications added to each path [81–83, 120]. The emission can be split by either a spatial light modulator (SLM) or an interferometer, details of the hologram formation be found in Chapter 2 and Chapter 3.

In SIDH, the final complex hologram is obtained from the three raw images captured with different phases, as shown in Figure 5.1(a). In a system with aberrations, the aberrations will be encoded in each complex hologram, H_{ab}. Because the detected final complex holograms (H_{ab}) are spatially separated based on the locations of the emitters, the corrected phase mask cannot be directly applied to H_{ab} at the camera plane to correct the full field of view (FOV). Therefore, there is a need to create a plane where all holograms overlap in the center. Our proposed method takes H_{ab} at the camera plane as the input, computationally forward propagates a distance of $f_v + f_d - z_h$, and then operates with a virtual lens ($f_v = 160$ mm), and further propagates a distance f_v to the virtual pupil plane.

The virtual lens is modeled as an ideal thin lens positioned along the optical axis. The effectiveness of the correction does not rely on the specific focal length of the virtual lens, as long as the size of the virtual correction phase mask is adjusted to match the size of the complex hologram at the virtual pupil plane. We chose $f_v = 160$ mm to create a complex hologram in the virtual plane with a radius roughly half (0.7 mm) of the field of view. The relation between the radius in the virtual plane and the virtual lens is shown in Figure 5.2. The aberrations are then corrected by applying the phase, φ_{A0}. The final complex hologram at the virtual pupil plane, $H_{vpA0}(x, y)$, as shown in the left panel of Figure 5.1(b), can be expressed as

$$H_{vpA0}(x,y) = \left\{ H_{ab}(x,y) \otimes Q\left(\frac{1}{f_d + f_v - z_h}\right) Q\left(\frac{1}{f_v}\right) Q\left(\frac{1}{f_v}\right) \right\} \exp[i\varphi_{A0}] \tag{5.1}$$

where Q stands for the quadratic phase function $Q(b) = \exp\left[i\frac{\pi b}{\lambda}(x^2 + y^2)\right]$. Then the corrected complex hologram, $H_{vpA0}(x, y)$, will be computationally back-propagated to the camera plane to obtain the aberration-free complex hologram H_{A0} for reconstruction, as shown in the middle panel of Figure 5.1(b). The final complex hologram after the AO correction is

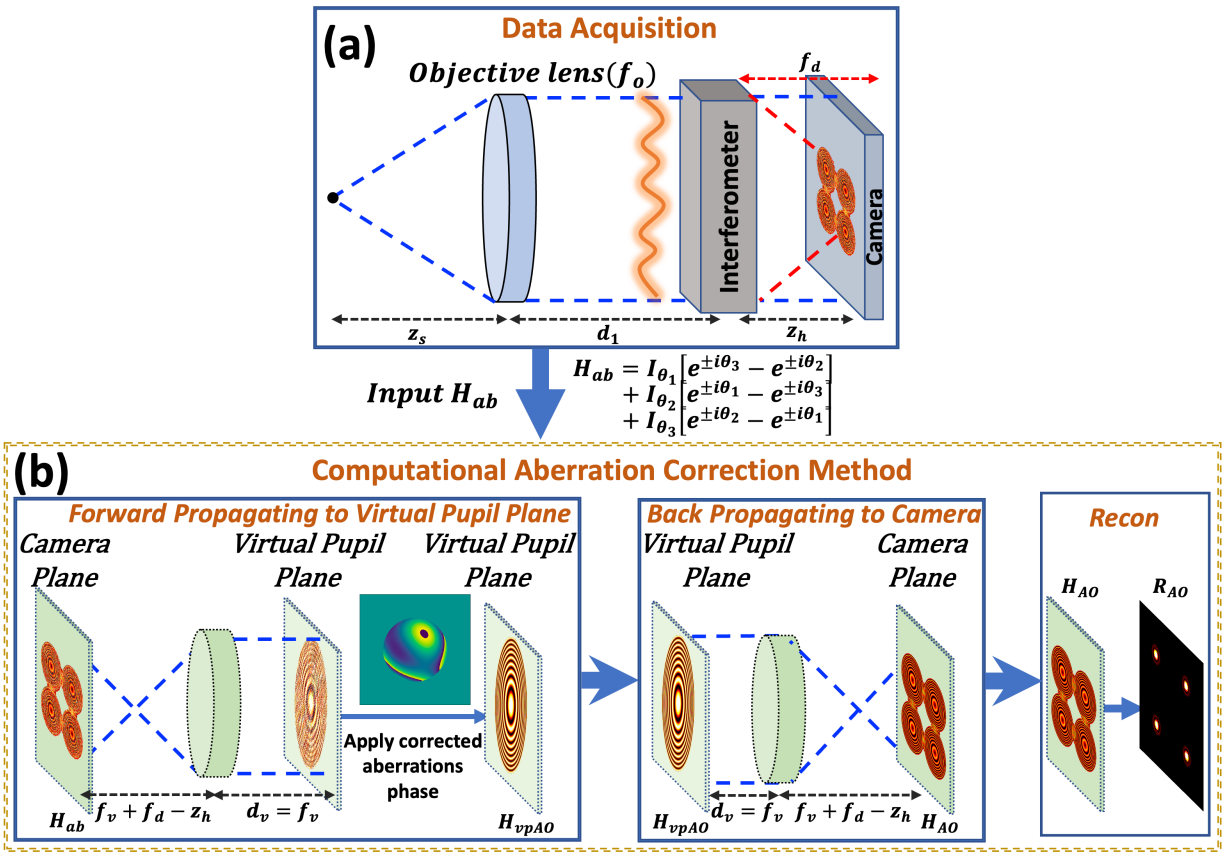

Figure 5.1: (a) Schematic of the imaging path of the SIDH system with aberrations. The hologram is formed by interfering a plane wave with a spherical wave created with a focal length of $f_d = 300$ mm. The z_h stands for the distance between the interferometer and the camera. The detected hologram is aberrated and may be spatially separated depending on different emitter locations. Three raw hologram images with different phases (I_{θ_1}, I_{θ_2}, and I_{θ_3}) are detected to get the complex hologram H_{ab}. (b) Schematic of the computational aberration correction method for SIDH. To overlap the spatially separated holograms, the input aberrated complex hologram H_{ab} will first be computationally forward propagated through a virtual lens ($f_v = 160$ mm) to the virtual pupil plane. The corrected aberration phase is applied at the virtual pupil plane. Then the corrected complex hologram will be computationally backpropagated to the camera plane to obtain the aberration-free complex holograms for reconstruction.

$$H_{A0}(x,y) = H_{vpA0}(x,y) \otimes Q\left(-\frac{1}{f_v}\right) Q\left(\frac{1}{f_v}\right) Q\left(-\frac{1}{f_v + f_d - z_h}\right) \tag{5.2}$$

The phase mask can be expressed as a linear combination of the Zernike polynomials,

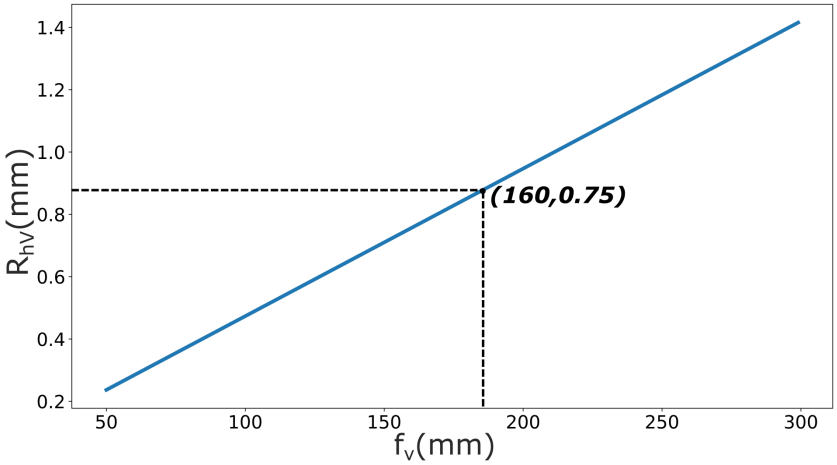

Figure 5.2: Relationship between the focal length of the virtual lens (f_v) and the radius of the complex hologram in the virtual plane ($R_h v$). The dashed lines illustrate the chosen focal length and corresponding hologram radius. The calculation was performed using ray matrix.

$$\varphi_{A0} = \sum_{m=0}^{N-1} c_m Z_m \tag{5.3}$$

where c_m are the coefficients, Z_m is the m-th Zernike mode, and N is the number of Zernike modes used. Then, as shown in the right panel of Figure 5.1(b), the reconstructed image after the aberration correction is,

$$R_{A0}(x, y, z_s) = H_{A0}(x, y) \otimes \exp\left[\pm \frac{i\pi}{\lambda z_r}(x^2 + y^2)\right] \tag{5.4}$$

where z_s is the axial position of the emitter. The $\pm$ solutions generate the image and twin image, respectively.

5.1.2 Sensorless-AO and the Metric function.

A sensorless-AO method with a frequency based metric function is used to search for the optimal coefficients of each Zernike mode [94, 115, 118, 121, 122]. For a 10 μm axial range, the correction mask is optimized at the objective focal plane ($z_s = f_o$) and applied to the complex holograms to reconstruct the entire axial range. The optimization process begins with the lowest order Zernike modes. For each Zernike mode, multiple phase masks are created with different amplitudes; each phase mask is applied to the hologram H_{vp} and the image is created from Eq. (2). The metric function is then calculated, and the best coefficient is determined through the solution of the one-dimensional parabolic fit of the coefficient vs. amplitude

curve. Once the best coefficients for all Zernike modes are identified, they are combined to form the final correction phase mask.

For modal-based sensorless-AO, the image quality metric is key to the AO performance. Many AO methods utilize intensity-based metric functions. However, given that the intensity of blinking fluorophores can show significant fluctuations, and the intensity of fluorophores in SMLM can both increase and decrease due to various photophysical phenomena like blinking or photobleaching, intensity-based metrics are not suited for single-molecule applications. Furthermore, single molecules typically emit only a few hundred to a few thousand photons and require high laser power for excitation, resulting in low signal-to-noise ratios (SNR) in detected hologram images. Under such conditions, intensity-based metrics are not reliable.

The frequency-based metric function, on the other hand, is an intensity-independent metric that is designed to normalize the high-frequency information of the image by the total intensity. Mathematically, the spatial frequency-based metric M is defined as [118],

$$M = \frac{\sum_{k_x,k_y} \left(1 - G_h(k_x,k_y)\right) |I(k_x,k_y)| \,\mathrm{circ}\left(\frac{k_x^2+k_y^2}{\sigma_{\mathrm{OTF}}}\right)}{\sum_{k_x,k_y} G_l(k_x,k_y) |I(k_x,k_y)| \,\mathrm{circ}\left(\frac{k_x^2+k_y^2}{\sigma_{\mathrm{OTF}}}\right)} \tag{5.5}$$

where $\mathrm{circ}(\cdot)$ is the circle function, $I(k_x,k_y)$ is the Fourier Transform of the image $I(x,y)$, and $G(k_x,k_y)$ is the Gaussian function that can be adjusted according to the frequency spectrum of the image to adjust the weight of the high $(1 - G_h(k_x,k_y))$ and low $(G_l(k_x,k_y))$ frequency components in the numerator and denominator,

$$G(k_x,k_y) = \exp\left(-\frac{k_x^2+k_y^2}{2\sigma^2}\right) \tag{5.6}$$

As we know, different aberrations manifest distinct effects on the PSH, consequently affecting the reconstructed PSF and optical transfer function (OTF), but the strength of the reconstructed OTF always gets reduced more at higher frequencies. Therefore, the high frequency Gaussian filter here is set to 0.8 times of the system OTF size ($\sigma_h = 0.8\sigma_{OTF}$) to emphasize high frequency components, and the low-frequency Gaussian filter is set to 0.06 times of the system OTF size ($\sigma_l = 0.06\sigma_{OTF}$) to target the frequencies near zero. Please note that unlike conventional wide field imaging system, for SIDH, the size of the OTF changes with z_s. The effective σ_{OTF} is given by

$$\sigma_{OTF} = \frac{M_T(z_s)}{M_T(z_s = f_o)} \left(\frac{2NA}{\lambda}\right) \tag{5.7}$$

where $M_T(z_s)$ is the transverse magnification of the system that can be calculated using the imaging equation of each lens in the system and taking the product of each of the magnifications, details of calculating $M_T(z_s)$ can be found in ref [87].

For each search iteration, at least three reconstructed images are required for each mode with three different amplitudes. The step size for the searched amplitudes decreases in subsequent iterations until

there is no further improvement in the image quality. After independently searching each Zernike mode, a one-dimensional parabolic fitting function ($y = ax^2 + bx + c$) is applied to get the optimal correction strength for the corresponding Zernike mode [88]. The process can be repeated a few times on all modes to ensure the best result. Then all modes are combined linearly to form the final correction phase mask.

5.1.3 Description of Simulations.

To demonstrate our approach, we conducted a series of simulations. Figure 5.3(a) shows the schematic of the optical layout used in the simulations, the details of which can be found in our previous publication [87].

The simulations use the method of optical propagators. The operators used in the simulations are the quadratic phase function Q and linear phase function L. The definition of Q can be found in section 2.2, and

$$L(\bar{r}_s) = \exp[i2\pi\lambda^{-1}(s_x x + s_y y)], \tag{5.8}$$

where $\bar{r}_s$ is the location vector (s_x, s_y). The detected hologram at the digital camera plane can be expressed as:

$$\begin{aligned} I_{\theta_n}(\bar{\mathbf{r}}_s) = |C(\bar{\mathbf{r}}_s)| L\left(-\frac{\bar{\mathbf{r}}_s}{z_s}\right) Q\left(\frac{1}{z_s}\right) Q\left(-\frac{1}{f_o}\right) Q\left(-\frac{1}{d_1}\right) Q\left(-\frac{1}{f_{TL}}\right) \\ \otimes Q\left(-\frac{1}{d_2}\right) Q\left(-\frac{1}{f_2}\right) Q\left(-\frac{1}{d_3}\right) Q\left(-\frac{1}{f_3}\right) \\ \otimes Q\left(-\frac{1}{d_4}\right) Q\left(-\frac{1}{f_4}\right) \otimes Q\left(-\frac{1}{d_5}\right) \exp(i\varphi_a) \\ \left[\frac{1}{2} + \frac{1}{2} Q\left(-\frac{1}{f_d}\right) \exp(i\theta_n)\right] \otimes Q\left(\frac{1}{z_h}\right) \Big|^2 \end{aligned} \tag{5.9}$$

where $C(\bar{\mathbf{r}}_s)$ is a complex constant dependent on the emitter's location. θ_n is the applied phase shift, and φ_a is the phase due to the optical aberrations.

The aberration is manually introduced at the interferometer plane where the spherical wave and the plane wave have the same wavefront size. The aberration, φ_a, as shown in Figure 5.5(a), contains a mix of astigmatism aberrations (Z_4, Z_5) and coma (Z_6, Z_7) because these modes correspond to the most common aberrations encountered in fluorescence microscopy. $\varphi_a = 0.5(Z_4 + Z_5 + Z_6 + Z_7)$. Each raw hologram stack contains 3 frames with phase constants $\theta_1 = 0°, \theta_2 = 120°, \theta_3 = 240°$. The final correction phase mask is obtained by running the aberration correction algorithm with the input of the aberrated complex hologram, as shown in Figure 5.1(a). For simulations performed in this paper, we use the in-focus plane ($z_s = f_o$) to search the correction phase mask and apply it to the entire reconstruction volume. If the aberration is not uniform across the entire volume in real experiments, the method can be adapted by dividing the imaging volume into smaller sub-volumes. The algorithm can then generate multiple correction phase masks, each optimized for a specific target region. This approach allows for

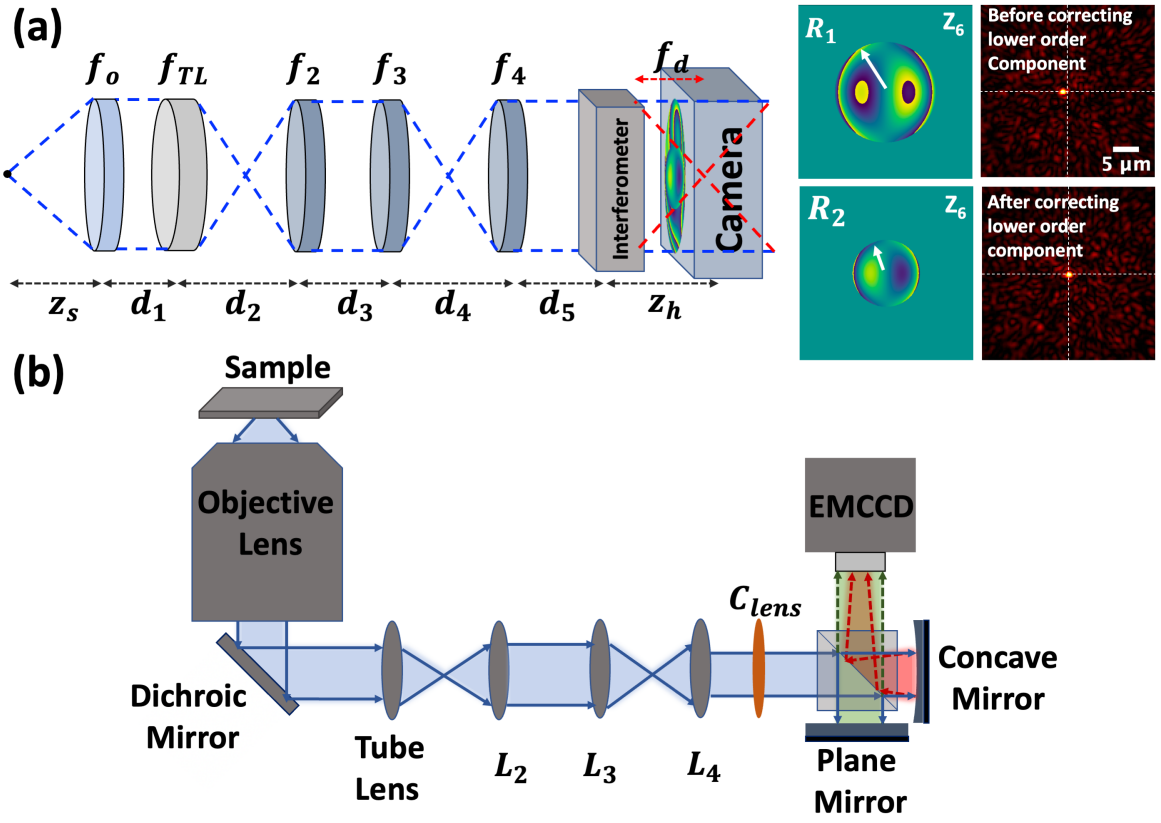

Figure 5.3: (a) Left panel: Schematic of simulation layout. Right panel: demonstration of the size difference between the simulated plane wave and spherical wave aberration phase masks leads to an error in the reconstructed PSF. (b) Detailed schematic of the imaging path of the SIDH setup with a Michelson interferometer. The blue square represents a beam splitter (BS). Interference will be observed as long as the path difference between the two arms of the interferometers is not greater than half the coherence length of the light source. For both simulation and experimental setup: the focal length of the objective lens is $f_o = 3$ mm. The focal length of the tube lens is $f_{TL} = 180$ mm. The focal length of L_2 is $f_2 = 120$ mm. The focal lengths of the relay lenses L_3 and L_4 are $f_3 = 200$ mm and $f_4 = 100$ mm, respectively. The focal length of the concave mirror is $f_d = 300$ mm. The distance between the optical components follows 4-f system, which $d_1 = 183$ mm, $d_2 = 400$ mm, $d_3 = 220$ mm, $d_4 = 300$ mm, $d_5 = 100$ mm and $z_h = 100$ mm. For the experimental setup, positive and negative focal length cylindrical lenses (C_{lens}) are combined to create ~ 0.7 μm of astigmatism.

more precise aberration correction tailored to the specific aberrations in different areas of the sample. Although the search process and reconstruction speed may decrease depending on the number of sub-

volumes required, the method remains entirely computational. This provides a high degree of flexibility for fine-tuning without the need to acquire additional data, thereby eliminating the risk of photodamage to the biological sample.

To demonstrate the ability of our algorithm to correct the entire imaging volume, we simulated a scenario where emitters are located at different axial planes. 11 emitters are placed along a diagonal with the displacement between adjacent emitters of $\Delta x = 3.5\,\mu$m, $\Delta y = 3.5\,\mu$m, and $\Delta z = 1\,\mu$m. Each fluorescent molecule emits 6000 photons. There is a background of 5 photons per pixel, and Poisson noise is added to each image after it has been constructed. The aberrated hologram is shown in Figure 5.5(b).

We also compare the localization precision of SIDH with aberrations, after aberration correction, and without aberrations (the ideal case). For simulations with a single emitter, the emitter is placed in the center of the field of view. For determining the localization precision, 100 PSH stacks of the emitter were generated (each PSH stack contains three images with different phases), and then reconstructed to get the coordinates of the molecule by localizing the center of the PSF using a 2D Gaussian fit. To calculate the localization precision, the standard deviations (STD) of the localized coordinates are found from the 100 individual simulated data stacks. A 10 μm axial range is simulated for both the before and after aberration correction scenarios. The pixel size for the simulations is 16 μm with an image size of 512×512 pixels. All the simulations were performed with custom written Python code [123].

The correction process is performed for Zernike modes 4, 5, 6, 7 within the range [-0.7, -0.4] with an initial step size of 0.1. Only two iterations are needed to obtain the desired results, as shown in Figure 5.5. The ideal reconstructed image with no aberrations is shown in Figure 5.7(a). The final correction phase mask is then formed and applied to get the aberration corrected complex hologram for reconstruction. To evaluate the performance of the AO, we calculated the peak intensity for the reconstructed PSF before and after correction and calculated the Strehl ratio. To quantify the localization precision improvement, we calculated the RMS differences between the ideal case (no aberration) and both the before and after correction cases.

Moreover, Figure 5.6 further demonstrates our method of correcting higher-order aberrations. Figure 5.6(a) shows non-axially symmetric spherical aberration correction results. Figure 5.6(b) addressed a complex aberration, defined as $\varphi_a = 1(Z_4 + Z_5 + \ldots + Z_{17} + Z_{18})$. The results demonstrate that our method can effectively apply to various aberration conditions.

5.1.4 Relation between the aberrations at the pupil plane and the hologram

The aberrated wavefront at the pupil plane is not the same hologram wavefront that is corrected at the hologram virtual pupil plane. This is because the hologram is formed by the interference of two aberrated waves. If the two beams are not the same size, then the hologram wavefront will result from the interference of two copies of the aberrated wavefront of different sizes. The aberration wavefront for the spherical wave undergoes a size reduction while the size of the aberration wavefront for the plane wave remains the same.

If the aberration is given by the expansion into Zernike modes as

$$\varphi_p = \sum c_n Z_n \left(\frac{r}{R}, \theta\right) \tag{5.10}$$

then the hologram wavefront can be described by

$$\varphi_h = \sum c_n \left(Z_n \left(\frac{r}{R_1}, \theta\right) - Z_n \left(\frac{r}{R_2}, \theta\right)\right) \tag{5.11}$$

The difference results in a new Zernike expansion which will not include any higher order terms than the original but may include new lower order terms. As an example, we can consider a system that introduces coma,

$$Z_8(r, \theta) = \sqrt{8}(3r^3 - 2r)\cos(\theta) \tag{5.12}$$

We use the Noll definition of the Zernike modes [124]. With R_1 as the radius of the aberration phase mask for the plane wave and R_2 for the spherical wave, the introduced aberration for the final complex hologram at the camera plane is,

$$\begin{aligned} \Delta Z_8 &= Z_8 \left(\frac{r}{R_1}, \theta\right) - Z_8 \left(\frac{r}{R_2}, \theta\right) \\ &= \left[3\left(\frac{r}{R_1}\right)^3 - 3\left(\frac{r}{R_2}\right)^3 - 2\left(\frac{r}{R_1}\right) + 2\left(\frac{r}{R_2}\right)\right]\cos(\theta) \end{aligned} \tag{5.13}$$

We can rewrite this expression as

$$\Delta Z_8 = \left(\left(\frac{R_2}{R_1}\right)^3 - 1\right) Z_8 \left(\frac{r}{R_2}, \theta\right) + \sqrt{8}\left(\frac{R_2}{R_1}\right)\left(\left(\frac{R_2}{R_1}\right)^2 - 1\right) Z_2 \left(\frac{r}{R_2}, \theta\right) \tag{5.14}$$

Z_2 is a tilt term and will cause a linear shift in the reconstructed PSF as shown in Figure 5.3(a). This linear shift will result in a shift in the localization of the emitters. It is interesting to note that as the camera gets closer to the interferometer, R_2 will approach R_1, and the hologram aberration will approach zero. This suggests that SIDH could be used to minimize aberrations when imaging in aberrating samples.

5.1.5 Description of experimental setup.

Figure 5.3(b) shows the imaging path of our experimental SIDH setup. The experimental data was collected using a custom-built inverted widefield microscope equipped with an oil immersion objective (Olympus, PlanApoN 60x/1.42). The back-pupil plane of the objective was demagnified using a tube lens ($f_{TL} = 180$ mm, Olympus, UTLU, USA) and an achromatic lens ($f_2 = 120$ mm). A pair of relay lenses in a 4f configuration were added before the interferometer to adjust the size of the hologram that enters the interferometer. For the interferometer, we chose the Michelson interferometer instead of an SLM be-

cause it is more light efficient. The Michelson interferometer contains a concave mirror ($f_d = 304.8$ mm, #32-818 $\lambda/4$ Precision Spherical Mirror, Edmund Optics, USA) on one arm and a plane mirror on the other arm. The plane mirror was mounted on a piezoelectric translational stage (Thorlabs, NFL5DP20) to implement the phase shift required to acquire three images. The fluorescence was detected with an electron-multiplying charge-coupled (EMCCD) camera (Andor iXon-897 Life, UK) which was placed approximately 100 mm away from the interferometer. To introduce astigmatism, two weak cylindrical lenses ($f_c = 1000$ mm and $f_c = -1000$ mm) were placed next to each other in a double rotation mount (Thorlabs DLM1) with their cylinder axes 2° with respect to each other. This results in $\sim 0.7\,\mu$m amplitude astigmatism and a negligible amplitude of defocus (assuming a beam diameter of 20 mm at the cylindrical lens). Details of the entire SIDH setup layout is shown in Figure 5.4. All the simulations and reconstruction processes were performed using a 2023 MacBook Pro equipped with an Apple M2 Pro chip, 12 cores and 16 GB of memory.

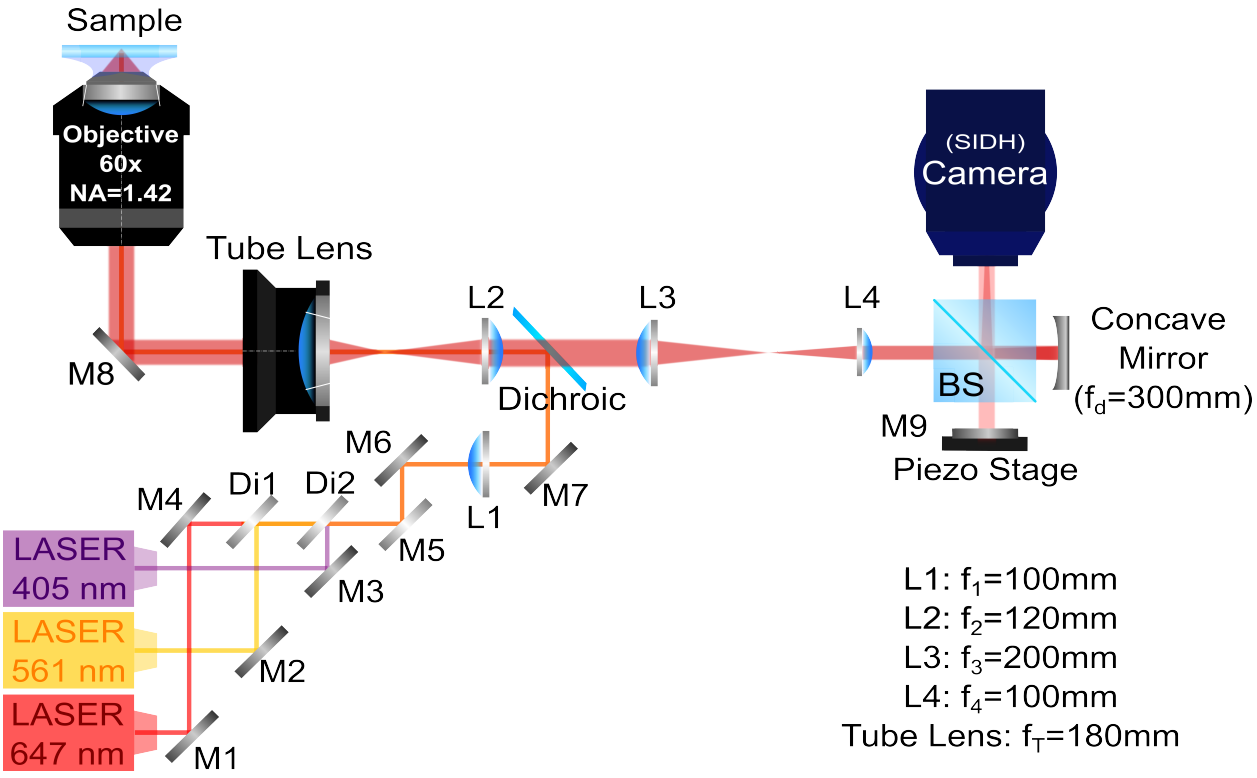

Figure 5.4: Schematic layout of the Self-Interference Digital Holography (SIDH) setup used in the experiments. The diagram shows the illumination path (orange line) and imaging path (red line). Optical components include plane mirrors (M1-M9), long bandpass dichroic mirrors Di1 (DMLP605T) and Di2 (DMLP425T), beam splitter (BS), and achromatic lenses (L1, L2, L3, L4). The emission light from sample was separated from the laser excitation light using a imaging dichroic mirror (XF2054,485-555-650TBDR, Omega, USA), a multi-band bandpass filter (FF01-446/523/600/677-25, Semrock, USA), and notch filters (ZET561NF notch filter and NF01-488/647 notch filter, Semrock, USA).

100 nm red fluorescent beads (FluoSpheres Carboxylate-Modified Microspheres, Excitation/Emission: 580/605 nm, Catalog number: F8801, Invitrogen, USA) were used in our experiments with a 561 nm excitation laser (OBIS 561 nm, 200 mW, Coherent, USA). The beads were prepared at a concentration of 10^{-5} and dried on a glass coverslip (Fisher Premium Cover Glass, no. 1.5, Fisher Scientific, USA). To selectively excite either a single bead or five beads, as shown in Figure 5.8, we moved the sample stage to search around the sample and identify a suitable region of interest (ROI) for imaging.

5.2 Results of SIDH-AO

5.2.1 Simulation results.

Figure 5.5 shows the simulation results of our algorithm. Figure 5.5(a) shows the introduced aberration mask for the simulation performed in Figure 5.5(b-e) and Figure 5.5(f). Figure 5.5(b) presents one of the detected holograms at the camera plane across a field of view of 68.48 by 68.48 μm^2. Figure 5.5(c) shows the complex hologram (from Figure 5.5(b)) at the virtual pupil plane. The detected holograms at the camera plane are spatially separated, but after computational propagation to the virtual pupil plane, they overlap in the center. This allows the correction mask to be applied to all holograms across the 3D volume simultaneously. Figure 5.5(d) shows the reconstruction (across 20 μm axially) before and after AO. As observed, the size of the hologram varies with the axial position of the emitter, affecting the FWHM of the reconstructed PSF. Even with relatively weak aberrations, the reconstructed image before correction is substantially distorted both laterally and axially. The sensorless-AO metric value is calculated from the reconstructed image at the in-focus plane, and then applied to all axial positions. After only 2 iterations of searching, as illustrated in Figure 5.5(e), the simulated PSF shows notable correction across the entire imaging range, and the Strehl ratio improves from 0.73 to 0.98 (Figure 5.5(d)). A more complex higher-order aberration can also be corrected, as shown in Figure 5.6, further demonstrates our method of correcting higher-order aberrations.

Moreover, we compared our algorithm with that of Man [95], as shown in Figure 5.7, using the same simulation raw data from Figure 5.5(b). Sensorless-AO is applied to the in-focus plane for both methods to search for the final correction phase mask, and we then apply the same phase correction to the whole reconstruction. Under the same simulation conditions of 6000 emitted photons and 5 photons/px background, the quality of the reconstructed images after AO for both methods shows no significant difference (Strehl ratio ~ 0.98 for both methods). However, the reconstruction speed for an axial range of 20 μm with a 200 nm step size (totaling 100 z-slices), as shown in Figure 5.5(d) and Figure 5.7(b), is different. Our method completes the reconstruction in 1.26 seconds, while Man's method takes 11.48 seconds under the same computational environment. This is because the reconstruction in Man's method does not have access to the final corrected complex hologram. Therefore, each axial position requires two Fourier transforms to obtain corrected images, which slows down the reconstruction speed. The $\sim$10-fold reconstruction speed improvement is critical for SIDH-based SMLM due to the large volume of data points required for

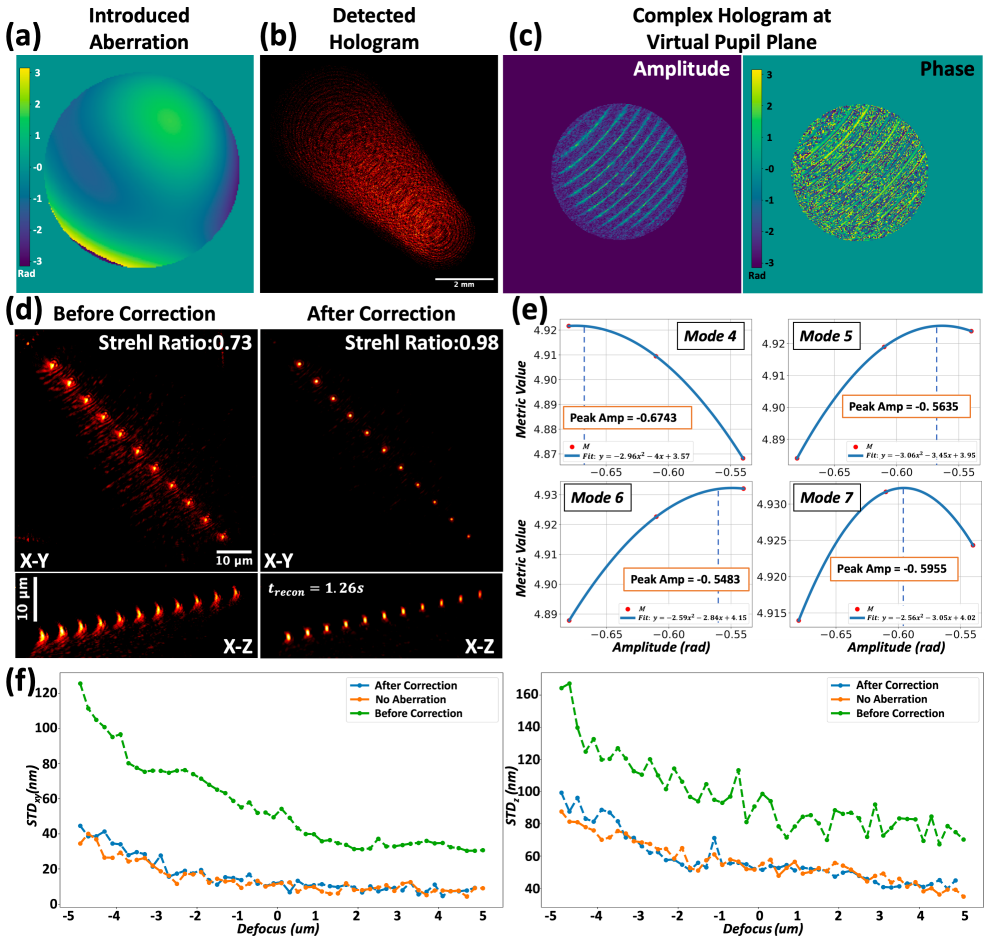

Figure 5.5: Simulation results of the SIDH aberration correction method. (a) shows the aberration introduced at the interferometer, defined as $\varphi_a = 0.5(Z_4 + Z_5 + Z_6 + Z_6)$ (b-e) Aberration impact and correction demonstration: (b) shows one of the detected hologram images at the camera plane. (c) shows the amplitude and phase of the complex hologram of (b) at the virtual pupil plane. (d) shows the reconstructed images in lateral and axial directions before and after AO. (e) shows the Metric function optimization of (b) for four Zernike modes after two iterations, displaying parabolic fits to determine peak amplitudes indicative of optimal correction strength. (f) Localization precision of localization precision in lateral and axial directions, respectively, under different conditions: 'No Aberration': no introduced aberration, 'Before Correction: with introduced aberrations from (a), 'After Correction': after second iterations of computational correction. For the localization precision simulations, the sources emit 6000 photons with a background of 5 photons/px.

acquiring a super resolution image, and it could also allow our method to perform real-time SIDH-based SPT with AO correction.

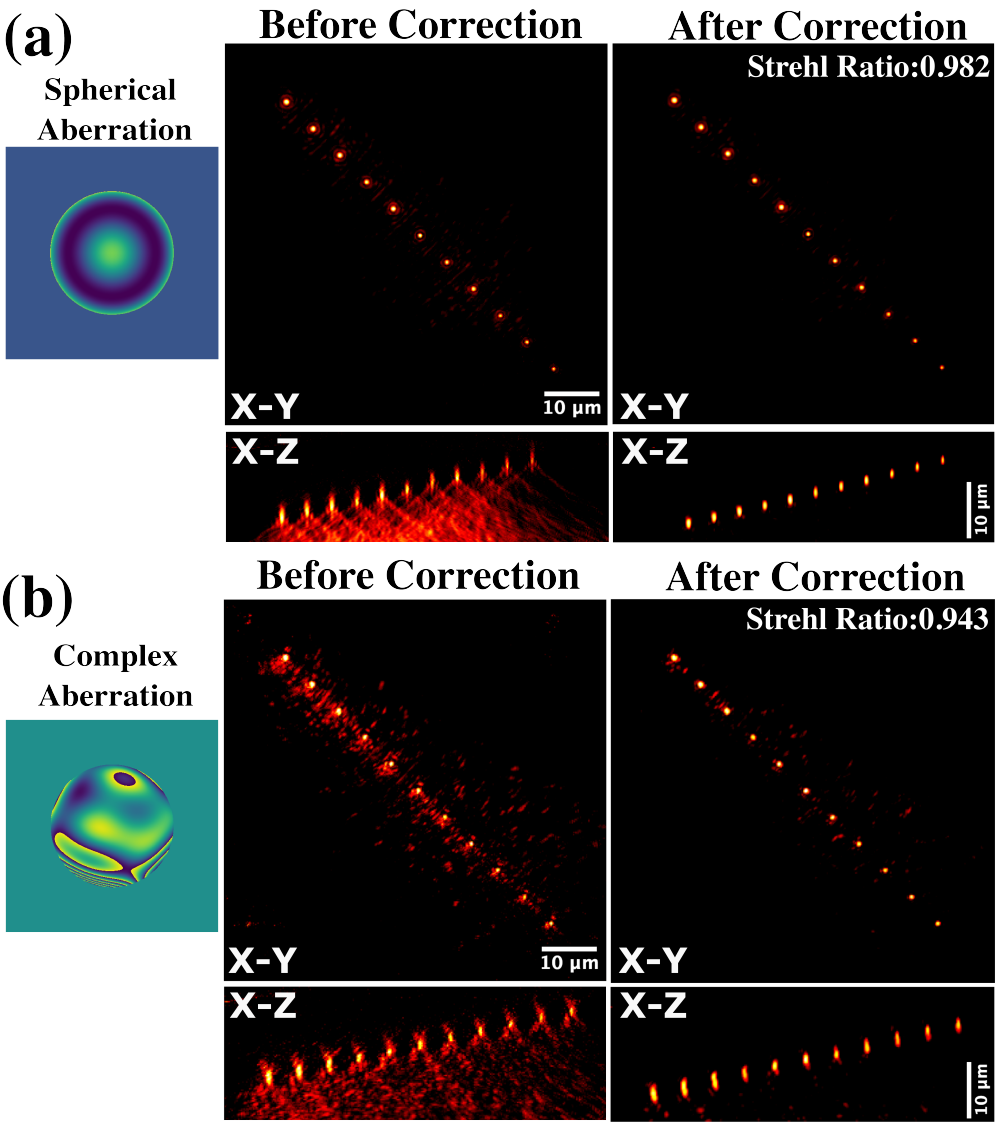

Figure 5.6: Simulation results demonstrating the effectiveness of the proposed aberration correction method for different types of aberrations. (a) Simulation results for spherical aberrations with an introduced amplitude of $1 radian$. (b) Simulation results for a complex aberration ($\varphi_a = 1(Z_4 + Z_5 + \ldots + Z_{17} + Z_{18})$). The phase profile of introduced aberration is displayed on the left inset of each panel.

To demonstrate the SIDH localization performance improvement with AO, the same aberration mask is employed, as shown in Figure 5.5(a). Figure 5.5(f) shows the lateral and axial localization results, respectively. In both graphs, the 'No Aberration' condition represents the system's performance in the absence of aberrations, serving as the ideal benchmark. The 'Before Correction' curve illustrates the degradation of localization precision caused by introduced aberrations. The 'After Correction' curve shows that after

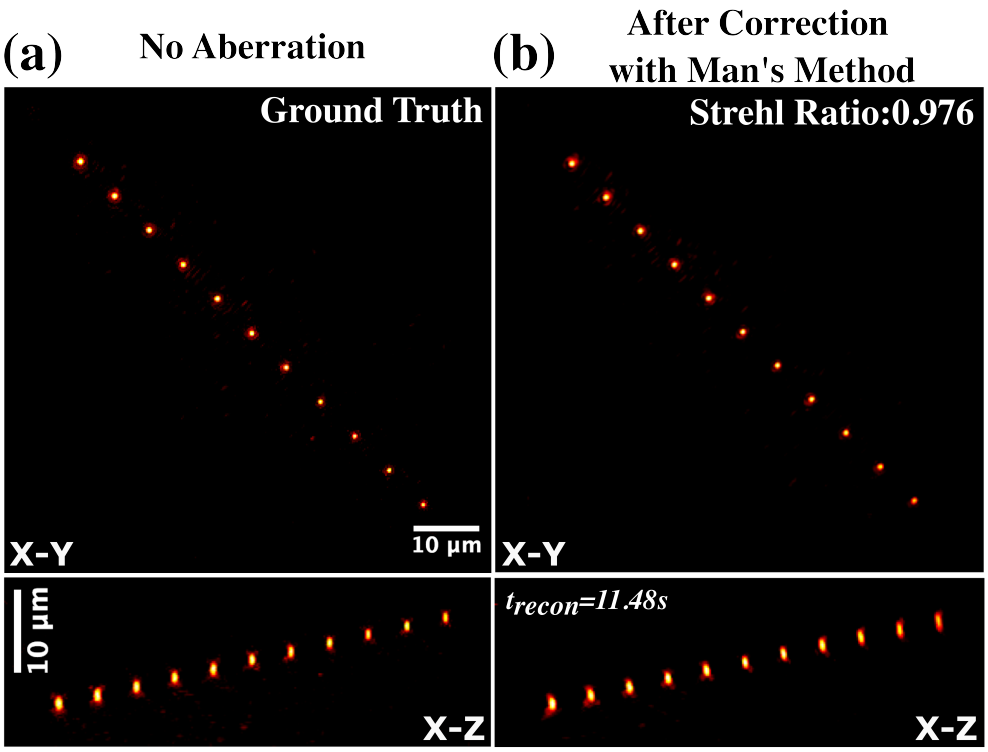

Figure 5.7: (a) Ground truth reconstructed image for performed simulation in Figure 5.5 and Figure 5.6. (b) Reconstructed Image for Man's method [95] with introduced aberration of $\varphi_a = 0.5(Z_4+Z_5+Z_6+Z_6)$. t_{recon} stands for the reconstruction time.

applying the correction phase mask, the aberration corrected localization precision approaches the ideal benchmark. The RMS difference of localization precision between the 'Before Correction' case and the 'No Aberration' case is approximately 59.21 nm for lateral localization and 49.58 nm for axial localization. In contrast, the RMS difference between the "after correction" case and the "no aberration" case is significantly reduced to approximately 3.69 nm for lateral localization and 2.36 nm for axial localization. These results demonstrate the effectiveness of our method in enhancing the performance of SIDH-based SMLM.

5.2.2 Experimental results.

Experimentally, we validated our algorithm by imaging 100 nm fluorescent beads. To better address the significant aberrations induced by the cylindrical lens used in the setup, we conducted a grid search with an amplitude step size of 2 radians in the range of [-10, 10], and visually checked the reconstructed images to refine the initial search parameters before implementing the sensorless-AO algorithm. Figure 5.8(a) shows the results of imaging a single 100 nm fluorescent bead that emits 9,000 photons with a background of

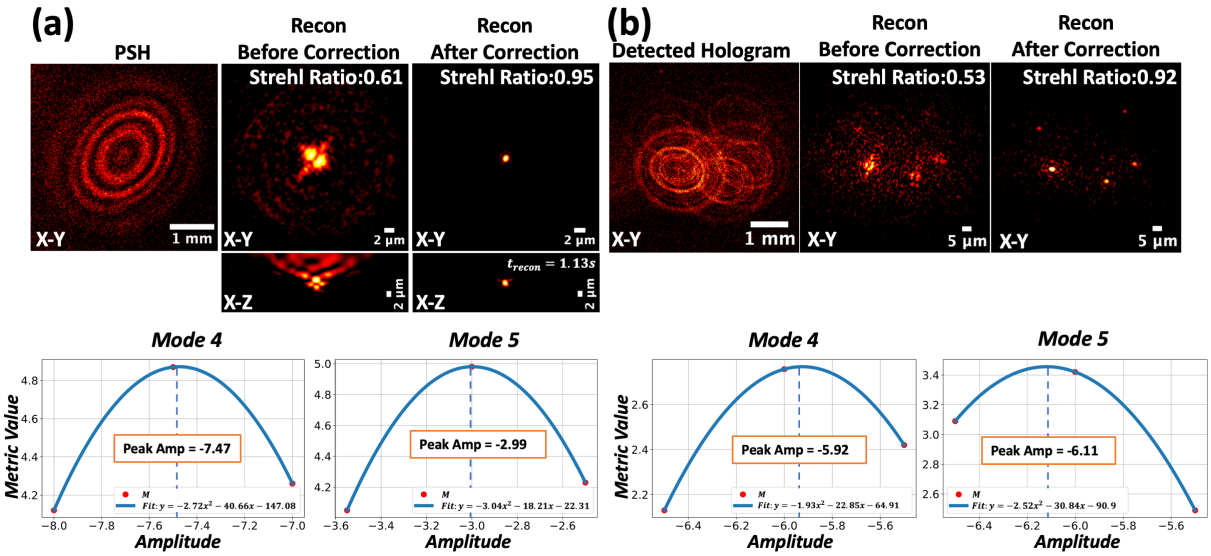

Figure 5.8: Experimental results of SIDH aberration correction method with fluorescent beads. The astigmatism aberration is introduced by a weak cylindrical lens (a) Results after the 2nd iteration of the correction for a 100 nm single fluorescent bead that contains 9,220 photons with a background of 8 photons/px. Top left panel: The aberrated PSH. The top middle and right panel: Reconstructed images before and after AO correction, respectively, in axial and lateral directions. Bottom panel: optimization plots for Zernike modes 4 and 5, respectively. (b) Experimental results of SIDH aberration correction method with 100 nm fluorescent beads at low signal light condition (each bead contains 7,800 photons with an estimated background of 18 photons/px). Top panels: The overlapped raw holograms and reconstructed images before and after correction. Bottom panels: the 2nd iterations of optimization plots for Zernike modes 4 and 5, respectively.

8 photons/px. Since the aberration is introduced by a cylindrical lens, we only correct for astigmatism (Zernike modes 4 and 5). After the grid search, we obtain the initial amplitudes of -8 radians for mode 4 and -4 radians for mode 5, and we begin the first iteration of the AO search in the amplitude range of [-9, -7] radians (for mode 4) and [-5, -3] radians (for mode 5) with a step size of 1 radian. The amplitude step size for the second iteration is set to 0.5 radians for both modes. After only 2 iterations, the Strehl ratio improves from 0.61 to 0.95, and both the lateral and axial PSF can be restored.

To demonstrate our method under SMLM imaging conditions, in Figure 5.8(b) we show the result of imaging spatially distinct and overlapped holograms under low light imaging conditions, in which each bead emits approximately 7,800 photons with a background of approximately 18 photons/px. A grid search is also applied with the same step size of 2 radians in the range of [-10, 10]. The amplitude range of [-7, -5] with a step size of 1 radian is set for the first iteration, and the amplitude range of [-6.5, -5.5]

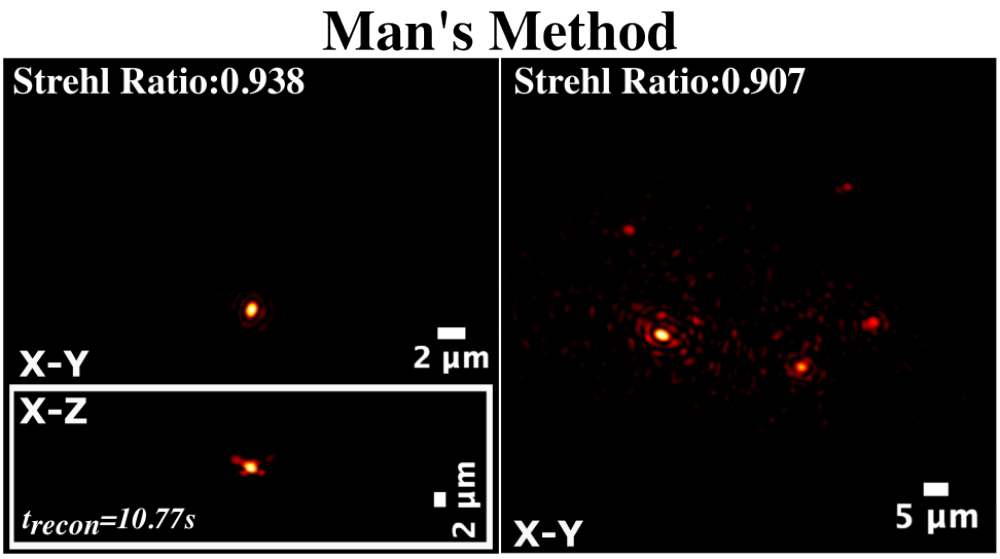

Figure 5.9: Experimental data reconstruction using Man's method [95]. The left panel shows the reconstructed image of a single PSH, corresponding to Figure 5.4(a). The left panel shows the reconstructed image of overlapped PSH, corresponding to Figure 5.4(b).

with a step size of 0.5 radians is set for the second iteration. After only 2 iterations, the Strehl ratio of the reconstructed image can be restored from 0.53 to 0.92. The same experimental data were used to compare our method with Man's method [95], as shown in Figure 5.9. While both methods demonstrate similar correction effectiveness, the increased computational efficiency of our method makes it more suitable for time-sensitive applications where rapid data processing is essential.

5.3 Conclusion

In conclusion, we introduced a novel, fast, and guide star-free computational aberration correction method for SIDH. Through a series of simulations and experimental results, we have demonstrated that our method can improve the Strehl ratio up to ~ 0.98 and restore the SIDH localization precision to near aberration-free conditions under low-signal imaging conditions. Moreover, the reconstruction speed of our method significantly outperforms the currently established method by 10-fold. This fast reconstruction is critical for the data-intensive demands of SMLM, enabling researchers to obtain high-resolution images more efficiently. The potential of our method extends beyond SIDH-based SMLM. Its adaptability and performance suggest it could be a valuable tool across various applications that rely on SIDH, such as sub-diffraction SIDH imaging and SIDH-based single particle tracking.

Chapter 6

2D PD-NSIM with rsEGFP2

As mentioned in Chapter 3, SIM is a very popular super-resolution method for live cell imaging and offers a revolutionary approach to surpassing the diffraction limits from the perspective of the frequency domain. However, the resolution enhancement offered by linear SIM is capped at a 2-fold improvement because the increase of the resolution is proportional to the spatial frequency of the structured illumination. NSIM utilizes reversible fluorescent proteins to introduce a nonlinear response of the fluorescence emission to the intensity of the illumination light, allowing the harmonics generated by the nonlinear pattern to shift high-frequency information into a domain that lies within the diffraction limit boundary. Consequently, NSIM theoretically allows for the collection of higher spatial frequency information, with the potential to infinitely extend resolution, as detailed in Chapter 3.

In real experiments, however, the ultimate resolution is influenced by the saturation level, where only frequency orders that rise above the noise level are distinguishable. Thus, achieving a strong nonlinear response is essential to obtain NSIM imaging with significant resolution enhancement. A weak nonlinear response limits the ability to resolve high-frequency details, thereby capping the resolution improvement.

In this dissertation, we utilize rsEGFP2 in conjunction with a patterned depletion approach to achieve 2D PD-NSIM imaging on live cells with sub-80 nm resolution. This chapter begins by introducing the characteristics of rsEGFP2, followed by the experimental design of our 2D PD-NSIM system and its alignment details. The chapter then presents the experimental results of 2D PD-NSIM, followed by a discussion of various potential approaches for further optimizing the experimental setup. Finally, the chapter concludes with an outline of future research directions.

6.1 Characteristic of rsEGFP2

rsEGFP2 is a rsFP derived from the enhanced green fluorescent protein (EGFP) by replacing threonine 65 by alanine [125]. Figure 6.1(a) shows the 3D structure of rsEGFP2. It operates in a negative switching mode, with the "off" state activated at 480 nm and the "on" state at 405 nm, as shown in Figure 6.1(b). One of the significant advantages of rsEGFP2 is its faster switching kinetics compared to rsEGFP. Studies have shown that at light intensities of 5.5 kW/cm^2, rsEGFP2 switches off around 6.5 times faster than

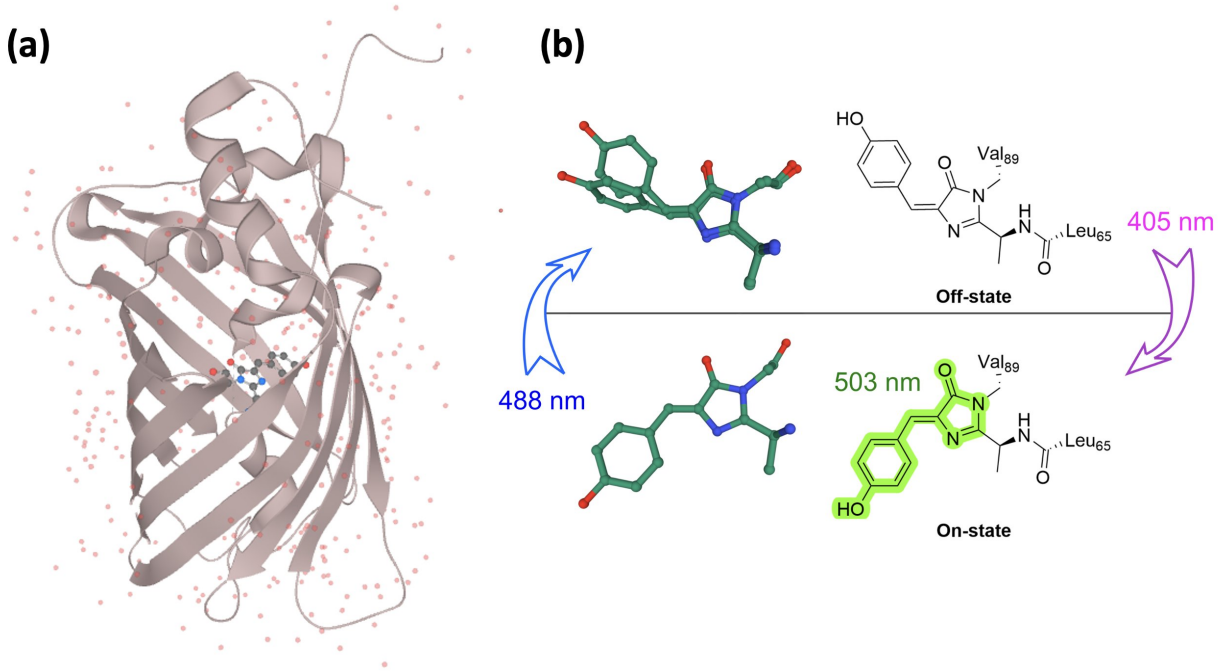

Figure 6.1: (a)Three-dimensional structure of rsEGFP2 (PDB: 5O89).(b)The chromophore of rsEGFP2. In the ON state, it absorbs 488 nm light and emits at 503 nm, while isomerization shifts it to the OFF state. In the OFF state, 405 nm light triggers isomerization back to the ON state.[125]

rsEGFP. With a light intensity of 100 W/cm^2, rsEGFP2 can achieve an off-rate greater than >90% with a 4 ms exposure at 480 nm. Similarly, it achieves an on-rate exceeding >90% with a 5 ms exposure to approximately 250 W/cm^2 light at 405 nm. Furthermore, rsEGFP2 can undergo over 2,100 switching cycles without a significant reduction in fluorescence intensity, making it highly durable for extended experiments. The relatively low light intensities required for switching between states help reduce phototoxicity and photobleaching, making rsEGFP2 particularly suited for long-term live-cell imaging. Its successful application in RESOLFT nanoscopy further demonstrates its utility in high-resolution imaging techniques.

In term of NSIM studies, as mentioned in section 3.4, the rsFPs that have been used include Dronpa [98], rsEGFP2 [104], Skylan-NS [75, 104], and Kohinoor [102]. Rego et al. [98] achieved 50 nm lateral resolution with TIRF-NSIM using Dronpa. However, Dronpa's slow switching rate and limited switching cycles limit its use in live-cell imaging. Li et al. [75] used Skylan-NS for patterned activation NSIM (PA-NSIM), claiming of achieving 60 nm spatial resolution with PA-NSIM. However, all resolution values reported by Li et al. are stated as "theoretical" on the basis of frequency-space arguments, and no evaluations are presented as to what extent the claims are supported by the data with demonstration in real

Table 6.1: Characteristics of Dronpa, rsEGFP, rsEGFP2, and Skylan-NS

RSFPs	**Dronpa**	**rsEGFP**	**rsEGFP2**	**Skylan-NS**
Absorption λ	503nm	493nm	478nm	499nm
Emissionλ	522nm	510nm	503nm	511nm
Quantum Yield	0.68	0.36	0.3	0.59
Switching-off lifetime (at 100 W/cm^2)	32ms	20ms	4ms	10ms
Number of switching cycles to bleach to 50% **of the initial fluor in the on-state**	90	1,100	2,100	710

space [108]. Zhang et al. [104] further compared Skylan-NS with rsEGFP2 and Dronpa using PA-NSIM, but still lack of demonstration of the proposed resolution improvement. Moreover, PA-NSIM not only requires precise alignment and calibration of 405 nm and 488 nm illumination patterns to eliminate the chromatic aberration, but also suffers from rapid contrast ratio reduction with increased switching cycles. While Skylan-NS offer higher photon yields and contrast ratios, rsEGFP2's fastest switching kinetics, longest fluorescence decay, and low light intensity requirements give it distinct advantages, as shown in Table 6.1, especially for PD-NSIM. Although other studies [75, 104] show that rsEGFP2 is not ideal for PA-NSIM, live cell imaging by PD-NSIM using rsEGFP2 hasn't been demonstrated so far.

6.2 Experimental setup of 2D PA-NSIM

Figure 6.2 shows the experimental setup for 2D PA-NSIM. The system is built on a Olympus IX71 inverted microscopy with a Prior Proscan XY Stage. It includes an activation laser (Coherent OBIS 405 nm Lasers), a depletion laser (Coherent OBIS 488 nm Lasers). The activation laser is reflected by a polarizing beam splitter (PBS) (10FC16PB.3, Newport) to the sample without reflecting from the SLM, provides a uniformed illumination that activate all the fluorescent proteins (rsEGFP2) in the FOV. The depletion laser is reflected by the PBS and sent to a Spatial light modulator (SLM, Forth Dimension QXGA-3DM) that displays binary grating patterns, which is further relayed and focused into the objective lens (UPLAPO60XOHR TIRF Objective, 60X, NA=1.50, Olympus). The fluorescent image is then directed to the Andor sCMOS camera (SONA 4BV6U, 6.5 μm pixel size) through the "imaging-flat" long bandpass dichroic mirror (Di03-R488-t3-25x36, Semrock). The total magnification of the system is 180x, so the effective pixel size of the final image is 36.1 nm. An emission filter (Semrock BrightLine quad band bandpass filter, FF01-446/523/600/677-25) and a notch filter (Semrock StopLine®quad-notch filter,

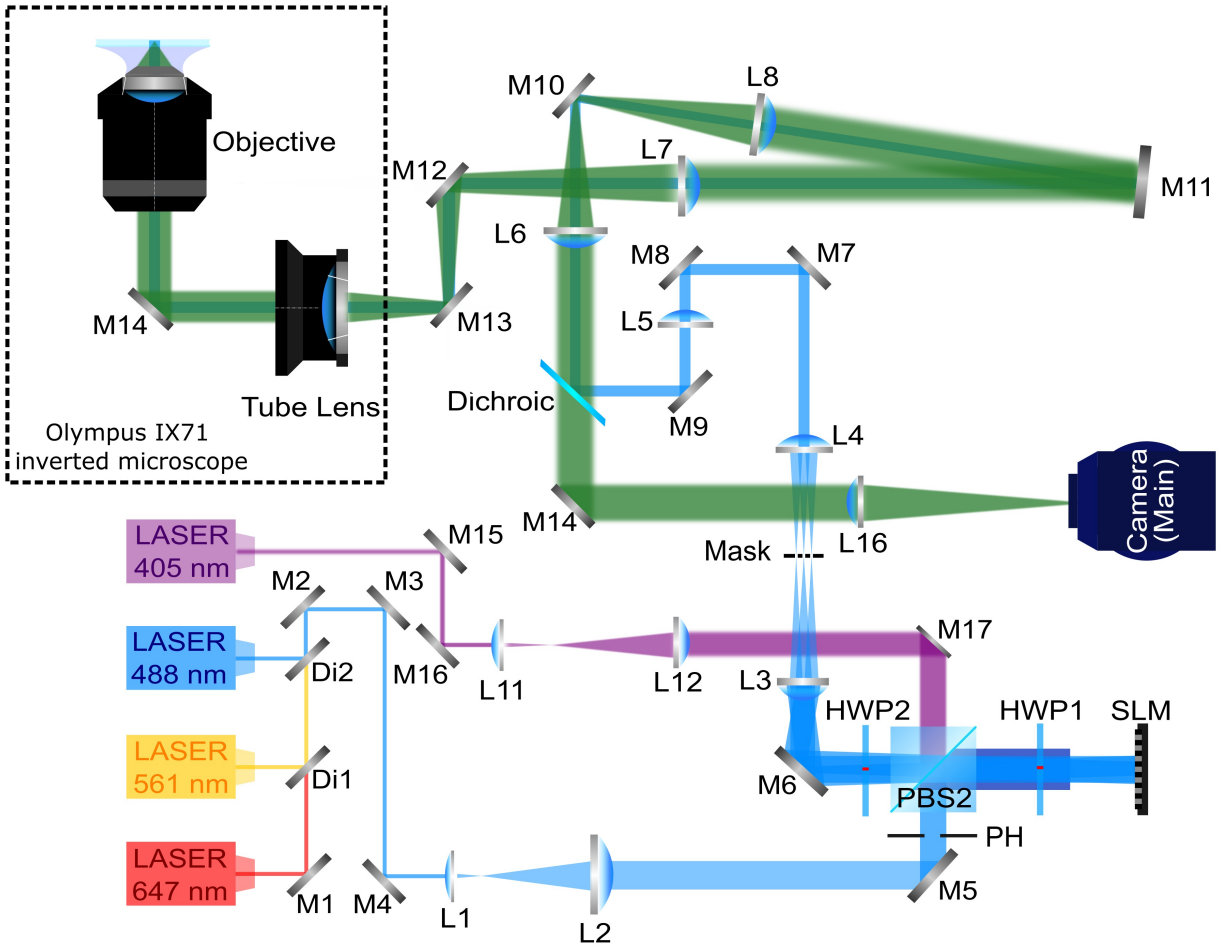

Figure 6.2: Experimental setup of 2D-NSIM. HWP: half-wave plate. PBS: polarized beam splitter. PH: pinhole. M1-M4: flat mirror. L1-L11: lens. f1 = 50 mm, f2 = 400 mm, f3 = 400 mm, f4 = 125 mm, f5 = 125 mm, f6 = 100 mm, f7 = 250 mm, f8 = 250 mm, f9 = 300 mm, f10 = 50 mm, f11 = 200 mm. The blue represents the illumination path (488nm) and the green path is the detection path.

NF03-405/488/561/635E-25) are put before the camera to block unwanted light, assuring a low background and noise level.

To achieve a good overlap of the two beams at the sample plane, especially for TIRF-SIM, the alignment needs to be extremely precise, much more so than in conventional SIM. The SLM must be placed in a plane that conjugates to the sample plane to ensure the two beams are overlapped perfectly in the sample plane. If the beams do not fully overlap this reduces the field of view over which the interference pattern is formed. Therefore, the position of the SLM, relay lenses, and objective must be fixed following

the principle of 4-f systems. To fine tune the focus, move the sample axially instead of the objective using a piezo z-stage. A detailed guideline of TIRF-SIM alignment can be found in ref [105]

6.2.1 Polarization control of the illumination path

Moreover, achieving the desired resolution in 2D-NSIM requires a strong nonlinear response from the sample. A stronger nonlinear response indicates that more high-frequency information is captured and shifted into the detectable range, resulting in improved spatial resolution. One of the factors that influences the strength of the linear/nonlinear response is the modulation contrast of the illumination pattern, which is highly dependent on the polarization state of the excitation light. Proper polarization alignment ensures that the sinusoidal light patterns generated by the SLM are projected onto the sample with minimal interference or reflection. In NSIM, this becomes even more important as any deviation in polarization can significantly reduce the modulation depth, thereby compromising the nonlinear fluorescence response.

To maximize the modulation depth of the sinusoidal pattern, the polarization state of the two interference beams must be normal to the direction of pattern wave vector (both be s-polarized) to reach the maximum contrast in the fringe pattern. Therefore, the polarization states of the incident beam need to be adjusted when switching the orientations of illumination patterns.

There are several ways of controlling the polarization state of the beams. The simplest way is to use a mechanical rotator with a half-wave plate to control polarization [43]. Another way is to use two ferroelectric liquid crystal phase retarders (FLC) were employed to rotate the polarization of the light and illumination pattern synchronously. However, FLCs have a switching time of over 20 ms, which limits the SIM imaging speed to around 50 ms per frame. To avoid the switching time of the FLCs, a passive polarization control scheme was presented where the FLCs were replaced with a quarter-wave plate and a pizza polarizer, which consists of multiple fan-shaped polarizer, each oriented at a specific polarization angle. However, implementing a pizza polarizer presents certain challenges. The manufacturing process is complex, requiring precise alignment of the segmented polarizer to ensure uniform polarization across the field of view. Additionally, the pizza polarizer can introduce a significant reduction in laser power—up to 50% —due to its segmented structure. Alternatively, the segmented half-wave plate can be replaced by a zero-order vortex half-wave retarder, which is a non-uniform half-wave plate [126]. It is efficient but only suitable for a single wavelength, which limits its application in multi-color imaging.

In our PD-NSIM setup, a mechanical rotator with a half-wave plate was used to control polarization. Specifically, the 488nm laser in Figure 6.2 is reflected by the PBS and passes through HWP1 (AHWP10M-600, Thorlabs) that is set to 11.25 degree ($\frac{\pi}{16}$). The SLM reflects the incident beam back to the HWP1 and only the horizontally polarized component is transmitted through the PBS and sent toward the sample. The second half-wave plate (HWP2) is mounted on a fast-motorized rotator (8MRU, Altechna) to adjust the polarization state, making it orthogonal to the pattern wave vector to achieve a high pattern contrast for all imaging angles. With the SLM, HWP1 and PBS, the vertically polarized incident light is eventually turned into two states, depending on the ON/OFF states of the pixels on the SLM. Specifically, the output light reflected by ON/OFF pixels are both horizontally polarized, but have the phase difference of

π, which functions as a binary phase grating. All but the ±1 diffraction orders must be filtered out by the spatial mask. In that case, 405 nm is set up in an inclined widefield illumination configuration by aligning the activation beam along with one of the first order diffracted beams that ensure the 405 beam will go pass the mask and get to the sample plane.

6.2.2 Data acquisition for 2D-NSIM

The data acquisition process for 2D PD-NSIM begins by activating all fluorophores using uniform 405 nm illumination. Following this, the patterned depletion illumination (488 nm) is applied to selectively switch off fluorophores around the maximum regions of the structured illumination pattern. Next, the phase of the illumination pattern is shifted by π, after which the patterned excitation illumination (488 nm) is applied to further deactivate additional fluorophores. A detailed explanation of the pattern depletion approach can be found in Chapter 2, section 2.1.2.

In the experiments, the nonlinear pattern generation is repeated with phase shifts and rotations to ensure isotropic resolution enhancement, similar to the approach used in linear SIM. The number of phases and orientations used depends on the harmonic orders included. To incorporate the first higher-order harmonic term, 5 equally distributed phases are required for each pattern angle to separate the OTF copies and resolve the pattern parameters, as explained in Chapter 3. For real imaging, patterns with 6 angles (0º, 30º, 60º, 90º, 120º, and 150º) were used instead of 5. This use of 6 angles provides more accurate pattern generation of 5 equally spaced phases than the patterns for 5 angles, requiring a total of 30 raw image frames to reconstruct a single 2D PD-NSIM image.

Given that rsEGFP2 achieves an off-rate with a 4 ms exposure at 480 nm, we opted to maximize the nonlinear response and SNR by repeating the acquisition process 5 times for each phase with shorter exposure times, rather than using a single long exposure. The images are then averaged to create a final raw image stacks for reconstruction.

6.3 Synchronization of components.

A highly efficient synchronization of the components in a 2D PD-NLSIM is crucial for achieving fast and accurate imaging. The lasers, SLM, camera, and fast-motorized rotator must work in precise harmony to ensure that illumination patterns are projected correctly. The synchronization of the lasers with the SLM is a key aspect of the system's performance. The pixels of the SLM behave as half-wave plates, modulating the phase of the incoming light only when they are fully in the "on" or "off" state. However, during the transition period (interframe switching time) between states, the pixels do not effectively modulate the light, which can reduce the pattern contrast if the laser is active during these intermediate states. To avoid this, it is essential that the lasers are synchronized to fire only when the SLM is in its fully active on or off states. In addition, the camera must be synchronized with the lasers to enable fast switching between the depletion and excitation patterns. For this purpose, an Arduino DUE board is used to manage the synchronization process. The external trigger signal from the camera is received by the Arduino as a digital

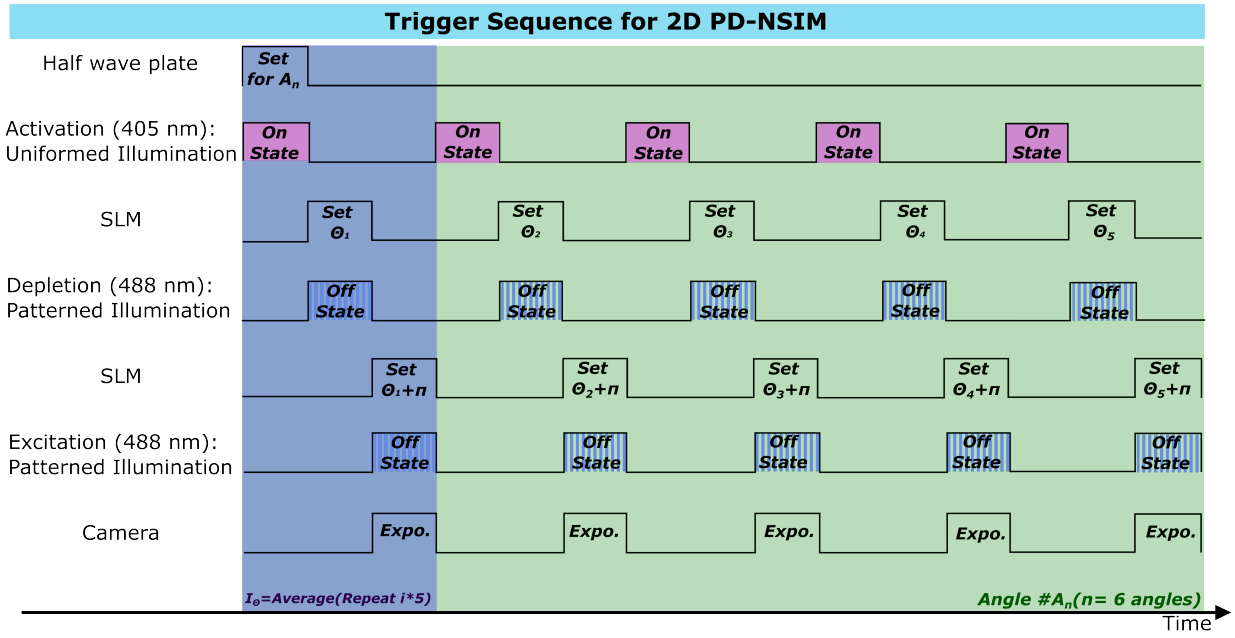

Figure 6.3: Synchronization trigger sequence of all the components for imaging cycle of one angle.

input, which triggers the 488 nm laser to turn on. Furthermore, the half-wave plate (HWP2), mounted on the fast-motorized rotator, is calibrated and adjusted to the correct pattern angle before each imaging cycle to ensure precise polarization control. Figure 6.3 illustrates the synchronization trigger sequence for all the components during the data acquisition process.

6.4 Timing of the depletion/excitation pattern

As mentioned in Chapter 2, the non-linear response is highly related to the depletion and excitation patterns, as well as the characteristics of rsEGFP2. In this section, we studied the relationship between the timing of the depletion/excitation patterns and the modulation strength for both linear and nonlinear orders.

Figure 6.4 shows simulation results demonstrating how depletion and excitation exposures affect modulation strength. The modulation strength is represented as the overlap magnitude (m). As expected, with excitation exposure time fixed in 10ms, an increase in depletion exposure time enhances modulation strength for the both linear and nonlinear order. Conversely, with depletion exposure fixed at 10ms, longer excitation times diminish modulation strength for both harmonic orders.

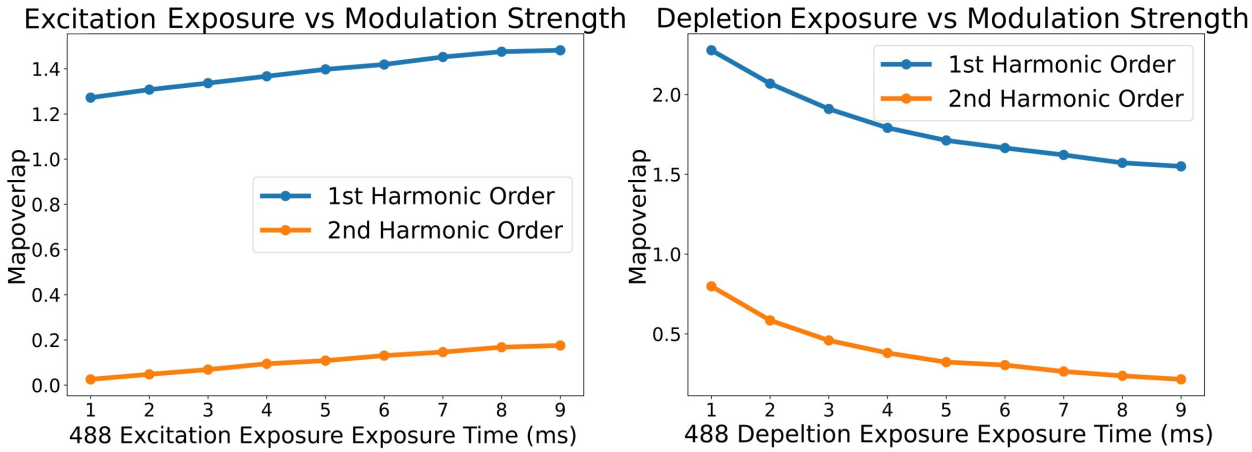

Figure 6.4: Simulation results showing the effects of depletion and excitation pattern exposure on the nonlinear response. The pattern frequency is set near the diffraction limit at of$2NA/\lambda$. (a) Relationship between depletion exposure time and modulation strength, with excitation exposure time fixed at 10 ms. (b) Relationship between excitation exposure time and modulation strength, with depletion exposure time fixed at 10 ms.

However, the simulation results do not account for specific characteristics of rsEGFP2, such as fluorophore saturation or photobleaching. Therefore, we conducted experiments using rsEGFP2-labeled U2OS cells to gather more accurate data, as shown in Figure 6.5. To ensure reliability, we repeated the experiment five times for each data point. When using rsEGFP2, the trends observed with rsEGFP2 diverged slightly from the simulations.

For excitation exposure, similar to the simulation results, increasing exposure time led to higher modulation strength for both harmonic orders. However, in the case of depletion, the modulation strength for the 1st harmonic initially increased with longer depletion times, peaking around 6 ms, after which it stabilized. In contrast, for the 2nd harmonic, increasing depletion exposure resulted in a reduction in modulation strength. Therefore, to balance the linear and nonlinear response, we chose 10 ms for depletion exposure and 6 ms for excitation exposure to perform the 2D PD-NSIM imaging.

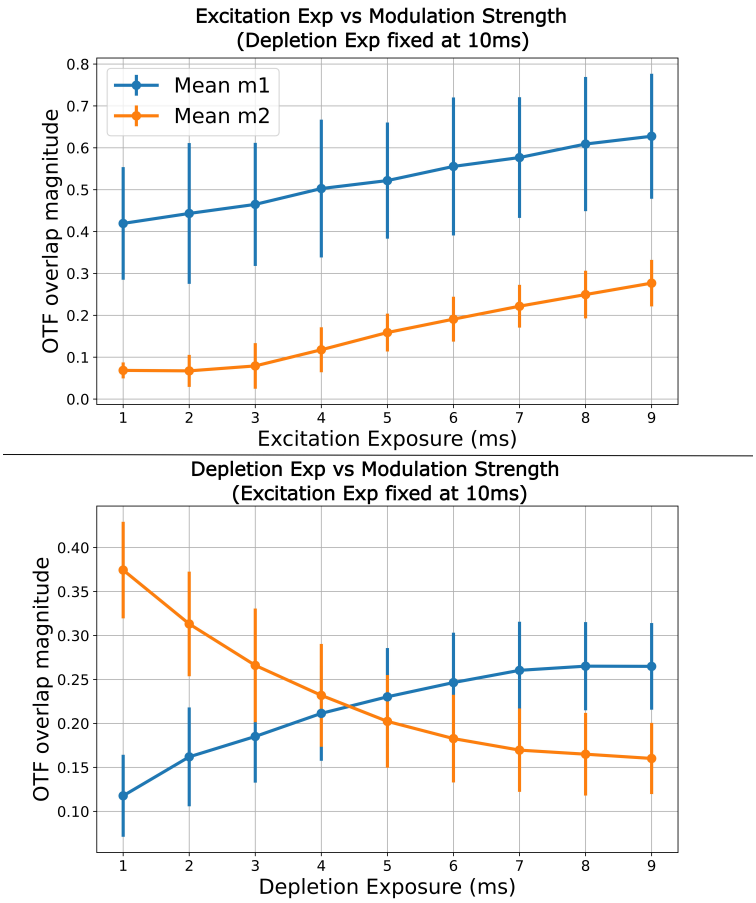

Figure 6.5: Experimental results showing the effects of depletion and excitation pattern exposure on the nonlinear response. Data was collected from rsEGFP2-labeled U2OS cells with a coarse pattern spacing of $0.5NA/\lambda$. For each plot, five cells were imaged, and the data represents the mean values with error bars indicating the standard deviation. (a) Relationship between excitation exposure time and modulation depth, with depletion exposure time fixed at 10 ms. (b) Relationship between depletion exposure time and modulation depth, with excitation exposure time fixed at 10 ms.

6.5 2D PD-NSIM imaging of U2OS cells.

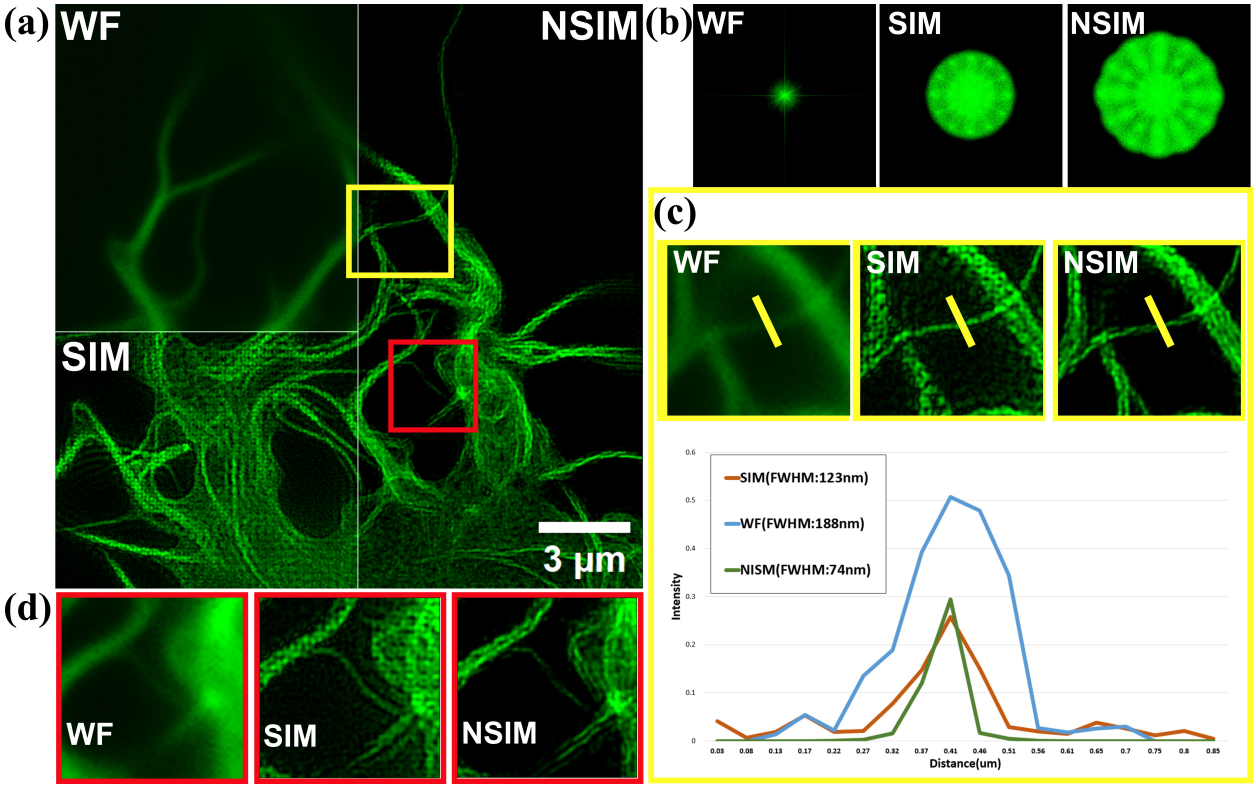

Figure 6.6: (a) A fixed U2OS cell transfected with rsEGFP2 imaged with PD-NSIM. (b) Corresponding frequency distribution of the imaged cell in Fourier space. (c) Top figures: Zoomed-in view of the yellow boxed region in (a). Bottom figures: Intensity plot of the yellow line marked in top figures. The full width half maximum (FWHM) is measured for corresponding images. (d) Zoomed- in view of the red boxed region in (a).

The performance of 2D PD-NSIM was demonstrated by imaging both fixed and live U2OS cells transfected with rsEGFP2. Figure 6.6 shows the results of NSIM imaging of actin labeled with rsEGFP2 in fixed U2OS cells with 75 nm resolution. Specifically, the first higher-order harmonic term is included, and 5 equally distributed phases are acquired for each angle of the pattern. The pattern spacing is $1.66NA/\lambda$. Moreover, the pattern is rotated to 6 angles to cover frequency space isotropically. The effective optical transfer function (OTF) after the reconstruction has an extended bandwidth of $4.98NA/\lambda$, as shown in Figure 6.6 (b), which is 2.5 times larger than the widefield OTF. A clear improvement in resolution can be observed between WF, SIM, and PD-NSIM images.

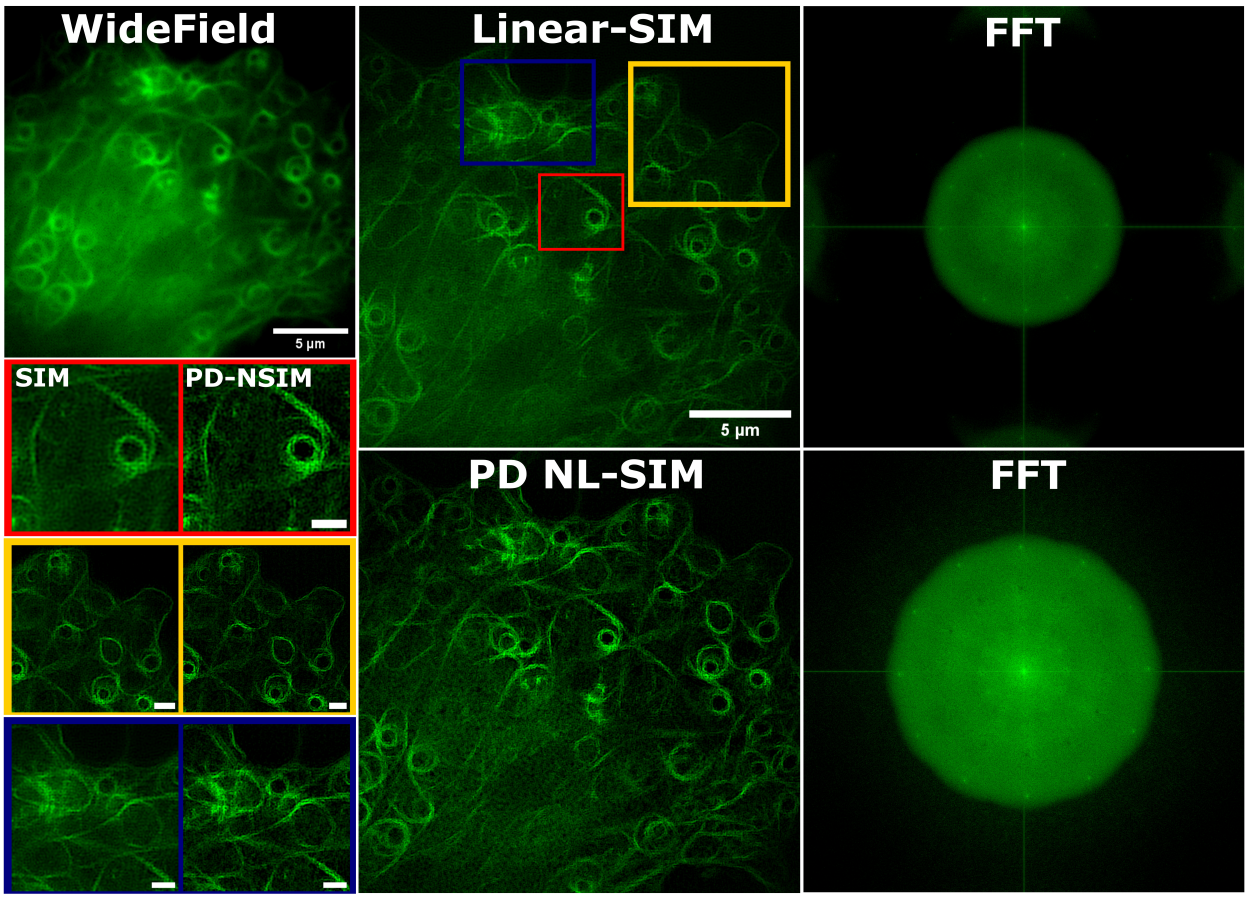

Figure 6.7: A live U2OS cell transfected with rsEGFP2 imaged with widefield, Linear SIM, and 2D PD-NSIM. Bottom left figures: Zoomed-in view of the yellow, red, and blue boxed regions in linear-SIM construction image, the scale bar indicated 1um. The FFT image is displayed with logarithmic scaling.

And Figure 6.7 and Figure 6.8 show live cell imaging of the U2OS cells with same imaging conditions and pattern spacing. In Figure 6.7 and and Figure 6.8, the zoomed-in views of the boxed regions, PD-NSIM consistently reveals finer structural details that are either blurred or completely lost in the widefield and linear SIM images. The fast Fourier transform (FFT) of the images in Figure 6.7 also demonstrates the broader spatial frequency content captured by PD-NSIM, indicating higher frequency information are collected to the other methods. The intensity plot in Figure 6.8 further demonstrated the resolution improvement up to 80nm in spatial space with real data measurement.

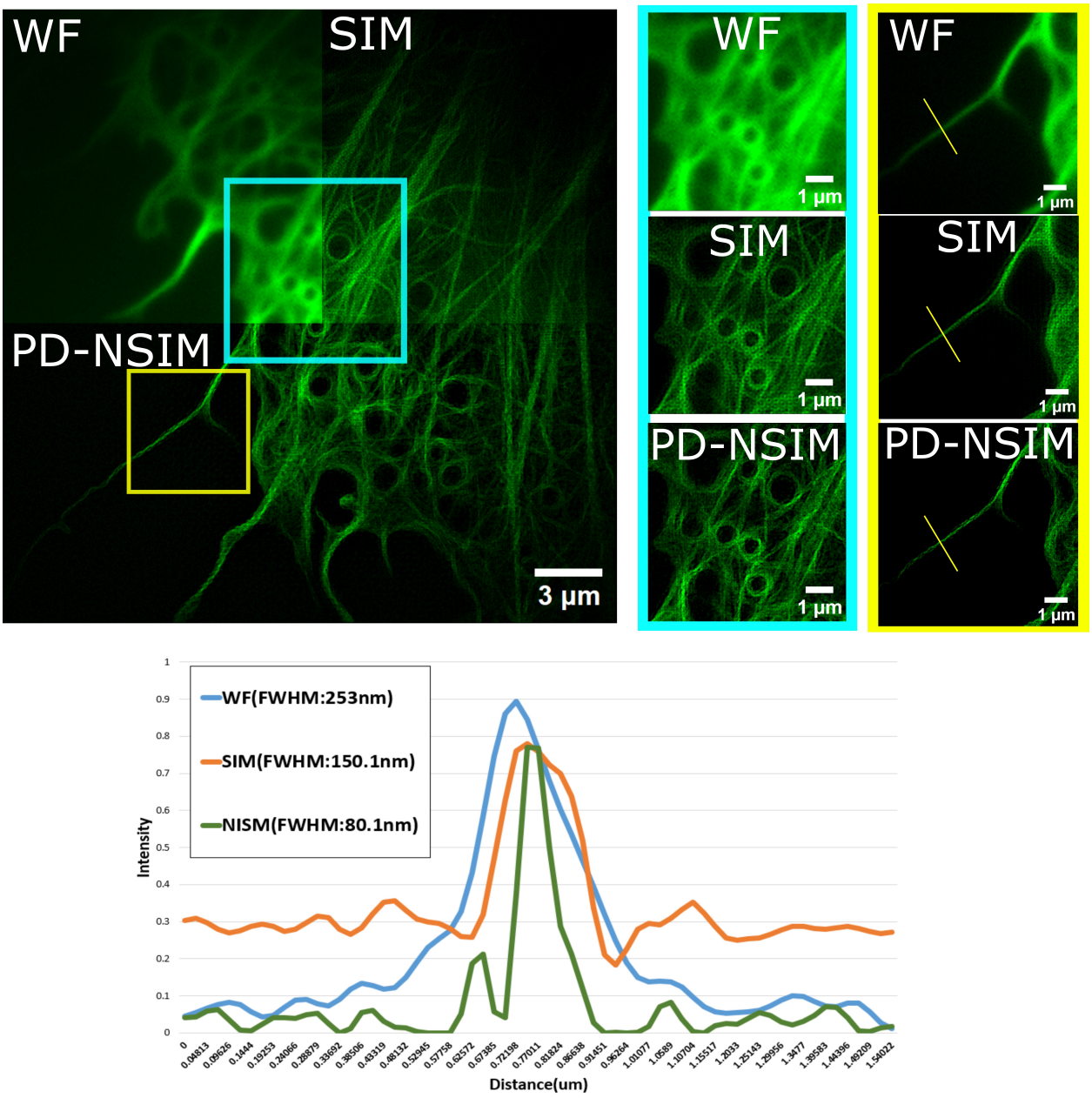

Figure 6.8: A live U2OS cell transfected with rsEGFP2 imaged with widefield, Linear SIM, and 2D PD-NSIM. Top right figures: Zoomed-in view of the blue and yellow boxed regions in the left construction image. Bottom figure: Intensity plot of the yellow line marked in yellow boxed region.

6.6 Future Development

The PD-NSIM setup can be further refined by optimizing the polarization control during data acquisition, details will be discussed in Chapter 7. This would help maintain an ideal polarization state and enhance modulation depth, leading to improved strength of nonlinear response and result in improved image resolution. Additionally, incorporating total internal reflection fluorescence (TIRF) illumination or lightsheet illumination could further reduce background noise, improving the SNR for better reconstruction.

Extending the 2D PD-NSIM technique to 3D is another direction. By applying three-dimensional structured illumination patterns and scanning axially, higher-resolution volumetric images could be achieved. Moreover, AO can be integrated into the system to correct optical aberrations, thereby improving image quality, especially for deep tissue live imaging. These developments could significantly enhance the performance of PD-NSIM for a wider range of biological applications, offering more precise and detailed live-cell imaging at subcellular levels.

Chapter 7

Polarization optimization of PD-NSIM

7.1 Introduction

Polarization control is a fundamental aspect not only in Structured Illumination Microscopy (SIM) but also in a variety of advanced optical imaging systems. For example, in Polarized Light Microscopy (PLM), it is used to enhance contrast in birefringent materials, enabling detailed visualization of structures such as crystals, fibers, and certain biological tissues. Second Harmonic Generation (SHG) Microscopy relies on precise polarization to probe non-centrosymmetric structures like collagen, as the intensity of the generated SHG signal is highly dependent on the orientation of the incident light polarization relative to the molecular alignment within the structure, leading to enhanced contrast and detailed structural information about the tissue. In Multiphoton Microscopy, polarization of the excitation light significantly impacts the efficiency of nonlinear optical processes and influences tissue penetration depth. In SIM, polarization affects the contrast of the illumination pattern and the quality of the reconstructed image.

For NSIM, maintaining a high modulation contrast (precise polarization control) is even more crucial than linear SIM because the effective resolution enhancement of NSIM relies on the detection of higher-order harmonic components introduced by nonlinear response from the sample. When the illumination intensity is high, the rsFPs switch to their ON (fluorescent) state, while in zero-intensity regions, they remain in the OFF (non-fluorescent) state. This contrast between ON and OFF states enhances the strength of the nonlinear response, resulting in the formation of higher-order harmonics in the fluorescence signal. However, if the illumination intensity in the supposed "zero-intensity" regions does not reach zero, it can partially excite the fluorophores in those regions, leading to residual fluorescence. This unwanted excitation reduces the contrast between ON and OFF states, diminishing the nonlinearity of the response. A weaker nonlinear response lowers the strength of the higher-order harmonics, making them harder to detect and limiting the achievable resolution improvement in NSIM. Therefore, to maximize the detectability of these higher-order harmonics and pattern spacing, it is essential to maintain a high modulation contrast.

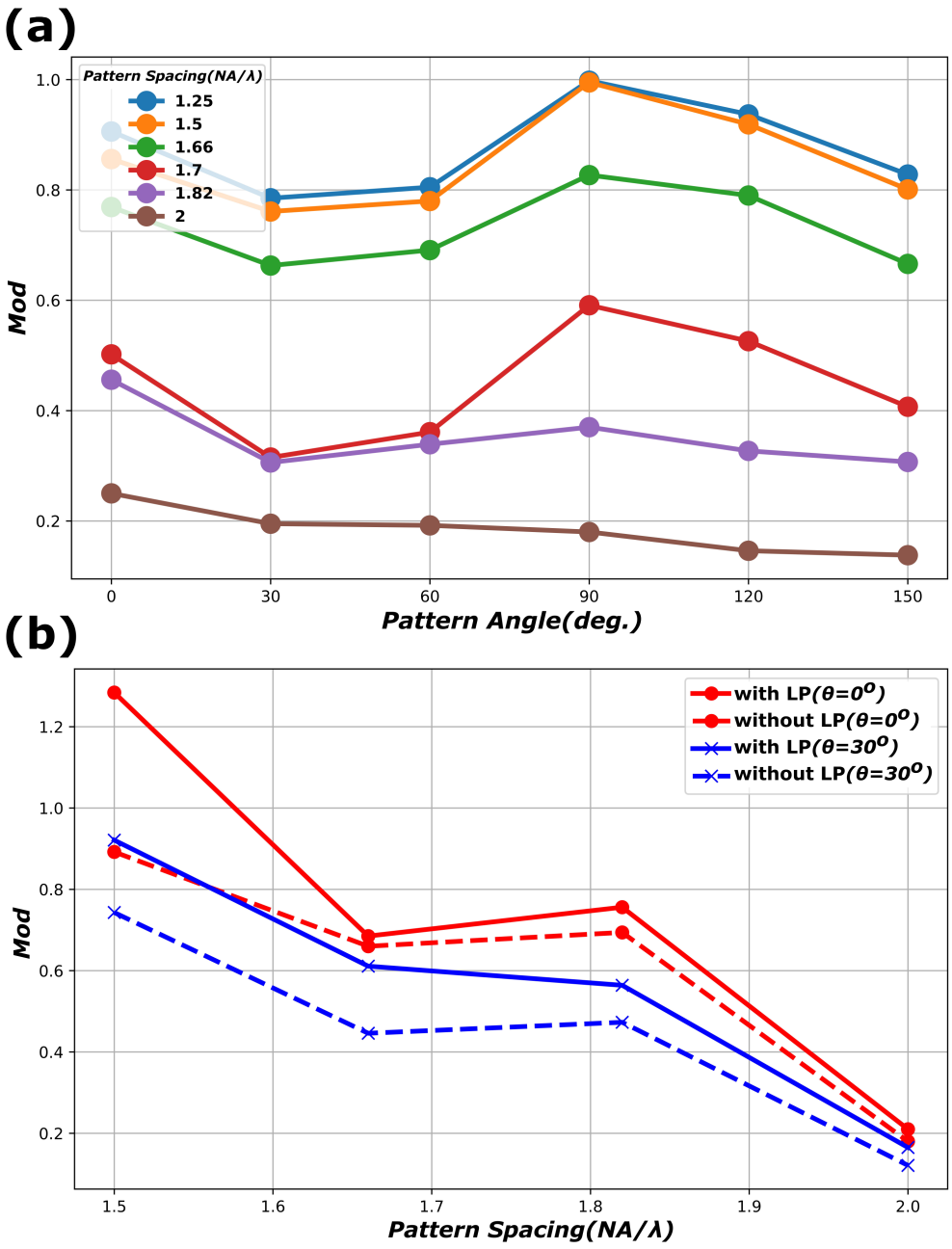

Figure 7.1: (a) The relationship between six illumination angles and modulation contrast for different pattern spacings without polarization optimization. (b) The relationship between pattern spacing and modulation contrast, comparing results before and after polarization optimization. "With LP" refers to the use of a linear polarizer placed in the imaging path (after the dichroic mirror) to restore the linearity of the polarization state. Data were collected by imaging U2OS cells labeled with rsEGFP2. The modulation contrast values (mod) were calculated using fairSIM [127].

However, achieving high modulation contrast becomes increasingly difficult as the spatial frequency of the illumination pattern approaches the cutoff frequency of the system's OTF. As the spatial frequency of the signal approaches the cutoff frequency of the system's OTF, the system's ability to accurately reproduce high-frequency components diminishes. Figure 7.1(a) illustrates how modulation contrast varies across different pattern angles, demonstrating a substantial drop in modulation contrast as the pattern spacings approach the edge of the OTF for all pattern angles. Figure 7.1(b) shows the improvement in modulation contrast achieved by restoring the linearity of the polarization state through the addition of a linear polarizer (LP) in the imaging path. Notably, the modulation contrast improves for both 0º and 30º imaging angles, with the 30º angle showing a larger improvement after adding the LP. The dichroic mirror has minimal influence on polarization at 0º. However, the inclusion of a LP reduces the collected emission signal, which makes it not ideal for imaging biological samples with limited photon budgets.

In summary, achieving clean and stable polarization states is essential for extracting high spatial frequency information and achieving the full resolution potential of PD-NSIM. In this Chapter, I will discuss the background of polarization compensation in SIM, the current methods and their pro and cons, and purpose our purposed method and findings of optimizing the polarization in SIM.

7.2 Polarization optimization of dichroic mirrors in SIM

Polarization control in optical imaging systems is often compromised by a variety of factors that distort the intended polarization state of the illuminating light. For the imaging system, other than the misalignment and optical path variations, another big distortion source is from optical component induced distortions, especially for the dichroic mirrors.

Even with proper alignment, dichroic mirrors can negatively affect the linearity of the polarization state in NSIM imaging. Dichroic mirrors are designed with multi-layered dielectric coatings that selectively reflect or transmit light based on wavelength. However, these coatings also introduce polarization-dependent phase shifts and intensity changes, as the transmission and reflection coefficients differ between s- and p-polarized components. When unpolarized or partially polarized light passes through a dichroic mirror, the varying interactions with these components can distort the polarization state, often converting linearly polarized light into elliptically polarized light.

7.2.1 Existing Polarization Optimization Methods

Several strategies have been developed to optimize the polarization distortion caused by dichroic mirrors.

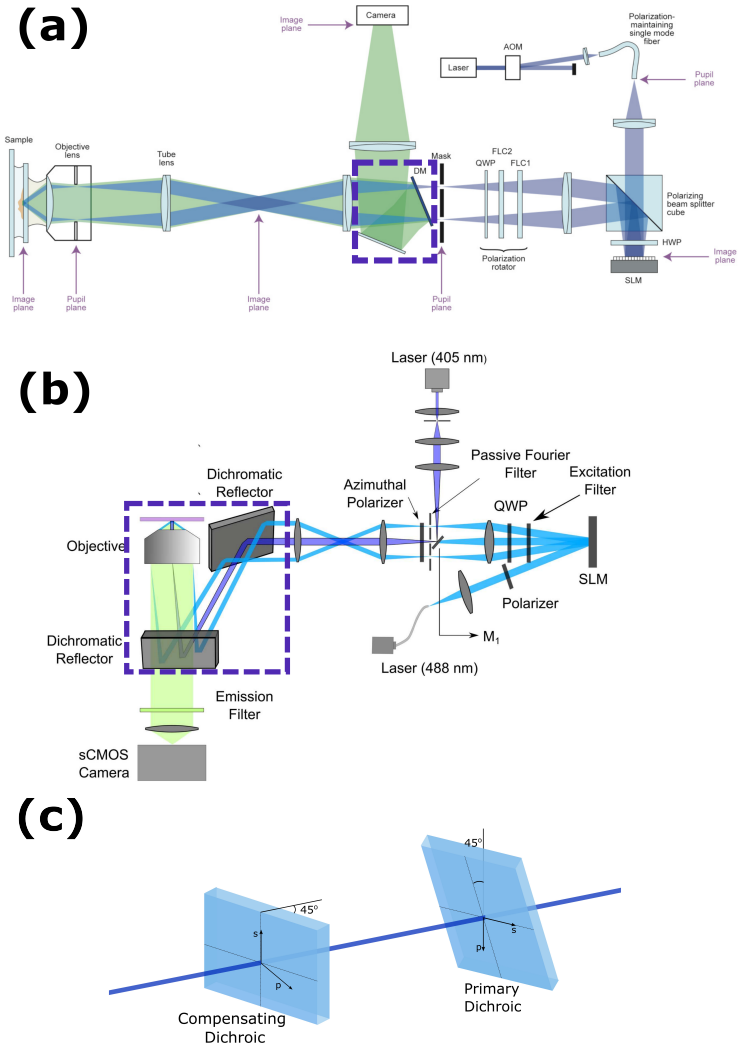

Figure 7.2: (a)Experimental setup of SIM using shortpass dichroic mirror. The dichroic mirror is set at a 22.5-degree angle relative to the incident beam (box with purple dashed line). Details of the setup can be found in ref [74].(b)Experimental setup of SIM using matched pairs of two identical longpass dichroic mirror (box with purple dashed line). Details of the setup can be found in ref[102]. (c) Polarization compensation using shortpass dichoric mirror pair. Details of the setup can be found in [128].

One common approach, as shown in Figure 7.2(a), involves positioning a customized shortpass dichroic mirror at a 22.5-degree angle relative to the incident beam [74, 129]. This configuration minimizes the differential phase retardation between s- and p-polarized components, helping to maintain the linear polarization state of the illumination light. This method has been effectively utilized in NSIM to enhance pattern contrast and resolution [98, 130]. However,standard imaging dichroic mirrors are often

optimized for common angles of incidence, such as 0° or 45°, and using a 22.5-degree angle may require custom-designed mirrors and extreme precise alignment, increasing the system's complexity and cost.

Another method, Figure 7.2(b), involves using matched pairs of two identical longpass dichroic mirror [102, 105]. Specifically, a pair of longpass dichroic mirrors are placed orthogonally at 90° to one another, effectively swapping the s- and p-axes to cancel out the polarization ellipticity introduced by the first mirror. However, this two-mirror configuration adds significant complexity to the optical setup. The orthogonal placement of the mirrors needs a two-layer, open-top design to accommodate the upward reflection of illumination light by the first mirror and the subsequent redirection by the second mirror. This arrangement requires precise alignment and careful consideration of beam paths, making both the design and alignment processes more challenging.

Alternatively, the strategy that uses two short bandpass dichroic mirror instead of a long bandpass dichroic mirror can avoid complicating the experimental setup, which has been successfully demonstrated with polarimetric multiphoton microscopy[128]. The approach also uses a pair of dichroic mirrors, with one acting as the primary dichroic and the other as a compensating dichroic, as shown in Figure 7.2 (c). The compensating dichroic is positioned at a 45° angle relative to the primary dichroic, with its s- and p-axes inverted. This configuration ensures that the distortions introduced by the primary dichroic are corrected when light passes through the compensating dichroic, restoring the polarization to its original state. However, this method has not yet been demonstrated with SIM, making it a promising direction for future development in SIM applications.

7.3 Longpass dichroic mirror polarization optimization using LCVR

In this section, we explore and report another potential alternative compensation method that aim to correct the phase shift induced by the dichroic mirror without adding unnecessary complexity to the imaging system.

The method involves utilizing a liquid crystal variable retarder (LCVR). An LCVR consists of a thin layer of liquid crystal material sandwiched between two glass plates, with transparent electrodes applied to the surfaces. The liquid crystal molecules naturally align in a specific direction, giving the device birefringent properties. This means that light polarized along different axes experiences different refractive indices, resulting in a phase difference (retardance) between the two orthogonal polarization components as the light passes through the device.

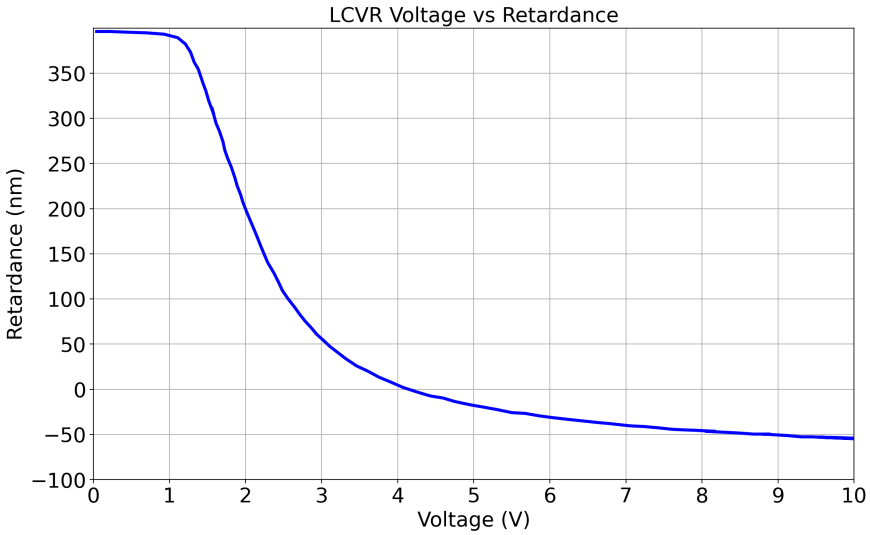

Figure 7.3: Voltage curve of the LCVR (Meadowlark Optics, LTN-200-VIS-TSC). The data is extracted from Meadowlark Optics.

The key feature of an LCVR is its ability to actively control retardance by applying a voltage across the liquid crystal layer. When no voltage is applied, the liquid crystal molecules are aligned to induce maximum retardance between the two polarization components. As the voltage increases, the alignment of the liquid crystal molecules shifts, reducing the retardance, as shown in Figure 7.3. By fine-tuning the voltage, the LCVR can introduce any desired phase shift to compensate for the phase delay caused by the dichroic mirror, allowing precise control over the polarization state of the transmitted light.

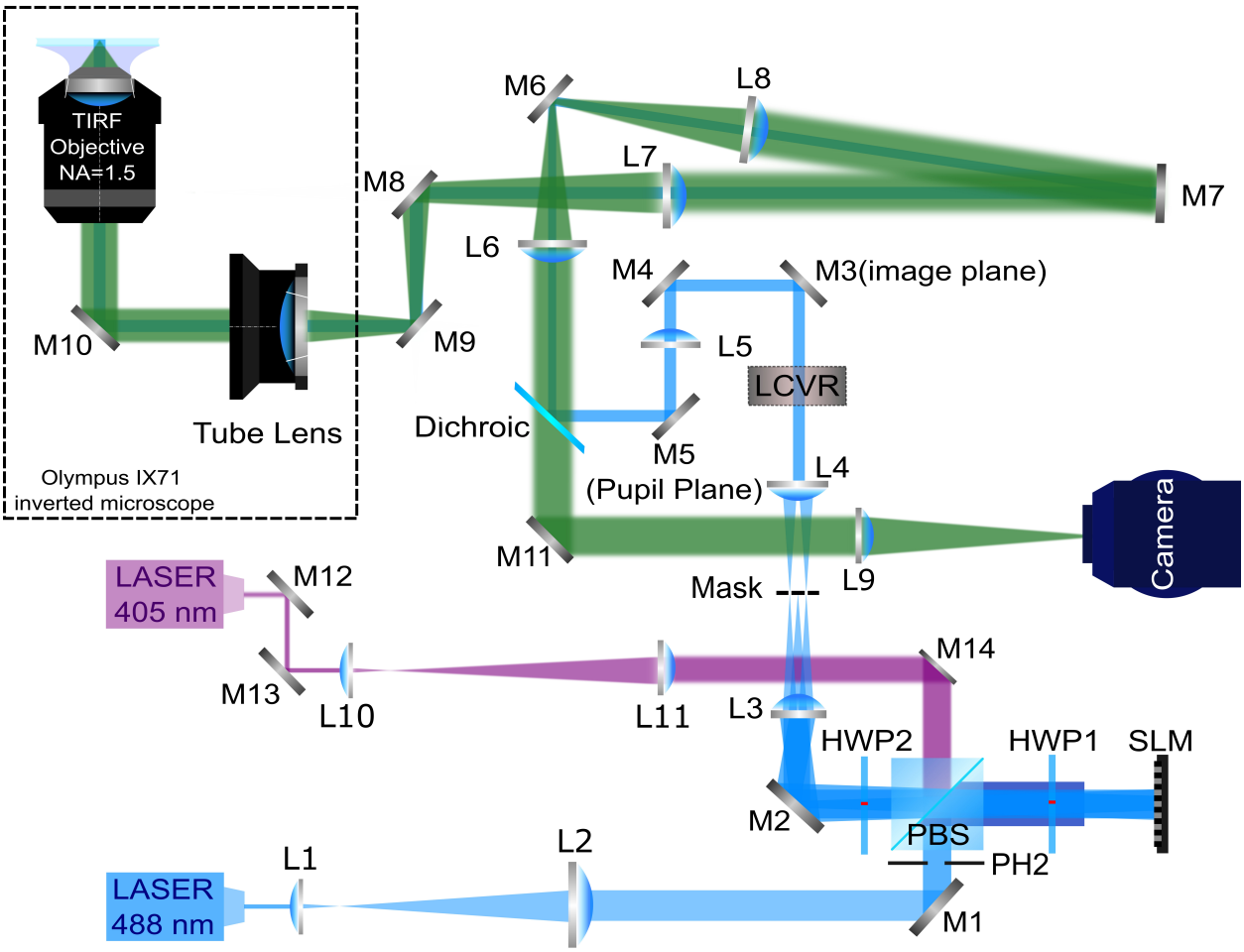

Figure 7.4: Experimental setup of NSIM with LCVR inserted in the illumination path before the dichroic mirror.

In our setup, the LCVR is positioned near the image plane before the dichroic mirror, as shown in Figure 7.4. The phase shifts introduced by the dichroic mirror are counteracted by pre-adjusting the polarization state of the light, ensuring that the desired phase delay is induced before the light interacts with the dichroic mirror. This method has a potential of providing an efficient way to maintain polarization control without adding significant complexity to the optical system.

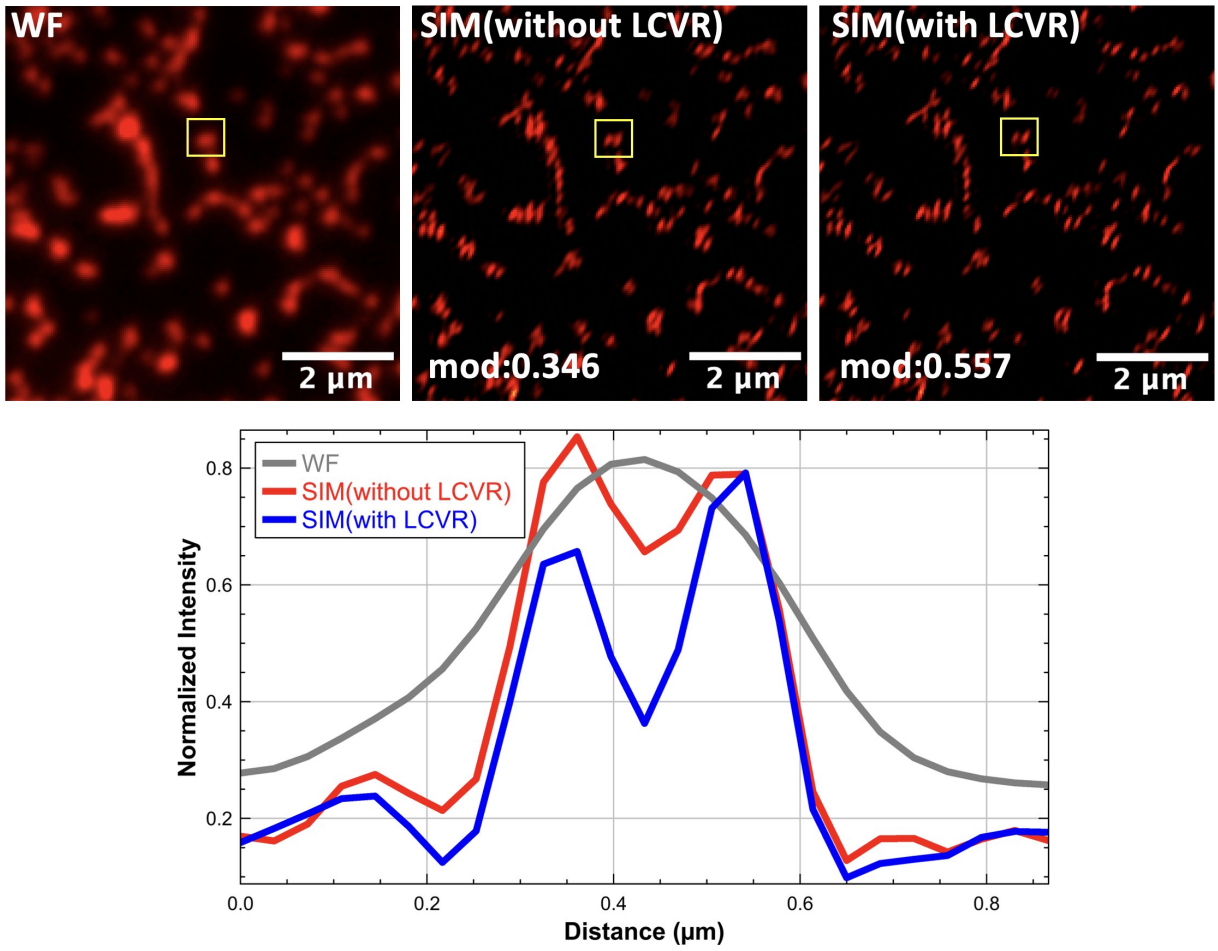

Figure 7.5: Demonstration of LCVR on 100nm fluorescent beads sample with pattern spacing of $1.99NA/\lambda$. Only the 30º angle is imaged. Top left inset: the widefield image. Top middle inset: SIM Reconstruction without LCVR. Top right inset: SIM Reconstruction with LCVR. Bottom inset: Normalized intensity chart showing SIM with LCVR has highest resolution. mod represent the reconstruction overlap amplitudes. The reconstruction and calculation of mod is done by using fairSIM [127]

Figure 7.5 demonstrates the experimental results by imaging 100 nm fluorescent beads with TIRF-SIM at 30º angle only, with a pattern spacing of $1.99NA/\lambda$. The top left inset displays the widefield (WF) image, where the resolution is limited by diffraction, resulting in blurred and less detailed bead structures. The top middle inset presents the SIM reconstruction without the LCVR. While this image shows some improvement in resolution compared to the WF image, it is still constrained by the lack of polarization control, leading to lower modulation contrast. In contrast, the top right inset demonstrates the SIM reconstruction with the LCVR, where enhanced polarization control significantly improves resolution and contrast, revealing finer details in the bead structures. The bottom inset shows the normalized intensity profiles across a bead, comparing WF, SIM without LCVR, and SIM with LCVR. The profile clearly

indicates that SIM with LCVR achieves the highest resolution, with sharper intensity peaks and narrower profiles, signifying greater modulation contrast and spatial resolution. The reconstruction overlap amplitudes (mod), which determine the pattern frequency and modulation strength, are quantified as 0.557 with LCVR compared to 0.346 without LCVR. These values are promising results for the effectiveness of the LCVR in enhancing image quality through optimized polarization control.

However, this improvement was not consistent across all pattern angles. To ensure more reliable results, we collected seven data points and averaged them to establish a clearer relationship. Figure 7.6 illustrates how modulation contrast is affected at different pattern angles with same pattern spacing of $1.82NA/\lambda$ when varying the phase delay applied to the LCVR. The red dashed line represents the reference modulation contrast (mod: the reconstruction overlap amplitude) without the LCVR in the system. Figure 7.6 (a) shows results at $\theta_1 = 0^o$, where the dichroic mirror minimally affects the polarization state compared to other angles. In this case, the modulation contrast remains relatively stable across the whole phase delay range, but the presence of the LCVR results in a slight reduction in modulation contrast (compared to the mean modulation of 0.1829 without the LCVR) at all phase delay. For $\theta_2 = 60^o$ and $\theta_2 = 120^o$, as shown in Figure 7.6 (b) and (c), a pronounced dip in modulation contrast occurs when the LCVR introduced a phase delay between approximately $\frac{1}{5}\pi$ and $\frac{9}{10}\pi$. This drop suggests that the LCVR introduces a phase shift that disrupts the polarization state, significantly reducing the pattern contrast. When the phase shift is near 0 (around $-\frac{1}{10}\pi$) and above π, the mod approaching the baseline mean (without the LCVR), but it does not surpass its baseline level consistently for all collected data.

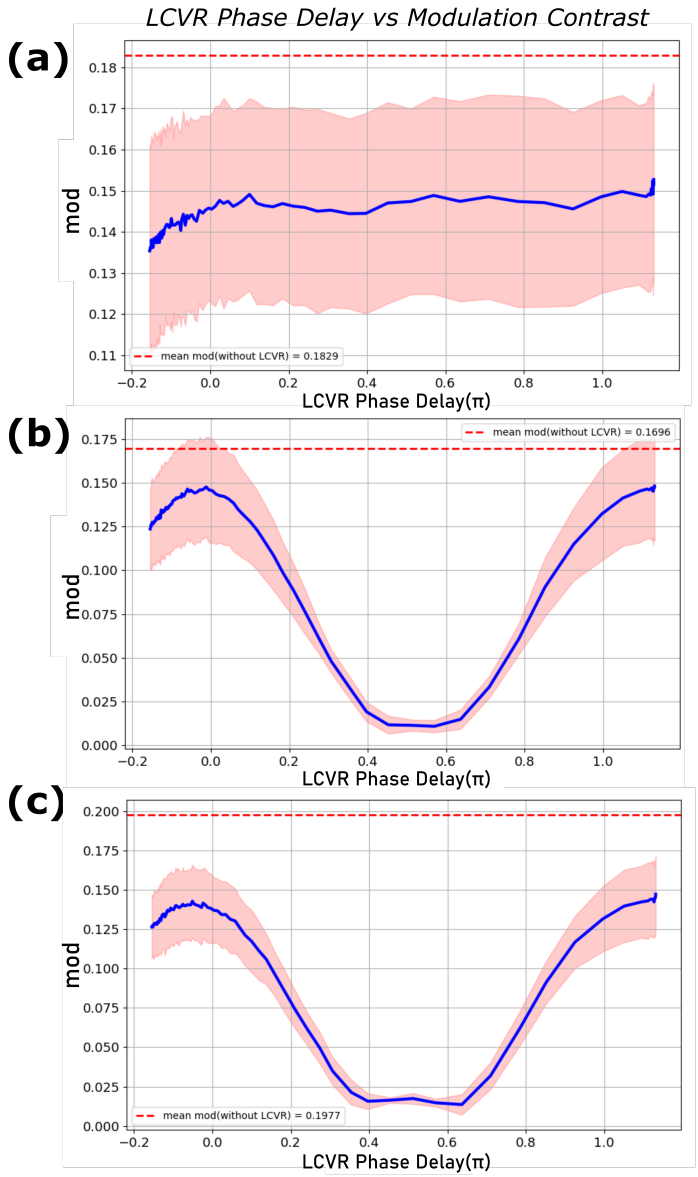

Figure 7.6: Relationship between LCVR phase delay and modulation contrast for three pattern angles with same pattern sapcing of $1.82NA/\lambda$, corresponding to (a) ($\theta_1 = 0^o$), (b) ($\theta_2 = 60^o$), and (c) ($\theta_3 = 120^o$). 7 data points were collected from 100nm Yellow-Green fluorescent beads with different sample positions imaged. The data represents the mean values with error bars indicating the standard deviation. The red dashed indicates the the mean values of the modulation contrast without LCVR as a reference. The modulation contrast is calculated from the reconstruction overlap amplitudes by our custom Python code.

Table 7.1: Polarization state (Laser power) measurements of the +k and -k beams for 2D illumination pattern with pattern spacing of $1.82NA/\lambda$.

Pattern Angle (deg)	**Laser Power (μ W) (+1 order)**	**Laser Power (μ W) (-1 order)**
0	1.5	9.1
30	100	6
60	50	13
90	1	5
120	20	56
150	125	9

This may be attributed to the spatial separation of the two beams (+/- 1 harmonic order) upon reflection from the dichroic mirror, resulting in different phase delays for each beam. Table 7.1 shows the presents the polarization measurements of the +1 and -1 beams in an illumination pattern with a spacing of $1.82\text{NA}/\lambda$. A linear polarizer, positioned after the dichroic mirror and aligned perpendicular to the polarization state of the pattern angle, was used for these measurements. A power meter (Thor Labs PM100D) was placed after the linear polarizer and before the tube lens to record the laser power. The half-wave plate was adjusted according to the pattern angle to ensure consistent polarization control of the beams before they reached the dichroic mirror. If the polarization states of the two beams remained the same after passing through the dichroic, their laser power readings should be similar after the linear polarizer. However, as indicated in Table 7.1, each pattern angle exhibits distinct laser power values for the +1 and -1 beams, suggesting that the dichroic mirror affects their polarization states differently. Unfortunately, the LCVR can only apply a uniform phase delay to both beams, limiting its ability to fully compensate for these differences.

Chapter 8

Conclusion and outlook

This dissertation has explored two advanced super-resolution microscopy techniques, contributing to the ongoing development of methods that surpass the diffraction limit and enhance our ability to observe fine cellular structures. The two methods developed and demonstrated in this work, SIDH-based 3D-SMLM and 2D PD-NSIM with rsEGFP2, target different applications. SIDH-based 3D-SMLM excels in resolving molecular details in the 10 μm axial imaging range, and 2D PD-NSIM is best for dynamic processes within living cells. Together, these methods address different challenges in super-resolution imaging, offering unique benefits in biological imaging for studying both molecular-level details or live-cell dynamics.

SIDH-based 3D-SMLM integrates digital holography with single-molecule localization microscopy, enabling nanometer-scale resolution over a large axial range without mechanical refocusing. Numerical simulations showed that this approach can achieve lateral resolutions between 5 nm and 58 nm and axial resolutions between 13 nm and 80 nm, even in low signal-to-noise conditions. Additionally, the incorporation of light-sheet illumination effectively reduces background noise, further expanding SIDH's capabilities in low-light imaging. Experimental validations demonstrated that with optimized parameters, LS-SIDH can detect as few as 2,400 photons in a hologram, highlighting its potential for single-molecule imaging. Furthermore, a fast, guide-star-free computational aberration correction method was developed and demonstrated, correcting complex aberrations without additional hardware and improving localization precision in both the lateral and axial directions.

Despite the success of SIDH in achieving three-dimensional imaging with nanometer-scale precision, single-molecule imaging of real biological samples using SIDH was not fully demonstrated in this work. One of the primary limitations was the implementation of the tilted light-sheet illumination with organic dyes. Due to the incident angle of the tilted light-sheet changes when the imaging chamber is at different position, it was challenging to quickly align the light-sheet beam waist to the optimal position for achieving the best signal-to-noise ratio (SNR) before the dyes bleaching out. To address this issue, a more advanced tilted light-sheet stage could be developed with the capability to automatically adjust the light-sheet position based on the sample stage 's position. Alternatively, implementing a different light-sheet illumination technique, such as Oblique Plane Illumination Microscopy, in combination with SIDH might help overcome these alignment challenges.

Additionally, the requirement for acquiring three images to reconstruct the holograms further complicates the application to single-molecule imaging. Achieving this requires an ultra-fast piezoelectric stage to introduce phase shifts at rates that match the switching dynamics of the organic dyes, ensuring that sufficient data points are captured before photobleaching occurs. A potential solution could involve developing a single-shot SIDH method, which eliminates the need for sequential phase acquisition and allows for faster imaging. This can be achieved through the application of deep learning methods for single shot SIDH imaging [131, 132]. By addressing these technical challenges, SIDH could be better equipped to achieve single-molecule imaging with real biological samples in future studies. Additionally, the computational AO method can be extended to broader applications involving SIDH, such as SIDH-based SPT aberration correction [133].

The second method, 2D PD-NSIM with rsEGFP2, successfully achieved live-cell super-resolution imaging. PD-NSIM utilizes the nonlinear response of rsFPs to extend the resolution capabilities of linear SIM. The data acquisition process was optimized based on the characteristic of rsEGFP2 to enhance both nonlinearity and modulation contrast. Live-cell imaging of U2OS cells was successfully demonstrated with sub-80 nm resolution. Additionally, potential methods for optimizing polarization control in the imaging system without adding complexity were discussed, with the aim of further improving pattern contrast and nonlinearity, which could lead to even higher resolution with higher harmonic orders being collected.

Looking ahead, beyond optimizing polarization control to maintain high modulation contrast, several promising developments could further enhance the utility and performance of 2D PD-NSIM. One promising direction involves combining 2D PD-NSIM with TIRF or light-sheet illumination, which could improve the SNR and thereby increase the strength of the nonlinear harmonic orders [75, 98]. Another potential direction is extending 2D PD-NSIM into three dimensions. By implementing 3D structured illumination patterns and performing axial scanning [43, 122, 134], higher-resolution volumetric live-cell imaging could be achieved, making the technique suitable for more complex 3D biological structures. Additionally, integrating AO into PD-NSIM systems could significantly improve image quality, particularly for deep tissue or thick sample imaging, where optical aberrations pose substantial challenges [122, 135, 136]. Real-time AO corrections could ensure high-resolution imaging is maintained at greater depths.

In conclusion, the advancements presented in this dissertation represent significant progress in the field of super-resolution microscopy. The techniques developed provide new tools for nanoscale bioimaging and have the potential to impact a wide range of biological and biomedical research.

References

[1] Oskar Heimstädt. "Das fluoreszenzmikroskop". In: Z Wiss Mikrosk 28.330-337 (1911), p. 14.

[2] Ernst Abbe. "Beiträge zur Theorie des Mikroskops und der mikroskopischen Wahrnehmung". In: Archiv für mikroskopische Anatomie 9.1 (1873), pp. 413–468.

[3] Lisa Tilokani et al. "Mitochondrial dynamics: overview of molecular mechanisms". In: Essays in biochemistry 62.3 (2018), pp. 341–360.

[4] Sydney Brenner, François Jacob, and Matthew Meselson. "An unstable intermediate carrying information from genes to ribosomes for protein synthesis". In: Nature 190 (1961), pp. 576–581.

[5] Jeff W Lichtman and José-Angel Conchello. "Fluorescence microscopy". In: Nature methods 2.12 (2005), pp. 910–919.

[6] Edgar Bright Wilson, John Courtney Decius, and Paul C Cross. Molecular vibrations: the theory of infrared and R Courier Corporation, 1980.

[7] WE Moerner and David P Fromm. "Methods of single-molecule fluorescence spectroscopy and microscopy". In: Review of Scientific instruments 74.8 (2003), pp. 3597–3619.

[8] Hellen C Ishikawa-Ankerhold, Richard Ankerhold, and Gregor PC Drummen. "Advanced fluorescence microscopy techniques—Frap, Flip, Flap, Fret and flim". In: Molecules 17.4 (2012), pp. 4047–4132.

[9] Jonathan A Kurvits, Mingming Jiang, and Rashid Zia. "Comparative analysis of imaging configurations and objectives for Fourier microscopy". In: JOSA A 32.11 (2015), pp. 2082–2092.

[10] Daniel Axelrod. "Total internal reflection fluorescence microscopy in cell biology". In: Traffic 2.11 (2001), pp. 764–774.

[11] ANDOR TECHNOLOGY. iXon Ultra. 2024. URL: https://andor.oxinst.com/assets/uploads/products/andor/documents/andor-ixon-ultra-emccd-specifications.pdf (visited on 11/17/2024).

[12] TELEDYNE VISION SOLUTIONS. EMCCDs: The Basics. 2024. URL: https://www.teledynevisionsolutions.com/learn/learning-center/scientific-imaging/emccds-the-basics/ (visited on 11/17/2024).

[13] Luchang Li et al. "Assessing low-light cameras with photon transfer curve method". In: Journal of Innovative Opt 9.03 (2016), p. 1630008.

[14] Venkataraman Krishnaswami et al. "Towards digital photon counting cameras for single-molecule optical nanoscopy". In: Optical Nanoscopy 3 (2014), pp. 1–11.

[15] David Dussault and Paul Hoess. "Noise performance comparison of ICCD with CCD and EM-CCD cameras". In: Infrared Systems and Photoelectronic Technology. Vol. 5563. SPIE. 2004, pp. 195–204.

[16] Olivier Daigle and Sébastien Blais-Ouellette. "Photon counting with an EMCCD". In: Sensors, Cameras, and Sys Vol. 7536. SPIE. 2010, pp. 48–57.

[17] E Mei et al. "A line scanning confocal fluorescent microscope using a CMOS rolling shutter as an adjustable aperture". In: Journal of microscopy 247.3 (2012), pp. 269–276.

[18] Fan Long, Shaoqun Zeng, and Zhen-Li Huang. "Localization-based super-resolution microscopy with an sCMOS camera Part II: Experimental methodology for comparing sCMOS with EMCCD cameras". In: Optics Express 20.16 (2012), pp. 17741–17759.

[19] Albert H Coons, Hugh J Creech, and R Norman Jones. "Immunological properties of an antibody containing a fluorescent group." In: Proceedings of the society for experimental biology and medicine 47.2 (1941), pp. 200–202.

[20] Richard Wombacher et al. "Live-cell super-resolution imaging with trimethoprim conjugates". In: Nature methods 7.9 (2010), pp. 717–719.

[21] Xinxin Duan, Meng Zhang, and Yu-Hui Zhang. "Organic fluorescent probes for live-cell super-resolution imaging". In: Frontiers of Optoelectronics 16.1 (2023), p. 34.

[22] Rita Strack. "Organic dyes for live imaging". In: Nature Methods 18.1 (2021), pp. 30–30.

[23] Sebastian Van de Linde et al. "Direct stochastic optical reconstruction microscopy with standard fluorescent probes". In: Nature protocols 6.7 (2011), pp. 991–1009.

[24] Teresa Klein et al. "Live-cell dSTORM with SNAP-tag fusion proteins". In: Nature methods 8.1 (2011), pp. 7–9.

[25] Osamu Shimomura, Frank H Johnson, and Yo Saiga. "Extraction, purification and properties of aequorin, a bioluminescent protein from the luminous hydromedusan, Aequorea". In: Journal of cellular and comparative physiology 59.3 (1962), pp. 223–239.

[26] Konstantin A Lukyanov et al. "Photoactivatable fluorescent proteins". In: Nature Reviews Molecular Cell Biolog 6.11 (2005), pp. 885–890.

[27] Jennifer Lippincott-Schwartz and George H Patterson. "Fluorescent proteins for photoactivation experiments". In: Methods in cell biology 85 (2008), pp. 45–61.

[28] Jennifer Lippincott-Schwartz and George H Patterson. "Photoactivatable fluorescent proteins for diffraction-limited and super-resolution imaging". In: Trends in cell biology 19.11 (2009), pp. 555–565.

[29] William E Moerner and Michel Orrit. "Illuminating single molecules in condensed matter". In: Science 283.5408 (1999), pp. 1670–1676.

[30] X Sunney Xie and Robert C Dunn. "Probing single molecule dynamics". In: Science 265.5170 (1994), pp. 361–364.

[31] George H Patterson and Jennifer Lippincott-Schwartz. "A photoactivatable GFP for selective photolabeling of proteins and cells". In: Science 297.5588 (2002), pp. 1873–1877.

[32] Fedor V Subach et al. "Photoactivatable mCherry for high-resolution two-color fluorescence microscopy". In: Nature methods 6.2 (2009), pp. 153–159.

[33] Jörg Wiedenmann et al. "EosFP, a fluorescent marker protein with UV-inducible green-to-red fluorescence conversion". In: Proceedings of the National Academy of Sciences 101.45 (2004), pp. 15905–15910.

[34] Ryoko Ando et al. "An optical marker based on the UV-induced green-to-red photoconversion of a fluorescent protein". In: Proceedings of the National Academy of Sciences 99.20 (2002), pp. 12651–12656.

[35] Tim Grotjohann et al. "Diffraction-unlimited all-optical imaging and writing with a photochromic GFP". In: Nature 478.7368 (2011), pp. 204–208.

[36] Karin Nienhaus and G Ulrich Nienhaus. "Fluorescent proteins for live-cell imaging with super-resolution". In: Chemical Society Reviews 43.4 (2014), pp. 1088–1106.

[37] James P Sumner and Raoul Kopelman. "Alexa Fluor 488 as an iron sensing molecule and its application in PEBBLE nanosensors". In: Analyst 130.4 (2005), pp. 528–533.

[38] Michael Cooper et al. "Cy3B™: improving the performance of cyanine dyes". In: Journal of fluorescence 14 (2004), pp. 145–150.

[39] Judith E Berlier et al. "Quantitative comparison of long-wavelength Alexa Fluor dyes to Cy dyes: fluorescence of the dyes and their bioconjugates". In: Journal of Histochemistry & Cytochemistry 51.12 (2003), pp. 1699–1712.

[40] Nora C Goossen-Schmidt et al. "Switching behaviour of dSTORM dyes in glycerol-containing buffer". In: Scientific Reports 10.1 (2020), p. 13746.

[41] Mickaël Lelek et al. "Single-molecule localization microscopy". In: Nature reviews methods primers 1.1 (2021), p. 39.

[42] Joseph W Goodman. Introduction to Fourier optics. Roberts and Company publishers, 2005.

[43] Mats GL Gustafsson. "Surpassing the lateral resolution limit by a factor of two using structured illumination microscopy". In: Journal of microscopy 198.2 (2000), pp. 82–87.

[44] Michael J Rust, Mark Bates, and Xiaowei Zhuang. "Sub-diffraction-limit imaging by stochastic optical reconstruction microscopy (STORM)". In: Nature methods 3.10 (2006), pp. 793–796.

[45] Stefan W Hell and Matthias Kroug. "Ground-state-depletion fluorscence microscopy: A concept for breaking the diffraction resolution limit". In: Applied Physics B 60 (1995), pp. 495–497.

[46] Alexey Sharonov and Robin M Hochstrasser. "Wide-field subdiffraction imaging by accumulated binding of diffusing probes". In: Proceedings of the National Academy of Sciences 103.50 (2006), pp. 18911–18916.

[47] Ralf Jungmann et al. "Single-molecule kinetics and super-resolution microscopy by fluorescence imaging of transient binding on DNA origami". In: Nano letters 10.11 (2010), pp. 4756–4761.

[48] Mike Heilemann et al. "Subdiffraction-resolution fluorescence imaging with conventional fluorescent probes". In: Angewandte Chemie-International Edition 47.33 (2008).

[49] Samuel T Hess, Thanu PK Girirajan, and Michael D Mason. "Ultra-high resolution imaging by fluorescence photoactivation localization microscopy". In: Biophysical journal 91.11 (2006), pp. 4258–4272.

[50] Angélique Jimenez, Karoline Friedl, and Christophe Leterrier. "About samples, giving examples: optimized single molecule localization microscopy". In: Methods 174 (2020), pp. 100–114.

[51] William E Moerner and Lothar Kador. "Optical detection and spectroscopy of single molecules in a solid". In: Physical review letters 62.21 (1989), p. 2535.

[52] Eric Betzig et al. "Imaging intracellular fluorescent proteins at nanometer resolution". In: science 313.5793 (2006), pp. 1642–1645.

[53] Andrew J Berglund et al. "Fast, bias-free algorithm for tracking single particles with variable size and shape". In: Optics express 16.18 (2008), pp. 14064–14075.

[54] Raghuveer Parthasarathy. "Rapid, accurate particle tracking by calculation of radial symmetry centers". In: Nature methods 9.7 (2012), pp. 724–726.

[55] Anish V Abraham et al. "Quantitative study of single molecule location estimation techniques". In: Optics express 17.26 (2009), pp. 23352–23373.

[56] Sjoerd Stallinga and Bernd Rieger. "Accuracy of the Gaussian point spread function model in 2D localization microscopy". In: Optics express 18.24 (2010), pp. 24461–24476.

[57] Russell E Thompson, Daniel R Larson, and Watt W Webb. "Precise nanometer localization analysis for individual fluorescent probes". In: Biophysical journal 82.5 (2002), pp. 2775–2783.

[58] Ismail M Khater, Ivan Robert Nabi, and Ghassan Hamarneh. "A review of super-resolution single-molecule localization microscopy cluster analysis and quantification methods". In: Patterns 1.3 (2020).

[59] Steven M Kay. Fundamentals of Statistical Signal Processing: Estimation Theory. 1993.

[60] Carlas S Smith et al. "Fast, single-molecule localization that achieves theoretically minimum uncertainty". In: Nature methods 7.5 (2010), pp. 373–375.

[61] EAK Cohen, D Kim, and RJ Ober. "Cramer-Rao lower bound for point based image registration with heteroscedastic error model for application in single molecule microscopy". In: IEEE transactions on medical imaging 34.12 (2015), pp. 2632–2644.

[62] Joerg Schnitzbauer et al. "Super-resolution microscopy with DNA-PAINT". In: Nature protocols 12.6 (2017), pp. 1198–1228.

[63] Lexy von Diezmann, Yoav Shechtman, and WE Moerner. "Three-dimensional localization of single molecules for super-resolution imaging and single-particle tracking". In: Chemical reviews 117.11 (2017), pp. 7244–7275.

[64] Michael Speidel, Alexandr Jonáš, and Ernst-Ludwig Florin. "Three-dimensional tracking of fluorescent nanoparticles with subnanometer precision by use of off-focus imaging". In: Optics letters 28.2 (2003), pp. 69–71.

[65] Sripad Ram et al. "3D single molecule tracking with multifocal plane microscopy reveals rapid intercellular transferrin transport at epithelial cell barriers". In: Biophysical journal 103.7 (2012), pp. 1594–1603.

[66] Sripad Ram et al. "High accuracy 3D quantum dot tracking with multifocal plane microscopy for the study of fast intracellular dynamics in live cells". In: Biophysical journal 95.12 (2008), pp. 6025–6043.

[67] Paul A Dalgarno et al. "Multiplane imaging and three dimensional nanoscale particle tracking in biological microscopy". In: Optics express 18.2 (2010), pp. 877–884.

[68] Sri Rama Prasanna Pavani et al. "Three-dimensional, single-molecule fluorescence imaging beyond the diffraction limit by using a double-helix point spread function". In: Proceedings of the National Academ 106.9 (2009), pp. 2995–2999.

[69] Elias Nehme et al. "DeepSTORM3D: dense 3D localization microscopy and PSF design by deep learning". In: Nature methods 17.7 (2020), pp. 734–740.

[70] Yoav Shechtman et al. "Precise three-dimensional scan-free multiple-particle tracking over large axial ranges with tetrapod point spread functions". In: Nano letters 15.6 (2015), pp. 4194–4199.

[71] MA Neil, R Juškaitis, and T Wilson. "Method of obtaining optical sectioning by using structured light in a conventional microscope". In: Optics letters 22.24 (1997), pp. 1905–1907.

[72] MA Neil and R Juškaitis. "A light efficient optically sectioning microscope". In: Journal of Microscopy 189.2 (1998), pp. 114–117.

[73] R Heintzmann and CG Cremer. "Laterally modulated excitation microscopy: improvement of resolution by using a diffraction grating". In: Optical biopsies and microscopic techniques III. Vol. 3568. SPIE. 1999, pp. 185–196.

[74] P Kner et al. "Super-resolution video microscopy of live cells by structured illumination". In: Nature methods 6.5 (2009), pp. 339–342.

[75] D Li et al. “Extended-resolution structured illumination imaging of endocytic and cytoskeletal dynamics”. In: Science 349.6251 (2015), aab3500.

[76] BC Chen et al. “Lattice light-sheet microscopy: imaging molecules to embryos at high spatiotemporal resolution”. In: Science 346.6208 (2014), p. 1257998.

[77] J Mertz and J Kim. “Scanning light-sheet microscopy in the whole mouse brain with HiLo background rejection”. In: Journal of biomedical optics 15.1 (2010), pp. 016027–016027-7.

[78] AN Kapanidis and T Strick. “Biology, one molecule at a time”. In: Trends in biochemical sciences 34.5 (2009), pp. 234–243.

[79] D Gabor. “A new microscopic principle”. In: Nature 161.4098 (1948), pp. 777–778.

[80] D Gabor. “Holography, 1948-1971”. In: Science 177.4046 (1972), pp. 299–313.

[81] J Rosen and G Brooker. “Fresnel incoherent correlation holography (FINCH): a review of research”. In: Advanced Optical Technologies 1.3 (2012), pp. 151–169.

[82] J Rosen, R Kelner, and Y Kashter. “Recent advances in self-interference incoherent digital holography”. In: Advances in Optics and Photonics 11.1 (2019), pp. 1–66.

[83] J Rosen et al. “Roadmap on recent progress in FINCH technology”. In: Journal of Imaging 7.10 (2021), p. 197.

[84] A Marar and P Kner. “Three-dimensional nanoscale localization of point-like objects using self-interference digital holography”. In: Optics letters 45.2 (2020), pp. 591–594.

[85] A Marar and P Kner. “Fundamental precision bounds for three-dimensional optical localization microscopy using self-interference digital holography”. In: Biomedical Optics Express 12.1 (2021), pp. 20–40.

[86] Y Zhou and G Carles. “Precise 3D particle localization over large axial ranges using secondary astigmatism”. In: Optics Letters 45.8 (2020), pp. 2466–2469.

[87] S Li and P Kner. “Optimizing self-interference digital holography for single-molecule localization”. In: Optics Express 31.18 (2023), pp. 29352–29367.

[88] D Débarre, MJ Booth, and T Wilson. “Image based adaptive optics through optimisation of low spatial frequencies”. In: Optics Express 15.13 (2007), pp. 8176–8190.

[89] N Ji. “Adaptive optical fluorescence microscopy”. In: Nature methods 14.4 (2017), pp. 374–380.

[90] N Ji, DE Milkie, and E Betzig. “Adaptive optics via pupil segmentation for high-resolution imaging in biological tissues”. In: Nature methods 7.2 (2010), pp. 141–147.

[91] William J Tango. “The circle polynomials of Zernike and their application in optics”. In: Applied physics 13 (1977), pp. 327–332.

[92] Changwon Jang et al. “Holographic fluorescence microscopy with incoherent digital holographic adaptive optics”. In: Journal of biomedical optics 20.11 (2015), pp. 111204–111204.

[93] Changgeng Liu, Xiao Yu, and Myung K Kim. "Fourier transform digital holographic adaptive optics imaging system". In: Applied optics 51.35 (2012), p. 8449.

[94] Travis J Gould et al. "Adaptive optics enables 3D STED microscopy in aberrating specimens". In: Optics express 20.19 (2012), pp. 20998–21009.

[95] Tianlong Man et al. "Adaptive optics via self-interference digital holography for non-scanning three-dimensional imaging in biological samples". In: Biomedical Optics Express 9.6 (2018), pp. 2614–2626.

[96] Rainer Heintzmann and Thomas Huser. "Super-resolution structured illumination microscopy". In: Chemical reviews 117.23 (2017), pp. 13890–13908.

[97] Mats GL Gustafsson. "Nonlinear structured-illumination microscopy: wide-field fluorescence imaging with theoretically unlimited resolution". In: Proceedings of the National Academy of Sciences 102.37 (2005), pp. 13081–13086.

[98] E Hesper Rego et al. "Nonlinear structured-illumination microscopy with a photoswitchable protein reveals cellular structures at 50-nm resolution". In: Proceedings of the National Academy of Sciences 109.3 (2012), E135–E143.

[99] Martin Andresen et al. "Structure and mechanism of the reversible photoswitch of a fluorescent protein". In: Proceedings of the National Academy of Sciences 102.37 (2005), pp. 13070–13074.

[100] Satoshi Habuchi et al. "Reversible single-molecule photoswitching in the GFP-like fluorescent protein Dronpa". In: Proceedings of the National Academy of Sciences 102.27 (2005), pp. 9511–9516.

[101] Martin Andresen et al. "Photoswitchable fluorescent proteins enable monochromatic multilabel imaging and dual color fluorescence nanoscopy". In: Nature biotechnology 26.9 (2008), pp. 1035–1040.

[102] Hui-Wen Lu-Walther et al. "Nonlinear structured illumination using a fluorescent protein activating at the readout wavelength". In: PLoS One 11.10 (2016), e0165148.

[103] Amit Lal, Chunyan Shan, and Peng Xi. "Structured illumination microscopy image reconstruction algorithm". In: IEEE Journal of Selected Topics in Quantum Electronics 22.4 (2016), pp. 50–63.

[104] Xi Zhang et al. "Highly photostable, reversibly photoswitchable fluorescent protein with high contrast ratio for live-cell superresolution microscopy". In: Proceedings of the National Academy of Sciences 113.37 (2016), pp. 10364–10369.

[105] Laurence J Young, Florian Ströhl, and Clemens F Kaminski. "A guide to structured illumination TIRF microscopy at high speed with multiple colors". In: JoVE (Journal of Visualized Experiments) 111 (2016), e53988.

[106] Reto Fiolka, Markus Beck, and Andreas Stemmer. "Structured illumination in total internal reflection fluorescence microscopy using a spatial light modulator". In: Optics letters 33.14 (2008), pp. 1629–1631.

[107] Dominique Bourgeois and Virgile Adam. "Reversible photoswitching in fluorescent proteins: a mechanistic view". In: IUBMB life 64.6 (2012), pp. 482–491.

[108] Steffen J. Sahl et al. "Comment on "Extended-resolution structured illumination imaging of endocytic and cytoskeletal dynamics"". In: Science 352.6285 (2016), pp. 527–527. DOI: 10.1126/science.aad7983.

[109] Anna-Karin Gustavsson et al. "3D single-molecule super-resolution microscopy with a tilted light sheet". In: Nature communications 9.1 (2018), p. 123.

[110] Joseph Rosen and Gary Brooker. "Digital spatially incoherent Fresnel holography". In: Optics letters 32.8 (2007), pp. 912–914.

[111] Shaoheng Li and Peter Kner. SIDH-STD. https://github.com/Knerlab/SIDH_STD. GitHub repository. 2023.

[112] Petr Bouchal et al. "Point spread function and two-point resolution in Fresnel incoherent correlation holography". In: Optics Express 19.16 (2011), pp. 15603–15620.

[113] Nisan Siegel, Joseph Rosen, and Gary Brooker. "Reconstruction of objects above and below the objective focal plane with dimensional fidelity by FINCH fluorescence microscopy". In: Optics express 20.18 (2012), pp. 19822–19835.

[114] Martin J Booth. "Adaptive optics in microscopy". In: Philosophical Transactions of the Royal Society A: Mathen 365.1861 (2007), pp. 2829–2843.

[115] Daniel Burke et al. "Adaptive optics correction of specimen-induced aberrations in single-molecule switching microscopy". In: Optica 2.2 (2015), pp. 177–185.

[116] Peter Kner et al. "High-resolution wide-field microscopy with adaptive optics for spherical aberration correction and motionless focusing". In: Journal of microscopy 237.2 (2010), pp. 136–147.

[117] Delphine Débarre et al. "Image-based adaptive optics for two-photon microscopy". In: Optics letters 34.16 (2009), pp. 2495–2497.

[118] Kayvan F Tehrani et al. "Adaptive optics stochastic optical reconstruction microscopy (AO-STORM) using a genetic algorithm". In: Optics express 23.10 (2015), pp. 13677–13692.

[119] Martin Booth et al. "Aberrations and adaptive optics in super-resolution microscopy". In: Microscopy 64.4 (2015), pp. 251–261.

[120] Joseph Rosen et al. "Roadmap on computational methods in optical imaging and holography". In: Applied Physics B 130.9 (2024), p. 166.

[121] Mantas Žurauskas et al. "IsoSense: frequency enhanced sensorless adaptive optics through structured illumination". In: Optica 6.3 (2019), pp. 370–379.

[122] Ruizhe Lin et al. “Subcellular three-dimensional imaging deep through multicellular thick samples by structured illumination microscopy and adaptive optics”. In: Nature communications 12.1 (2021), p. 3148.

[123] Shaoheng Li and Peter Kner. SIDH_SensorlessAO. `https://github.com/Knerlab/SIDH_SensorlessAO.git`. GitHub repository. 2024.

[124] Robert J Noll. “Zernike polynomials and atmospheric turbulence”. In: JOsA 66.3 (1976), pp. 207–211.

[125] Tim Grotjohann et al. “rsEGFP2 enables fast RESOLFT nanoscopy of living cells”. In: Elife 1 (2012), e00248.

[126] Yuting Guo et al. “Visualizing intracellular organelle and cytoskeletal interactions at nanoscale resolution on millisecond timescales”. In: Cell 175.5 (2018), pp. 1430–1442.

[127] Marcel Müller et al. “Open-source image reconstruction of super-resolution structured illumination microscopy data in ImageJ”. In: Nature communications 7.1 (2016), p. 10980.

[128] Erik Bélanger et al. “Maintaining polarization in polarimetric multiphoton microscopy”. In: Journal of Biophotonics 8.11-12 (2015), pp. 884–888.

[129] Lin Shao et al. “Super-resolution 3D microscopy of live whole cells using structured illumination”. In: Nature methods 8.12 (2011), pp. 1044–1046.

[130] Meiqi Li et al. “Structured illumination microscopy using digital micro-mirror device and coherent light source”. In: Applied Physics Letters 116.23 (2020).

[131] Yuheng Wang et al. “Unsupervised Deep Learning Enables 3D Imaging for Single-Shot Incoherent Holography”. In: Laser & Photonics Reviews (2024), p. 2301091.

[132] Huiyang Wang et al. “Single-shot Fresnel incoherent correlation holography based on digital self-calibrated point source holograms”. In: Optics and Lasers in Engineering 184 (2025), p. 108616.

[133] Yuhong Wan et al. “Three-dimensional tracking of dynamic nanoparticles based on direct correlation method in fluorescence self-interference microscopy”. In: Optics and Lasers in Engineering 178 (2024), p. 108126.

[134] Lothar Schermelleh et al. “Subdiffraction multicolor imaging of the nuclear periphery with 3D structured illumination microscopy”. In: science 320.5881 (2008), pp. 1332–1336.

[135] Delphine Débarre et al. “Adaptive optics for structured illumination microscopy”. In: Optics express 16.13 (2008), pp. 9290–9305.

[136] Benjamin Thomas et al. “Enhanced resolution through thick tissue with structured illumination and adaptive optics”. In: Journal of biomedical optics 20.2 (2015), pp. 026006–026006.

Appendix A

rsEGFP2 U2OS Sample Preparation Protocol

Materials:

1. 35mm iBidi dish (Coated with1000ul of 0.1% PBS diluted fibronectin human plasma for 24hours at room temperature)
2. T25 Cell culture flasks
3. Dulbecco's Modified Eagle Medium (DMEM) with high glucose
4. Fetal Bovine Serum (FBS)
5. Penicillin-Streptomycin (Pen-Strep)
6. 1x Phosphate-Buffered Saline (PBS)
7. 1x Trypsin-EDTA solution
8. Paraformaldehyde (PFA), 4% (wt/vol) in PBS
9. 5ml Centrifuge tubes
10. Opti-MEM medium
11. PEI reagent
12. rsEGFP2 plasmid DNA
13. U2OS cells

Prepare the culture medium (D10) Mix 500ml DMEM + 50ml FBS (10%) + 5ml penicillin-streptomycin (1%). Store at $4°C$.

Thawing U2OS Cells

1. Take out the U2OS stock vial from liquid nitrogen and thaw it at room temperature.
2. Re-suspend thawed cells in 1000 ul growth media and transfer cells into 25ml cell culture flasks.
3. Cells are grown in a $37°C$ incubator with humidified atmosphere of 5% CO2.

Subculturing of U2OS Cells

- Aspirate growth media from the cell culture flask.
- Remove the culture medium and rinse the cells with sterile PBS.
- Add 500μl of Trypsin-EDTA solution and allow the cells to incubate in the $37°C$ incubator until cells detach (approximately 5min).
- Add 2000 μl of fresh growth media to neutralize the trypsin and collect cells in a centrifuge tube (the ratio of Trypsin-EDTA solution and growth media is 1:4).
- Spin at 1500 rpm for 5 minutes.
- Aspirate supernatant and add 1000 μl fresh growth media to resuspend the cells.
- Transfer 15μl cell suspension liquid (about 10^-6 concentration) to a new culture flask with 5000ul fresh medium and place in a $37°C$ incubator at 5% CO2.

Freezing of U2OS Cells

- Aspirate growth media from the cell culture flask.
- Add 500ul of Trypsin-EDTA solution and incubate in the 37°C incubator until cells detach.
- Add 2000ul of growth media with 5% DMSO and collect cells in a centrifuge tube.
- Spin at 1500 rpm for 5 minutes.
- Aspirate supernatant and re-suspend cells in growth media with 5% DMSO.
- Transfer cells to cryovials and store in liquid nitrogen.

rsEGFP2 U2OS cell transfection protocol

- Use 1000ul of 0.1% PBS diluted fibronectin human plasma to coat the 35mm iBidi dish for 30min at room temperature.
- Aspirate the fibronectin human plasma and make U2OS cell suspension liquid into iBidi dish with fresh D10 as concentration of 10^{-2} and plate the cells in a $37°C$ incubator at 5% CO2 for 18-24hours before transfection. An appropriate seeding density should be used so the cell culture plate is 90-95% confluent at the time of transfection.

- Rinse the cells with sterile PBS to remove residual culture media, add 1000ul fresh growth medium.
- Tube A: Prepare plasmid DNA by diluting 3 µg of plasmid DNA in 50 μl of Opti-MEM medium in a sterile tube.
- Tube B: Prepare transfection reagent by adding 6 μl of PEI to 50 μl of Opti-MEM medium in a sterile tube. Vortex gently.
- Add the transfection reagent solution (tube B) to the tube containing plasmid DNA (tube A), and vortex immediately. Spin down gently and allow the complexes to form for 10 minutes at room temperature.
- Add 100 µL of the complex mixture (tube A+B), drop-wise, to each dish containing cells and medium. Mix gently by swirling the plate. Incubate the cells at $37°C$ incubator at 5% CO2 for 24 hours.
- Aspirate the growth media from the dish. Add the fixation solution to the cells and incubate for 15 minutes at 37°C to fix the cells.
- Image cells in 12 hours after the fixation.

Appendix B

STORM Buffer Preparation Protocol

Materials:

1. MEA: Cysteamine (Sigma, #30070-10G) - store at $4°C$ (not for Alexa 647 or CF 647)
2. BME: 2-Mercaptoethanol (Sigma, #63689-25ML-F) - store at $4°C$
3. Glucose oxidase type seven from *Aspergillus* (Sigma, #G2133-50KU) - store at $-20°C$
4. Catalase from Bovine liver C40-100 mg (Sigma) - store at $-20°C$
5. Tris-HCl, 1 M Solution, pH 8.0 (Affymetrix / USB, #22638 500 ML) - store at room temperature
6. Sodium Chloride (NaCl) (Sigma, #S7653-250G) - store at room temperature
7. D-Glucose (Sigma, #G8270-1KG) - store at room temperature

Preparation Protocol using MEA

1. Buffer A: 50 mM Tris-HCl (pH 8.0) + 10 mM NaCl. Store at room temperature.
2. Buffer B: 50 mM Tris-HCl (pH 8.0) + 10 mM NaCl + 10% (w/v) glucose - store at $4°C$.
3. 1 M MEA: 77 mg MEA dissolved in 1 mL Buffer A. Store at $4°C$.
4. GLOX solution: Glucose oxidase + catalase mixture dissolved in Buffer A. Store at $4°C$.

   (When making GLOX solution, calculate the amount to add based on the active units (AU) since not all the protein in the bottle is active. Both the Catalase and Glucose from Sigma should have the information written on the tube. For 50x stock of GLOX solution, mix 8440 AU Gluox + 70200 AU Catalase into 1 mL of 50 mM Tris + 10 mM NaCl (pH 8.0) and vortex.)

5. **1 ml Imaging buffer:** (Mix the following in a 1.5 ml centrifuge tube and vortex.)
    - 50 μL of 1 M MEA or 50 μL of 1 M BME
    - 20 μL of 50x GLOX solution
    - 930 μL of Buffer B

Preparation Protocol using BME

1. Prepare 1000 μl 50 mM Tris-HCl: 500 μl DI Water + 500 μl 1M Tris-HCl
2. Prepare 1000 μl 10 mM NaCl: 0.05844 g NaCl + 1000 μl water
3. Prepare 1000 μl 10% glucose: 0.1 g glucose + 1000 μl DI Water
4. Prepare 50 μl 1M BME: 3.49 μl 1M BME + 50 μl DI Water
5. 1 ml Tube A: 500 μl DI Water + 500 μl 1M Tris-HCl + 0.05844 g NaCl
6. 1 ml Tube B: 500 μl DI Water + 500 μl 1M Tris-HCl + 0.05844 g NaCl + 0.1 g glucose
7. 500 μl GLOX solution: 500 μl Tube A + 3.51 mg Catalase + 0.422 mg GLUOX
8. 50 μl 1M BME: 3.49 μl 1M BME + 50 μl DI Water
9. **1 ml Imaging buffer:** 50 μl 1M BME + 20 μl GLOX solution + 930 μl Tube B

Final buffer can be used at room temperature imaging for approximately 2 hours.

Appendix C

Numerical Derivation of SIDH

The derivation is based on wave optics, with the definitions of the operators provided in Appendix 4. The colored terms highlight the component currently being derived, enhancing readability and clarity.

As mentioned in Section 2.2, the intensity profile of the recorded hologram at the digital camera plane (for SIDH configuration 1) can be expressed as:

$$\begin{aligned} I_c(x,y) = \Bigg| C_1(\mathbf{r}_s) L\left(-\frac{\mathbf{r}_s}{z_s}\right) Q\left(\frac{1}{z_s}\right) Q\left(-\frac{1}{f_o}\right) \otimes \\ Q\left(\frac{1}{d_1}\right) \left[\frac{1}{2} + \frac{1}{2}\exp(i\theta) Q\left(-\frac{1}{f_d}\right)\right] \otimes Q\left(\frac{1}{z_h}\right) \Bigg|^2 \end{aligned} \tag{C.1}$$

As:

$$\begin{aligned} Q\left(\frac{1}{z_s}\right) Q\left(-\frac{1}{f_o}\right) &= Q\left(\frac{1}{z_s} - \frac{1}{f_o}\right) \\ &= Q\left(\frac{f_o - z_s}{z_s f_o}\right) \end{aligned} \tag{C.2}$$

Let $f_e = \frac{z_s f_o}{f_o - z_s}$, then $Q\left(\frac{1}{f_e}\right) = Q\left(\frac{1}{z_s}\right) Q\left(-\frac{1}{f_o}\right)$, Equation 1.1 can be written as:

$$\begin{aligned} I_c(x,y) = \Bigg| C_1(\mathbf{r}_s) L\left(-\frac{\mathbf{r}_s}{z_s}\right) Q\left(\frac{1}{f_e}\right) \otimes Q\left(\frac{1}{d_1}\right) \\ \left[\frac{1}{2} + \frac{1}{2}\exp(i\theta) Q\left(-\frac{1}{f_d}\right)\right] \otimes Q\left(\frac{1}{z_h}\right) \Bigg|^2 \end{aligned} \tag{C.3}$$

As $\mathbf{r_s} = (x_s, y_s)$, if I define:

$$\mathbf{r'_s} \equiv \frac{\mathbf{r_s}}{z_s} = \left(\frac{x_s}{z_s}, \frac{y_s}{z_s}\right) \equiv (x'_s, y'_s) \tag{C.4}$$

then $C_1(\mathbf{r}_s)L\left(-\frac{\mathbf{r}_s}{z_s}\right)Q\left(\frac{1}{f_e}\right)\otimes Q\left(\frac{1}{d_1}\right)$ can be written as:

$$
\begin{aligned}
&C_1(\mathbf{r}_s)L\left(-\frac{\mathbf{r}_s}{z_s}\right)Q\left(\frac{1}{f_e}\right)\otimes Q\left(\frac{1}{d_1}\right)\\
&\quad= C_1(\mathbf{r_s})L(-\mathbf{r'_s})Q\left(\frac{1}{f_e}\right)\otimes Q\left(\frac{1}{d_1}\right)\\
&\quad= \int_{-\infty}^{+\infty}\int_{-\infty}^{+\infty} C_1(\mathbf{r_s})\exp\left[-\frac{i\pi}{\lambda}\left(2x'_st_x+2y'_st_y\right)\right.\\
&\quad\left.+\frac{i\pi}{\lambda}\left(\frac{1}{f_e}\right)\left(t_x^2+t_y^2\right)+\frac{i\pi}{\lambda}\left(\frac{1}{d_1}\right)\left((x-t_x)^2+(y-t_y)^2\right)\right]dt_xdt_y\\
&\quad= C_1(\mathbf{r_s})\int_{-\infty}^{+\infty}\int_{-\infty}^{+\infty}\exp\left[\frac{i\pi}{\lambda}\left(\frac{1}{f_e}+\frac{1}{d_1}\right)\left(t_x^2+t_y^2\right)\right.\\
&\quad\left.-\frac{i\pi}{\lambda}(2x'_st_x+2y'_st_y)-\frac{i\pi}{\lambda}\frac{1}{d_1}(2xt_x+2yt_y)+\frac{i\pi}{\lambda}\frac{1}{d_1}(x^2+y^2)\right]dt_xdt_y\\
&\quad= C_1(\mathbf{r_s})\exp\left[\frac{i\pi}{\lambda}\left(\frac{1}{d_1}\right)(x^2+y^2)\right]\int_{-\infty}^{+\infty}\int_{-\infty}^{+\infty}\exp\left[\frac{i\pi}{\lambda}\left(\frac{1}{f_e}+\frac{1}{d_1}\right)\left(t_x^2+t_y^2\right)\right.\\
&\quad\left.-\frac{i\pi}{\lambda}(2x'_st_x+2y'_st_y)-\frac{i\pi}{\lambda}\left(\frac{1}{d_1}\right)(2xt_x+2yt_y)\right]dt_xdt_y\\
&\quad= C_1(\mathbf{r_s})Q\left(\frac{1}{d_1}\right)\int_{-\infty}^{+\infty}\int_{-\infty}^{+\infty}\exp\left[\frac{i\pi}{\lambda}\left(\left(\frac{1}{f_e}+\frac{1}{d_1}\right)\left(t_x^2+t_y^2\right)\right.\right.\\
&\quad\left.\left.-(2x'_st_x+2y'_st_y)-\left(\frac{1}{d_1}\right)(2xt_x+2yt_y)\right)\right]dt_xdt_y\\
&\quad= C_1(\mathbf{r_s})Q\left(\frac{1}{d_1}\right)\int_{-\infty}^{+\infty}\int_{-\infty}^{+\infty}\exp\left[\frac{i\pi}{\lambda}\left(\left(\frac{1}{f_e}+\frac{1}{d_1}\right)\left(t_x^2+t_y^2\right)\right.\right.\\
&\quad\left.\left.-t_x\left(2x'_s-\frac{2x}{d_1}\right)-t_y\left(2y'_s-\frac{2y}{d_1}\right)\right)\right]dt_xdt_y
\end{aligned}
\tag{C.5}
$$

if I define:

$$\frac{1}{f_ed}\equiv\frac{1}{f_e}+\frac{1}{f_1}$$

then equation 1.5 can be expressed as:

$$
\begin{aligned}
&C_1(\mathbf{r}_s)L\left(-\frac{\mathbf{r}_s}{z_s}\right)Q\left(\frac{1}{f_e}\right)\otimes Q\left(\frac{1}{d_1}\right)\\
&\quad= C_1(\mathbf{r_s})Q\left(\frac{1}{d_1}\right)\int_{-\infty}^{+\infty}\int_{-\infty}^{+\infty}\exp\left[\frac{i\pi}{\lambda}\left(\frac{1}{f_{ed}}\right)(t_x^2+t_y^2)\right.\\
&\quad\left.-\frac{i\pi}{\lambda}\left(2t_x(x_s'+\frac{x}{d_1})+2t_y(y_s'+\frac{y}{d_1})\right)\right]dt_xdt_y\\
&\quad= C_1(\mathbf{r_s})Q\left(\frac{1}{d_1}\right)\int_{-\infty}^{+\infty}\int_{-\infty}^{+\infty}\exp\left[\frac{i\pi}{\lambda}\frac{1}{f_{ed}}\left(t_x^2-2f_{ed}(x_s'+\frac{x}{d_1})t_x\right.\right.\\
&\quad+(f_{ed}(x_s'+\frac{x}{d_1}))^2+t_y^2-2f_{ed}(y_s'+\frac{y}{d_1})t_y+(f_{ed}(y_s'+\frac{y}{d_1}))^2\\
&\quad\left.\left.-(f_{ed}(x_s'+\frac{x}{d_1}))^2-(f_{ed}(y_s'-\frac{y}{d_1}))^2\right)\right]dt_xdt_y\\
&\quad= C_1(\mathbf{r_s})Q\left(\frac{1}{d_1}\right)\exp\left[-\frac{i\pi}{\lambda}\left(f_{ed}x_s'^2+2f_{ed}\frac{x}{d_1}x_s'+f_{ed}\frac{x^2}{d_1^2}+f_{ed}y_s'^2+2f_{ed}\frac{y}{d_1}y_s'+f_{ed}\frac{y^2}{d_1^2}\right)\right]\\
&\quad\int_{-\infty}^{+\infty}\int_{-\infty}^{+\infty}\exp\left[\frac{i\pi}{\lambda}\frac{1}{f_{ed}}\left(\left(t_x-f_{ed}\left(x_s'+\frac{x}{d_1}\right)\right)^2+\left(t_y-f_{ed}\left(y_s'+\frac{y}{d_1}\right)\right)^2\right)\right]dt_xdt_y\\
&\quad= C_1(\mathbf{r_s})Q\left(\frac{1}{d_1}\right)\exp\left[-\frac{i\pi}{\lambda}f_{ed}\left(x_s'^2+y_s'^2\right)\right]\exp\left[-\frac{i2\pi}{\lambda}\left(\frac{f_{ed}}{d_1}x_s'x+\frac{f_{ed}}{d_1}y_s'y\right)\right]\\
&\quad\exp\left[-\frac{i\pi}{\lambda d_1^2}f_{ed}\left(x^2+y^2\right)\right]\int_{-\infty}^{+\infty}\int_{-\infty}^{+\infty}\exp\left[\frac{i\pi}{\lambda}\frac{1}{f_{ed}}\left(\left(t_x-f_{ed}\left(x_s'+\frac{x}{d_1}\right)\right)^2\right.\right.\\
&\quad\left.\left.+\left(t_y-f_{ed}\left(y_s'+\frac{y}{d_1}\right)\right)^2\right)\right]dt_xdt_y\\
&\quad= C_1(\mathbf{r_s})\exp\left[-\frac{i\pi}{\lambda}f_{ed}\left(x_s'^2+y_s'^2\right)\right]Q\left(\frac{1}{d_1}\right)L\left(-f_{ed}\frac{1}{d_1}\mathbf{r_s'}\right)Q\left(-f_{ed}\frac{1}{d_1^2}\right)\\
&\quad\int_{-\infty}^{+\infty}\int_{-\infty}^{+\infty}\exp\left[\frac{i\pi}{\lambda}\frac{1}{f_{ed}}\left(\left(t_x-f_{ed}\left(x_s'+\frac{x}{d_1}\right)\right)^2+\left(t_y-f_{ed}\left(y_s'+\frac{y}{d_1}\right)\right)^2\right)\right]dt_xdt_y\\
&\quad= C_1(\mathbf{r_s})\exp\left[-\frac{i\pi}{\lambda}f_{ed}\left(x_s'^2+y_s'^2\right)\right]Q\left(\frac{1}{d_1}-f_{ed}\frac{1}{d_1^2}\right)L\left(-f_{ed}\frac{1}{d_1}\mathbf{r_s'}\right)\\
&\quad\int_{-\infty}^{+\infty}\int_{-\infty}^{+\infty}\exp\left[\frac{i\pi}{\lambda}\frac{1}{f_{ed}}\left(\left(t_x-f_{ed}\left(x_s'+\frac{x}{d_1}\right)\right)^2+\left(t_y-f_{ed}\left(y_s'+\frac{y}{d_1}\right)\right)^2\right)\right]dt_xdt_y
\end{aligned}
\tag{C.6}
$$

As:

$$\frac{1}{f_{ed}}=\frac{1}{f_e}+\frac{1}{d_1}=\frac{f_e+d_1}{f_ed_1},\quad\text{and}\quad\mathbf{r_s'}=\frac{\mathbf{r_s}}{z_s}$$

then Equaiton 1.6 can be expressed as:

$$
\begin{aligned}
&C_1(\mathbf{r}_s)L\left(-\frac{\mathbf{r}_s}{z_s}\right)Q\left(\frac{1}{f_e}\right)\otimes Q\left(\frac{1}{d_1}\right)\\
&\quad= C_1(\mathbf{r_s})\exp\left[-\frac{i\pi}{\lambda}f_{ed}(x_s'^2+y_s'^2)\right]Q\left(\frac{1}{d_1}-\frac{f_e d_1}{f_e+d_1}\frac{1}{d_1^2}\right)\\
&\quad\quad L\left(-\frac{\mathbf{r_s}}{z_s}\frac{f_e}{f_e+d_1}\right)\int_{-\infty}^{+\infty}\int_{-\infty}^{+\infty}\exp\left[\frac{i\pi}{\lambda}\frac{1}{f_{ed}}\left(\left(t_x-f_{ed}\left(x_s'+\frac{x}{d_1}\right)\right)^2\right.\right.\\
&\quad\quad\left.\left.+\left(t_y-f_{ed}\left(y_s'+\frac{y}{d_1}\right)\right)^2\right)\right]dt_x dt_y\\
&\quad= C_1(\mathbf{r_s})\exp\left[-\frac{i\pi}{\lambda}f_{ed}(x_s'^2+y_s'^2)\right]Q\left(\frac{1}{f_e+d_1}\right)L\left(-\frac{\mathbf{r_s}}{z_s}\frac{f_e}{f_e+d_1}\right)\\
&\quad\quad\int_{-\infty}^{+\infty}\int_{-\infty}^{+\infty}\exp\left[\frac{i\pi}{\lambda}\frac{1}{f_{ed}}\left(\left(t_x-f_{ed}\left(x_s'+\frac{x}{d_1}\right)\right)^2\right.\right.\\
&\quad\quad\left.\left.+\left(t_y-f_{ed}\left(y_s'+\frac{y}{d_1}\right)\right)^2\right)\right]dt_x dt_y
\end{aligned}
\tag{C.7}
$$

If I define:

$$
t_x' \equiv t_x - f_{ed}\left(x_s'+\frac{x}{d_1}\right),\quad t_y' \equiv t_y - f_{ed}\left(y_s'+\frac{y}{d_1}\right)
$$

then:

$$
dt_x' = d\left(t_x - f_{ed}\left(x_s'+\frac{x}{d_1}\right)\right) = dt_x,\quad dt_y' = d\left(t_y - f_{ed}\left(y_s'+\frac{y}{d_1}\right)\right) = dt_y
$$

therefore, Equation 1.7 can be expressed as:

$$
\begin{aligned}
&C_1(\mathbf{r}_s)L\left(-\frac{\mathbf{r}_s}{z_s}\right)Q\left(\frac{1}{f_e}\right)\otimes Q\left(\frac{1}{d_1}\right)\\
&\quad= C_1(\mathbf{r_s})\exp\left[-\frac{i\pi}{\lambda}f_{ed}(x_s'^2+y_s'^2)\right]Q\left(\frac{1}{f_e+d_1}\right)L\left(-\frac{\mathbf{r_s}}{z_s}\frac{f_e}{f_e+d_1}\right)\\
&\quad\quad\int_{-\infty}^{+\infty}\int_{-\infty}^{+\infty}\exp\left[\frac{i\pi}{\lambda}\frac{1}{f_{ed}}\left(t_x'^2+t_y'^2\right)\right]dt_x dt_y
\end{aligned}
\tag{C.8}
$$

Given

$$
t_x'^2 + t_y'^2 = r^2 \quad , \quad dt_x dt_y = r dr d\theta
$$

Then the integral becomes:

$$
\begin{aligned}
&\int_{-\infty}^{+\infty}\int_{-\infty}^{+\infty}\exp\left[\frac{i\pi}{\lambda}\frac{1}{f_{ed}}\left(t_x'^2+t_y'^2\right)\right]dt_x dt_y \\
&=\int_0^{2\pi}\left(\int_0^{\infty}\exp\left[-\frac{i\pi}{\lambda}\frac{1}{f_{ed}}r^2\right]rdr\right)d\theta \\
&=\int_0^{2\pi}\left(\int_0^{\infty}\frac{1}{2}\exp\left[-\frac{i\pi}{\lambda}\frac{1}{f_{ed}}r^2\right]dr^2\right)d\theta \\
&=\int_0^{2\pi}\left(\int_0^{\infty}\frac{1}{2}\exp\left[-\frac{i\pi}{\lambda}\frac{1}{f_{ed}}r^2\right]dr^2\right)d\theta \\
&=\int_0^{2\pi}\left(\frac{1}{2}\frac{\lambda f_{ed}}{i\pi}\right)d\theta \qquad\qquad \left(\text{for}R_e(\frac{i\pi}{\lambda f_{ed}})>0\right) \\
&=\frac{\lambda f_{ed}}{2i\pi}\int_0^{2\pi}d\theta \\
&=\frac{\lambda f_{ed}}{2i\pi}2\pi \\
&=\frac{\lambda f_{ed}}{i} \\
&=-i\lambda f_{ed}
\end{aligned}
\tag{C.9}
$$

Then, Equation 1.7 now becomes:

$$
\begin{aligned}
&C_1(\mathbf{r_s})L\left(-\frac{\mathbf{r}_s}{z_s}\right)Q\left(\frac{1}{f_e}\right)\otimes Q\left(\frac{1}{d_1}\right) \\
&\qquad=C_1(\mathbf{r_s})(-i\lambda f_{ed})\exp\left[-\frac{i\pi}{\lambda}f_{ed}(x_s'^2+y_s'^2)\right]L\left(-\frac{\mathbf{r_s}}{z_s}\frac{f_e}{f_e+d_1}\right)Q\left(\frac{1}{f_e+d_1}\right)
\end{aligned}
\tag{C.10}
$$

If we define a complex constant $C_2(\mathbf{r_s})\equiv C_1(\mathbf{r_s})(-i\lambda f_{ed})\exp\left[-\frac{i\pi}{\lambda}f_{ed}(x_s'^2+y_s'^2)\right]$, then $C_1(\mathbf{r}_s)L\left(-\frac{\mathbf{r}_s}{z_s}\right)Q\left(\frac{1}{f_e}\right)\otimes Q\left(\frac{1}{d_1}\right)$ can now be written as:

$$
\begin{aligned}
&C_1(\mathbf{r}_s)L\left(-\frac{\mathbf{r}_s}{z_s}\right)Q\left(\frac{1}{f_e}\right)\otimes Q\left(\frac{1}{d_1}\right) \\
&\qquad=C_2(\mathbf{r_s})L\left(-\frac{\mathbf{r_s}}{z_s}\frac{f_e}{f_e+d_1}\right)Q\left(\frac{1}{f_e+d_1}\right)
\end{aligned}
\tag{C.11}
$$

Put Equation 1.11 back to Equation 1.4, then the intensity profile of the recorded hologram becomes:

$$
\begin{aligned}
I_c(x,y) = & |C_2(\mathbf{r_s})L\left(-\frac{\mathbf{r_s}}{z_s}\frac{f_e}{f_e+d_1}\right)Q\left(\frac{1}{f_e+d_1}\right) \\
& \left[\frac{1}{2}+\frac{1}{2}\exp(i\theta)Q\left(-\frac{1}{f_d}\right)\right]\otimes Q\left(\frac{1}{z_h}\right)\Bigg|^2 \\
= & |\left(\frac{1}{2}C_2(\mathbf{r_s})L\left(-\frac{\mathbf{r_s}f_e}{z_s(f_e+d_1)}\right)Q\left(\frac{1}{f_e+d_1}\right)\right. \\
& +\frac{1}{2}C_2(\mathbf{r_s})\exp(i\theta)L\left(-\frac{\mathbf{r_s}f_e}{z_s(f_e+d_1)}\right) \\
& \left.Q\left(\frac{1}{f_e+d_1}\right)Q\left(-\frac{1}{f_d}\right)\right)\otimes Q\left(\frac{1}{z_h}\right)|^2 \\
= & |\left(\frac{1}{2}C_2(\mathbf{r_s})L\left(-\frac{\mathbf{r_s}f_e}{z_s(f_e+d_1)}\right)Q\left(\frac{1}{f_e+d_1}\right)\right. \\
& +\frac{1}{2}C_2(\mathbf{r_s})\exp(i\theta)L\left(-\frac{\mathbf{r_s}f_e}{z_s(f_e+d_1)}\right) \\
& \left.Q\left(\frac{1}{f_e+d_1}\right)Q\left(-\frac{1}{f_d}\right)\right)\otimes Q\left(\frac{1}{z_h}\right)|^2 \\
= & |\left(\frac{1}{2}C_2(\mathbf{r_s})L\left(-\frac{\mathbf{r_s}f_e}{z_s(f_e+d_1)}\right)Q\left(\frac{1}{f_e+d_1}\right)\right. \\
& +\frac{1}{2}C_2(\mathbf{r_s})\exp(i\theta)L\left(-\frac{\mathbf{r_s}f_e}{z_s(f_e+d_1)}\right) \\
& \left.Q\left(\frac{1}{f_e+d_1}-\frac{1}{f_d}\right)\right)\otimes Q\left(\frac{1}{z_h}\right)|^2
\end{aligned}
\tag{C.12}
$$

Assume

$$\frac{1}{f_1} \equiv \frac{1}{f_e+d_1}-\frac{1}{f_d}$$

, then:

$$
\begin{aligned}
I_c(x,y) = |\, & \left(\frac{1}{2}C_2(\mathbf{r_s})L\left(-\frac{\mathbf{r_s}f_e}{z_s(f_e+d_1)}\right)Q\left(\frac{1}{f_e+d_1}\right)\right. \\
& +\frac{1}{2}C_2(\mathbf{r_s})\exp(i\theta)L\left(-\frac{\mathbf{r_s}f_e}{z_s(f_e+d_1)}\right) \\
& \left.Q\left(\frac{1}{f_1}\right)\right) \otimes Q\left(\frac{1}{z_h}\right)|^2 \\
= |\, & \frac{1}{2}C_2(\mathbf{r_s})L\left(-\frac{\mathbf{r_s}f_e}{z_s(f_e+d_1)}\right)Q\left(\frac{1}{f_e+d_1}\right)\otimes Q\left(\frac{1}{z_h}\right) \\
& +\frac{1}{2}C_2(\mathbf{r_s})\exp(i\theta)L\left(-\frac{\mathbf{r_s}f_e}{z_s(f_e+d_1)}\right) \\
& Q\left(\frac{1}{f_1}\right)\otimes Q\left(\frac{1}{z_h}\right)|^2
\end{aligned}
\tag{C.13}
$$

Since Equation 1.11 has shown that:

$$
\begin{aligned}
& C_1(\mathbf{r_s})L\left(-\frac{\mathbf{r}_s}{z_s}\right)Q\left(\frac{1}{f_e}\right)\otimes Q\left(\frac{1}{d_1}\right) \\
& \qquad = C_2(\mathbf{r_s})L\left(-\frac{\mathbf{r_s}}{z_s}\frac{f_e}{f_e+d_1}\right)Q\left(\frac{1}{f_e+d_1}\right)
\end{aligned}
\tag{C.14}
$$

Therefore :

$$
\begin{aligned}
& C_2(\mathbf{r_s})L\left(-\frac{\mathbf{r_s}f_e}{z_s(f_e+d_1)}\right)Q\left(\frac{1}{f_e+d_1}\right)\otimes Q\left(\frac{1}{z_h}\right) \\
& = C_3(\mathbf{r_s})L\left(-\frac{\mathbf{r_s}f_e}{z_s(f_e+d_1)}\frac{f_e+d_1}{f_e+d_1+z_h}\right)Q\left(\frac{1}{f_e+d_1+z_h}\right) \\
& = C_3(\mathbf{r_s})L\left(-\frac{\mathbf{r_s}f_e}{z_s(f_e+d_1+z_h)}\right)Q\left(\frac{1}{f_e+d_1+z_h}\right)
\end{aligned}
\tag{C.15}
$$

and,

$$
\begin{aligned}
& C_2(\mathbf{r_s})\exp(i\theta)L\left(-\frac{\mathbf{r_s}f_e}{z_s(f_e+d_1)}\right)Q\left(\frac{1}{f_1}\right)\otimes Q\left(\frac{1}{z_h}\right) \\
& = C_3(\mathbf{r_s})L\left(-\frac{\mathbf{r_s}f_e}{z_s(f_e+d_1)}\frac{f_1}{f_1+z_h}\right)Q\left(\frac{1}{f_1+z_h}\right)
\end{aligned}
\tag{C.16}
$$

Then, Equation 1.13 can be written as:

$$
\begin{aligned}
I_c(x,y) = |&\frac{1}{2}C_3(\mathbf{r_s})L\left(-\frac{\mathbf{r_s}f_e}{z_s(f_e+d_1+z_h)}\right)Q\left(\frac{1}{f_e+d_1+z_h}\right)\\
&+\frac{1}{2}\exp(i\theta)C_3(\mathbf{r_s})L\left(-\frac{\mathbf{r_s}f_e}{z_s(f_e+d_1)}\frac{f_1}{f_1+z_h}\right)Q\left(\frac{1}{f_1+z_h}\right)|^2\\
=|&\left[\frac{1}{2}C_3(\mathbf{r_s})L\left(-\frac{\mathbf{r_s}f_e}{z_s(f_e+d_1+z_h)}\right)Q\left(\frac{1}{f_e+d_1+z_h}\right)\right]\\
&\left[1+\exp(i\theta)L\left(-\frac{\mathbf{r_s}}{z_s}\left(\frac{f_ef_1}{(f_e+d_1)(f_1+z_h)}-\frac{f_e}{f_e+d_1+z_h}\right)\right)\right.\\
&\left.Q\left(\frac{1}{f_1+z_h}-\frac{1}{f_e+d_1+z_h}\right)\right]|^2\\
=|&\left[\frac{1}{2}C_3(\mathbf{r_s})L\left(-\frac{\mathbf{r_s}f_e}{z_s(f_e+d_1+z_h)}\right)Q\left(\frac{1}{f_e+d_1+z_h}\right)\right]\\
&\left[1+\exp(i\theta)L\left(-\frac{\mathbf{r_s}}{z_s}\frac{f_e}{(f_e+d_1)}\left(\frac{f_1}{(f_1+z_h)}-\frac{f_e+d_1}{f_e+d_1+z_h}\right)\right)\right.\\
&\left.Q\left(\frac{1}{f_1+z_h}-\frac{1}{f_e+d_1+z_h}\right)\right]|^2\\
=|&\left[\frac{1}{2}C_3(\mathbf{r_s})L\left(-\frac{\mathbf{r_s}f_e}{z_s(f_e+d_1+z_h)}\right)Q\left(\frac{1}{f_e+d_1+z_h}\right)\right]\\
&\left[1+\exp(i\theta)L\left(-\frac{\mathbf{r_s}}{z_s}\frac{f_e}{(f_e+d_1)}\left(\frac{z_h(f_1-f_e-d_1)}{(f_1+z_h)(f_e+d_1+z_h)}\right)\right)\right.\\
&\left.Q\left(\frac{1}{f_1+z_h}-\frac{1}{f_e+d_1+z_h}\right)\right]|^2
\end{aligned}
\tag{C.17}
$$

Define the reconstruction distance z_r as:

$$
-\frac{1}{z_r}\equiv\frac{1}{f_1+z_h}-\frac{1}{f_e+d_1+z_h}=-\frac{f_1-f_e-d_1}{(f_1+z_h)(f_e+d_q+z_h)}
$$

$$
z_r\equiv\frac{(f_1+z_h)(f_e+d_q+z_h)}{f_1-f_e-d_1}
$$

After simplifying the combined terms and taking the magnitude squared to compute the intensity, the final form Equation 1.17 becomes:

$$
\begin{aligned}
I_c(x,y) = & \left| \left[\frac{1}{2} C_3(\mathbf{r_s}) L \left(-\frac{\mathbf{r_s} f_e}{z_s(f_e + d_1 + z_h)} \right) Q \left(\frac{1}{f_e + d_1 + z_h} \right) \right] \right. \\
& \left. \left[1 + \exp(i\theta) L \left(-\frac{\mathbf{r_s}}{z_s} \frac{f_e}{(f_e + d_1)} \frac{z_h}{z_r} \right) Q \left(-\frac{1}{z_r} \right) \right] \right|^2 \\
= & A_0 \left(2 + \exp \left\{ \frac{i\pi}{\lambda z_r} \left[\left(x - \frac{z_h f_e x_s}{z_s(f_e + d_1)} \right)^2 + \left(y - \frac{z_h f_e y_s}{z_s(f_e + d_1)} \right)^2 \right] + i\theta \right\} \right. \\
& \left. + \exp \left\{ \frac{-i\pi}{\lambda z_r} \left[\left(x - \frac{z_h f_e x_s}{z_s(f_e + d_1)} \right)^2 + \left(y - \frac{z_h f_e y_s}{z_s(f_e + d_1)} \right)^2 \right] - i\theta \right\} \right)
\end{aligned}
\tag{C.18}
$$

Appendix D

Operator notation used in this dissertation.

The operator notation presented in this dissertation is based on a set of basic operations for Fourier optics. Fourier optics calculations are often made for monochromatic light, which is usually described with complex amplitudes, containing information both on amplitude and phase of the electrical installation. Typically, these operators have parameters that are influenced by the configuration of the optical system under examination.

Fourier transformation: This operator is represented by the symbol $\mathcal{F}e$ or with '~' and is defined by:

$$\mathcal{F}e\{U(x,y)\} = \tilde{U}(k_x,k_y) = \iint U(x,y)\exp\left[-i2\pi(xk_x+yk_y)\right]dx\,dy \tag{D.1}$$

where k_x and k_y are coordinators in frequency domain. The inverse Fourier transform operator is defined as $\mathcal{F}e^{-1}$ as:

$$\mathcal{F}^{-1}\{\tilde{U}(k_x,k_y)\} = U(x,y) = \iint \tilde{U}(k_x,k_y)\exp\left[i2\pi(xk_x+yk_y)\right]dk_x\,dk_y \tag{D.2}$$

The field in the entrance pupil of the lens and the field in the focal plane are related by a Fourier transform. In another word, a lens performs a Fourier transform. details can be found in ref [27].

Quadratic phase function : $\mathcal{Q}$stands for quadratic phase function defined as:

$$Q(b) = \exp\left[\left(\frac{i\pi b}{\lambda}\right)(x^2+y^2)\right] \tag{D.3}$$

Under paraxial approximation, a thin lens or concave mirror is modeled as a quadratic phase transformation. Assuming a thin lens or concave mirror has a focal length of {, then transmission function is the

paraxial approximation to the spherical phase, such as:

$$t_{\text{lens}}(x,y) = Q\left(-\frac{1}{f}\right) = \exp\left[\left(-\frac{i\pi}{\lambda f}\right)(x^2+y^2)\right] \tag{D.4}$$

where Q characterizes the modulation imposed by the lens on the incident wave. If f is positive, the incident plane wave is converted to a spherical wave converging to a point after propagating a distance f behind the lens. If f is negative, it will diverge from the point at f in front of lens.

Linear phase function : L is the linear phase function such that:

$$L(\bar{s}) = \exp\left[i2\pi\lambda^{-1}(s_x x + s_y y)\right] \tag{D.5}$$

As fluorescence microscopy is an incoherent system, the incoherent transfer function (OTF) can be evaluated by the Fourier transform of the incoherent impulse response (PSF), the translation of the incoherent impulse response produces a linear phase in the OTF.